eISSN 2450-8071
ISSN 0867-888X
Index 35726 X

INSTITUTE
OF FUNDAMENTAL
TECHNOLOGICAL
RESEARCH
POLISH
ACADEMY
OF SCIENCES

in cooperation with:

UNIVERSITÉ
DE LORRAINE

POZNAN
UNIVERSITY
OF TECHNOLOGY

ENGINEERING TRANSACTIONS

ROZPRAWY INŻYNIERSKIE – TRAITE d'INGENIERIE

QUARTERLY
VOLUME 74 ISSUE 2

WARSAW – METZ – POZNAN 2026

INSTITUTE
OF FUNDAMENTAL
TECHNOLOGICAL
RESEARCH
POLISH
ACADEMY
OF SCIENCES

UNIVERSITÉ
DE LORRAINE

POZNAN
UNIVERSITY
OF TECHNOLOGY

ENGINEERING TRANSACTIONS

ROZPRAWY INŻYNIERSKIE – TRAITE d'INGENIERIE

QUARTERLY
VOLUME 74
ISSUE 2

WARSAW – METZ – POZNAN 2026

ENGINEERING TRANSACTIONS

Founded 1952
Appears since 1953

Aims and Scope

ENGINEERING TRANSACTIONS promotes research and practise in engineering science and provides a forum for interdisciplinary publications combining **mechanics** with material science, mechatronics, biomechanics, and biotechnologies, environmental science, photonics, information technologies, and other engineering applications. The journal publishes original papers covering a broad area of research activities including experimental and hybrid techniques as well as analytical and numerical approaches. Engineering Transactions is a quarterly issued journal for researchers in academic and industrial communities.

Editorial Office
Institute of Fundamental Technological Research, Polish Academy of Sciences
Pawińskiego 5B, 02-106 Warsaw, Poland
e-mail: engtrans@ippt.pan.pl https://et.ippt.pan.pl/

Abstracted/indexed in: Web of Science (Clarivate) JCR Core Collection, EBSCO, Elsevier – Scopus, DOAJ, BazTech, Biblioteka Nauki, ICI Journal Master List.

Impact stats: Journal Impact Factor (IF) 2025: 1.1, SCImago Journal Rank (SJR) 2025: 0.245, CiteScore 2025 (Scopus): 1.9, SNIP 2025: 0.636.

Typesetting in LaTeX: Jezierska Katarzyna Publisher's sheets 18.0 Printed sheets 14.5

Engineering Transactions, **74**(2): 125–144, 2026, https://doi.org/10.24423/engtrans.2026.3610
Institute of Fundamental Technological Research Polish Academy of Sciences (IPPT PAN)
Université de Lorraine • Poznan University of Technology

Research Paper

On the Out-of-Plane Deviation of Bending Deformation States in Moderately Thick Bars with Asymmetric Cross-Sections

Radosław Czubacki*, Zofia Kozyra, Tomasz Lewiński

Faculty of Civil Engineering, Warsaw University of Technology
Warsaw, Poland

*Corresponding Author: radoslaw.czubacki@pw.edu.pl

A characteristic feature of the six-parameter theories of bars is the coupled form of the constitutive equations; in particular the equations linking transverse forces with transverse shear deformations cannot be, in general, decoupled while keeping a separate form of the remaining constitutive equations. The mentioned feature of the constitutive equations implies that, within the six-parameter theories of straight elastic prismatic bars, there do not exist, in general, plane states of bending/shearing deformations. Thus, any vertical load causes lateral deflections, the only exception being the pure bending problem. The present paper delivers analytical solutions: closed-form formulae for shape functions, i.e., deformation states associated with kinematic loads at the ends, and solutions to selected static problems corresponding to transverse span load. Although elementary, the presented solutions seem to be derived for the first time. In particular, the hitherto published shape functions concerned the theories of moderately thick bars in which all the constitutive equations are decoupled.

Keywords: six-parameter theory of bars, moderately thick bars, shape functions.

1. INTRODUCTION

Among the theories of linearly elastic straight prismatic bars the most important are: the theory by Vlasov [1] for bars with thin-walled and open profiles and the six-parameter theories of moderately thick bars attributed to Timoshenko, see Bazoune *et al.* [2], or to Saint-Venant, see Petrolo and Cassciaro [3]. A peculiar feature of the Vlasov theory is the decoupling of the constitutive equations: the axial force is linked to the axial strain, the bending moments are proportional to the corresponding bending strains, the torsional moment is linked to the measure of torsion and the bimoment is proportional to the measure of warping due to torsion. This decoupling is possible by applying special measures:

– assuming the principal axes y and z of the cross-section $\mathcal{A}$,

– an appropriate choice of the starting point of the sectorial coordinate,

– an appropriate choice of the position of the pole.

The formalism of the Vlasov theory can be extended to the case of straight prismatic bars with arbitrary cross-sections, see Lewiński and Czarnecki [4, Sec. 9], still preserving the mentioned decoupling of the constitutive equations by making appropriate measures concerning the position of the axes to which the internal forces are referred.

The theory of Vlasov neglects the transverse shear deformations thus removing the transverse forces from the set of internal forces of the theory. However, including transverse shear effects is possible since the Saint-Venant theory provides analytical expressions for the functions modeling warping due to shear, see Love [5] and Ieşan [6]. Such a bar theory has been proposed by Librescu and Song [7]. By neglecting in this theory the contribution of warping due to torsion to the elastic energy one arrives at a six-parameter theory. Its form in the 3D setting is not unique. In a standard approach, all the internal forces are referred to the neutral axis, i.e., the axis linking the centroids of the cross-sections, see, e.g., Petrolo and Casciaro [3]. In this model, the axial force is proportional to the axial strain, the bending moments are linked to the corresponding measures of bending while the triple $(T_y, T_z, \mathcal{M})$ or the transverse forces and the torsional moment are linked with the triple: $(\gamma_y, \gamma_z, \rho)$, where γ_y and γ_z stand for the measures of transverse shear and ρ is the measure of torsional deformation. The 3×3 matrix linking these quantities is fully populated, see Petrolo and Casciaro [3, Eq. (40)].

The papers discussing more complicated models of bars, such as Dikaros *et al.* [8], El Fatmi [9, 10], show that, as in the Vlasov theory, it is expedient to shift the transverse forces to the axis $x_{(s)}$ linking the shear centers S. By an appropriate choice of functions modeling warping due to torsion and shear one can derive a bar model in which the torsional moment is only linked to the strain ρ, and the pair (T_y, T_z) is linked to the pair (γ_y, γ_z), the latter 2×2 matrix being, in general, fully filled up, i.e., the off-diagonal components are in general non-zero. If we decouple the latter 2×2 system by a certain rotation of the axes y and z, we introduce coupling in the constitutive equations for the bending moments. Indeed, there is no reason to change the parametrization y and z referred to the principal axes of the cross-section. We conclude: coupling of the constitutive equations linking (T_y, T_z) with the pair (γ_y, γ_z) is an immanent feature of the six-parameter theory of bars in all its versions.

The six-parameter model is the simplest theory of deformation of bars in space in which the kinematic unknowns are: u, v, w, θ, φ, β or, subsequently, the axial displacement, displacements of the shear center in the y- and z-directions, the angle of torsion, and the angles of rotations around the axes $(-z)$ and y. The internal forces of this theory are: N, T_y, T_z, $\mathcal{M}$, M_y, M_z or, respectively, the axial force, the transverse forces, torsional moment, and the bending moments in the y- and z-directions. The internal forces are linked to the measures of deformation: ϵ, γ_y, γ_z, ρ, κ_y, κ_z, or, respectively, the measures of axial strain, transverse shear strains, the measure of torsion, and measures of bending. The main feature of this theory is equality between the number of internal forces (always equal to the number of strains) and the number of kinematic fields. Thanks to this equality there exists a family of statically determinate problems, which paves the way for the force method, a helpful tool of structural mechanics.

If the cross-section of the bar is monosymmetric (or bisymmetric, in particular) then the problem of bending/transverse shearing in 3D decouples into two planar problems in the $x-y$ and $x-z$ planes. If the shape of the domain $\mathcal{A}$ of the cross-section is arbitrary then there do not exist plane states of bending/transverse shearing deformation. In particular, a load in the z-direction causes bending in two directions: z and y. It is precisely this problem that is studied in the present paper. The aim is to deliver explicit formulae for the deformation states of a bar subjected to kinematic loads and to selected transverse span loads.

The present paper draws upon the six-parameter theory of straight prismatic bars made of an isotropic and homogeneous material developed in [4, Sec. 10], called there the Timoshenko-like theory. A prerequisite of the theory is the construction of solutions to the three auxiliary elliptic problems posed on the domain $\mathcal{A}$ [4, Secs. 2–4]. Upon solving these problems one can fix the position of the shear center S with coordinates y_S, z_S referred to the principal axes and then determine all the required characteristics and stiffnesses of the bar. This algorithm will not be repeated in the present paper.

One of the aims of the present paper is to provide explicit formulae for the so-called shape functions or the deformation forms of a bar subjected to arbitrary kinematic loads. These functions are given in the compact Eq. (4.14). Interestingly, these formulae are not available in the literature. There is only one paper, namely the paper by SCHRAMM *et al.* [11] in which this problem is considered at a similar level of accuracy, but the explicit form of the solution (4.14) has not been published there. Other papers, such as [12–14], present solutions corresponding to the special case when the coupling of the constitutive equations is absent. This means that either these papers refer to monosymmetric cross-sections or the authors assume, usually tacitly, that the constitutive equations can be accepted in their decoupled form. This assumption paves the way for planar forms of the shape functions, which are incorrect in general or refer to the special case of the cross-section being mono- or bisymmetric.

Moreover, another aim of the present paper is to derive the specific shapes of deformation caused by span loads. In particular, the paper shows that the point loads generate rather unexpected lateral deflections in the form of zigzag lines.

2. EQUATIONS OF THE THEORY

Consider a straight prismatic bar with the cross-section $\mathcal{A}$, for which we construct the principal axes y and z, the centroid being its center. The axis x is orthogonal to the domain $\mathcal{A}$; this axis links the centroids of all cross-sections. They are x-independent, which means that the bar is prismatic. The domain of the bar is filled with a homogeneous and isotropic elastic material with Young's modulus E and shear modulus G. The shear center S has the coordinates (y_S, z_S); their construction is explained in [4, Sec. 2]. According to the underlying theory this center coincides with the center of torsion; in more complicated formulations these centers do not coincide, see comments in [4]. By linking points S we form the straight line $x_{(s)}$. Having solved the elliptic problems set up [4, Secs. 2–4] one can compute: the area A of $\mathcal{A}$, the principal moments of inertia J_y, J_z, and the shear correction factors k_y, $k_{yz} = k_{zy}$, k_z forming the matrix $\mathbf{k}$; its inverse is denoted by $\boldsymbol{\alpha}$:

$$\mathbf{k} = \begin{bmatrix} k_y & k_{yz} \\ k_{zy} & k_z \end{bmatrix}, \qquad \boldsymbol{\alpha} = \mathbf{k}^{-1}, \qquad \boldsymbol{\alpha} = \begin{bmatrix} \alpha_y & \alpha_{yz} \\ \alpha_{zy} & \alpha_z \end{bmatrix}. \tag{2.1}$$

Both the matrices $\mathbf{k}$ and $\boldsymbol{\alpha}$ are positive definite. One can compute also the torsional constant J and the torsional stiffness GJ.

The state of deformation of the bar is determined by the kinematic fields $u(x)$, $v(x)$, $w(x)$, $\theta(x)$, $\varphi(x)$, $\beta(x)$ given along the bar, see Fig. 1a. The field u is an average of the displacements $u_x(x, y, z)$ over $\mathcal{A}$, while θ is the angle of rotation of $\mathcal{A}$ around the axis x, the functions v and w represent the displace-

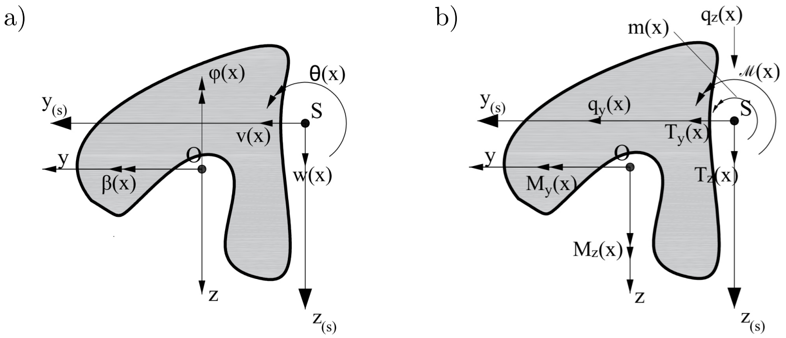

FIG. 1. Sign conventions concerning the kinematic unknowns (a) and the static unknowns (b) at the cross-section $x = \text{const}$.

ments of the point S along the y- and z-axes, respectively, φ and β are defined by the averages:

$$\beta(x) = \frac{1}{J_y}\int\limits_{\mathcal{A}} z u_x \, \mathrm{d}\mathcal{A}, \qquad \varphi(x) = \frac{1}{J_z}\int\limits_{\mathcal{A}} y u_x \, \mathrm{d}\mathcal{A}. \tag{2.2}$$

Their signs are chosen such that they cause positive displacements $u_x(x, y, z)$ if $y > 0$ and $z > 0$.

The loads acting along the bar are reduced to: the axial load of intensity $p(x)$, the transverse loads $q_y(x)$, $q_z(x)$ acting along the axes $y_{(s)}$, $z_{(s)}$, and the distributed moments $m(x)$ acting along the axis $x_{(s)}$.

The following internal forces (or stress and couple resultants) appear in the bar: the axial force $N(x)$, the transverse forces $T_y(x)$, $T_z(x)$ acting along the $y_{(s)}$, and $z_{(s)}$ directions, the bending moments $M_y(x)$, $M_z(x)$ acting along the axes y and z, and $\mathcal{M}(x)$ or the torsional moment acting along the axis $x_{(s)}$, see Fig. 1b.

The following strains are defined within the theory:

$$\begin{aligned} &\epsilon = \frac{\mathrm{d}u}{\mathrm{d}x}, \qquad &&\gamma_y = \frac{\mathrm{d}v}{\mathrm{d}x} + \varphi, \qquad &&\gamma_z = \frac{\mathrm{d}w}{\mathrm{d}x} + \beta, \\ &\kappa_y = \frac{\mathrm{d}\beta}{\mathrm{d}x}, \qquad &&\kappa_z = -\frac{\mathrm{d}\varphi}{\mathrm{d}x}, \qquad &&\rho = \frac{\mathrm{d}\theta}{\mathrm{d}x}, \end{aligned} \tag{2.3}$$

where ϵ represents the relative elongation of the bar, γ_y, γ_z are the measures of transverse shear strains in the planes: $x-y$ and $x-z$, respectively; κ_z, κ_y are the measures of bending in the planes $x-y$ and $x-z$, and ρ is the measure of torsion.

By virtue of special measures, i.e., specific interpretations of the internal forces, strains, and kinematic fields, the problem of statics of a bar decomposes into three independent problems:

($\mathcal{P}_1$) The tension/compression problem:
find $N(x)$, $\epsilon(x)$, $u(x)$ such that

$$\frac{\mathrm{d}N}{\mathrm{d}x} + p = 0, \qquad N = EA\epsilon, \qquad \epsilon = \frac{\mathrm{d}u}{\mathrm{d}x}, \tag{2.4}$$

while at the ends $x = 0$, $x = l$, either N or u is given.

($\mathcal{P}_2$) The torsion problem:
find $\mathcal{M}(x)$, $\rho(x)$, $\theta(x)$ such that

$$\frac{\mathrm{d}\mathcal{M}}{\mathrm{d}x} + m = 0, \qquad \mathcal{M} = GJ\rho, \qquad \rho = \frac{\mathrm{d}\theta}{\mathrm{d}x}, \tag{2.5}$$

while at the ends $x = 0$, $x = l$, either $\mathcal{M}$ or θ is given

($\mathcal{P}_3$) The bending/transverse shearing problem:
find $T_y(x)$, $T_z(x)$, $M_y(x)$, $M_z(x)$, $\kappa_z(x)$, $\kappa_y(x)$, $\gamma_y(x)$, $\gamma_z(x)$, $v(x)$, $w(x)$, $\varphi(x)$, $\beta(x)$ such that

$$\begin{gathered}\frac{\mathrm{d}T_z}{\mathrm{d}x} + q_z = 0, \qquad T_z = \frac{\mathrm{d}M_y}{\mathrm{d}x}, \qquad M_y = EJ_y\kappa_y,\\ \kappa_y = \frac{\mathrm{d}\beta}{\mathrm{d}x}, \qquad \gamma_y = \varphi + \frac{\mathrm{d}v}{\mathrm{d}x},\end{gathered} \tag{2.6}$$

$$\begin{gathered}\frac{\mathrm{d}T_y}{\mathrm{d}x} + q_y = 0, \qquad T_y = -\frac{\mathrm{d}M_z}{\mathrm{d}x}, \qquad M_z = EJ_z\kappa_z,\\ \kappa_z = -\frac{\mathrm{d}\varphi}{\mathrm{d}x}, \qquad \gamma_z = \beta + \frac{\mathrm{d}w}{\mathrm{d}x},\end{gathered} \tag{2.7}$$

$$T_y = GA(k_y\gamma_y + k_{yz}\gamma_z), \qquad T_z = GA(k_{zy}\gamma_y + k_z\gamma_z). \tag{2.8}$$

At the ends $x = 0$ or $x = l$, the following are given: either w or T_z, either β or M_y, either v or T_y, and either φ or M_z.

Let us stress once again that in the standard setting the bending/shearing problem and the torsion problem are coupled, see Petrolo and Casciaro [3].

3. Simplifications in the case of mono-symmetric profiles

If the axis $y = 0$ is a symmetry axis of the domain $\mathcal{A}$ then $k_{yz} = k_{zy} = 0$, $\alpha_{yz} = \alpha_{zy} = 0$, and the bending/shearing problem splits up into two problems:

- find $T_y(x)$, $M_z(x)$, $\kappa_z(x)$, $\gamma_y(x)$, $v(x)$, $\varphi(x)$, such that

$$\begin{aligned} \frac{\mathrm{d}T_y}{\mathrm{d}x} + q_y &= 0, & T_y &= -\frac{\mathrm{d}M_z}{\mathrm{d}x},\\ T_y &= k_yGA\gamma_y, & M_z &= EJ_z\kappa_z,\\ \gamma_y &= \varphi + \frac{\mathrm{d}v}{\mathrm{d}x}, & \kappa_z &= -\frac{\mathrm{d}\varphi}{\mathrm{d}x}. \end{aligned} \tag{3.1}$$

At the ends $x = 0$, $x = l$, either v or T_y; either φ or M_z are prescribed;

- find $T_z(x)$, $M_y(x)$, $\kappa_y(x)$, $\gamma_z(x)$, $w(x)$, $\beta(x)$, such that

$$\begin{aligned} \frac{\mathrm{d}T_z}{\mathrm{d}x} + q_z &= 0, & T_z &= \frac{\mathrm{d}M_y}{\mathrm{d}x},\\ T_z &= k_zGA\gamma_z, & M_y &= EJ_y\kappa_y,\\ \gamma_z &= \beta + \frac{\mathrm{d}w}{\mathrm{d}x}, & \kappa_y &= \frac{\mathrm{d}\beta}{\mathrm{d}x}. \end{aligned} \tag{3.2}$$

At the ends $x = 0$, $x = l$, either w or T_z; either β or M_y are prescribed.

The majority of analyses available in the literature concern the aforementioned problems.

If one assumes that, additionally, $z = 0$ is a symmetry axis, then the domain $\mathcal{A}$ is bisymmetric and S coincides with the centroid; $(y_S = 0, z_S = 0)$; the axes x and $x_{(s)}$ coincide. Then, the loads q_z, q_y applied along the x-axis do not cause torsion. However, Eq. (3.1) and Eq. (3.2) do not change. Solving the static problems of bars with a mono-symmetric cross-section is no more complicated than in the case of bisymmetric cross-sections.

4. DEFORMATIONS CAUSED BY KINEMATIC LOADS

Assume that the cross-section $\mathcal{A}$ is of arbitrary shape, and the bar is clamped at both ends: $x = 0$, $x = l$. The span load is absent. The kinematic boundary conditions have the form:

$$\begin{aligned} &u(0) = {}^*u, && u(l) = u^*, && \theta(0) = {}^*\theta, && \theta(l) = \theta^*,\\ &w(0) = {}^*w, && w(l) = w^*, && \beta(0) = {}^*\beta, && \beta(l) = \beta^*,\\ &v(0) = {}^*v, && v(l) = v^*, && \varphi(0) = {}^*\varphi, && \varphi(l) = \varphi^*. \end{aligned} \tag{4.1}$$

The solutions to problems $(\mathcal{P}_1)$ and $(\mathcal{P}_2)$ are elementary:

$$\begin{aligned} u(x) &= {}^*u \cdot (1-\xi) + u^*\xi,\\ \theta(x) &= {}^*\theta \cdot (1-\xi) + \theta^*\xi, \qquad \xi = \frac{x}{l}. \end{aligned} \tag{4.2}$$

In order to solve problem $(\mathcal{P}_3)$, let us note that the deflections satisfy the following uncoupled system of equations:

$$\begin{aligned} EJ_z\frac{\mathrm{d}^4v}{\mathrm{d}x^4} &= q_y - \frac{EJ_z}{GA}\left(\alpha_y\frac{\mathrm{d}^2q_y}{\mathrm{d}x^2} + \alpha_{yz}\frac{\mathrm{d}^2q_z}{\mathrm{d}x^2}\right),\\ EJ_y\frac{\mathrm{d}^4w}{\mathrm{d}x^4} &= q_z - \frac{EJ_y}{GA}\left(\alpha_{yz}\frac{\mathrm{d}^2q_y}{\mathrm{d}x^2} + \alpha_z\frac{\mathrm{d}^2q_z}{\mathrm{d}x^2}\right), \end{aligned} \tag{4.3}$$

provided that the span loads $q_z(x)$, $q_y(x)$ are smooth. In our case $q_y = 0$, $q_z = 0$, hence we see that both deflections are expressed by polynomials of degree 3, while the angles of rotation β, φ are expressed by polynomials of degree 2. Let us introduce the non-dimensional parameters:

$$\varkappa_y = \frac{12EJ_y}{l^2GA}, \qquad \varkappa_z = \frac{12EJ_z}{l^2GA}. \tag{4.4}$$

Let (α_1, α_2) and $(\widetilde{\alpha}_1, \widetilde{\alpha}_2)$ be solutions to the systems:

$$\begin{bmatrix} k_y + \varkappa_z & k_{yz} \\ k_{yz} & k_z + \varkappa_y \end{bmatrix} \begin{bmatrix} \alpha_1 \\ \alpha_2 \end{bmatrix} = \begin{bmatrix} 0 \\ \varkappa_y \end{bmatrix}, \tag{4.5}$$

$$\begin{bmatrix} k_z + \varkappa_y & k_{yz} \\ k_{yz} & k_y + \varkappa_z \end{bmatrix} \begin{bmatrix} \widetilde{\alpha}_1 \\ \widetilde{\alpha}_2 \end{bmatrix} = \begin{bmatrix} 0 \\ \varkappa_z \end{bmatrix}. \tag{4.6}$$

Let us introduce the polynomials:

$$\begin{gathered} a(\xi) = 1 - 3\xi^2 + 2\xi^3, \quad b(\xi) = \xi - 3\xi^2 + 2\xi^3, \quad c(\xi) = \xi - 2\xi^2 + \xi^3, \\ d(\xi) = 6\xi - 6\xi^2, \quad e(\xi) = 1 - 4\xi + 3\xi^2, \end{gathered} \tag{4.7}$$

with plots for $0 \leq \xi \leq 1$ presented in Fig. 2.

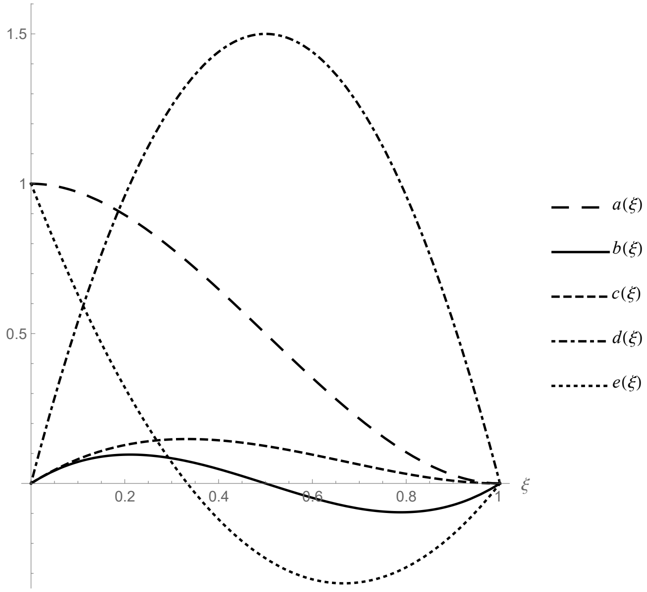

FIG. 2. Plots of the polynomials a, b, c, d, e.

The factorized forms of these polynomials read:

$$\begin{gathered} a(\xi) = (1-\xi)^2(1+2\xi), \quad b(\xi) = \xi(1-\xi)(1-2\xi), \quad c(\xi) = \xi(1-\xi)^2, \\ d(\xi) = 6\xi(1-\xi), \quad e(\xi) = (1-\xi)(1-3\xi). \end{gathered} \tag{4.8}$$

Let us introduce the angles of slopes in the $x - z$ and $x - y$ planes:

$$\psi = \frac{1}{l}\left(w^* - {}^*w\right), \qquad \chi = \frac{1}{l}\left(v^* - {}^*v\right), \tag{4.9}$$

as well as the mean values of the angles of rotation at the ends of the bar:

$$\beta_o = \frac{1}{2}\left({}^*\beta + \beta^*\right), \qquad \varphi_o = \frac{1}{2}\left({}^*\varphi + \varphi^*\right). \tag{4.10}$$

According to the Bernoulli–Euler theory (i.e., the theory of thin bars), the deflection functions and the functions representing variation of the angles of rotations of the bar's cross-sections are expressed as follows:

$$\begin{aligned}
\widehat{w}(x) &= l\left[\frac{{}^*w}{l}a(\xi) + \frac{w^*}{l}a(1-\xi) - {}^*\beta c(\xi) + \beta^* c(1-\xi)\right],\\
\widehat{v}(x) &= l\left[\frac{{}^*v}{l}a(\xi) + \frac{v^*}{l}a(1-\xi) - {}^*\varphi c(\xi) + \varphi^* c(1-\xi)\right],\\
\widehat{\beta}(x) &= {}^*\beta e(\xi) + \beta^* e(1-\xi) - \psi d(\xi),\\
\widehat{\varphi}(x) &= {}^*\varphi e(\xi) + \varphi^* e(1-\xi) - \chi d(\xi),
\end{aligned} \tag{4.11}$$

where

$$a(1-\xi) = 3\xi^2 - 2\xi^3, \quad c(1-\xi) = \xi^2 - \xi^3, \quad e(1-\xi) = -2\xi + 3\xi^2. \tag{4.12}$$

Thus, the angles of rotation are linked to the deflection functions by:

$$\widehat{\beta} = -\frac{\mathrm{d}\widehat{w}}{\mathrm{d}x}, \qquad \widehat{\varphi} = -\frac{\mathrm{d}\widehat{v}}{\mathrm{d}x}, \tag{4.13}$$

since the theory of thin bars imposes constraints on the angles of rotation of cross-sections, this assures the zero values of the transverse shear deformations in both the planes: $x - z$, $x - y$.

The deflection functions and the functions representing the variation of the angles of rotation within the six-parameter theory of bars differ from the mentioned solutions by terms involving the quantities $\psi + \beta_o$, $\chi + \varphi_o$, namely:

$$\begin{aligned}
w(x) &= \widehat{w}(\xi) + l\left[\alpha_2(\psi + \beta_o) + \widetilde{\alpha}_1(\chi + \varphi_o)\right] b(\xi),\\
\beta(x) &= \widehat{\beta}(\xi) + \left[\alpha_2(\psi + \beta_o) + \widetilde{\alpha}_1(\chi + \varphi_o)\right] d(\xi),\\
v(x) &= \widehat{v}(\xi) + l\left[\alpha_1(\psi + \beta_o) + \widetilde{\alpha}_2(\chi + \varphi_o)\right] b(\xi),\\
\varphi(x) &= \widehat{\varphi}(\xi) + \left[\alpha_1(\psi + \beta_o) + \widetilde{\alpha}_2(\chi + \varphi_o)\right] d(\xi).
\end{aligned} \tag{4.14}$$

Note that the quantities $\psi + \beta_o$, $\chi + \varphi_o$ are discrete deformation measures in the natural approach by Argyris (see comments in Petrolo and Casciaro [3]).

Since $T_y = \text{const}$ and $T_z = \text{const}$, the deformation measures $\gamma_y = \gamma_y^o$, $\gamma_z = \gamma_z^o$ are constant and equal:

$$\begin{aligned} \gamma_y^o &= \alpha_1(\psi + \beta_0) + \widetilde{\alpha}_2(\chi + \varphi_0), \\ \gamma_z^o &= \alpha_2(\psi + \beta_0) + \widetilde{\alpha}_1(\chi + \varphi_0). \end{aligned} \tag{4.15}$$

The shear deformations are expressed by the functions:

$$\begin{aligned} w_T(x) &= l\gamma_z^o b\left(\frac{x}{l}\right), \\ \beta_T(x) &= \gamma_z^o d\left(\frac{x}{l}\right), \\ v_T(x) &= l\gamma_y^o b\left(\frac{x}{l}\right), \\ \varphi_T(x) &= \gamma_y^o d\left(\frac{x}{l}\right). \end{aligned} \tag{4.16}$$

Thus, the final deformation (4.14) is also expressed as the superposition as follows:

$$\begin{aligned} w(x) &= \widehat{w}(x) + w_T(x), \\ \beta(x) &= \widehat{\beta}(x) + \beta_T(x), \\ v(x) &= \widehat{v}(x) + v_T(x), \\ \varphi(x) &= \widehat{\varphi}(x) + \varphi_T(x). \end{aligned} \tag{4.17}$$

The shear load is skew–symmetric with respect to the plane $x = l/2$, hence the functions $w_T(x)$, $v_T(x)$ are skew–symmetric, while the functions $\beta_T(x)$, $\varphi_T(x)$ are symmetric with respect to $x = l/2$. The extremal values of the latter functions are attained in the middle of the bar and read:

$$\beta_T\left(\frac{l}{2}\right) = \frac{3}{2}\gamma_z^o, \qquad \varphi_T\left(\frac{l}{2}\right) = \frac{3}{2}\gamma_y^o. \tag{4.18}$$

Let us conclude that the final deformation is a sum of the bending deformation predicted by the thin bar theory and the shear deformation added by the six-parameter theory.

The bar theoretical results (4.17) determine the shapes of deformation of the bar viewed as a 3D body; in particular one can predict the transverse deformation of the cross-sections $x = \text{const}$; it is given by the function $u_x(x, y, z)$ which represents the displacement along the x-axis of the point (x, y, z). According to El-Fatmi's kinematical hypothesis, this function has the form, see [4]:

$$u_x = u(x) + y\varphi(x) + z\beta(x) + \omega(y,z)\rho(x) + [\eta(y,z) - y]\gamma_y(x) + [\zeta(y,z) - z]\gamma_z(x), \tag{4.19}$$

where ρ is the measure of torsion, $\omega(y,z)$ is the warping function due to torsion, and $\eta(y,z)$, $\zeta(y,z)$ characterize warping due to transverse shear in the $x-y$ and $x-z$ planes. In the problem discussed here, axial deformation and torsion are not present (which is a justified assumption due to the decoupling phenomena of the discussed theory). Since

$$\begin{aligned} &\int\limits_{\mathcal{A}} y(\eta - y)\,\mathrm{d}\mathcal{A} = 0, &\qquad &\int\limits_{\mathcal{A}} z(\zeta - z)\,\mathrm{d}\mathcal{A} = 0, \\ &\int\limits_{\mathcal{A}} z(\eta - y)\,\mathrm{d}\mathcal{A} = 0, &\qquad &\int\limits_{\mathcal{A}} y(\zeta - z)\,\mathrm{d}\mathcal{A} = 0, \end{aligned} \tag{4.20}$$

Eq. (2.2) holds; consequently the last two terms in Eq. (4.19) do not affect the angles of rotation β, φ understood as the averaged quantities, see Eq. (2.2). In Fig. 3, for simplicity, we shall not show the deformations generated by these

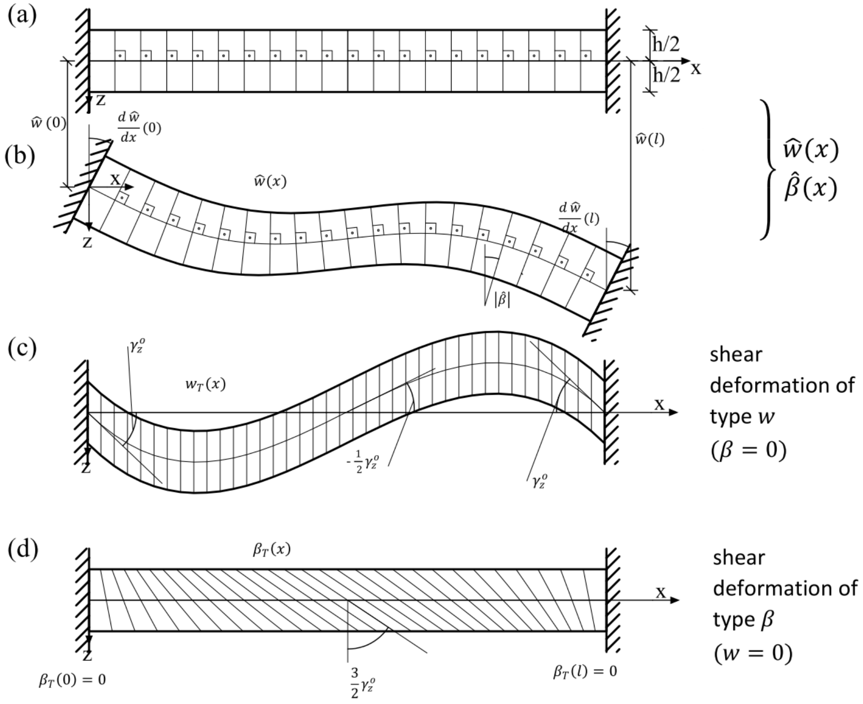

Fig. 3. Orthogonal net in the plane $x - z$ (a), bending deformation according to the thin bar theory (b), the deformation due to shear with $\beta = 0$ (c), the deformation due to shear with $w = 0$ (d).

quantities; the deformation of the orthogonal net of lines along x- and z-axes will be approximated by $u_x = y\varphi(x) + z\beta(x)$, $u_z = w(x)$, or within the assumption of planar cross-sections.

For the illustration of the deformation state of the bar assume that:

$$w(0) > 0, \qquad w(l) > w(0), \qquad \frac{\mathrm{d}w}{\mathrm{d}x}(0) > 0, \qquad \frac{\mathrm{d}w}{\mathrm{d}x}(l) > 0, \qquad \gamma_z^o > 0.$$

Before deformation, the net $x = \text{const}$, $z = \text{const}$ is orthogonal, see Fig. 3a. The fields $\widehat{w}$, $\widehat{\beta}$ determine bending deformation preserving orthogonality, see Fig. 3b. The transverse end forces act in a skew–symmetric manner and generate the deflection $w_T(x)$ characterizing shear deformation: the angles of rotation of tangents to the neutral line are γ_z^o at the ends and equal to $(-1/2)\gamma_z^o$ in the middle of the bar, see Fig. 3c. Here to the angles of rotation of the transverse cross-sections vanish. The angles of rotation generated by the shear forces are expressed by the function $\beta_T(x)$; this function vanishes at both the ends and is extremal in the middle of the bar, see Fig. 3d; the corresponding deflection is 0.

Kinematic loads in the plane $x - z$ generate, in general, deformation in the plane $x - y$. This phenomenon will be discussed below by considering two kinds of kinematic loads.

4.1. CASE 1

Consider the kinematic load:

$$(4.21) \qquad {}^*w = 1, \qquad w^* = {}^*v = v^* = 0, \qquad {}^*\beta = \beta^* = {}^*\varphi = \varphi^* = 0.$$

The deformation of the bar is given by:

$$(4.22) \qquad \begin{aligned} w(x) &= (1 - 3\xi^2 + 2\xi^3)\underline{-\alpha_2(\xi - 3\xi^2 + 2\xi^3)},\\ \beta(x) &= \frac{1}{l}(1 - \alpha_2)(6\xi - 6\xi^2),\\ v(x) &= -\alpha_1(\xi - 3\xi^2 + 2\xi^3),\\ \varphi(x) &= -\frac{1}{l}\alpha_1(6\xi - 6\xi^2), \qquad \xi = x/l. \end{aligned}$$

To be specific let us fix the domains $\mathcal{A}$ as Z-shape, U-shape, and RI60 rail, denoted as A1, A2, A3, see Fig. 4. Their characteristics are set up in Table 1. Assume that the length of the bar is $l = 1\,\mathrm{m}$ for case (a), $l = 2\,\mathrm{m}$ for case (b); $E = 210\,\mathrm{GPa}$, $G = 81\,\mathrm{GPa}$. Their non-dimensional parameters $\varkappa_y$, $\varkappa_z$, α_1, α_2, $\widetilde{\alpha}_1$, $\widetilde{\alpha}_2$ are given in Table 2.

The shape of the line $x_{(s)}$ upon deformation, determined by Eq. (4.22), is spatial, see Fig. 5; the points (x, y_S, z_S) displace in two directions: z (let us call it transverse) and y (let us call it lateral).

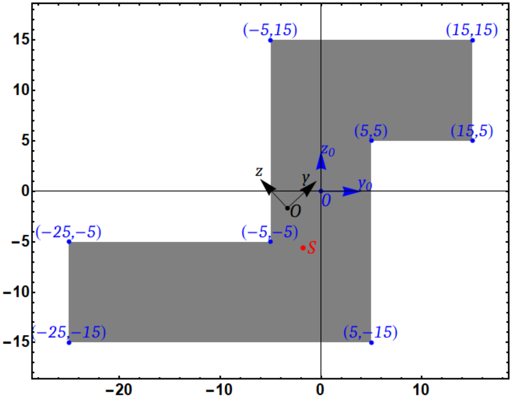
a) Z – cross-section

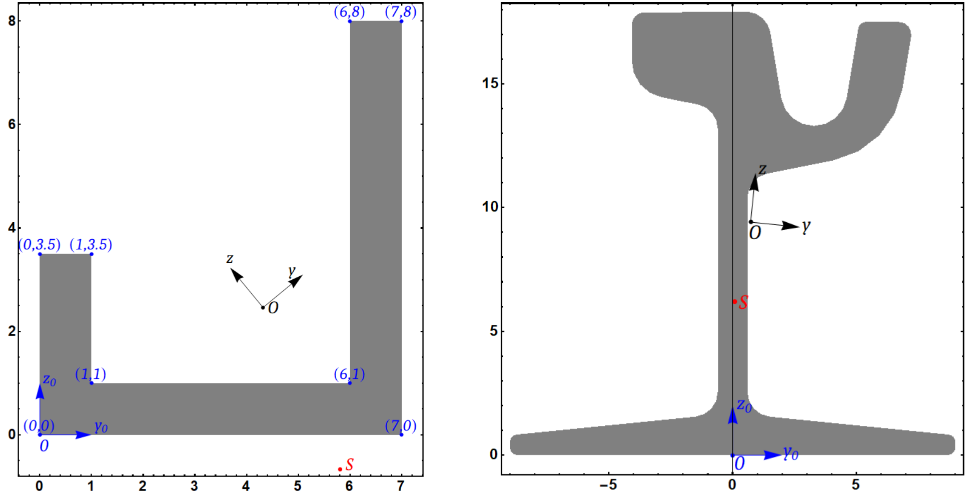
b) U – cross-section

c) RI60 rail cross-section

FIG. 4. Chosen cross-sections of the bar, called A1 (a), A2 (b), A3 (c).

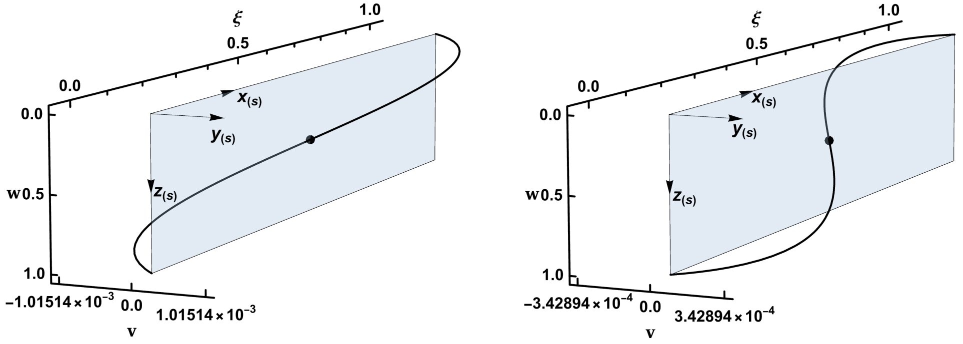
a) for Z – cross-section

b) for U – cross-section

FIG. 5. Deflections caused by the kinematic load in case 1 for the length of the bar 1 m and the cross-sections A1 (a), A2 (b).

TABLE 1. Characteristics of the cross-sections shown in Fig. 4.

	A [cm^2]	J_y [cm^4]	J_z [cm^4]	J [cm^4]	$y_{0(O)}$ [cm]	$z_{0(O)}$ [cm]	$y_{0(S)}$ [cm]	$z_{0(S)}$ [cm]	$\measuredangle(y_0, y)$ [°]	k_y [–]	$k_{yz} = k_{zy}$ [–]	k_z [–]
A1	600	19 082	92 585	19 338	−3.333	−1.667	−1.812	−5.598	43.0	0.555	−0.075	0.587
A2	16.5	50	140.43	5.438	4.318	2.462	5.815	−0.675	39.5	0.351	0.0669	0.471
A3	77.1	3367.3	902.05	129.67	0.727	9.415	0.0792	6.189	−5.83	0.491	0.0027	0.288

TABLE 2. Characteristics of the bars with the cross-sections shown in Fig. 4, for lengths of 1 m (Ana) and lengths 2 m (Anb), $n = 1, 2, 3$.

	$\varkappa_y$	$\varkappa_z$	α_1	α_2	$\widetilde{\alpha}_1$	$\widetilde{\alpha}_2$
A1a	0.09894	0.4801	0.01055	0.1455	0.05119	0.4674
A1b	0.02474	0.1200	0.004561	0.04102	0.02213	0.1802
A2a	0.009428	0.02648	−0.003563	0.02013	−0.01001	0.07186
A2b	0.002357	0.006620	−0.0009561	0.005116	−0.002685	0.01900
A3a	0.1359	0.03640	−0.001674	0.3209	−0.0004484	0.06907
A3b	0.03397	0.009100	−0.0005812	0.1056	−0.0001557	0.01821

TABLE 3. Maximal absolute values of horizontal displacement v and maximal absolute values of w_α for the analyzed bars.

	A1a	A1b	A2a	A2b	A3a	A3b
10^3 max $\lvert v \rvert$	1.015	0.4389	0.343	0.0920	0.1611	0.0559
10^3 max $\lvert w_\alpha \rvert$	14.00	3.948	1.937	0.4923	30.88	10.17

The term underlined in Eq. $(4.22)_1$ denoted here by $w_\alpha(x)$ represents the deflection due to transverse shear. The extremal values of this term are attained for $x = ((3-\sqrt{3})/6)l$ and $x = ((3+\sqrt{3})/6)l$, and are equal to $-(\sqrt{3}\alpha_2)/18$, $(\sqrt{3}\alpha_2)/18$, respectively. The lateral deflection $v(x)$ is skew–symmetric with respect to $x = l/2$. Maximal absolute values of v and w_a for the analyzed bars are given in Table 3.

4.2. CASE 2

We shall consider the state of deformation caused by the kinematic load:

$$ {}^*w = 0, \quad w^* = 0, \quad {}^*v = v^* = 0, \quad {}^*\beta = 1, \quad \beta^* = 0, \quad {}^*\varphi = \varphi^* = 0. \tag{4.23}$$

The deformation of the bar is determined by:

$$\begin{aligned} w(x) &= -l(\xi - 2\xi^2 + \xi^3) + \frac{l}{2}\alpha_2(\xi - 3\xi^2 + 2\xi^3), \\ \beta(x) &= (1 - 4\xi + 3\xi^2) + \frac{1}{2}\alpha_2(6\xi - 6\xi^2), \\ v(x) &= \frac{l}{2}\alpha_1(\xi - 3\xi^2 + 2\xi^3), \\ \varphi(x) &= \frac{1}{2}\alpha_1(6\xi - 6\xi^2), \qquad \xi = x/l. \end{aligned} \tag{4.24}$$

The deformation is spatial, a lateral deflection $v(x)$ appears, which is skew–symmetric with respect to $x = l/2$, see Fig. 6.

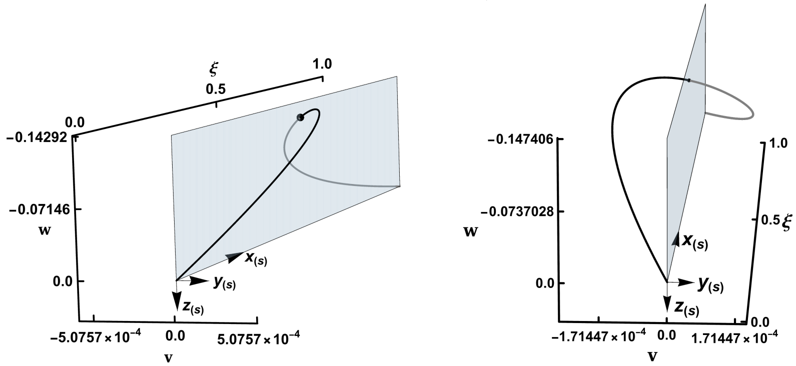

a) for Z – cross-section b) for U – cross-section

FIG. 6. Deflections caused by the kinematic load in case 2 for the length of the bar of 1 m and cross-sections A1 (a), A2 (b).

5. Deformations caused by span loads

5.1. Bar clamped at both ends, subjected to the transverse load $q_z = \text{const}$

The load $q_z = q = \text{const}$ acts along the axis $x_{(s)}$ linking the shear centers. The bar is clamped at both ends, i.e.:

$$\begin{aligned} &w(0)=0, \qquad w(l)=0, \qquad v(0)=0, \qquad v(l)=0,\\ &\beta(0)=0, \qquad \beta(l)=0, \qquad \varphi(0)=0, \qquad \varphi(l)=0. \end{aligned} \tag{5.1}$$

The solution to problem ($\mathcal{P}_3$) has the form:

$$\begin{aligned} w &= \frac{ql^4}{24EJ_y}\xi^2(1-\xi)^2 + \alpha_z\frac{ql^2}{2GA}\xi(1-\xi),\\ \beta &= -\frac{ql^3}{12EJ_y}(\xi - 3\xi^2 + 2\xi^3),\\ v &= \alpha_{yz}\frac{ql^2}{2GA}\xi(1-\xi),\\ \varphi &= 0. \end{aligned} \tag{5.2}$$

Let us note that $\beta_T = 0$, $\widehat{v} = 0$, $\widehat{\varphi} = 0$, $\varphi_T = 0$. The deformation is spatial, and there appears a lateral deflection $v(x)$ in the shape of a parabola. Its extremal value is $\alpha_{yz}ql^2/(8GA)$ and occurs at $x = l/2$. The distribution of internal forces is the same as in the thin bar theory and is given by:

$$\begin{aligned} M_y &= -\frac{ql^2}{12}(1 - 6\xi + 6\xi^2),\\ T_z &= ql\left(\frac{1}{2} - \xi\right),\\ M_z &= 0, \qquad T_y = 0. \end{aligned} \tag{5.3}$$

5.2. Bar simply supported in two directions at both ends, subjected to the transverse load $q_z = \text{const}$

The load $q_z = q = \text{const}$ acts along the axis $x_{(s)}$ linking the shear centers. The bar is simply supported in two directions at both the ends, i.e.:

$$\begin{aligned} &w(0)=0, \qquad w(l)=0, \qquad M_y(0)=0, \qquad M_y(l)=0,\\ &v(0)=0, \qquad v(l)=0, \qquad M_z(0)=0, \qquad M_z(l)=0. \end{aligned} \tag{5.4}$$

The solution to problem ($\mathcal{P}_3$) has the form:

$$
\begin{aligned}
w &= \frac{ql^4}{24EJ_y}\xi(1-\xi)(1+\xi-\xi^2)+\alpha_z\frac{ql^2}{2GA}\xi(1-\xi),\\
\beta &= -\frac{ql^3}{24EJ_y}(1-6\xi^2+4\xi^3),\\
v &= \alpha_{zy}\frac{ql^2}{2GA}\xi(1-\xi),\\
\varphi &= 0.
\end{aligned}
\tag{5.5}
$$

We see that the lateral deflection is the same as in the previous example. The distribution of internal forces is the same as in the thin bar theory:

$$
\begin{aligned}
M_y &= \frac{1}{2}ql^2\xi(1-\xi),\\
T_z &= ql\left(\frac{1}{2}-\xi\right),\\
M_z &= 0, \qquad T_y = 0.
\end{aligned}
\tag{5.6}
$$

5.3. CANTILEVER UNDER A POINT LOAD P AT ITS END

The boundary conditions read:

$$
\begin{aligned}
&w(0)=0, \qquad v(0)=0, \qquad \varphi(0)=0, \qquad \beta(0)=0,\\
&T_y(l)=0, \qquad T_z(l)=P, \qquad M_y(l)=0, \qquad M_z(l)=0.
\end{aligned}
\tag{5.7}
$$

The solution to problem ($\mathcal{P}_3$) has the form:

$$
\begin{aligned}
w &= \frac{Pl^3}{6EJ_y}\xi^2(3-\xi)+\alpha_z\frac{Pl}{GA}\xi,\\
\beta &= -\frac{Pl^2}{2EJ_y}\xi(2-\xi),\\
v &= \alpha_{yz}\frac{Pl}{GA}\xi,\\
\varphi &= 0.
\end{aligned}
\tag{5.8}
$$

There appears a lateral deflection in the shape of a straight line; an extremal value of this deflection is $\alpha_{yz}Pl/(GA)$.

The distribution of internal forces is the same as in the thin bar theory, i.e.:

$$
M_y=-Pl(1-\xi), \qquad M_z=0, \qquad T_z=P, \qquad T_y=0.
\tag{5.9}
$$

5.4. PURE BENDING

Consider a bar simply supported in two directions at both ends, loaded by two end moments in opposite directions at both ends. The boundary conditions read:

$$\begin{aligned} &w(0)=0, \qquad w(l)=0, \qquad v(0)=0, \qquad v(l)=0,\\ &M_y(0)=M, \qquad M_y(l)=M, \qquad M_z(0)=0, \qquad M_z(l)=0. \end{aligned} \tag{5.10}$$

The solution to problem ($\mathcal{P}_3$) has the form:

$$\begin{aligned} &w=\frac{Ml^2}{2EJ_y}\xi(1-\xi),\\ &\beta=-\frac{Ml}{2EJ_y}(1-2\xi),\\ &v=0, \qquad \varphi=0,\\ &M_y=M, \qquad T_z=0, \qquad M_z=0, \qquad T_y=0, \end{aligned} \tag{5.11}$$

which coincides with that predicted by the thin bar theory.

6. FINAL REMARKS

The present paper discussed the predictions of the six-parameter theory of bars of arbitrary cross-sections proposed in [4, Sec. 10]. The presence of coupling terms in the constitutive equations linking the transverse forces to the transverse shear measures induces asymmetry in the solutions and results in deplanation of the deformation states. This effect is clearly seen in the shape functions corresponding to kinematic loads. In general, the response to the static load is not planar. There is only one exception in which the deplanation is absent: the problem of pure bending.

If the plane $x=l/2$ is the section of a symmetry plane of the static problem, a constant load applied in the z-direction along the $x_{(s)}$ axis generates a parabolic deflection in the y-direction, without causing the angles of rotation φ along the $-z$-axis, while the state of stress resultants remains planar, i.e., $M_z=0$, $T_y=0$. Moreover, the rotation angles β in y-direction coincide with those predicted by the thin bar theory, i.e., they are not affected by transverse shear.

If the static problem is asymmetric with respect to the plane $x=l/2$, a constant load along the z-direction induces all stress resultants and the deflections along the y-direction are given by polynomials of degree 3. For instance, in a bar subjected to the load q_z which is clamped at the left end and simply supported in both y- and z-directions at the right end there appear two non-zero reactions in the y- and z-directions at the right end, generating the stress resultants in both planes. Moreover, note that point loads applied to cantilevers in the z-direction cause lateral deflections of straight shape. Thus, the lateral deflection $v(x)$ of cantilever loaded in the z-direction by several point loads will assume the shape of a zigzag. These lateral deflections are caused by the transverse forces T_z which generate the shear deformations γ_y.

Let us emphasize that within the standard six-parameter theory of bars, e.g., PETROLO and CASCIARO [3], a load along the z-direction will, in general, generate torsion. Moreover, kinematic loads will cause torsional deformation. This shows that the six-parameter theory discussed in the presented paper makes the static problems as simple as possible.

We conclude that, in general, none of the six-parameter theories admit planar bending/shearing states of deformation. This phenomenon is of vital importance when analyzing stability of bending states, since the standard description of lateral buckling phenomenon assumes an ideally planar initial bending configurations.

Let us stress here that this problem of occurring spatial deformation states is not observed in the theory by Vlasov (or the Vlasov-like theory developed in [4]), because transverse shear deformation is neglected and all constitutive equations may be decoupled by an appropriate choice of free parameters of this theory, such as the position of the pole. Thus, the standard theory of lateral buckling works correctly, as the initial planar bending states are admissible. This shows how difficult it is to extend the results concerning Vlasov thin bars to moderately thick bars. As usually, a direct extension of the known predictions is impossible.

FUNDINGS

This research did not receive any specific grant from funding agencies in the public, commercial, or not-for-profit sectors.

CONFLICT OF INTERESTS

The authors declare that there are no known competing financial interests or personal relationships that could have influenced the work described in this paper.

AUTHORS' CONTRIBUTIONS

All authors contributed equally to this work, reviewed, and approved the final manuscript.

References

1. Vlasov V.Z., Thin-walled bars [in Russian], [in:] *Collected Works of V.Z. Vlasov*, Sokolovskii V.V. *et al.* [Eds], Vol. II, The Publisher House of the Academy of Sciences of SSSR, Moscow, 1963.
2. Bazoune A., Khulief Y.A., Stephen N.G., Shape functions of three-dimensional Timoshenko beam element, *Journal of Sound and Vibration*, **259**(2): 473–480, 2003, https://doi.org/10.1006/jsvi.2002.5122.
3. Petrolo A.S., Casciaro R., 3D beam element based on Saint Venànt's rod theory, *Computers & Structures*, **82**(29): 2471–2481, 2004, https://doi.org/10.1016/j.compstruc.2004.07.004.
4. Lewiński T., Czarnecki S., On incorporating warping effects due to transverse shear and torsion into the theories of straight elastic bars, *Acta Mechanica*, **232**(1): 247–282, 2021, https://doi.org/10.1007/s00707-020-02849-7.
5. Love A.E.H., *Treatise on the Mathematical Theory of Elasticity*, Cambridge University Press, Cambridge, 1927.
6. Ieşan D., On Saint–Venant's problem, *Archive for Rational Mechanics and Analysis*, **91**(4): 363–373, 1986, https://doi.org/10.1007/BF00282340.
7. Librescu L., Song O., *Thin-Walled Composite Beams: Theory and Application*, Springer, Dordrecht, 2006, https://doi.org/10.1007/1-4020-4203-5.
8. Dikaros I.C., Sapountzakis E.J., Argyridi A.K., Generalized warping effect in the dynamic analysis of beams of arbitrary cross section, *Journal of Sound and Vibration*, **369**: 119–146, 2016, https://doi.org/10.1016/j.jsv.2016.01.022.
9. El Fatmi R., Non-uniform warping including the effects of torsion and shear forces. Part I: A general beam theory, *International Journal of Solids and Structures*, **44**(18–19): 5912–5929, 2007, https://doi.org/10.1016/j.ijsolstr.2007.02.006.
10. El Fatmi R., Non-uniform warping including the effects of torsion and shear forces. Part II: Analytical and numerical applications, *International Journal of Solids and Structures*, **44**(18–19): 5930–5952, 2007, https://doi.org/10.1016/j.ijsolstr.2007.02.005.
11. Schramm U., Kitis L., Kang W., Pilkey W.D., On the shear deformation coefficient in beam theory, *Finite Elements in Analysis and Design*, **16**(2): 141–162, 1994, https://doi.org/10.1016/0168-874X(94)00008-5.
12. Kączkowski Z., Statics of bars and systems of bars, [in:] *Technical Mechanics Strength of Structural Elements* [in Polish: *Mechanika Techniczna. Wytrzymałość Elementów Konstrukcyjnych*], Życzkowski M. [Ed.], pp. 19–179, Warszawa, 1988.
13. Pełczyński J., Gilewski W., Algebraic formulation for moderately thick elastic frames, beams, trusses, and grillages within Timoshenko theory, *Mathematical Problems in Engineering*, **2019**(1): 7545473, 2019, https://doi.org/10.1155/2019/7545473.
14. Luo Y., An efficient 3D Timoshenko beam element with consistent shape functions, *Advances in Applied Mechanics*, **1**(3): 95–106, 2008.

Received July 10, 2025; revised September 17, 2025; accepted October 9, 2025;
available online January 20, 2026; version of record April 16, 2026;
published issue June 24, 2026.

Engineering Transactions, **74**(2): 145–171, 2026, https://doi.org/10.24423/engtrans.2025.3639
Institute of Fundamental Technological Research Polish Academy of Sciences (IPPT PAN)
Université de Lorraine • Poznan University of Technology

Research Paper

Numerical Modeling of the Aluminum Alloy AW5083 Using Large-Strain Thermo-Elasto-Plasticity

Agnieszka Sobierańska, Balbina Wcisło*

Chair of Computational Engineering, Cracow University of Technology
Kraków, Poland

*Corresponding Author: balbina.wcislo@pk.edu.pl

This paper deals with the constitutive modeling and finite element (FE) simulations of advanced models related to large-strain thermo-elasto-plastic behavior of aluminum alloy AW5083, which can reproduce the material response at different temperatures from room temperature up to 500 °C. Significant focus is placed on internal sources of cooling and heating resulting from thermo-elastic and thermo-plastic couplings, respectively, and on the influence of elevated temperature on these couplings. The formulation of the constitutive description is based on a thermodynamic approach. Two models are presented and tested, including temperature-dependent and temperature-independent plastic free energy function. Numerical tests of the developed models are carried out for a uniaxial tensile test. For the sake of comparison with experimental results, a dogbone specimen examined in a tensile machine is analyzed.

Keywords: aluminum alloy AW5083, thermo-elasto-plasticity, temperature dependent parameters, large-strains, finite element method.

1. INTRODUCTION

This paper presents a constitutive modeling and a numerical investigation of aluminum alloy AW5083 using a large-strain thermo-elasto-plastic model that incorporates internal heat sources and temperature-dependent material parameters.

Various large strain thermo-elasto-plasticity models can be found in the literature. This work is focused on thermodynamically consistent models presented, e.g., in [1, 2], derived based on the first and second laws of thermodynamics. Such an approach leads to a formulation that involves internal (often called structural) sources of cooling or heating in the analyzed material. In particular, thermo-elastic coupling related to the Gough–Joule effect, typically associated with entropic materials such as polymers [3], manifests itself in aluminum as cooling in tensioned samples in the elastic regime, whereas the thermomechanical coupling in plasticity results in temperature increase due to plastic dissipation. The crucial quantity in these formulations is the Helmholtz free energy, which can include a reversible part (related to elasticity and thermal expansion), a plastic part, and a purely thermal part [2].

Constitutive modeling of an aluminum alloy undergoing large strains at elevated temperatures requires the introduction of temperature-dependent material parameters. Such models are included in some papers, e.g., in [4], presenting a small-strain constitutive model for case-hardening steel, or in [5] related to thermo-elasto-plasticity of metals with material properties being linear functions of temperature. In this work, the material model based on [2] is enhanced with dependencies of material properties on temperature, based on [6, 7]. Moreover, the study focuses on two distinct models of the plastic part of the free energy: one that accounts for temperature-dependent material parameters in the free energy formulation and another that assumes temperature-independent hardening in plasticity.

The goal of this research is to develop and test a comprehensive constitutive framework capable of accurately predicting the response of aluminum alloy AW5083 under mechanical loads at different temperatures, ranging from 20 °C up to 500 °C. The research is a continuation of the work presented in [8], which was restricted to room temperature. The following assumptions are taken into account in the research. The material is initially isotropic, also regarding hardening in plasticity, and associative plastic flow is applied. The model reproduces the quasi-static case; thus, it does not include viscous effects in elasticity or in plasticity and the inertial term in the balance of linear momentum is dropped. The thermomechanical coupling incorporates thermal expansion, temperature-dependent parameters, internal heat sources and the influence of geometry change on the heat flow in the material, i.e., it takes into account Fourier's law in the deformed configuration.

This advanced and strongly non-linear model is implemented and tested utilizing symbolic-numerical packages AceGen/AceFEM of Wolfram Mathematica [9]. Simulations are performed for a uniaxial tension test and for a dogbone specimen typically used in experimental conditions [10]. By comparing the selected models, the paper aims to show the influence of temperature-hardening coupling on the mechanical and thermal behavior of the material. The key phenomena of thermo-elastic cooling and heat generation due to plastic dissipation are analyzed in detail. Through numerical simulations of the dogbone specimen, the study explores the effects of temperature-dependent parameters, mesh refinement sensitivity, and thermal boundary conditions on the specimen's response. The results highlight the significance of thermo-plastic coupling in the plastic part of the free energy in reducing self-heating and softening effects, particularly in the temperature range from 200 °C to 300 °C. The paper also addresses different forms of localization.

The research presented in the paper can be applied to advanced numerical simulations of structures and elements made of aluminum alloy AW5083, which is widely used in shipbuilding, railroad cars, pressure vessels, and many other fields, under various mechanical and/or thermal loading. The development of a formulation valid at elevated temperatures enables simulations under fire conditions.

The paper is laid out as follows. Section 2 presents the formulation of the thermo-elasto-plastic material model based on the laws of thermodynamics. Section 3 contains functional dependencies of material parameters, both the mechanical and thermal ones, with respect to temperature. The core part of the paper is Sec. 4 including the description and results of numerical simulations, whereas conclusion and final remarks are provided in Sec. 5.

The notation used in the paper is as follows: round brackets introduce arguments of functions, whereas square brackets specify the sequence of operations.

2. MODEL OF MATERIAL

2.1. KINEMATICS

The material description developed in the paper is based on a thermo-elasto-plastic model presented in [2]. The model is based on the decomposition of the deformation gradient into a reversible part $\mathbf{F}^r$, related to elastic deformation and thermal expansion, and an irreversible (plastic) part $\mathbf{F}^p$ in the following form:

$$\mathbf{F} = \mathbf{F}^r \mathbf{F}^p. \tag{2.1}$$

The deformation gradient is defined in the standard form as $\mathbf{F} = \partial \mathbf{x}(\mathbf{X}, t)/\partial \mathbf{X}$ with $J = \det(\mathbf{F}) > 0$, where $\mathbf{X}$ and $\mathbf{x}$ are vectors denoting the referential and the current placement of a particle in the Cartesian coordinate system, respectively, and the variable t represents time. Based on the decomposition (2.1), the reversible left Cauchy–Green tensor is defined as follows:

$$\mathbf{b}^r = \mathbf{F}^r (\mathbf{F}^r)^{\mathrm{T}}, \qquad J^{br} = \det(\mathbf{b}^r). \tag{2.2}$$

The velocity gradient and its symmetric part, called the deformation rate, are defined as usual:

$$\mathbf{l} = \dot{\mathbf{F}} \mathbf{F}^{-1}, \qquad \mathbf{d} = \frac{1}{2} \left(\mathbf{l} + \mathbf{l}^{\mathrm{T}} \right), \tag{2.3}$$

where the dot over a quantity denotes its rate. The plastic velocity gradient is defined as follows:

$$\mathbf{L}^p = \dot{\mathbf{F}}^p \left[\mathbf{F}^p\right]^{-1}, \tag{2.4}$$

and the plastic deformation rate:

$$\mathbf{d}^p = \frac{1}{2}\left(\mathbf{l}^p + [\mathbf{l}^p]^{\mathrm{T}}\right), \qquad \mathbf{l}^p = \mathbf{F}^r \mathbf{L}^p \left[\mathbf{F}^{\mathrm{r}}\right]^{-1}. \tag{2.5}$$

The Helmholtz free energy is assumed to depend on the reversible left Cauchy–Green deformation tensor $\mathbf{b}^r$, the internal variable α related to hardening, and the absolute temperature T:

$$\psi = \psi(\mathbf{b}^r, \alpha, T). \tag{2.6}$$

The specific form of the Helmholtz free energy will be given in the subsequent subsection.

2.2. Governing equations

The first governing equation, i.e., the balance of linear momentum for the large-strain problem, is written for the quasi-static case with mass forces neglected [11]:

$$\operatorname{div}(\boldsymbol{\tau}/J) = \mathbf{0}, \tag{2.7}$$

where the symbol div $(\cdot)$ denotes the spatial divergence of the quantity $\cdot$, and $\boldsymbol{\tau}$ is the Kirchhoff stress tensor. The quasi-static assumption results in neglecting the inertial term in Eq. (2.7). The model can then be applied to simulate deformation at low-strain rates. Consequently, viscous effects are also neglected.

The second governing equation is the first law of thermodynamics, i.e., the balance of energy, which can be written using spatial quantities [2]:

$$\rho\dot{u} = \boldsymbol{\tau} : \mathbf{d} - J\operatorname{div}(\mathbf{q}), \tag{2.8}$$

where ρ is the material density of the undeformed configuration which can be temperature-dependent, u is the internal energy per unit of mass, and $\mathbf{q}$ is the Kirchhoff heat flux density vector. In Eq. (2.8), an external heat source (per unit of mass) is not taken into account.

The second law of thermodynamics, i.e., the dissipation inequality, can be written in the following form [2]:

$$\rho T\dot{\eta} - \rho\dot{u} + \boldsymbol{\tau} : \mathbf{d} - \frac{J}{T}\mathbf{q} \cdot \operatorname{grad}(T) \geq 0, \tag{2.9}$$

where η denotes the entropy per unit of mass and $\operatorname{grad}(\cdot)$ is the spatial gradient of quantity $\cdot$. Using the Legendre transformation:

$$\psi(\mathbf{b}^r, \alpha, T) = u(\mathbf{b}^r, \alpha, \eta - \eta T), \tag{2.10}$$

after some manipulations, the dissipation inequality can be written as

$$\left[\boldsymbol{\tau} - 2\rho\frac{\partial\psi}{\partial\mathbf{b}^r}\right] : \mathbf{d} + \left[2\rho\frac{\partial\psi}{\partial\mathbf{b}^r}\mathbf{b}^r\right] : \mathbf{d}^p - \rho\frac{\partial\psi}{\partial\alpha}\dot{\alpha} - \frac{J}{T}\mathbf{q}\cdot\operatorname{grad}(T) \geq 0. \tag{2.11}$$

Because inequality (2.11) should be fulfilled for any arbitrary $\mathbf{d}$, the Kirchhoff stress tensor is equal to:

$$\boldsymbol{\tau} = -2\rho\frac{\partial\psi}{\partial\mathbf{b}^r}. \tag{2.12}$$

The thermodynamic force conjugated to α is defined as

$$\beta = \rho\frac{\partial\psi}{\partial\alpha}. \tag{2.13}$$

Now, the reduced form of the dissipation inequality is obtained:

$$\underbrace{\left[\boldsymbol{\tau} : \mathbf{d}^p - \beta\dot{\alpha}\right]}_{\mathcal{D}_{\text{mech}}} + \underbrace{\left[-\frac{J}{T}\mathbf{q}\cdot\operatorname{grad}(T)\right]}_{\mathcal{D}_{\text{therm}}} \geq 0. \tag{2.14}$$

It is assumed that both parts of the dissipation, mechanical $\mathcal{D}_{\text{mech}}$ and thermal $\mathcal{D}_{\text{therm}}$, are greater than or equal to 0. In the latter case, the inequality is fulfilled by the application of the isotropic spatial Fourier law as the constitutive relationships for the heat flux density vector, for details see [12],

$$\mathbf{q} = -Jk\operatorname{grad}(T), \tag{2.15}$$

where k is the conductivity coefficient, which can be temperature-dependent, i.e., $k(T)$.

Using Eq. (2.10) and Eq. (2.11), the energy balance Eq. (2.8) can be rewritten in the so-called temperature form, which will be further implemented in numerical simulations:

$$c\dot{T} = J\operatorname{div}(\mathbf{q}) + \mathcal{D}_{\text{mech}} + \mathcal{H} + \mathcal{A}, \tag{2.16}$$

where

$$c = -\rho T\frac{\partial^2\psi}{\partial T^2}, \tag{2.17}$$

$$\mathcal{H} = \left[2\rho T \frac{\partial^2 \psi}{\partial T \partial \mathbf{b}^r} \mathbf{b}^r\right] : [\mathbf{d} - \mathbf{d}^p], \tag{2.18}$$

$$\mathcal{A} = \rho T \frac{\partial^2 \psi}{\partial T \partial \alpha} \dot{\alpha}. \tag{2.19}$$

In Eq. (2.16), there are three internal (structural) sources of heating/cooling, which can change the temperature of the material even if there are no external heat sources. $\mathcal{D}_{\text{mech}}$ is related to the heat production during a plastic process and $\mathcal{H}$ to the thermo-elastic source of heating/cooling. The term $\mathcal{A}$ is in turn a source related to the coupling between hardening in plasticity and temperature, which will further be called temperature-hardening coupling. This term is active when the plastic part of the free energy function is temperature-dependent.

Note that the internal sources depend on the adopted form of the Helmholtz free energy which will be specified in the next subsection.

2.3. HELMHOLTZ FREE ENERGY

In this paper, the following decoupled form of the Helmholtz free energy is adopted:

$$\psi = \psi^r(\mathbf{b}^r, T) + \psi^p(\alpha, T) + \psi^\theta(T), \tag{2.20}$$

where ψ^r is the free energy related to the reversible deformation due to elastic response and thermal expansion, ψ^p is the plastic part, which can be dependent on the hardening variable and optionally on temperature. The reversible part of the free energy follows the neo-Hookean formulation, which is a basic approach for elastic materials in a large deformation framework. The last term ψ^θ is the purely thermal part. The specific form of reversible Helmholtz free energy is as follows:

$$\psi^r(\mathbf{b}^r, T) = \frac{1}{\rho(T)}\left[\frac{\kappa(T)}{2}\left[\ln\left(\sqrt{J^{br}}\right)\right]^2 + \frac{G(T)}{2}\left[\operatorname{tr}\left([J^{br}]^{-1/3}\,\mathbf{b}^r\right) - 3\right]\right.$$
$$\left. - 3\kappa\,\alpha_T(T)\,[T - T_0]\ln\left(\sqrt{J^{br}}\right)\right]. \tag{2.21}$$

The temperature-dependence of the material parameters present in Eq. (2.21) is now explicitly written. The symbol κ denotes the bulk modulus, G – the shear modulus, and α_T – thermal expansion coefficient.

The plastic part of the free energy is related to exponential hardening which is observed for the considered aluminum alloy, cf. [6, 10]. The form of the plastic part of the free energy influences also the source defined in Eq. (2.19). In this study, two models are compared.

The first one, hereafter called Model 1, incorporates the plastic free energy function depending on the hardening variable and temperature. The temperature dependency is achieved by the application of temperature-dependent parameters: the initial and final yield stresses σ_{y0} and $\sigma_{y\infty}$, respectively, as follows:

$$\psi^p(\alpha, T) = \frac{1}{\rho(T)}\left[\sigma_{y\infty}(T) - \sigma_{y0}(T)\right]\left[\alpha + \frac{1}{\delta}\exp(-\delta\alpha)\right]. \tag{2.22}$$

The final yield stress represents the saturated flow stress, i.e., the maximum stress level the material can reach after a large amount of plastic deformation, when further hardening becomes negligible. Examples of such assumption can be found, e.g., in [5]. For Model 1, the temperature-hardening coupling is present and in the energy balance Eq. (2.16) the term $\mathcal{A}$ in non-zero. The saturation parameter δ in Eq. (2.22) is assumed in the paper as constant.

The second model, called hereafter Model 2, includes a temperature-independent plastic part of the free energy function:

$$\psi^p(\alpha) = \frac{1}{\rho(T)}\left[\sigma_{y\infty}(T_0) - \sigma_{y0}(T_0)\right]\left[\alpha + \frac{1}{\delta}\exp(-\delta\alpha)\right], \tag{2.23}$$

and involves the values of the initial and final yield stresses at initial temperature of the experiment T_0. The temperature-independent plastic part of the free energy function is used, e.g., in [4].

The thermal part of the free energy is not specified here explicitly. It is assumed that it has a form such that the heat capacity from Eq. (2.17) is temperature-dependent in a form given, in the next section.

2.4. PLASTICITY

The yield function is assumed in the following form:

$$\mathcal{F} = f(\boldsymbol{\tau}) - \sigma_y(\alpha, T) \leq 0, \tag{2.24}$$

where $f(\boldsymbol{\tau})$ is a stress measure governing plasticity. Here, the Huber–Mises measure is applied:

$$f(\boldsymbol{\tau}) = \sqrt{\mathbf{t} : \mathbf{t}}, \qquad \mathbf{t} = \boldsymbol{\tau} - \frac{1}{3}\mathrm{tr}\,(\boldsymbol{\tau})\,\mathbf{I}. \tag{2.25}$$

The yield stress $\sigma_y(\alpha, T)$ for Model 1 is as follows:

$$\begin{aligned}\sigma_y(\alpha, T) &= \sigma_{y0}(T) + \beta(\alpha, T)\\ &= \sigma_{y0}(T) + \left[\sigma_{y\infty}(T) - \sigma_{y0}(T)\right]\left[1 - \exp(-\delta\alpha)\right],\end{aligned} \tag{2.26}$$

whereas for Model 2 it is as follows:

$$\begin{aligned}\sigma_y(\alpha,T) &= \sigma_{y0}(T) + s(T)\beta(\alpha) \\ &= \sigma_{y0}(T) + s(T)\left[\sigma_{y\infty}(T_0) - \sigma_{y0}(T_0)\right]\left[1-\exp(-\delta\alpha)\right],\end{aligned} \tag{2.27}$$

where the thermal softening function $s(T)$ is proposed in the following form to obtain the same yield stress as in Model 1:

$$s(T) = \frac{\sigma_{y\infty}(T) - \sigma_{y0}(T)}{\sigma_{y\infty}(T_0) - \sigma_{y0}(T_0)}. \tag{2.28}$$

The associative flow rule is adopted in the following form:

$$-\frac{1}{2}\mathcal{L}_v(\mathbf{b}^r) = \dot{\gamma}\frac{\partial\mathcal{F}}{\partial\boldsymbol{\tau}}\mathbf{b}^r, \tag{2.29}$$

where the Lie derivative of the reversible left Cauchy–Green deformation tensor is defined as [2]:

$$\mathcal{L}_v(\mathbf{b}^r) = \mathbf{F}\frac{\partial}{\partial t}\left[\mathbf{F}^{-1}\mathbf{b}^r\mathbf{F}^{-T}\right]\mathbf{F}^{\mathrm{T}}, \tag{2.30}$$

where $\dot{\gamma}$ is the plastic multiplier, which is related to the hardening variable through the equation $\alpha = \sqrt{2/3}\dot{\gamma}$.

The standard Kuhn–Tucker conditions complete the plasticity description:

$$\dot{\gamma} \geq 0, \qquad \mathcal{F} \leq 0, \qquad \dot{\gamma}\mathcal{F} = 0. \tag{2.31}$$

3. TEMPERATURE-DEPENDENT PARAMETERS

The temperature-dependent parameters of aluminum alloy AW5083, related to both the mechanical and thermal properties are taken from the literature, in particular from [6, 7]. Paper [6] provides values of the density, Young's modulus, heat conductivity, heat capacity, initial yield stress and final yield stress at selected temperatures in the range from room temperature up to 500 °C, denoted by red dots in Fig. 1 to Fig. 6. The temperature on the horizontal axes is given in Kelvins. The blue lines in the figures represent approximations obtained using the least-squares method for the assumed basis functions. In particular, polynomial of a selected degree are used for Young's modulus, density, heat conductivity, and heat capacity, whereas a logistic function is used for the initial and final yield stresses.

The diagram of the thermal expansion coefficient in Fig. 7 is prepared based on the information provided in [7].

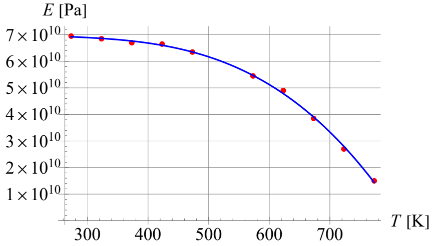

FIG. 1. Young's modulus vs. temperature.

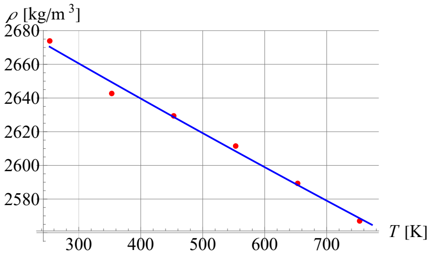

FIG. 2. Density vs. temperature.

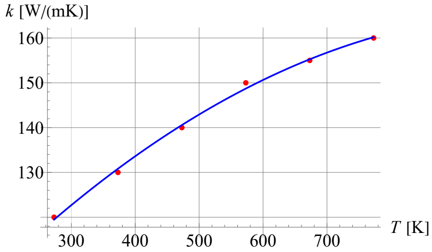

FIG. 3. Heat conductivity vs. temperature.

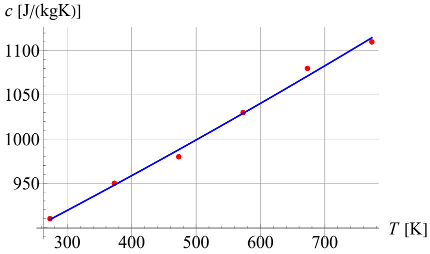

FIG. 4. Heat capacity vs. temperature.

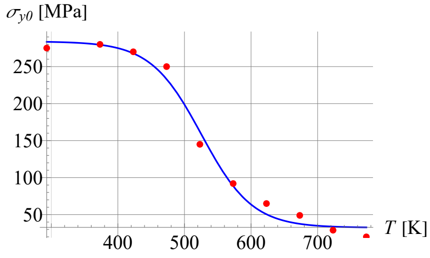

FIG. 5. Initial yield stress vs. temperature.

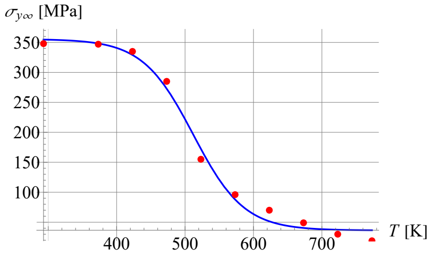

FIG. 6. Ultimate yield stress vs. temperature.

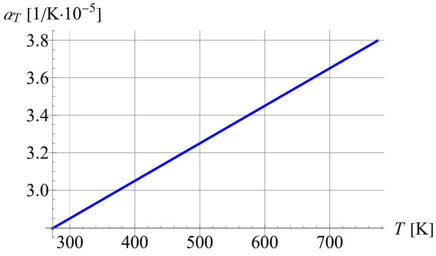

FIG. 7. Thermal expansion coefficient vs. temperature.

The specific formulas describing the temperature-dependent parameters are given in Table 1. The proper values of the parameters are obtained for temperatures given in Kelvins. The resulting units are provided in square brackets.

TABLE 1. Material parameters depending on temperature.

Quantity	Formula
Density $[\mathrm{kg/m^3}]$	$\rho(T) = 2724.97 - 0.219593\,T + 1.58929 \times 10^5\,T^2$
Young's modulus [Pa]	$E(T) = 7.7915 \times 10^{10} - 7.98531 \times 10^7\,T + 273938\,T^2 - 358.197\,T^3$
Thermal expansion coefficient [1/K]	$\alpha_T(T) = 2.25 \times 10^{-5} + 2 \times 10^{-8}\,T$
Heat conductivity $[\mathrm{W/(m \cdot K)}]$	$k(T) = 80.2766 + 0.165482\,T - 8.03571 \times 10^5\,T^2$
Heat capacity $[\mathrm{J/(kg \cdot K)}]$	$c(T) = 807.914 + 0.355393\,T + 5.35714 \times 10^5\,T^2$
Initial yield stress [Pa]	$\sigma_{y0}(T) = 2.83973 \times 10^8 - \dfrac{2.51535 \times 10^8}{1 + \exp(13.769 - 0.0262\,T)}$
Ultimate yield stress [Pa]	$\sigma_{y\infty}(T) = 3.55575 \times 10^8 - \dfrac{3.19238 \times 10^8}{1 + \exp(13.827 - 0.027\,T)}$

It is assumed that Poisson's ratio is constant and equal to $\nu = 0.3$. The bulk and shear moduli present in Eq. (2.21) are calculated on the basis of Young's modulus and Poisson's ratio in the standard way:

$$G(T) = \frac{E(T)}{2[1+\nu]}, \qquad \kappa(T) = \frac{E(T)}{3[1-2\nu]}. \tag{3.1}$$

The value of the saturation parameter is assumed to be equal to $\delta = 19.618$, see [10].

4. NUMERICAL SIMULATIONS

4.1. IMPLEMENTATION

The numerical verification of the presented models of the aluminum alloy AW5083 with the temperature-dependent parameters is performed using the finite element method. The model is implemented within symbolic-numerical packages of Wolfram Mathematica called AceGen/AceFEM, see, e.g., [9]. The finite element (FE) code is developed for 3D hexahedral FEs with the linear interpolation of temperature and displacement fields and the so-called F-bar modification [13], preventing the volumetric locking that occurs in Huber–Mises plasticity. The implementation of large-strain plasticity can be found in [9], whereas the implementation of the coupled thermomechanical model is presented in [14].

Numerical tests include two elongated specimens: one cubic FE in a uniaxial tension state and a dogbone sample which is used commonly for experiments in laboratory, see [10]. For the former sample, the elastic stage is analyzed firstly, followed by the plastic one occurring under greater loading.

Attention is focused on the internal heat sources and their influence on the sample behavior at room temperature and at elevated temperatures up to 500 °C (i.e., 773.15 K).

4.2. UNIAXIAL TENSION TEST

A simulation of a single FE in uniaxial tension is conducted. The cubic specimen has dimensions $L = 10\,\mathrm{mm}$, $W = 10\,\mathrm{mm}$, $H = 10\,\mathrm{mm}$. The visual representation of the FE in 3D space can be seen in Fig. 8. Mechanical boundary conditions are assumed in such a way that uniform deformation is reproduced, and free transverse deformation is allowed. Insulation is applied as thermal boundary conditions.

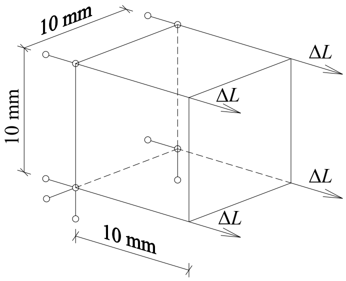

FIG. 8. Visual representation of a single FE in 3D.

4.2.1. ELASTIC REGIME ANALYSIS

Firstly, the sample is subjected to an enforced elongation of $\Delta L = L/180 = 0.056\,\mathrm{mm}$, applied over a time $t = 10\,\mathrm{s}$. Such elongation allows for the simulation of the sample in the elastic range of as well as the beginning of the plastic deformation phase.

In Fig. 9, the reaction diagrams versus the enforced displacement for different initial temperatures $T_0 = (20, 100, 200, 300, 400, 500)\,°\mathrm{C}$, are presented. With the increase of the initial temperature, the stiffness of the sample decreases. This phenomenon manifests itself in the graph as a decreasing slope of the gradient. It is shown that the material subjected to elongation enters the plastic range of deformation at different values of ΔL depending on the initial temperature T_0 of the sample, which is an effect of dependence of the initial yield stress on temperature. As the temperature rises, the yield stress decreases. Through the numerical analysis, it is found that the elastic deformation range is the shortest at an initial temperature $T_0 = 400\,°\mathrm{C}$. Although the initial yield stress is lower at temperature 500 °C, the elastic stiffness is significantly smaller and this causes the onset of plasticity to occur later.

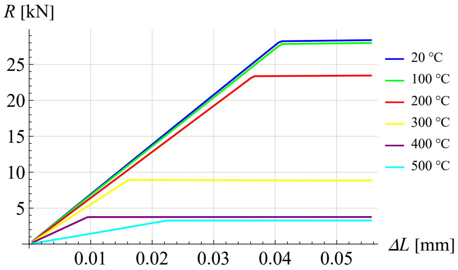

FIG. 9. Sum of reactions vs. enforced displacement for different initial temperatures.

In Fig. 10, the change in the temperature of the sample vs. applied elongation is shown, for the analyzed initial temperatures. In the elastic range of deformations, a decrease in temperature of the sample is seen, and the Gough–Joule effect is observed, which manifests itself as thermo-elastic cooling. An upward tendency of the curves starts at a point at which the behavior of the sample changes, and the material enters the plastic range of deformations. The results of the test presented in Fig. 10 show that depending on the initial temperature the sample enters the state of irreversible deformations at different stages of elongation. It is noted that the biggest thermo-elastic cooling effect is observed at an initial temperature $T_0 = 200\,°\mathrm{C}$.

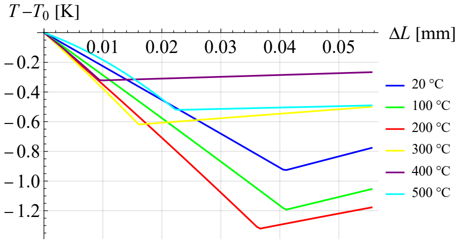

FIG. 10. Relative temperature of the sample vs. enforced displacement for different initial temperatures.

To investigate the influence of the thermo-elastic cooling on the material behavior more thoroughly, Fig. 11 is prepared. It presents the relative temperature at the stage of deformation $\Delta L = 0.0095\,\mathrm{mm}$ for the analyzed initial temperatures. This loading step is the last one at which all tested samples undergo elastic deformation. It can be observed that the strongest effect of the thermo-elastic cooling at the analyzed stage of deformation is for the initial temperature $T_0 = 300\,°\mathrm{C}$. As the initial temperature grows from $T_0 = 20\,°\mathrm{C}$ up to $T_0 = 300\,°\mathrm{C}$ the absolute value of the relative temperature increases gradually. After reaching the $300\,°\mathrm{C}$ threshold, the absolute value of relative temperature starts to decrease. This is a result of the value of thermo-elastic cooling source presented in Fig. 12. The observed phenomenon can be explained as follows.

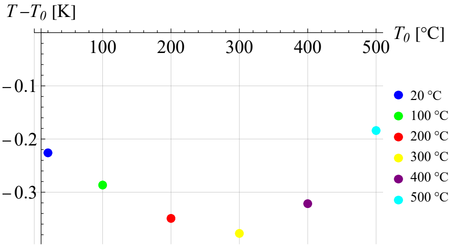

FIG. 11. Relative temperature at $\Delta L = 0.0095$ mm for tests conducted at different initial temperatures.

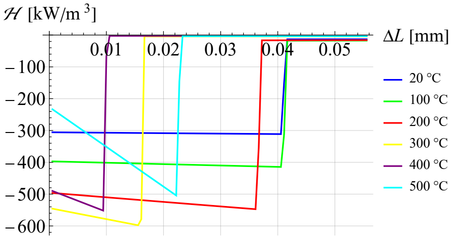

FIG. 12. Elastic cooling for tests conducted at different initial temperatures.

In the analyzed model, the thermo-elastic cooling depends on temperature in two ways, see Eq. (2.18). Firstly, with rising absolute temperature of the sample, the value of the cooling source due to thermo-elastic coupling increases. Secondly, the cooling source also depends on the elastic parameters of the material, especially on Young's modulus which decreases with temperature increase, see Fig. 1. At temperature 623.15 K = 350 °C, Young's modulus is reduced by almost half. From this moment on, the second effect dominates, leading to a decrease of the source of cooling because of the decreasing stiffness of the material.

4.2.2. PLASTIC REGIME ANALYSIS

The cubic sample is now subjected to an enforced elongation $\Delta L = L/5 = 2$ mm applied over 1 s, resulting in plastic deformation. Figure 13 and Fig. 14 depict the relationship between the sum of reactions and the enforced displacement for the sample shown in Fig. 8. Both diagrams present the influence of the initial temperature on the mechanical response of the material, but they differ in the type of constitutive model used for testing of the samples. Results obtained for Model 1 are presented in Fig. 13, and for Model 2 in Fig. 14. The graphs capture the transition from elastic to plastic deformation, where the sum of reactions exhibits nonlinear behavior as the displacement increases. Higher initial temperatures typically reduce the yield stress and hardening modulus of aluminum due to thermal softening. This can manifest itself as lower reaction forces for equal displacements for elevated temperatures in Fig. 13 and Fig. 14.

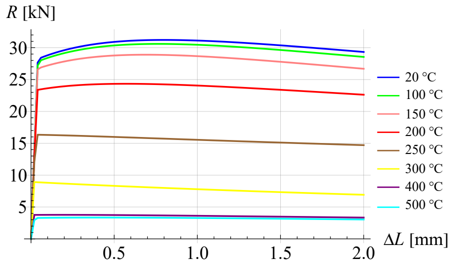

FIG. 13. Sum of reactions vs. enforced displacement at different initial temperatures for Model 1.

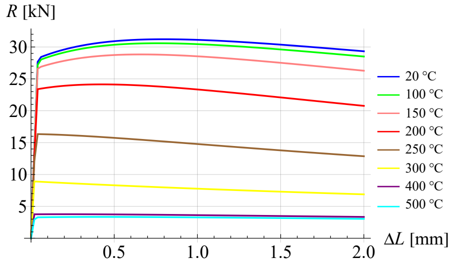

FIG. 14. Sum of reactions vs. enforced displacement at different initial temperatures for Model 2.

Comparing the reactions for Model 1 and Model 2, one can see that a visible difference is present only for two examined reference temperatures: $T_0 = 200\,^\circ\mathrm{C}$ and $T_0 = 250\,^\circ\mathrm{C}$. In comparison with Model 1, Model 2 shows stronger softening of the material at $T_0 = 200\,^\circ\mathrm{C}$. A larger softening can also be observed at $T_0 = 250\,^\circ\mathrm{C}$. After closer examination of the obtained results the differences in reactions at the end of the process between the two models is equal to 8.2 % for $T_0 = 200\,^\circ\mathrm{C}$, and 17.1 ‰ for $T_0 = 500\,^\circ\mathrm{C}$.

Figure 15 and Fig. 16 illustrate the evolution of relative temperature in the aluminum sample subjected to progressive elongation, culminating in plastic deformation. The graphs emphasize the thermomechanical coupling inherent to plastic work and dissipation, with distinct curves representing different initial

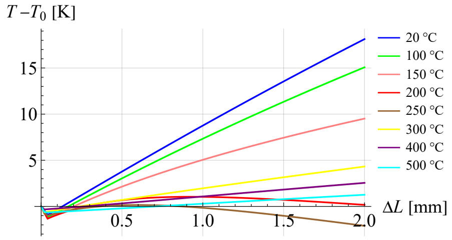

FIG. 15. Relative temperature in the sample vs. enforced displacement at different initial temperatures with Model 1.

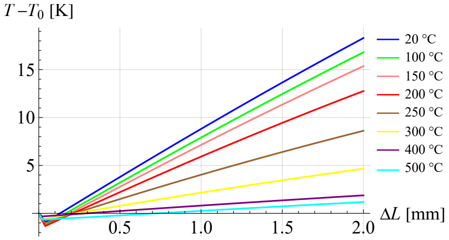

FIG. 16. Relative temperature in the sample vs. enforced displacement at different initial temperatures with Model 2.

temperatures. In the elastic regime, a relative temperature drop is observed, as expected. In the plastic phase of deformation, a pronounced increase in relative temperature occurs due to plastic work conversion to heat. The slope of the diagram of relative temperature vs. displacement increases post-yield, reflecting greater energy dissipation. For higher initial temperatures T_0 the sample exhibits lower values of $T - T_0$ at similar displacements due to lower dissipation. Model 2 reproduces higher heating of the sample compared to Model 1.

Figure 17 and Fig. 18 present the relative temperature $T - T_0$ measured in the aluminum sample at the end of the process, i.e., for the enforced displacement of 2 mm for varying initial temperatures. The graphs compare how temperature evolution differs for various thermomechanical starting conditions. It is clear that

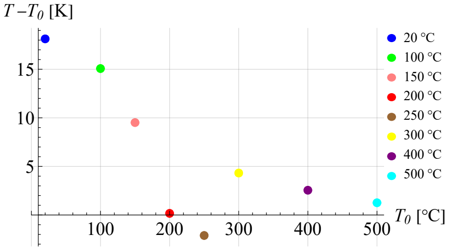

FIG. 17. Relative temperature at $\Delta L = 2\,\text{mm}$ for tests conducted at different initial temperatures for Model 1.

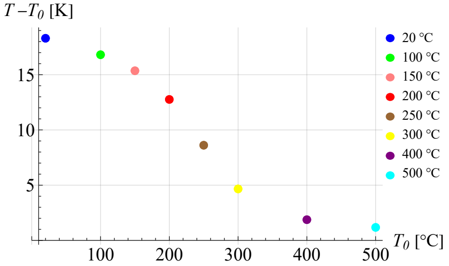

FIG. 18. Relative temperature at $\Delta L = 2\,\text{mm}$ for tests conducted at different initial temperatures for Model 2.

the response of the material differs depending on the type of the computational model applied.

For $T_0 = 20\,^\circ\mathrm{C}$, the difference is hardly noticeable, but at elevated temperatures the sample tested with Model 1 exhibits a smaller raise in relative temperature than samples tested with Model 2. The biggest difference in temperature at the end of the process is observed for $T_0 = 200\,^\circ\mathrm{C}$. For Model 1, the difference is 0.167 K, which means the temperature is almost the same as the reference temperature. For Model 2 it is 20.766 K, which makes for a 20.6 K difference between the two applied models. The analysis presented in Subsec. 4.2.1 shows that at $T_0 = 200\,^\circ\mathrm{C}$, the elastic cooling effect is strong. The heat source associated with plasticity is balanced by the relatively strong Gough–Joule effect, but not exclusively. In Model 1, the heat sources arising from plasticity include not only dissipation, but also the source due to the dependence of material parameters on temperature in the plastic part of the Helmholtz free energy. In such case, this effect manifests itself as heat sinking, which additionally reduces the influence of dissipation. When assuming ψ^p as in Model 2, which is independent of temperature, the sinking effect is absent, which allows for stronger heating of the sample. It is also important that in Model 1 the reduced heating causes smaller thermal softening, which explains why in Fig. 13 the reactions for $T_0 = 200\,^\circ\mathrm{C}$ are much larger in Model 1 than in Model 2. Comparing the graphs from Fig. 17 and Fig. 18, one can notice that Model 2 provides a regular distribution of results over the entire range of analyzed temperatures; therefore, an approximation carried out for the given points decreases monotonously. In turn, in Model 1, with the increase of the initial temperature, the temperature at the end of the process decreases to the point marked in brown, then rises $T_0 = 300\,^\circ\mathrm{C}$. Finally, a downward trend line is observed again.

The quantitative analysis of heating (or sinking) sources for Model 1 can be performed on the basis of Fig. 19 and Fig. 20. The dissipated energy decreases with increasing initial temperature. In contrast, the temperature-hardening coupling causes heat sinking which increases significantly with the growth of the initial temperature up to 200 °C and then decreases, and even exhibits heating

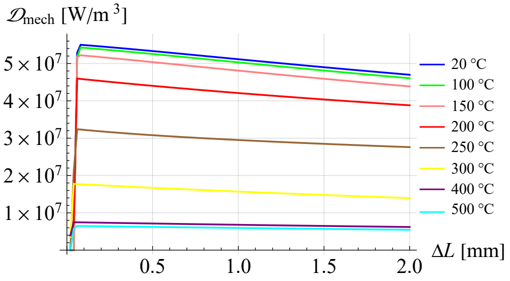

Fig. 19. Dissipated mechanical energy at tests conducted for different initial temperatures for Model 1.

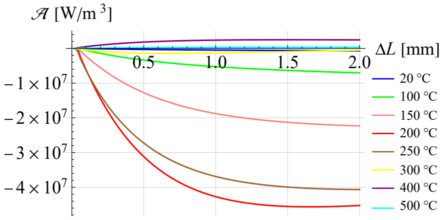

FIG. 20. Heat source related to temperature-hardening coupling for Model 1.

at 400 °C. Note that for $T_0 = 200\,°\mathrm{C}$ in the middle of the process, plastic heating due to energy dissipation is counteracted by heat sinking, cf. red diagrams for $\Delta L = 1$ mm in Fig. 19 and Fig. 20.

4.3. DOGBONE SPECIMEN IN TENSION

To reproduce real experimental testing condition simulations are performed for a dogbone sample geometry described in [10]. The geometry and dimensions of the sample are shown in Fig. 21. The thickness of the specimen is 2 mm. The sample is subjected to maximum elongation of $\Delta L = 30$ mm in time duration of $t_{\max} = 4.95$ s.

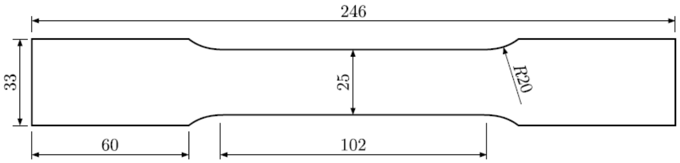

FIG. 21. Dogbone sample – geometry and dimensions (in mm).

4.3.1. TESTS FOR DIFFERENT MESHES

The first set of simulations with Model 1 are performed for three different discretizations. In Fig. 22, one can find visual representation of the three meshes

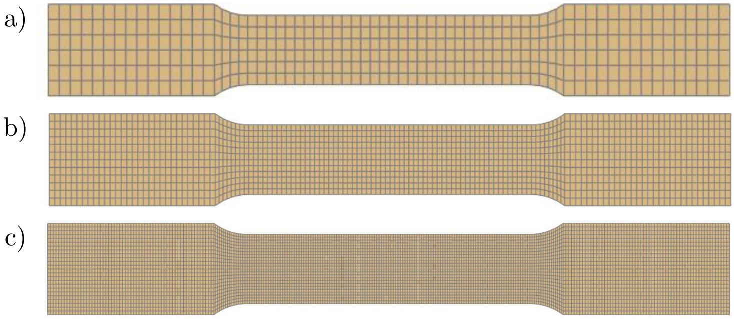

FIG. 22. Visual representation of analyzed meshes: a) coarse, b) medium, c) fine.

used for the tests. The first mesh includes 408 FE, the second 3264, and the third 26 112 elements. In the thickness direction, the coarsest mesh contains one FE, medium mesh two FE, and the finest mesh has four FE. For mesh density analysis, the insulation boundary conditions on all surfaces are assumed and the initial temperature of the sample is the room temperature, i.e., $T_0 = 293.15\,\text{K}$.

The reaction diagram obtained for the analyzed discretizations is presented in Fig. 23. For the thermo-elastic range the results for all three meshes coincide. The same conclusion can be made for the plastic range when material hardens, which takes place until about $\Delta L = 10\,\text{mm}$. After the peak point the decreasing reaction diagrams for different meshes slightly diverge. The descending diagrams are a result of strain localization due to geometrical and thermal softening. Although the results do not coincide, the mesh dependence does not seem to be pathological: the results for the medium and the fine meshes are very close to each other. It is worth mentioning that heat conductivity present in the simulations has a regularizing effect, cf. [15].

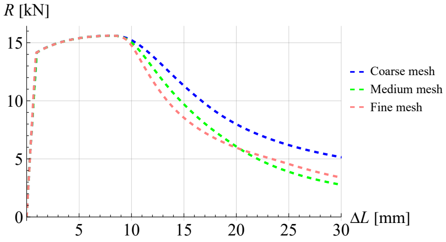

Fig. 23. Reactions depending on the mesh refinement at the midpoint of the sample.

It is observed in Fig. 24 that the temperature in the elastic range and during the hardening phase of plasticity is also the same for all meshes. When localization of deformations occurs, the temperature starts increasing rapidly, because the temperature of the sample is read at the center of the specimen, where plastic deformations are largest. It can also be noticed that the temperature for the medium and fine mesh, starts to decrease at a certain point, but this is not the case for the coarsest mesh. Such phenomenon is an effect of the different forms of localization observed in the considered meshes, presented

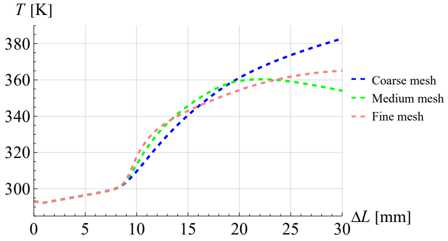

Fig. 24. Temperature depending on the refinement of the mesh at the midpoint of the sample.

in Fig. 25. For the coarse and medium meshes, necking is visible, whereas for the fine mesh, shear bands are present. The finest mesh is chosen for the remaining tests to preserve the accuracy of the obtained results.

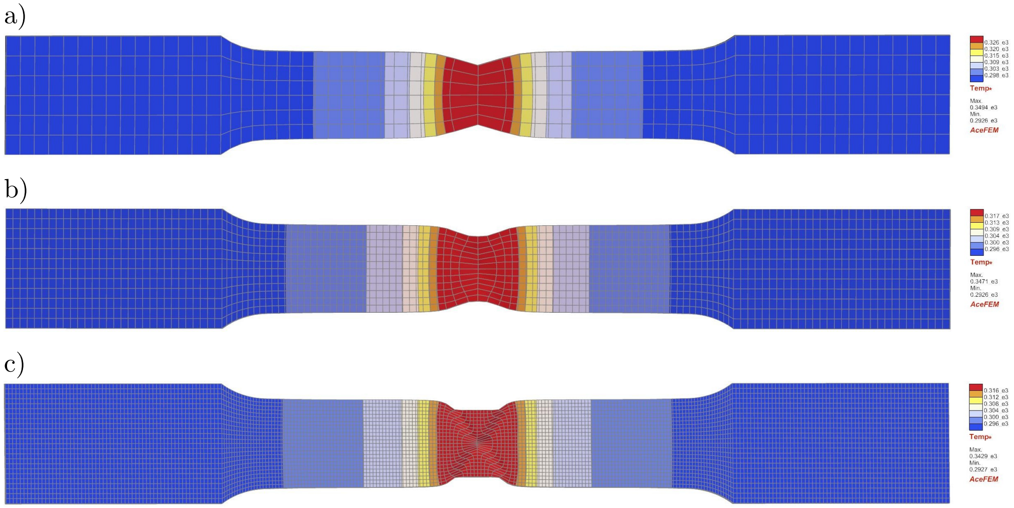

Fig. 25. Deformed meshes with temperature for $\Delta L = 30\,\mathrm{mm}$: a) coarse, b) medium, c) fine.

4.3.2. Influence of thermal boundary conditions

The second set of simulations is performed for Model 1 at room temperature and different thermal boundary conditions, i.e., for insulation and for convection. The heat flux density normal to the specimen surface with convection is defined in the following way:

$$q_n = h_{\mathrm{conv}}(T - T_\infty), \tag{4.1}$$

where T_∞ is the temperature of surrounding and h_{conv} is the convection coefficient. The parameters used in simulations are given in Table 2. A value $h_{\mathrm{conv}} = 0$ corresponds to the insulation boundary condition.

Table 2. Convection parameters.

Property	Symbol	Value
Temperature of surrounding [K]	T_∞	T_0
Convection coefficient $[\mathrm{J}/(\mathrm{s}\cdot\mathrm{K}\cdot\mathrm{m}^2)]$	h_{conv}	0, 10, 100

The results shown in Fig. 27 indicate that for all convection coefficients h_{conv} taken into consideration, the temperature response in the range of reversible deformations and in the plastic hardening range coincides. Starting from $\Delta L = 20\,\mathrm{mm}$ the temperature stops increasing, and the slopes of the curves become increasingly different from each other. Such a phenomenon happens because of the presence of the temperature-hardening coupling in Model 1. With a bigger convection coefficient, greater temperature decrease is observed. Figure 26 shows that the reactions are independent of the chosen convection parameter. For the remaining tests, a convection coefficient $h_{\text{conv}} = 10$ is chosen. For tests performed at elevated temperatures, it is assumed that $T_\infty = T_0$.

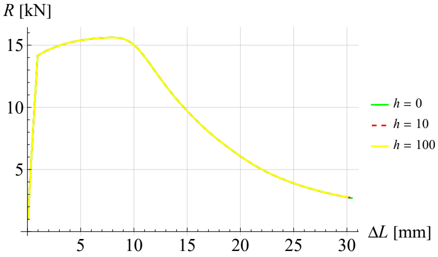

FIG. 26. Reactions independent of the convection coefficient.

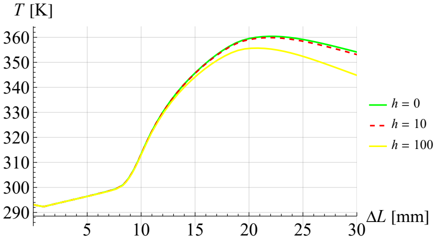

FIG. 27. Temperature difference depending on the value of the convection coefficient h_{conv}.

4.3.3. MODEL 1 VS. MODEL 2

The third and core set of simulations includes the tests of sample tension for different initial temperatures. Now, the sample is subjected to an elongation of $\Delta L = L/8 = 30.8\,\text{mm}$ in time duration of $t = 10\,\text{s}$.

Figure 28 and Fig. 29 show the reaction force vs. enforced displacement for Model 1 and Model 2, respectively. For higher initial temperatures, the magni-

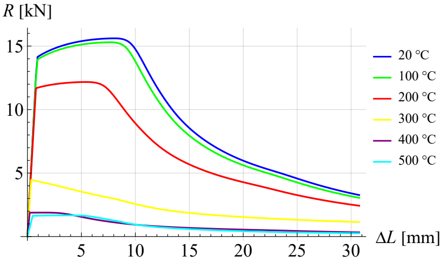

FIG. 28. Sum of reactions vs. enforced displacement at different initial temperatures for Model 1.

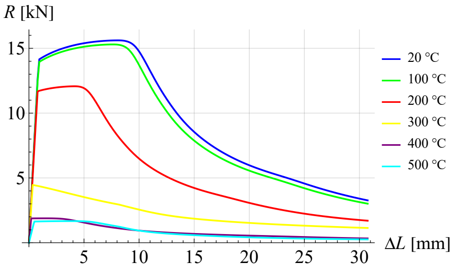

Fig. 29. Sum of reactions vs. enforced displacement at different initial temperatures for Model 2.

tude of reactions decreases, which is consistent with the analysis performed for one FE. The biggest difference between the models is observed for $T_0 = 200\,^\circ\mathrm{C}$, similarly to Fig. 14. For Model 2, the material softens earlier than for Model 1. Such behavior is a result of more substantial self-heating in Model 2, causing greater thermal softening.

Figure 30 and Fig. 31 provide a comparison of temperature change versus elongation. Differences between the models are seen for all analyzed temperatures. Model 2 reproduces a bigger temperature rise for lower T_0, but a smaller rise for higher initial temperatures, i.e., $T_0 = 400\,^\circ\mathrm{C}$ and $T_0 = 500\,^\circ\mathrm{C}$. A significant difference is observed for $T_0 = 200\,^\circ\mathrm{C}$, as in this case the amount of

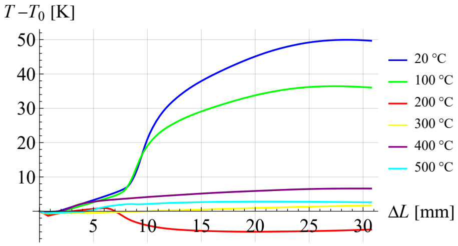

Fig. 30. Relative temperature vs. enforced displacement at different initial temperatures for Model 1.

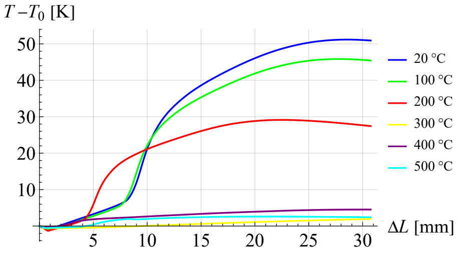

Fig. 31. Relative temperature vs. enforced displacement at different initial temperatures for Model 2.

source sinking due to temperature-hardening coupling exceeds the heat production due to plastic dissipation in the central part of the specimen, where the localization zone occurs. It should also be noted that the results obtained for $T_0 = 300\,^\circ\mathrm{C}$ are not comparable with the remaining results because, in this case, the localization zone is not at the center of the dogbone specimen where the temperature is read, see Fig. 32c. For this reason, the temperature diagram shows a decrease in relative temperature as a result of unloading.

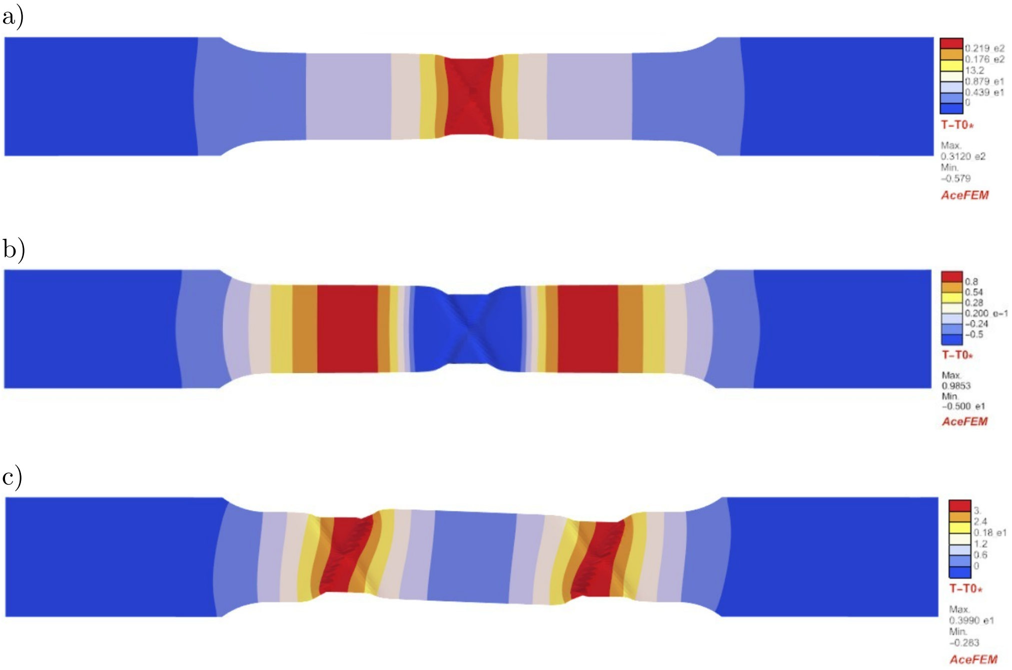

FIG. 32. Deformed mesh with relative temperature at $\Delta L = 12.3\,\mathrm{mm}$ for Model 1: a) $T_0 = 20\,^\circ\mathrm{C}$, b) $T_0 = 200\,^\circ\mathrm{C}$, c) $T_0 = 300\,^\circ\mathrm{C}$.

Figure 32 to Fig. 35 present deformed meshes with temperature and hardening variable distributions for selected initial temperatures, i.e., 20 °C, 200 °C, 300 °C. For $T_0 = 20\,^\circ\mathrm{C}$ and $T_0 = 200\,^\circ\mathrm{C}$, strain localization occurs in the middle part of the sample in the form of two shear bands. As it was mentioned above, the localization for $T_0 = 300\,^\circ\mathrm{C}$ appears in two zones in the web. Only for Model 1 and $T_0 = 200\,^\circ\mathrm{C}$ is the highest temperature not in the shear band areas but outside them. The reason is that thermo-plastic sinking, in this case, is so strong that the area of active plastic process undergoes cooling. Comparing the temperature and hardening variable distributions, it can be observed that the temperature field is more diffused due to heat conductivity.

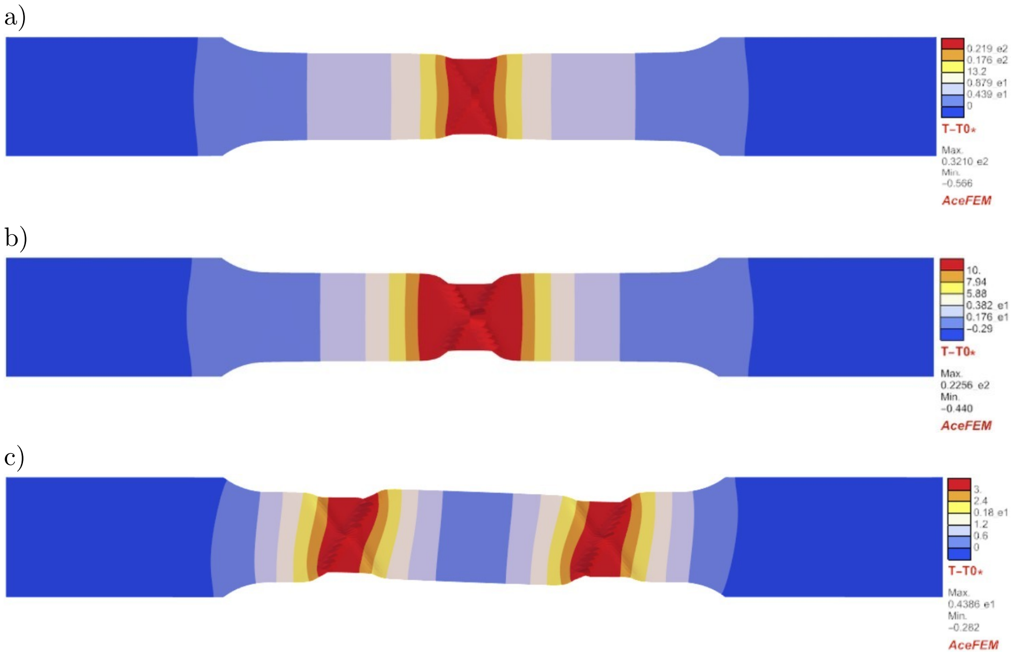

FIG. 33. Deformed mesh with relative temperature at $\Delta L = 12.3$ mm for Model 2: a) $T_0 = 20\,^{\circ}$C, b) $T_0 = 200\,^{\circ}$C, c) $T_0 = 300\,^{\circ}$C.

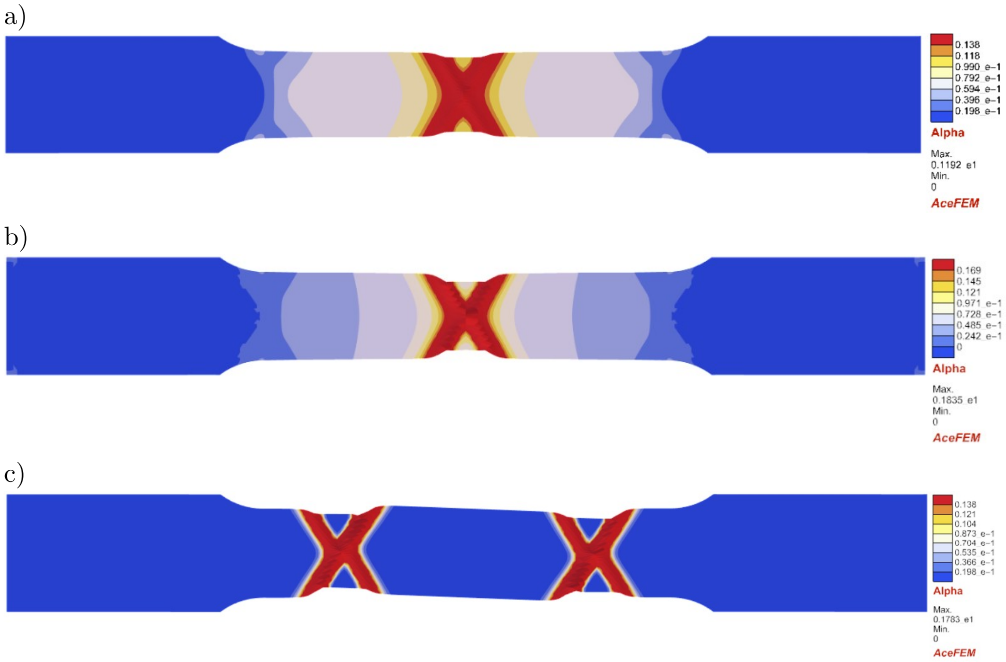

FIG. 34. Deformed mesh with hardening variable at $\Delta L = 12.3$ mm for Model 1: a) $T_0 = 20\,^{\circ}$C, b) $T_0 = 200\,^{\circ}$C, c) $T_0 = 300\,^{\circ}$C.

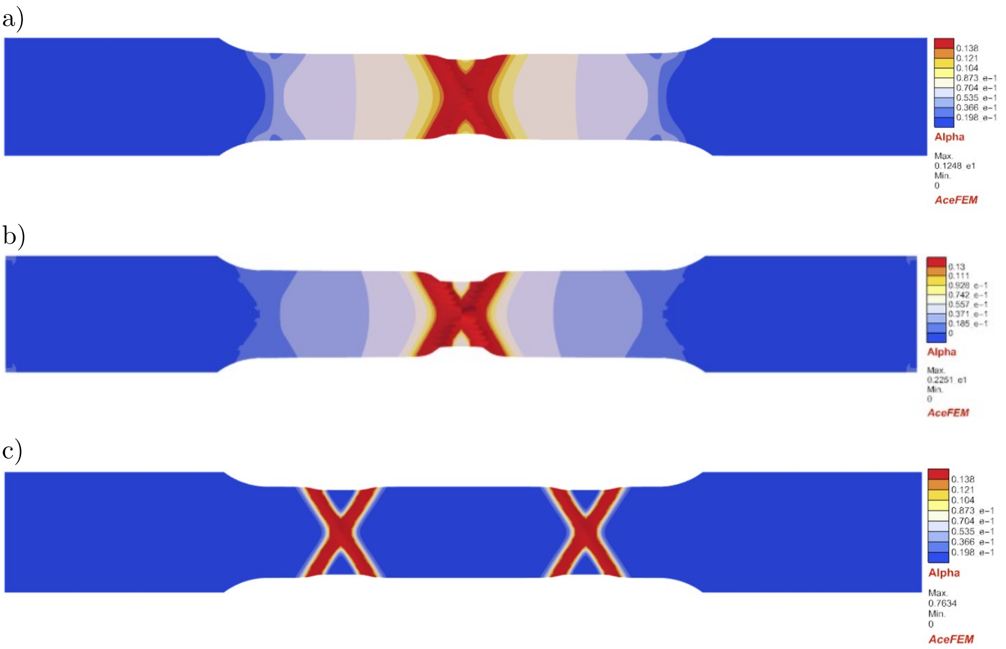

Fig. 35. Deformed mesh with hardening variable at $\Delta L = 12.3\,\text{mm}$ for Model 2: a) $T_0 = 20\,^\circ\text{C}$, b) $T_0 = 200\,^\circ\text{C}$, c) $T_0 = 300\,^\circ\text{C}$.

5. Conclusions

The research presented a comprehensive numerical investigation of aluminum alloy AW5083 under tensile loading, using large-strain thermo-elasto-plastic models. An important aspect of the constitutive description is the application of temperature-dependent material parameters valid in the range from room temperature up to 500 °C together with the employment of internal heat sources. This allowed for numerical simulations of experiments performed at elevated temperatures. The study of the plastic range of deformation was focused on two models of the plastic part of the free energy function. The verification of the influence of temperature-dependent properties on the outcome was performed through simulations of a single cubic FE and dogbone specimens. The models successfully captured fundamental thermo-mechanical phenomena, such as thermo-elastic cooling during elastic deformation and heat generation due to plastic dissipation.

Simulations at different initial temperatures revealed that the Gough–Joule effect is strongest at initial temperature of 300 °C. The elastic modulus, yield stress, and hardening parameters exhibit strong temperature dependence, leading to a reduction of stiffness and earlier yielding at elevated initial temperatures (e.g., 400 °C to 500 °C).

Mesh sensitivity studies show that fine discretization is necessary to reproduce properly the localized deformation modes in the form of shear band(s). Coarser meshes underestimate post-peak softening and misrepresent the localization pattern limiting it to necking. Convection boundary conditions affect the temperature field. Higher convection coefficient accelerate sample cooling and reduce thermal softening.

A thorough comparison between models, including temperature-dependent and temperature-independent plastic free energy, revealed that the largest discrepancies occur between the models at T_0 from 200 °C to 300 °C, where Model 2 predicts stronger material softening due to higher temperature increase. Model 1, including the additional source sinking term resulting from the temperature-hardening coupling, reduces the effect of plastic heating. Moreover, heat sinking for Model 1 is particularly significant in the temperature range from 100 °C to 300 °C and the observed disturbance in this range does not seem consistent with the physics.

Future work should focus on experimental validation in controlled thermal environments to calibrate and refine the models. This would provide crucial data for parameter identification and enhance the models' predictive capabilities. Additionally, extending the framework to include viscous effects, anisotropic behavior, and propagative instabilities such as Portevin–Le Chatelier bands would significantly broaden the model's applicability. Such developments would not only improve the accuracy of the simulations but also contribute to safer and more efficient design of components exposed to extreme thermal and mechanical loads.

FUNDINGS

The work was supported within the Weave-UNISONO program by the German Research Foundation (DFG grant no. 527828607) and by the National Science Centre, Poland (NCN grant no. 2023/05/Y/ST8/00006).

CONFLICT OF INTERESTS

The authors declare that there are no known competing financial interests or personal relationships that could have influenced the work described in this paper.

AUTHORS' CONTRIBUTIONS

Agnieszka Sobierańska carried out the numerical simulations, performed the analysis of the results and wrote the original draft. Balbina Wcisło conceptualized the study, developed the theoretical formulation and implemented the finite element codes. All authors reviewed literature on the topic, interpreted the results, developed, reviewed, and approved the final manuscript.

ACKNOWLEDGEMENT

The authors acknowledge valuable discussions on the research with Prof. Jerzy Pamin and Dr. Marzena Mucha from Cracow University of Technology, Prof. Andreas Menzel from TU Dortmund/Lund University and Dr. Lars Rose from TU Dortmund.

REFERENCES

1. SIMO J.C., Numerical analysis and simulation of plasticity, [in:] *Handbook of Numerical Analysis*, Ciarlet P.G., Lions J.L. [Eds], **6**: 183–499, Elsevier Science B.V., Boca Raton, 1998, https://doi.org/10.1016/S1570-8659(98)80009-4.
2. RISTINMAA M., WALLIN M., OTTOSEN N.S., Thermodynamic format and heat generation of isotropic hardening plasticity, *Acta Mechanica*, **194**: 103–121, 2007, https://doi.org/10.1007/s00707-007-0448-6.
3. HOLZAPFEL G.A., *Nonlinear Solid Mechanics. A Continuum Approach for Engineering*, John Wiley & Sons, Chichester, 2000, https://doi.org/10.1023/A:1020843529530.
4. OPPERMANN P., DENZER R., MENZEL A., A thermo-viscoplasticity model for metals over wide temperature ranges – Application to case hardening steel, *Computational Mechanics*, **69**: 541–563, 2022, https://doi.org/10.1007/s00466-021-02103-4.
5. ĈANADIJA M., BRNIĆ J., Associative coupled thermoplasticity at finite strain with temperature-dependent material parameters, *International Journal of Plasticity*, **20**(10): 1851–1874, 2004, https://doi.org/10.1016/j.ijplas.2003.11.016.
6. SUMMERS P.T., CHEN Y., RIPPE C.M., ALLEN B., MOURITZ A.P., CASE S.W., LATTIMER B.Y., Overview of aluminum alloy mechanical properties during and after fires, *Fire Science Reviews*, **4**: 3, 2015, https://doi.org/10.1186/s40038-015-0007-5.
7. European Committee for Standardization (CEN), *Eurocode 9 – Design of aluminium structures – Part 1–2: Structural fire design* (Standard no. EN 1991-1-2:2023), p. 16, 2023.
8. WCISŁO B., MUCHA M., PAMIN J., Internal heat sources in large strain thermo-elasto-plasticity – Theory and finite element simulations, *Journal of Theoretical and Applied Mechanics*, **62**(2): 293–306, 2024, https://doi.org/10.15632/jtam-pl/185614.
9. KORELC J., WRIGGERS P., *Automation of Finite Element Methods*, Springer, Cham, 2016, https://doi.org/10.1007/978-3-319-39005-5.
10. MUCHA M., ROSE L., WCISŁO B., MENZEL A., PAMIN J., Experiments and numerical simulations of Lueders bands and Portevin–Le Chatelier effect in aluminium alloy AW5083, *Archives of Mechanics*, **75**(3): 301–336, 2023, https://doi.org/10.24423/aom.4204.
11. MIEHE C., Entropic thermoelasticity at finite strains. Aspects of the formulation and numerical implementation, *Computer Methods in Applied Mechanics and Engineering*, **120**(3–4): 243–269, 1995, https://doi.org/10.1016/0045-7825(94)00057-T.

12. Wcisło B., Pamin J., Rose L., Menzel A., On spatial vs referential isotropic Fourier's law in finite deformation thermomechanics, *Engineering Transactions*, **71**(1): 111–140, 2023, https://doi.org/10.24423/EngTrans.2460.20230214.

13. de Souza Neto E.A., Perić D., Owen D.R.J., *Computational Methods for Plasticity: Theory and Applications*, John Wiley & Sons, Chichester, 2008, https://doi.org/10.1002/9780470694626.

14. Wcisło B., Pamin J., Local and non-local thermomechanical modeling of elastic-plastic materials undergoing large strains, *International Journal for Numerical Methods in Engineering*, **109**(1): 102–124, 2017, https://doi.org/10.1002/nme.5280.

15. Lemonds J., Needleman A., Finite element analyses of shear localization in rate and temperature dependent solids, *Mechanics of Materials*, **5**(4): 339–361, 1986, https://doi.org/10.1016/0167-6636(86)90039-6.

Received August 13, 2025; revised October 26, 2025; accepted October 30, 2025;
available online December 18, 2025; version of record April 16, 2026;
published issue June 24, 2026.

Engineering Transactions, **74**(2): 173–186, 2026, https://doi.org/10.24423/engtrans.2025.3626
Institute of Fundamental Technological Research Polish Academy of Sciences (IPPT PAN)
Université de Lorraine • Poznan University of Technology

Research Paper

Simulation Study of Direct-Shear Tests on FRP-to-Concrete Bonded Joints by Means of XFEM

Iwona Jankowiak

Poznan University of Technology
Poznań, Poland

e-mail: iwona.jankowiak@put.poznan.pl

A proper numerical modelling of FRP-to-concrete bonded joints is crucial for determining their strength. In this paper, the results of numerical analyses performed using XFEM on such joints in direct-shear test are presented. The study uses a fracture mechanics approach based on the traction-separation law to define the FRP-concrete interface. It includes the definition of damage initiation as well as damage evolution, taking advantage of the fracture energy of plain concrete as well as the interfacial fracture energy of the analysed joint. The interfacial fracture energy of the bonded joint is essential for accurately describing the local bond–slip behaviour. The numerical study aims to investigate the sensitivity of direct-shear test models to the magnitude of fracture energies, material strengths, the type of adhesive, and the length of FRP-to-concrete joint. Some general results and conclusions of the performed analyses are presented.

Keywords: FRP strengthening, XFEM analysis, modes of fracture energy, FRP-to-concrete joints, interfacial fracture energy, traction-separation law.

NOTATIONS

σ_n, τ_s	– normal and shear bond strengths of the interface,
σ, τ	– normal and shear stresses of the contact under mixed-mode loading,
G_{I}, G_{II}	– fracture energy components of Modes I and II,
$G_{F\mathrm{I}}$, $G_{F\mathrm{II}}$	– critical fracture energies under pure Modes I and II loading,
P	– reaction force at the FRP-concrete interface in the direct-shear test on FRP-to-concrete bonded joints,
s	– relative movement (slip) between the FRP and the concrete under shear stress in the direct-shear test of FRP-concrete bonded joints,
u	– displacement at the end of the FRP strip due to the reaction force P in the direct shear-test,
L	– lengths of the FRP-concrete joint,
G_{cr}	– interfacial fracture energy; value equal to the value of fracture energy $G_{F\mathrm{II}}$ for Mode II,
ε_{11}	– axial strain along the FRP-concrete joint.

1. Introduction

Externally bonded fibre-reinforced polymer (FRP) materials have been widely used for many years as an alternative method to traditional techniques for strengthening reinforced concrete (RC) structural members [1, 2]. The principles of application of this type of strengthening are well recognized and described in the literature [3, 4]. However, aspects related to the failure of FRP-strengthened concrete members are still a subject of research. They are mainly focused on the FRP strip debonding from the concrete surface. This debonding is initiated at the toe of flexural or flexural/shear cracks of concrete members (interfacial debonding, IC) and usually leads to a premature and brittle member failure [5, 6]. Therefore, to design RC beams against FRP debonding failures, proper modelling of the FRP-to-concrete interface is required, and the results obtained from direct-shear tests provide very valuable inputs in this regard.

There are many available results of laboratory tests performed on direct-shear FRP-concrete joints [7–10]. The tests consider the influence of the main parameters on the strength of the bonded joint, such as the length, width, and thickness of the FRP strip, its modulus of elasticity, and the shear span-to-depth ratio. They have been implemented in the development of design methods for RC beam strengthening [11, 12]. These results are also very useful for the validation of analytical and numerical models proposed in recent years. The analytical models, often simplified, presented in [7, 13, 14] are based on an assumed stress-slip relation between the FRP strip and concrete; they use elements of linear elastic fracture mechanics (LEFM), or cohesive crack model (CCM), as well as finite fracture mechanics (FFM). Different bond-slip models for FRP-to-concrete bonded joints have been proposed and presented, for example in [8]. They are based on different τ-slip relation and on interfacial fracture energy [7]. It was also pointed out that the type of adhesive layer (rigid or flexible) can influence the behaviour of FRP-to-concrete joint, mainly affecting the effective bond length and the bond strength itself [9].

The application of the finite element method (FEM) to the analysis of FRP-concrete joints has made it possible to create much more detailed models of the FRP-concrete interface. For example, in [6], the modelling of debonding failure in FRP-strengthened RC beams used the concept of a cohesive zone model, and for concrete cover separation, special cohesive elements were implemented.

Using the classical FEM, it is very difficult or impossible to address fracture mechanics problems, such as modelling material separation and fracture processes with realistic crack initiation and propagation, which is particularly valuable for concrete [16–19].

The extended finite element method (XFEM) allows to model cracks using discontinuous functions, such as the Heaviside step function, without the need to explicitly mesh the crack itself; cracks can occur arbitrarily in the interior of finite elements. XFEM enables detailed analysis of cracks, material interfaces, and multiple crack interactions within a single model.

The strip debonding failure has been observed in laboratory tests on RC beam elements strengthened with FRP strips, performed and described extensively in [5]. In these experiments, the main goal was to recognise the overall response of strengthened concrete beams in terms of their load-carrying capacity and stiffness increase. The local effects, such as debonding and its impact on the behaviour of the entire system, were not considered at that time. The concrete damaged plasticity material model [5, 6, 15] was employed in the analyses, which allowed the ultimate load-carrying capacity to be estimated with sufficient accuracy. These results were then validated by laboratory tests. A very good agreement with the experimental results was observed. It was concluded that if only the ultimate load capacity estimation is required, XFEM does not need to be applied.

The present study is aimed at the detailed modelling of a direct-shear test, which is a highly discontinuous and nonlinear phenomenon. In the study, XFEM was applied. A parametric analysis of the main characteristics affecting the performance of these joints has been carried, and its results will be used for preparing the planned laboratory tests.

2. Application of XFEM for crack modelling of FRP-concrete bonded joints

The XFEM was first proposed in the context of fracture by Belytschko and Black [20], subsequently, the method was further developed [21, 22] and is still successfully used for the analysis of cracking phenomena in concrete elements. A comprehensive study of the fracture process in concrete and RC, by means of constitutive models formulated within continuum mechanics, where both continuous and discontinuous modelling approaches (using CCM and XFEM) were used, is presented in [23]. It has been proven that XFEM is an alternative method to FEM that extends the allowable basis functions, known as partition of unity methods [23, 24]. This method can be used not only to model cracks in homogenous material but also cracking occurring between two different materials (bimaterial interface cracks) [25]. Numerical modelling of crack propagation in plain concrete under Mode II and mixed-mode condition, with successful comparison with experiment results, was given in [26, 27].

When applied to crack propagation problems, XFEM introduces two extra sets of functions in addition to standard FEM nodal basis functions: a step function $H(x)$ to capture the discontinuity in displacement across a crack, and a set of functions $F_i(x)$, typically expressed in polar coordinates centred at the crack tip, capturing stress singularity in that region. The extra basis functions are defined as the product of these enrichment functions and the standard nodal basis function to ensure that the basis functions remain mesh-based and local to the enriched nodes.

This method does not require the mesh to match the geometry of discontinuities. It can be used to simulate the initiation and propagation of a discrete crack by using a fracture energy criterion along an arbitrary, solution-dependent path in the bulk material, without the need for remeshing (crack propagation is not tied to element boundaries in the mesh) [23, 25].

In XFEM modelling of the FRP-concrete shear test, the failure mechanism, including degradation and eventual separation between the two surfaces, consists of two components: a damage initiation criterion and a damage evolution law.

Damage is initiated (either when an additional crack is introduced, or when the crack length of an existing crack is extended after an equilibrium increment), when the contact stresses and/or contact separations satisfy the damage initiation criterion, i.e., when the fracture criterion reaches a value of 1 within a given tolerance.

In 2D analysis concerning the phenomena of the direct-shear test of FRP strips from the concrete surface, the quadratic nominal stress criterion [15, 28] was assumed as the damage initiation criterion:

$$\left(\frac{\langle\sigma\rangle}{\sigma_n}\right)^2 + \left(\frac{\tau}{\tau_s}\right)^2 = 1, \tag{2.1}$$

where σ_n and τ_s are the normal and shear bond strengths of the interface, respectively; σ and τ are the normal and shear stresses at the interface under mixed-mode loading, respectively. The symbol $\langle\ \rangle$ is used to signify that purely compressive stress does not initiate damage, i.e., $\langle\sigma\rangle = 0$ if $\sigma < 0$ and $\langle\sigma\rangle = \sigma$ if $\sigma \geq 0$.

The damage evolution law defines the post damage-initiation material behaviour and describes the rate of degradation of the material stiffness once the initiation criterion has been reached. In the analysis of the direct-shear test of FRP strips from the concrete surface, the damage evolution is described using a linear softening model expressed in terms of fracture energy. The adopted power-law fracture energy criterion (with a power of 2) [15, 28, 29] is defined as a function of mode mix, using normal-mode fracture energy G_{I} (Mode I) for plain concrete and shear-mode fracture energy G_{II} (Mode II) for the interfacial FRP-concrete joint:

$$\left(\frac{G_{\mathrm{I}}}{G_{F\mathrm{I}}}\right)^2 + \left(\frac{G_{\mathrm{II}}}{G_{F\mathrm{II}}}\right)^2 = 1, \tag{2.2}$$

where G_{I} and G_{II} are the fracture energy components of Modes I and II, respectively; $G_{F\mathrm{I}}$ and $G_{F\mathrm{II}}$ are the critical fracture energies under pure Modes I and II loading, respectively.

The interfacial fracture energy, which is crucial in the analysis of the FRP-concrete bonded joint, represents the total external energy required to create, propagate and fully open a crack along the FRP-concrete interface. Finding the right value of the interfacial fracture energy of the analysed interface remains an open issue due to the number of parameters governing the local bond–slip behaviour as well as the bond strength of the FRP-concrete joint itself. These include the tensile, compressive, and shear strengths of concrete, the tensile strengths of the adhesive and the FRP strip, the moduli of elasticity of all components of the joint, as well as its main dimensions.

It is worth mentioning that, in the case of mixed-mode conditions, the Mode I (tensile) fracture energy of concrete-FRP joints can be approximated by the Mode I fracture energy of plain concrete, provided that debonding in the concrete-FRP bonded joint takes place within concrete. A second observation is that the Mode II (shear) fracture energy of both plain concrete and FRP-concrete joint appears to be an order of magnitude higher than that for Mode I [14].

3. NUMERICAL ANALYSIS OF THE DIRECT-SHEAR TEST

The subject of this study is the simulation of a single direct-shear test on an FRP-to-concrete bonded joint, as presented in Fig. 1, where the main dimensions are shown. The applied constraints are intended to prevent the concrete prism from uplifting and shifting under loading. The FRP strip is bonded with an adhesive layer to the top surface of the concrete prism. Three lengths of joint – 10 cm, 15 cm, and 20 cm, and two types of adhesive layers with different stiffnesses were considered. Displacement-controlled loading was used by incrementing the displacement u at the end of the FRP strip (Fig. 1).

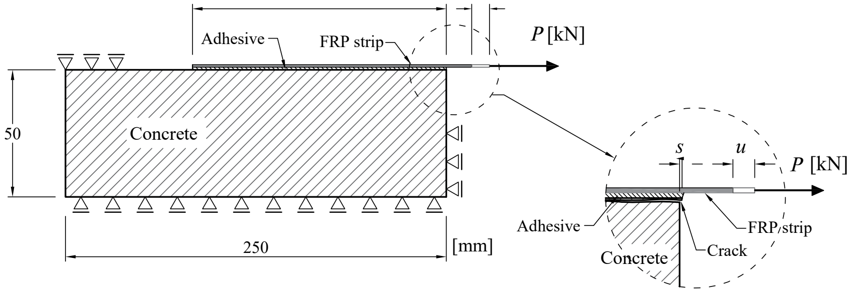

FIG. 1. Setup of the analysed direct-shear test.

The plots of reaction force P and slip s at the FRP-concrete interface were then obtained.

In the numerical analyses, the XFEM method implemented in Abaqus ver. 2024 code [15] was used. The failure mechanism definition includes damage initiation as well as damage evolution, which are based on a fracture mechanics approach and on the assumed bilinear traction-separation law for the FRP-concrete interface (Fig. 2). It was not necessary to predefine the crack initiation in the mesh layout for further propagation. This is one of the most convenient capabilities provided by the XFEM method.

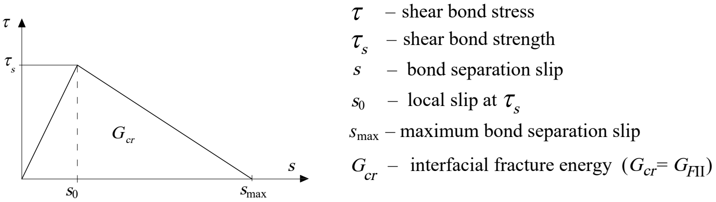

FIG. 2. Bilinear traction-separation law for the FRP-concrete interface.

When analysing the traction-separation law for the FRP-concrete interface, the area under the entire curve (Fig. 2) represents the interfacial fracture energy G_{cr}, which is equal to the value of the fracture energy $G_{F\mathrm{II}}$ for Mode II.

All parts of the numerical model are defined as elastic materials. The concrete prism, as well as the adhesive layer and FRP strip, are modelled using 4-node 2D plane strain elements (Fig. 3) of 1 mm × 1 mm dimensions. Although XFEM is often described as mesh-independent because cracks can propagate through elements without the mesh conforming to the crack geometry, it still requires a sufficiently fine mesh to obtain accurate results, especially near crack tips where stresses are singular. For this reason, a convergence study was performed by varying the element size. Analyses with different element sizes were performed, namely 1 mm × 1 mm, 1.5 mm × 1.5 mm, and 2 mm × 2 mm meshes. Finally, a mesh with an element size of 1 mm × 1 mm was used in all calculations,

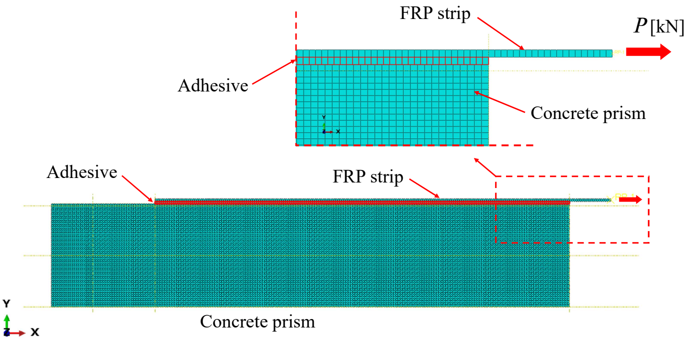

FIG. 3. 2D mesh of concrete prism with FRP strip.

for which the peak load did not change by more than 0.7 % compared to that obtained with the 1.5 mm × 1.5 mm mesh.

It was observed in laboratory tests [5] that the quasi-brittle behaviour of concrete influences the FRP debonding process. Fracture propagation during IC debonding starts within a thin concrete layer underlying the adhesive layer [5, 18, 30]. It was assumed that, in the case of the shear test for all tested bond lengths, delamination also starts within a thin concrete layer, beginning close to the loaded end of the FRP strip [16, 30]. For this reason, a one-element-thick layer of finite elements in the concrete part of the numerical model was given additional enrichment with additional degrees of freedom according to XFEM.

The material data used in the numerical analyses were taken from a previously performed research program concerning the flexural strengthening of simply supported RC beams using FRP strips [5]. For concrete, the modulus of elasticity and Poisson's ratio before cracking were determined as 29.98 GPa and 0.164, respectively. The concrete compressive cylinder strength was assumed as 44.40 MPa, while the tensile strength was determined as 3.467 MPa. The modulus of elasticity and Poisson's ratio of the FRP strips were taken as 158.95 GPa and 0.2, respectively. For the flexible adhesive, the modulus of elasticity and Poisson's ratio were equal to 7.10 GPa and 0.3, respectively. To check the influence of the stiffness of the adhesive layer on the behaviour of the entire joint, a case with a rigid adhesive with an elastic modulus 10 times higher than the stiffness modulus assumed for the flexible adhesive, was also considered [9].

The proper definition of the traction-separation law for the FRP-concrete interface is a key issue in delamination analysis by XFEM (Fig. 2). It mainly concerns the stress value τ_s, which is used to define the damage initiation criterion, as well as the interfacial fracture energy G_{cr}, which is equal to the value $G_{F\mathrm{II}}$ for the FRP-concrete joint. This value is, in turn, used in the definition of crack evolution. In our case of 2D analysis, in Eq. (2.1), two stress components, namely σ_n and τ_s, must be defined as the component normal to the potential cracked surface and as the shear component to the likely cracked surface, respectively. While the first component corresponds to the tensile strength of concrete, the second component cannot be determined directly. According to [8], the value of the shear strength τ_s depends on both the tensile strength of concrete as well as on the geometry of the FRP-concrete joint. Taking into account the width of the FRP strip and the width of the concrete prism, τ_s was calculated as 5.721 MPa [8].

Another important issue in delamination analysis is to assume correct and reliable values of fracture energy G_{Fi} parameters [14, 30]. While finding the fracture energy value $G_{F\mathrm{I}}$, which refers to fracture energy for Mode I (tensile) is rather straightforward, then finding the proper fracture energy value $G_{F\mathrm{II}}$ for Mode II (shear), which refers to the interface failure of the FRP-concrete joint, is not easy. In this study, the value of $G_{F\mathrm{I}}$ is assumed as 0.090 kN/m as a function of both maximum aggregate size and the strength class of concrete [31]. The value of fracture energy for the FRP-concrete interface $G_{F\mathrm{II}}$ depends strongly on the geometry of a joint as well as on one of two basic strengths of concrete. According to [6, 8, 10] the value of fracture energy $G_{F\mathrm{II}}$ for Mode II is calculated as 0.694 kN/m as a function of tensile strength of concrete, but in accordance to [14] it could be also assumed as 1.524 kN/m as a function of compressive strength of concrete. There is a significant discrepancy between the two calculated values, which confirms the need for future laboratory verification of that interface fracture energy value. In the present numerical analyses to estimate the influence of different parameters on the behaviour of the FRP-concrete bonded joint, both above mentioned values of $G_{F\mathrm{II}}$ are used in definition of damage evolution law.

4. Numerical results

A series of numerical analyses was performed, and some general conclusions are drawn hereafter.

The influence of different values of the interfacial fracture energy $G_{F\mathrm{II}}$ on the strength of the FRP-concrete bonded joint was examined first. It was noted earlier that the value of this energy is crucial in modelling the FRP-concrete joint and it has a significant effect on its strength. The results of the study for a bond length equal to 20 cm are presented in Fig. 4. They are in good agreement with those proposed in [6], where, for considered fracture energies, the ultimate load capacity of the bonded joints were calculated as approximately 26 kN and 38 kN, respectively. It is worth noticing that, in the simplified analytical formula, the ultimate load does not depend on the bond length.

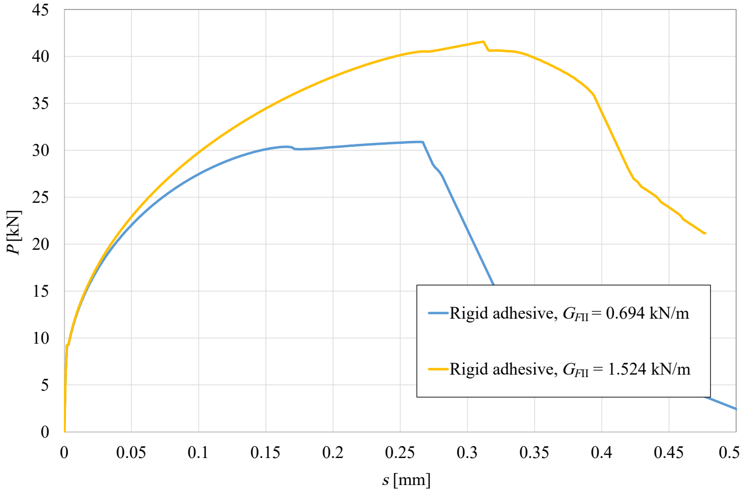

Fig. 4. Load-slip curves for a 20 cm joint for different values of interfacial fracture energy.

Most debonding models neglect the effect of adhesive stiffness. In reliable modelling, this effect should be taken into consideration because, as it was shown, for example, in [9], the adhesive stiffness may affect the ultimate bond capacity of the FRP-concrete interface. The results of the analyses for one bond length, for rigid and flexible adhesive, and for the two considered interfacial fracture energies are presented in Fig. 5. It is shown that the use of a rigid adhesive increases the bond strength of the FRP-concrete joint – the lower the value of interfacial fracture energy, the greater the increase of bond strength of the joint. It is also seen that a flexible adhesive shifts the bond capacity horizontally and makes the FRP-concrete interface more ductile.

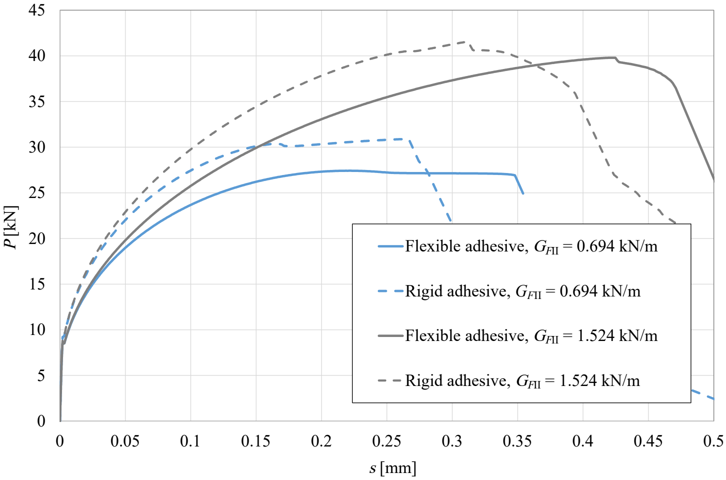

Fig. 5. Load-slip curves for a 20 cm joint for different types of adhesives and different values of interfacial fracture energy.

The effective bond length is defined as the length of the composite strip beyond which, there would be no increase in the force transferred between concrete and the FRP strip. So, a properly assumed effective length of the FRP strip is another key parameter in the modelling of such joints. This aspect is examined next in our study.

Analyses were performed for three different bonding lengths: 10 cm, 15 cm, and 20 cm. The results of these analyses are presented in Fig. 6, where it can be seen that the bond strength is higher for longer bond lengths.

To find out the value of the effective length of the FRP strips, the analysis of the axial strain ε_{11} along the joint between the strip and the concrete is carried out for different levels of loadings. In Fig. 7 and Fig. 8, the results of these analyses are shown, and the strain ε_{11} distributions along the strip are presented for two cases of joint lengths (10 cm and 20 cm). It can be noticed from Fig. 7b that the strain ε_{11} approaches zero at about $x = 3.5$ cm for a load close to the

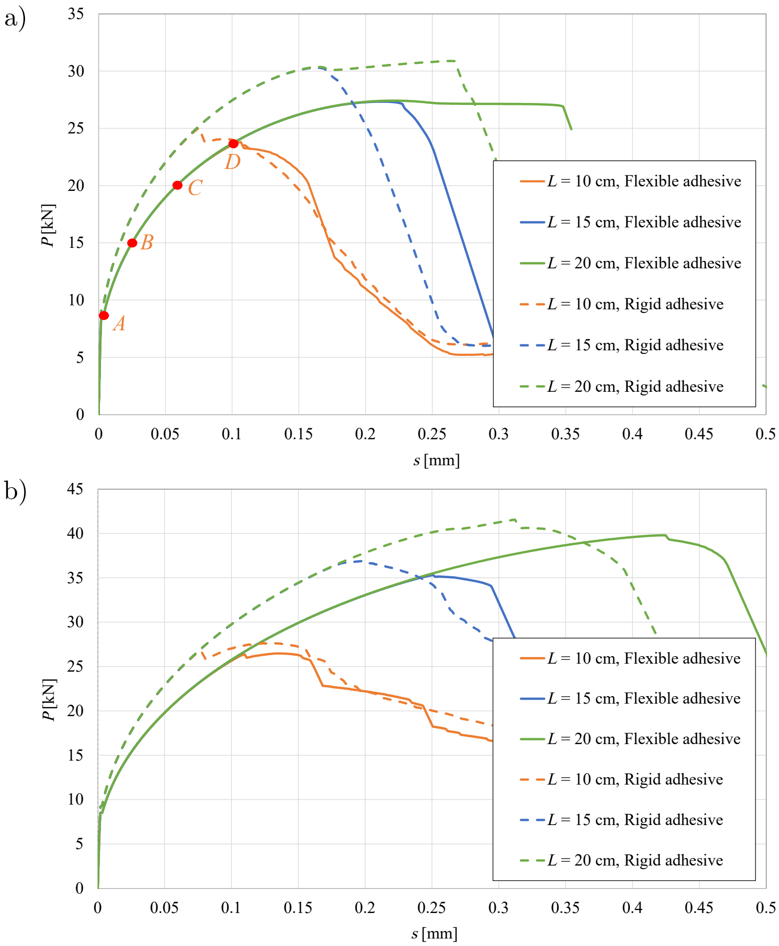

FIG. 6. Load-slip curves for different bond lengths and different types of adhesive layer: a) $G_{F\mathrm{II}} = 0.694\,\mathrm{kN/m}$, b) $G_{F\mathrm{II}} = 1.524\,\mathrm{kN/m}$.

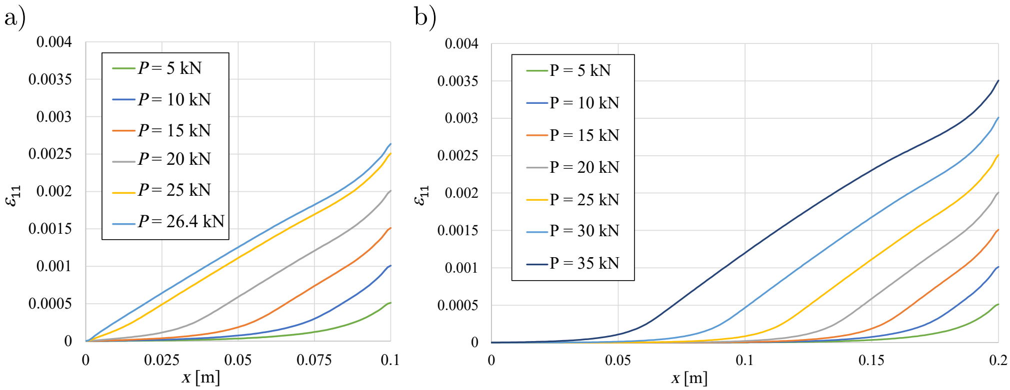

FIG. 7. Strain ε_{11} along the strips for flexible adhesive with $G_{F\mathrm{II}} = 1.524\,\mathrm{kN/m}$ and for different bond lengths: a) $L = 10\,\mathrm{cm}$, b) $L = 20\,\mathrm{cm}$.

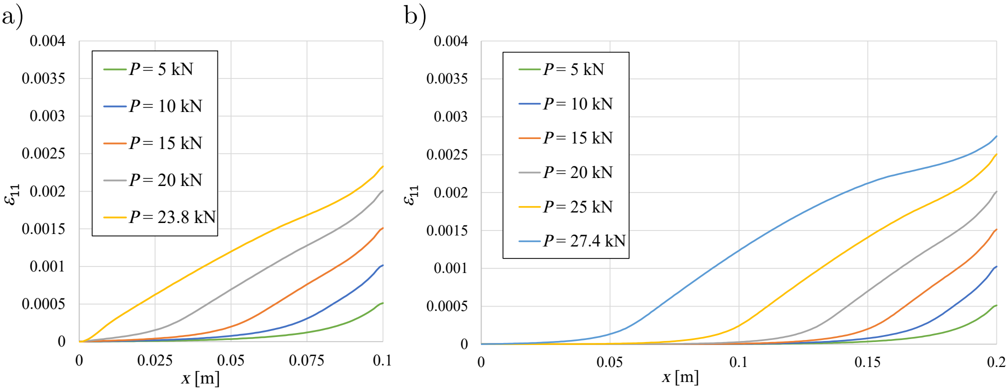

FIG. 8. Strain ε_{11} along the strips for flexible adhesive with $G_{F\text{II}} = 0.694\,\text{kN/m}$ and for different bond lengths: a) $L = 10\,\text{cm}$, b) $L = 20\,\text{cm}$.

ultimate value. This means that the effective bond length value is about 16.5 cm, which corresponds very well to that obtained in [31]. For the strip length equal to 10 cm, a similar trend does not occur, what is clearly seen in Fig. 7a. This confirms that a length of 10 cm turns out to be underestimated.

The strain paths show the higher strain ε_{11} levels and better utilization of the FRP strip for a strip length of 20 cm, regardless of the type of adhesive layer.

To illustrate crack progression during the shear test, contour plots of crack progression (scaled ×10) for different load levels indicated in Fig. 6a are shown in Fig. 9, for the case of a flexible adhesive with $G_{F\text{II}} = 0.694\,\text{kN/m}$ and a bond length equal to 10 cm.

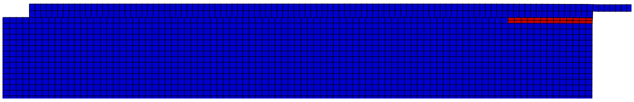

Point A (8.5 kN)

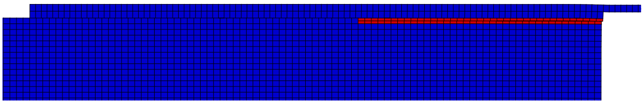

Point B (15 kN)

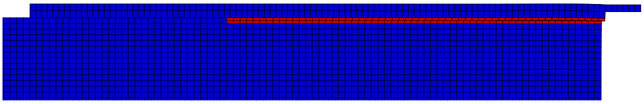

Point C (20 kN)

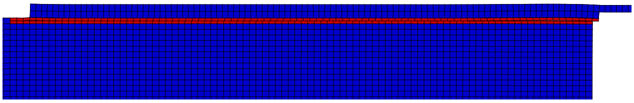

Point D (23.8 kN)

FIG. 9. Contour plots of crack progression (flexible adhesive; $G_{F\text{II}} = 0.694\,\text{kN/m}$; bond length 10 cm) for different load levels (Fig. 6a).

5. FINAL CONCLUSIONS

This paper presented the major results of the study on the direct-shear test on the FRP-concrete bonded joints using the XFEM. The applied method successfully allowed to analyze the FRP-concrete joint, which is a highly discontinuous and nonlinear phenomenon that cannot be fully captured by standard FEM.

Based on the performed numerical analyses, it was found that a key issue in modelling is to adopt an appropriate interfacial fracture energy.

The effective bond length is another important parameter, as it not only determines the effectiveness of the joint but also affects its strength.

Consideration of the adhesive stiffness in modelling is important because it impacts the local bond-slip behaviour of the FRP-concrete interface and, subsequently, affects its load-carrying capacity.

The aforementioned parameters are the most important ones in governing the bond–slip behaviour as well as the bond strength of the FRP-concrete joints. These parameters will be the subject of planned laboratory tests to validate them.

FUNDINGS

The work was financially supported by Poznan University of Technology, Institute of Civil Engineering (grant no. 0413/SBAD/6602).

CONFLICT OF INTERESTS

The author declares that there are no known competing financial interests or personal relationships that could have influenced the work described in this paper.

AUTHOR'S CONTRIBUTION

The author conceptualized the study, performed the analysis, wrote the original draft, and approved the final manuscript.

REFERENCES

1. TENG J.G., CHEN J.F., SMITH S.T., LAM L., *FRP-Strengthened RC Structures*, John Wiley & Sons, Chichester, England, 2002.
2. HAMMAD M., BAHRAMI A., KHOKHAR S.A., KHUSHNOOD R.A., A state-of-the-art review on structural strengthening techniques with FRPs: Effectiveness, shortcomings, and future research directions, *Materials*, **17**(6): 1408, 2024, https://doi.org/10.3390/ma17061408.
3. ORTIZ J.D., KHEDMATGOZAR DOLATI S.S., MALLA P., NANNI A., MEHRABI A., FRP-reinforced/strengthened concrete: State-of-the-art review on durability and mechanical effects, *Materials*, **16**(5): 1990, 2023, https://doi.org/10.3390/ma16051990.

4. Kotynia R., *FRP Composites for Flexural Strengthening of Concrete Structures. Theory, Testing, Design*, Lodz University of Technology Press, Poland, 2019, https://doi.org/10.34658/9788372839961.

5. Jankowiak I., Analysis of RC beams strengthened by CFRP strips – Experimental and FEA study, *Archives of Civil and Mechanical Engineering*, **12**(3): 376–388, 2012, https://doi.org/10.1016/j.acme.2012.06.010.

6. Al-Saawani M.A., Al-Negheimish A.I., El-Sayed A.K., Alhozaimy A.M., Finite element modeling of debonding failures in FRP-strengthened concrete beams using cohesive zone model, *Polymers*, **14**(9): 1889, 2022, https://doi.org/10.3390/polym14091889.

7. Dai J., Ueda T., Sato Y., Unified analytical approaches for determining shear bond characteristics of FRP-concrete interfaces through pullout tests, *Journal of Advanced Concrete Technology*, **4**(1): 133–145, 2006, https://doi.org/10.3151/jact.4.133.

8. Lu X.Z., Teng J.G., Ye L.P., Jiang J.J., Bond–slip models for FRP sheets/plates bonded to concrete, *Engineering Structures*, **27**(6): 920–937, 2005, https://doi.org/10.1016/j.engstruct.2005.01.014.

9. Diab H.M., Farghal O.A., Bond strength and effective bond length of FRP sheets/plates bonded to concrete considering the type of adhesive layer, *Composites Part B: Engineering*, **58**: 618–624, 2014, https://doi.org/10.1016/j.compositesb.2013.10.075.

10. Chen J.F., Teng J.G., Anchorage strength models for FRP and steel plates bonded to concrete, *Journal of Structural Engineering*, **127**(7): 784–791, 2001, https://doi.org/10.1061/(ASCE)0733-9445(2001)127:7(784).

11. American Concrete Institute, *Guide for the design and construction of externally bonded FRP systems for strengthening concrete structures* (ACI 440.2R-08), USA, 2008.

12. FIB Bulletin 90, *Externally applied FRP reinforcement for concrete structures*, Technical report, Lausanne, Switzerland, 2019, https://doi.org/10.35789/fib.BULL.0090.

13. Cornetti P., Corrado M., De Lorenzis L., Carpinteri A., An analytical cohesive crack modeling approach to the edge debonding failure of FRP-plated beams, *International Journal of Solids and Structures*, **53**: 92–106, 2015, https://doi.org/10.1016/j.ijsolstr.2014.10.017.

14. Gunes O., Buyukozturk O., Karaca E., A fracture-based model for FRP debonding in strengthened beams, *Engineering Fracture Mechanics*, **76**(12): 1897–1909, 2009, https://doi.org/10.1016/j.engfracmech.2009.04.011.

15. Dassault Systemes, *Abaqus user's guide*, USA, 2024.

16. Benvenuti E., Vitarelli O., Tralli A., Delamination of FRP-reinforced concrete by means of an extended finite element formulation, *Composites Part B: Engineering*, **43**(8): 3258–3269, 2012, https://doi.org/10.1016/j.compositesb.2012.02.035.

17. Mohammadi T., *Failure mechanisms and key parameters of FRP debonding from cracked concrete beams*, Ph.D. Thesis, Marquette University, USA, 2014.

18. Jankowiak I., XFEM analysis of intermediate crack debonding of FRP strengthened RC beam, [in:] *Advances in Mechanics – Theoretical, Computational and Interdisciplinary Issues*, Kleiber M., Burczyński T., Wilde K., Górski J., Winkelmann K., Smakosz Ł. [Eds], pp. 235–239, CRC Press, London, 2016.

19. Mohammadi T., Wan B., Harries K., Intermediate crack debonding model of FRP-strengthened concrete beams using XFEM, SIMULIA Community Conference, Dassault Systèmes, Paris, 2013, https://doi.org/10.13140/RG.2.1.3597.2641.

20. Belytschko T., Black T., Elastic crack growth in finite elements with minimal remeshing, *International Journal for Numerical Methods in Engineering*, **45**(5): 601–620, 1999, https://doi.org/10.1002/(SICI)1097-0207(19990620)45:5<601::AID-NME598>3.0.CO;2-S.

21. Moës N., Dolbow J., Belytschko T., A finite element method for crack growth without remeshing, *International Journal for Numerical Methods in Engineering*, **46**(1): 131–150, 1999, https://doi.org/10.1002/(SICI)1097-0207(19990910)46:1<131::AID-NME726>3.0.CO;2-J.

22. Moës N., Belytschko T., Extended finite element method for cohesive crack growth, *Engineering Fracture Mechanics*, **69**(7): 813–833, 2002, https://doi.org/10.1016/S0013-7944(01)00128-X.

23. Tejchman J., Bobiński J., *Continuous and Discontinuous Modelling in Fracture in Concrete Using FEM*, Springer, Berlin, Heidelberg, 2013, https://doi.org/10.1007/978-3-642-28463-2.

24. Melenk J.M., Babuška I., The partition of unity finite element method: Basic theory and applications, *Computer Methods in Applied Mechanics and Engineering*, **139**(1–4): 289–314, 1996, https://doi.org/10.1016/S0045-7825(96)01087-0.

25. Sukumar N., Huang Z.Y., Prévost J.-H., Suo Z., Partition of unity enrichment for bimaterial interface cracks, *International Journal for Numerical Methods in Engineering*, **59**(8): 1075–1102, 2004, https://doi.org/10.1002/nme.902.

26. Golewski G.L., Golewski P., Sadowski T., Numerical modelling crack propagation under Mode II fracture in plain concretes containing siliceous fly-ash additive using XFEM method, *Computational Materials Science*, **62**: 75–78, 2012, https://doi.org/10.1016/j.commatsci.2012.05.009.

27. Watkins J., Fracture toughness test for soil-cement samples in mode II, *International Journal of Fracture*, **23**: R135–R138, 1983, https://doi.org/10.1007/BF00020700.

28. Rocha R.J.B., Campilho R.D.S.G., Evaluation of different modelling conditions in the cohesive zone analysis of single-lap bonded joints, *The Journal of Adhesion*, **94**(7): 562–582, 2018, https://doi.org/10.1080/00218464.2017.1307107.

29. Whitcomb J.D., *Analysis of instability-related growth of a through-width delamination*, NASA Technical Memorandum (TM), Report no. NASA-TM-86301, 1984.

30. Carloni C., Analyzing bond characteristics between composites and quasi-brittle substrates in the repair of bridges and other concrete structures, [in:] *Advanced Composites in Bridge Construction and Repair*, Kim Y.J. [Ed.], Woodhead Publishing, pp. 61–93, 2014, https://doi.org/10.1533/9780857097019.1.61.

31. CEB-FIP, *Model Code 1990. Design Code*, Comité Euro-International du Béton, Lausanne, Switzerland, 1993 (Republished 1998).

Received July 28, 2025; revised September 30, 2025; accepted November 1, 2025;
available online December 12, 2025; version of record April 13, 2026;
published issue June 24, 2026.

Engineering Transactions, **74**(2): 187–206, 2026, https://doi.org/10.24423/engtrans.2026.3649
Institute of Fundamental Technological Research Polish Academy of Sciences (IPPT PAN)
Université de Lorraine • Poznan University of Technology

Research Paper

A Small-Sample Fault Diagnosis Method for Rolling Bearings Based on Balanced Distribution Adaptation and Support Vector Machine

Dong Chen*, Mingshan Zhang, Yaguang Gao

Jinan Technician College
Handan, China

*Corresponding Author: chendong859052@163.com

To address the issue of low diagnostic accuracy caused by distribution differences between the source and target domains in rolling bearing fault diagnosis, this study proposes a method combining balanced distribution adaptation (BDA) and support vector machines (SVMs). The approach utilizes BDA to simultaneously minimize discrepancies in both the marginal and conditional distributions between domains, enabling effective feature alignment and enhancing the model's cross-domain generalization in small-sample scenarios. After extracting time- and frequency-domain features, BDA adaptively adjusts the feature distributions, and SVMs are employed for fault classification. Experimental results demonstrate that the BDA-SVM method achieves over 94 % diagnostic accuracy, showcasing strong performance and robustness in bearing fault diagnosis. Compared with traditional SVMs and other methods without transfer learning, the proposed approach shows a significant improvement in diagnostic accuracy under cross-domain conditions.

Keywords: rolling bearings, fault diagnosis, balanced distribution adaptation, transfer learning, support vector machines (SVMs).

1. INTRODUCTION

Bearings in industrial equipment generally play a critical role in support and power transmission, and their health status directly affects the operational stability and service life of the entire equipment [1, 2]. Especially in critical fields such as mechanical manufacturing, wind power, and rail transportation, sudden failures of rolling bearings can lead to equipment shutdowns, causing significant economic losses and even safety accidents. However, due to their long-term operation in high-temperature, heavy-load, and high-frequency alternating-load environments, rolling bearings are prone to various faults [2, 3]. Existing research indicates that approximately 30 % of failures in rotating machinery are caused by rolling bearing failures [1, 4]. Therefore, achieving precise early fault diagnosis [21] is of great significance for ensuring normal equipment operation, extending equipment service life, and preventing loss escalation [5].

Traditional fault diagnosis relies on manual experience analysis, which is inefficient, highly subjective, and requires precise mechanistic models as support, thus presenting numerous challenges in practical applications [6]. With technological advancements and the accumulation of experience, data-driven intelligent diagnostic methods, by leveraging machine learning and deep learning's ability to fit complex nonlinear functions, have demonstrated outstanding performance in industrial equipment fault diagnosis [4].

However, the performance of data-driven methods highly depends on large-scale labeled data, which is a significant bottleneck in industrial settings due to the scarcity of fault data. While data collected under normal operating conditions are relatively abundant in most industrial scenarios, fault data are often scarce due to various challenges such as the difficulty of fault detection, characterization, and reproduction [6]. Existing supervised learning models rely on large amounts of labeled data and are prone to overfitting under small-sample conditions, significantly reducing diagnostic accuracy.

Besides, recent studies have further explored transfer learning for fault diagnosis. For instance, a comparative study [7] is conducted on classical shallow transfer learning methods using the Case Western Reserve University (CWRU) bearing dataset, including balanced distribution adaptation (BDA)+K-nearest neighbor (KNN) and BDA+support vector machines (SVMs), and reported that BDA+KNN achieved the highest accuracy, while BDA+SVMs ranked second. Similarly, Lei *et al.* [8] provided a comprehensive review of deep-learning-based fault diagnosis methods and highlighted their effectiveness in feature extraction under varying working conditions. Although these deep learning-based methods have shown promising performance, they often require a larger number of parameters and substantial computational resources, and their performance can degrade in extreme small-sample scenarios.

To address the issue of insufficient model generalization under small-sample conditions, transfer learning provides a solution. Its core objective is to reduce the distribution differences between the source and target domains to achieve knowledge transfer, enabling the model to effectively reuse source-domain knowledge in the target domain [7]. Existing studies mostly focus on marginal distribution features between the source and target domains while neglecting conditional distribution differences [1, 8]. BDA achieves effective cross-domain feature transfer by jointly optimizing differences between marginal and conditional distributions and introducing a tuning parameter to balance the weights of marginal and conditional distributions. This approach preserves category-discriminative information while minimizing domain-specific bias, thereby providing an effective method for fault diagnosis under different operating conditions and across different devices [8–10].

In specific fault diagnosis tasks, the model's ability to fit nonlinear functions is crucial. This ability is usually achieved through deep learning, random forests, and SVMs [11–13]. Among them, SVM is a classic supervised learning method with flexible kernel functions and penalty factors, which has demonstrated stable performance in both binary and multi-class classification problems [15]. Its core idea is to maximize the margin between different categories of samples by constructing an optimal hyperplane to achieve classification [16].

Based on the above considerations, this study proposes a rolling bearing fault diagnosis method combining BDA and SVM: the BDA algorithm is used to jointly align the marginal and conditional distributions of the source and target domains, thereby addressing the limitation of existing studies that only consider marginal distributions to achieve feature-level adaptation. Meanwhile, SVM is utilized to leverage its advantages in classification tasks. The synergistic effect of the two methods not only alleviates the data scarcity constraint through transfer learning but also ensures diagnostic accuracy by leveraging the strong classification capabilities of SVM, ultimately achieving high-precision fault diagnosis under cross-domain and small-sample conditions.

2. Signal time- and frequency-domain feature analysis and extraction

The essence of SVM classification is eigenvector-oriented, while the extracted raw signals are discrete time series. Therefore, time-domain and frequency-domain feature extraction (such as the mean value, root mean square (RMS), spectral energy, etc.) is required to convert the signals into quantitative indicators that reflect the key features of these signals. These indicators are first aligned between the source domain and target domain using BDA, and are then used as the training basis for SVM.

Time-domain signals and frequency-domain signals are linearly correlated through the Fourier transform, reflecting signal characteristics from different dimensions. This paper intends to integrate multiple time- and frequency-domain features as the inputs to BDA [22] and SVM.

2.1. Time-domain feature extraction

Time-domain signals are used to describe the amplitude, trend, and changes of a signal. They can intuitively reflect the original characteristics of the signal and are commonly used to describe the overall level and sudden faults of vibration signals [17]. Time-domain features are directly extracted from the time series of vibration signals. Feature indicators such as the mean value, RMS, and variance are commonly used in signal analysis and also have practical significance in engineering applications.

The mean value is used to reflect the overall level of a signal. In bearing-rotor systems, it can indirectly indicate bearing misalignment, etc. Its definition is

$$\mu = \frac{1}{N}\sum_{i=1}^{N} x_i, \tag{2.1}$$

where x_i is the sample value of the vibration signal, and N is the total number of sampling points in the signal.

The RMS value is used to measure the energy level of a signal. A higher RMS value typically indicates that the equipment is experiencing significant vibration. Its definition is

$$\mathrm{RMS} = \sqrt{\frac{1}{N}\sum_{i=1}^{N} x_i^2}. \tag{2.2}$$

Skewness (S) is a statistical measure describing the symmetry of a signal and is used to analyze signal asymmetry. Its expression is

$$S = \frac{1}{N}\sum_{i=1}^{N}\left(\frac{x_i-\mu}{\sigma}\right)^3, \tag{2.3}$$

where σ is the standard deviation of the signal.

Kurtosis (K) is a statistical measure of signal sharpness, indicating whether the signal contains sudden anomalies or impact-related faults. Its expression is

$$K = \frac{1}{N}\sum_{i=1}^{N}\left(\frac{x_i-\mu}{\sigma}\right)^4. \tag{2.4}$$

Variance (V) is used to describe the degree of fluctuation in a signal. The larger the variance, the more intense the vibration and the higher the likelihood of a fault. Its expression is

$$V = \frac{1}{N}\sum_{i=1}^{N}(x_i-\mu)^2. \tag{2.5}$$

The crest factor (C) is defined as the ratio of the maximum value of the signal to its RMS value. It is typically related to the impacts experienced by the system and can be used to assess the intensity of transient impacts in the signal. Its expression is

$$C = \frac{\max(|x_i|)}{X_{\mathrm{RMS}}}. \tag{2.6}$$

2.2. FREQUENCY-DOMAIN FEATURE EXTRACTION

Frequency-domain features can effectively capture the periodicity or characteristic frequency information of equipment faults [18] and are suitable for detecting fault modes in specific frequency bands. Various types of faults in rolling bearings have distinct characteristic frequencies and are closely related to the inner and outer rings, rolling element dimensions, contact conditions, and relative rotational frequency [19]. In this paper, we extract two common frequency-domain features: spectral center frequency and spectral energy.

The spectral center frequency (CF) is used to describe the central position of a frequency-domain signal, i.e., the average value of the signal frequency distribution, and can indicate the dominant frequency where the signal energy is concentrated. Its expression is

$$\mathrm{CF} = \frac{\sum\limits_{i=1}^{N} f_i P(f_i)}{\sum\limits_{i=1}^{N} P(f_i)}, \tag{2.7}$$

where f_i is the frequency component of the signal, and $P(f_i)$ is the corresponding power spectral density.

Faults cause a significant increase in energy at the characteristic frequency locations [19]. Spectral energy (SE) represents the total energy of a signal in the frequency domain and is commonly used to assess signal intensity across different frequency bands. Its expression is

$$\mathrm{SE} = \sum_{i=1}^{N} |X(f_i)|^2, \tag{2.8}$$

where $X(f_i)$ is the amplitude of the Fourier transform spectrum of the signal.

3. BDA-SVM ALGORITHM PRINCIPLE

3.1. BDA TRANSFER LEARNING PRINCIPLE AND FRAMEWORK

Traditional machine learning methods typically assume that the data distributions of the training set and the test set are consistent. However, in practical applications, there are inevitably significant differences in the distributions of the source and target domains [7–9]. The objective of transfer learning is to mitigate the problem of insufficient samples in the target domain by acquiring knowledge from the source domain and transferring it to the target domain, thereby improving learning performance. Its core idea is to utilize knowledge learned from the source domain (such as model parameters, feature distributions, or latent-space representations) to improve the performance of tasks in the target domain, enabling models trained on the source domain to be effectively applied to the target domain after fine-tuning.

Let the source-domain and target-domain datasets be denoted as

$$D_s = \left\{(x_s^{(i)}, y_s^{(i)})\right\}_{i=1}^{n_s}, \tag{3.1}$$

$$D_t = \left\{x_t^{(j)}\right\}_{j=1}^{n_t}, \tag{3.2}$$

where x_i^s and x_i^t represent the sample features in the source-domain and target-domain datasets, respectively, n_s and n_t are the numbers of samples in the source and target domains, respectively, and y_i^s are the corresponding sample labels. In practical applications, the labels y_j^T in the target domain are often unknown. Therefore, we employ pseudo-labeling techniques to estimate the conditional distribution, where initial predictions from the source domain model are used to approximate the true target-domain labels.

The feature distributions of the source and target domains $P_S(X)$ and $P_T(X)$, as well as the joint distributions $P_S(XY)$ and $P_T(XY)$, are typically different. Therefore, the objective of transfer learning is to train a model $f_S(x)$ in the source domain that can also perform well in the target domain, i.e., $f_T(x) \approx f_S(x)$. Here, $f_T(x)$ represents the model performance in the target domain, which is the ultimate objective of transfer learning.

3.2. Introduction to BDA algorithms

BDA is a domain adaptation technique that simultaneously minimizes differences between marginal and conditional distributions, thereby aligning the source and target domains in terms of feature space and enhancing the transferability of cross-domain data [1, 8, 20]. The original BDA method was proposed by Wang et al. [25], who introduced a framework for simultaneously minimizing marginal and conditional distribution discrepancies. Its objective is to find a mapping function $\Phi(X)$ such that the source domain D_S and the target domain D_T have more similar distributions in the mapping space.

This is achieved by simultaneously optimizing two objectives: minimizing the marginal distribution discrepancy (MDD) and the conditional distribution discrepancy (CDD). The MDD reflects the distribution deviation of data features between the source and target domains over the entire feature space, whereas the CDD considers the distribution differences between samples belonging to the same category in the source and target domains, thereby ensuring that classification-related information remains consistent during the transfer process. The expressions are as follows:

$$\text{MDD} = \left\| \mathrm{E}_{x_i^S \sim P_S(X)} \left[\Phi(x_i^S) \right] - \mathrm{E}_{x_i^T \sim P_T(X)} \left[\Phi(x_i^T) \right] \right\|^2, \tag{3.3}$$

$$\text{CDD} = \sum_{c \in C} \left\| \mathrm{E}_{x_i^S \sim P_S(X|Y=c)} \left[\Phi(x_i^S) \right] - \mathrm{E}_{x_i^T \sim P_T(X|Y=c)} \left[\Phi(x_i^T) \right] \right\|^2. \tag{3.4}$$

In practical applications where the target-domain labels are unknown, BDA employs an iterative pseudo-labeling strategy. Initially, a base classifier (e.g., SVM) trained on the source domain is used to predict pseudo-labels for the target-domain samples. These pseudo-labels are then used to estimate the conditional distribution $P(y^T|x^T)$. It is important to note that although a constant mapping function Φ might trivially minimize distribution discrepancies, BDA avoids this degenerate solution by incorporating constraints that preserve the intrinsic data structure and feature variance. The optimization framework ensures that the mapping Φ not only aligns the distributions but also maintains the discriminative information necessary for classification. During the BDA optimization process, the pseudo-labels are iteratively refined as feature alignment improves, leading to more accurate conditional distribution matching. This approach allows BDA to effectively handle conditional distribution adaptation even when target-domain labels are unavailable during training.

BDA introduces a balancing factor λ to control the balance between MDD and CDD:

$$L_{\text{BDA}} = \text{MDD} + \lambda \text{CDD}, \tag{3.5}$$

where λ is a hyperparameter used to adjust the influence of marginal and conditional distributions during transfer learning. By adjusting λ, the model's adaptability to distribution differences between the source and target domains can be controlled. The core idea of BDA is to simultaneously coordinate the optimization of MDD and CDD by introducing the balancing parameter λ.

3.3. SVM model construction

SVM is a classic supervised learning method commonly used for binary classification problems. The SVM classifier was originally introduced by Cortes and Vapnik [26], while the kernel trick for nonlinear mapping follows the formulation proposed by Schölkopf and Smola [27]. The core idea of SVM is to maximize the separation margin between samples from different categories by constructing a hyperplane, thereby achieving classification. The basic objective is to find an optimal hyperplane that separates the different categories in the dataset [13].

Although SVM is fundamentally a binary classifier, it can be extended to multi-class problems using strategies such as one-versus-rest or one-versus-one. In this study, we employ the one-versus-rest approach for the four-class bearing fault diagnosis task. Assume that the data points in the dataset are $(x_i y_i)$, where $x_i \in R^n$ denotes the input feature vectors, andy_i represents the corresponding class label. The SVM classification hyperplane can be expressed as follows:

$$d = \frac{\left|w^T x_i + b\right|}{\|w\|}, \tag{3.6}$$

where w is the normal vector of the hyperplane, and b is the offset.

For each sample point x_i, the distance to the hyperplane is

$$\frac{y_i(w^T x + b)}{\|w\|}. \tag{3.7}$$

To maximize this margin while ensuring correct classification, the concept of a soft margin is introduced to allow certain sample points to lie on or inside the decision boundary, thereby determining the final position of the classification hyperplane. To find the optimal classification hyperplane, SVM solves the following optimization problem:

$$\min_{w,b} \frac{1}{2} \|w\|^2, \tag{3.8}$$

under the constraints:

$$y_i(w^T x_i + b) \geq 1, \qquad i = 1, 2, ..., n, \tag{3.9}$$

where $\frac{1}{2}\|w\|^2$ is the regularization term, which prevents overfitting and ensures that the classifier has good generalization ability.

However, in practical applications, many datasets cannot be well separated by a single linear hyperplane. To address this issue, SVM introduces kernel functions that map the input data into a higher-dimensional feature space, thereby achieving linear separability in high-dimensional spaces. Since the radial basis function (RBF) kernel effectively handles nonlinear classification problems and exhibits strong classification capabilities in high-dimensional spaces, it is selected as the built-in kernel function for the SVM model in this paper, and its expression is as follows:

$$K(x_i x_j) = \exp(-\gamma \|x_i - x_j\|^2). \tag{3.10}$$

Typically, in SVM, a slack variable ξ_i is introduced to find the optimal hyperplane. After introducing the slack variable, the optimization problem can be reformulated as follows:

$$\min_{w,b,\xi} \frac{1}{2}\|w\|^2 + C\sum_{i=1}^{n}\xi_i, \tag{3.11}$$

where C is the penalty parameter that controls the trade-off between margin maximization and classification error. By adjusting C, a balance can be found between maximizing the margin and minimizing the classification error. Therefore, the final decision function of the SVM can be expressed as

$$f(z) = \operatorname{sign}\left(\sum_{i=1}^{n}\alpha_i y_i K(z_i, z) + b\right), \tag{3.12}$$

where α_i is the Lagrange multiplier obtained by solving the optimization problem.

3.4. BDA-SVM ROLLING BEARING FAULT DIAGNOSIS STRATEGY

By combining the advantages of BDA and SVM, this study proposes a BDA-SVM-based rolling bearing fault diagnosis strategy to address fault diagnosis problems when there is significant feature distribution discrepancy between the source and target domains. The workflow of the proposed model is shown in Fig. 1. The white boxes represent the inputs and outputs, while the black boxes represent the intermediate processes.

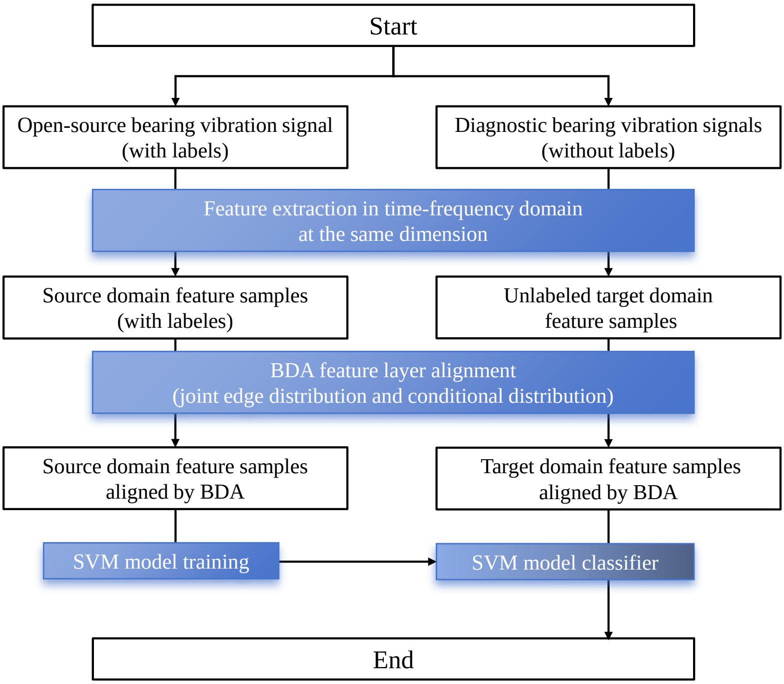

FIG. 1. BDA-SVM fault diagnosis flowchart.

As shown in Fig. 1, first vibration signals from open-source datasets and rolling bearing fault vibration signals are acquired. Time-domain and frequency-domain feature extraction are then performed on these two types of signals. The extracted time-domain features used in this study typically include the mean value, variance, skewness, and kurtosis, while the frequency-domain features involve frequency components and power spectral density information. The extracted feature signals are divided into source-domain feature samples and target-domain feature samples, corresponding to the open-source data and rolling bearing fault data, respectively. Then, the BDA algorithm is applied to adjust and transfer the feature distributions of the source and target domains. Finally, the transformed feature data are input into the SVM classifier to train the fault classification and diagnosis model. The SVM model is then trained and performs classification on the input target-domain features to identify different fault types and ultimately complete the fault diagnosis task.

4. EXPERIMENTS AND ANALYSIS

4.1. EXPERIMENTAL SETUP

The experiment uses the MATLAB platform for algorithm development, data processing and visualization operations. Machine learning models were trained and tested using MATLAB toolboxes, while signal processing tools were employed for feature extraction to ensure accurate analysis and processing of the experimental data. The vibration signals were sampled at 12 kHz with a duration of 1 s per sample, resulting in 12 000 data points for each signal segment. Sequential sampling was used without overlap between adjacent segments. To validate the effectiveness of the proposed method for rolling bearing fault diagnosis, the CWRU bearing dataset was used. The CWRU dataset includes four main fault modes: normal condition, inner ring fault, outer ring fault, and rolling element fault. The fault category codes are shown in Table 1.

TABLE 1. Bearing dataset fault labels.

Fault type	Fault label
Normal	0
Outer ring	1
Inner ring	2
Roller	3

Inner ring faults manifest as physical damage on the inner race of the bearing, while outer ring faults are associated with damage to the outer race. Rolling element faults indicate abnormal damage to the balls or rollers. Each fault category includes different damage levels (0.007 inch, 0.014 inch, and 0.021 inch).

The data are collected by recording vibration signals during bearing operation using an accelerometer.

Additionally, the experiment utilizes rolling bearing fault data collected from actual industrial equipment. These data serve as the target domain to validate the model's transferability in real-world industrial applications. The experimental setup, shown in Fig. 2, employed SKF 6205 deep-groove ball bearings. Faults were artificially introduced using electrical-discharge machining to create single-point defects on the inner race, outer race, and rolling elements, with fault diameters of 0.007 inch, 0.014 inch, and 0.021 inch, respectively. Vibration acceleration signals were acquired using a piezoelectric accelerometer (model: PCB 352C33) mounted vertically on the drive-end bearing housing. The signals were sampled at 12 kHz using a 16-bit data acquisition system. The experimental setup is shown in Fig. 2.

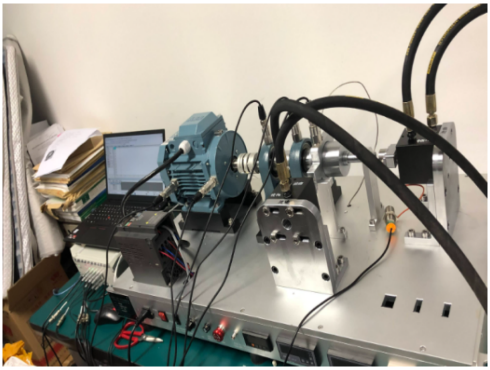

Fig. 2. Bearing signal acquisition device.

4.2. TIME- AND FREQUENCY-DOMAIN RESPONSES OF NORMAL AND FAULTY BEARINGS

The signals acquired by the device are shown in Fig. 3. Figure 3 displays representative time-domain signals from both the CWRU dataset and the in-house collected industrial data to illustrate characteristic waveform patterns: (a) normal condition, (b) rolling element fault, and (c) inner ring fault are from the CWRU dataset, while (d) outer ring fault is from the industrial data collected in-house. The signals acquired by the device are shown in Fig. 3. By comparing different fault conditions, it can be observed that any fault types cause an increase in the amplitude of the response in the time domain. Under normal conditions, the maximum amplitude is approximately 0.2 mV, while under fault conditions, the maximum amplitude increases by approximately 5 to 40 times, and the low-frequency harmonic components become significantly more pronounced, indicating the validity of using time- and frequency-domain features for fault characterization.

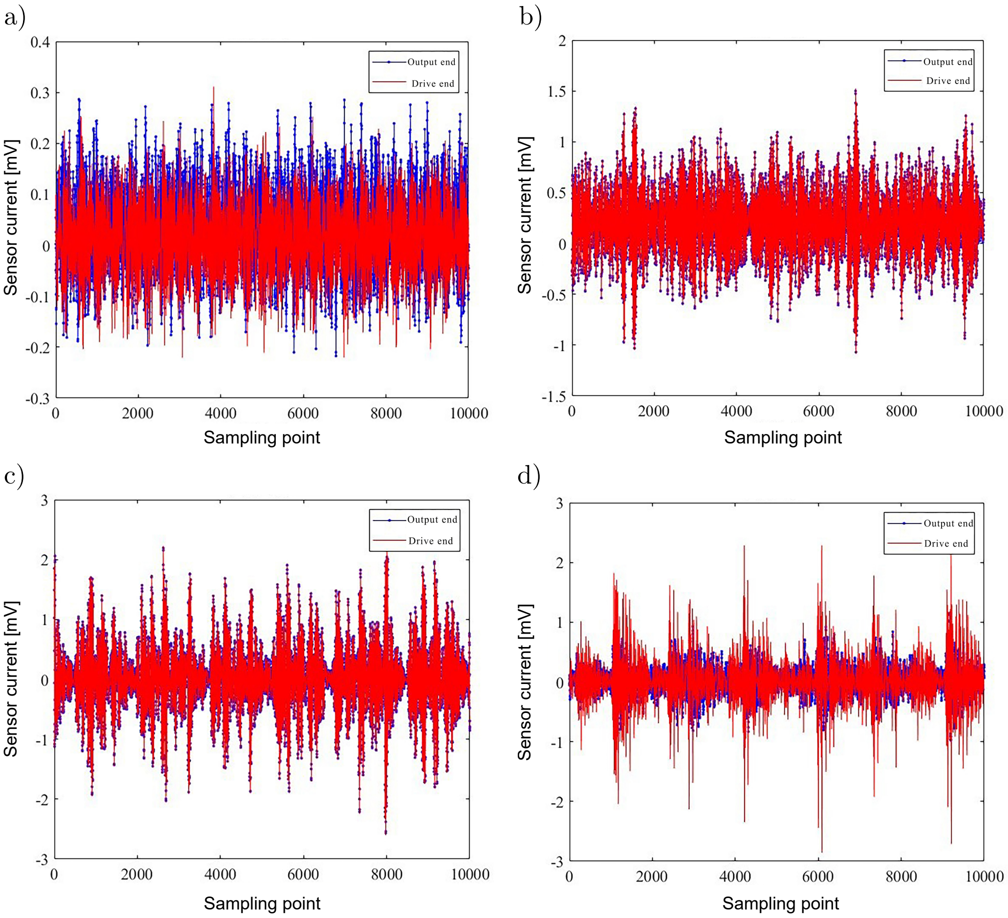

Fig. 3. Time-domain signals collected in the experiment: a) normal condition, b) rolling element fault, c) inner ring fault, d) outer ring fault.

To further investigate the frequency components of the signal, we normalized the frequency-domain features, and the resulting frequency-domain signal is shown in Fig. 4.

As shown in Fig. 4a, the characteristic frequencies of a healthy bearing are clearly visible, with the fundamental frequency (0.17) and overtone (0.35) being prominent, exhibiting a typical frequency modulation phenomenon. This is related to the time-varying support stiffness characteristics of rolling bearings, while wide-band frequency characteristics are not prominent. Under rolling element fault conditions, the amplitude near the characteristic frequency (0.12) of the rolling elements is significantly higher than that of the fundamental frequency (0.17). Under inner ring fault conditions, the energy is primarily concentrated in the low-frequency range, and the fundamental frequency cannot be identified from the frequency-domain signals. Under outer ring fault condi-

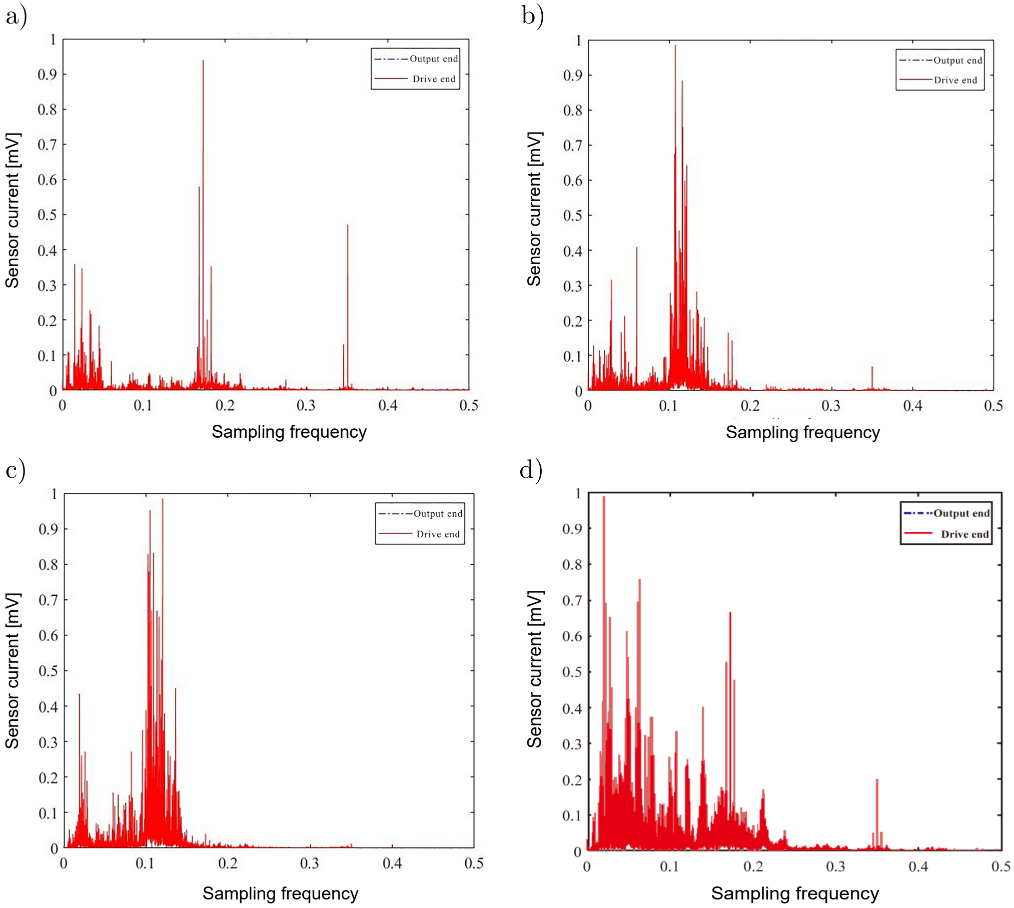

Fig. 4. Frequency-domain features of signals acquired in the experiment: a) normal condition, b) rolling element fault, c) inner ring fault, d) outer ring fault.

tions, the wide-band frequency characteristics are more pronounced, and the frequency components of the response are more complex. Although the fundamental frequency and its harmonics can be identified, the formation mechanisms of other frequency components cannot be inferred. This is because the outer ring is closer to the sensor, resulting in a more pronounced response to fault-induced impacts. As shown in Fig. 3d, the fault signals are easier to identify in the time-domain signals compared with the frequency-domain signals in Fig. 4d. Therefore, using combined time- and frequency-domain characteristics as diagnostic indicators is more reasonable.

4.3. Validation of the BDA method

In this experiment, the source domain consists of the CWRU dataset under specific operating conditions, while the target domain comprises collected under different operating conditions from CWRU and industrial field data, creating a challenging cross-domain scenario. The dataset composition and division are as follows. The source domain (CWRU dataset) comprises 800 samples, with 200 samples for each health state (normal, inner ring fault, outer ring fault, and roller fault). The target domain (industrial field data) contains 400 samples, with 100 samples per category. To ensure the representativeness of the data and to maintain the class distribution in both domains, we employ a stratified random sampling strategy to divide the datasets. To achieve effective transfer learning, 70 % of the source domain data (560 samples) was used for training and 30 % (240 samples) for validation. The target domain data was similarly divided into a 70 % training set (280 samples) and a 30 % test set (120 samples) to evaluate the model's performance in cross-domain fault diagnosis. It is important to note that, during the BDA adaptation process, the labels of the target domain training set are treated as unknown and are estimated using pseudo-labels generated by the source domain model. The final diagnostic accuracy is reported based on the predictions on the target domain test set using the ground-truth labels.

In the BDA algorithm parameter settings, the regularization parameter λ is used to balance the distribution differences and the relationship between the feature matrices. Its value typically ranges from 0.1 to 1 and is optimized through experiments to determine the optimal value. The embedding dimension d determines the dimension of the subspace after feature mapping. A larger dimension retains more feature information but increases computational complexity. The optimal dimension is determined through cross-validation in the experiments. The number of iterations T in BDA is set to 100 to ensure minimization of feature distribution differences.

In actual bearing fault diagnosis, the source and target domain data often exhibit significant distribution differences, which can lead to poor performance of traditional models when applied across domains. Therefore, this paper further optimizes feature transfer effects by adaptively adjusting the feature distributions of the source and target domains, ensuring better classification performance in fault diagnosis in the target domain.

This paper uses the transfer component analysis (TCA) transfer learning method as an example to compare the performance improvement of the proposed method. Figure 5 shows the visualization results of BDA and TCA before and after feature transfer.

As can be clearly seen from the classification results in Fig. 5a, before feature migration, due to the significant differences in data distribution between the source domain and target domains, data points from different categories overlap in the feature space, resulting in blurred classification boundaries and making it difficult to perform effective fault classification. After applying the TCA method for feature transfer (Fig. 5b), the distribution of sample data from

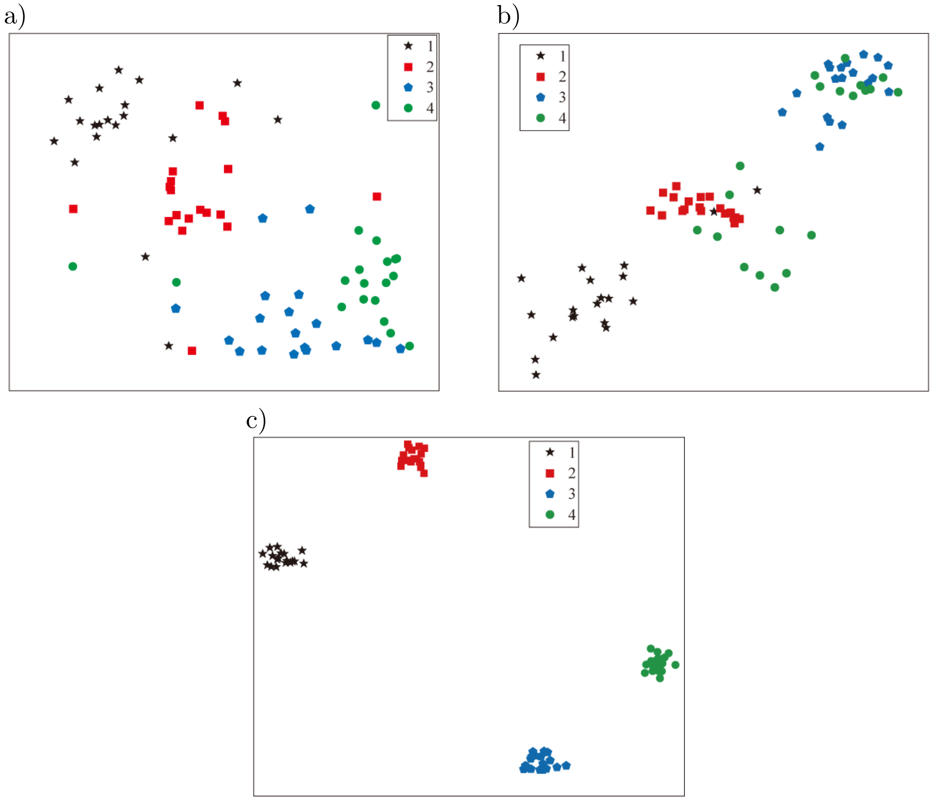

Fig. 5. Visualization results before and after feature transfer: a) before feature transfer, b) after TCA-based feature transfer, c) after BDA-based feature transfer.

different fault categories in the feature space improves, with some categories beginning to cluster together and distribute more densely. This is because TCA can reduce the distribution differences between the source and target domains. However, some categories still overlap in the figure, indicating that TCA has limited effectiveness in adjusting cross-domain feature distributions. This is because TCA does not adequately account for imbalances in feature distributions between the source domain and target domains, resulting in insufficient separation of some data categories and thereby affecting classification accuracy.

After feature transfer using the BDA method (Fig. 5c), the data distribution of the source domain and target domain are significantly optimized. Data points of different fault categories become more compact and distinct in the feature space, and the distribution differences between the source and target domains are greatly reduced. BDA achieves this by adaptively adjusting the feature distributions between the source and target domains, making samples from the same category to be more consistently distributed across domains while enhancing the separation between categories. This significantly improves classification accuracy and stability. These results indicate that BDA is indeed effective in cross-domain fault diagnosis, effectively addressing distribution differences and aiding in resolving the small-sample problem in engineering applications. Figure 5 visualizes the feature distributions of the source and target domain data. The original feature space consists of the nine time-frequency domain features extracted in Sec. 1 (including mean, RMS, skewness, kurtosis, variance, crest factor, spectral center frequency, and spectral energy). To visualize these high-dimensional features in a 2D plane, we employ the t-SNE (t-distributed stochastic neighbor embedding) dimensionality reduction method, which is widely used for visualizing high-dimensional data while preserving the structure of local neighborhoods.

4.4. PERFORMANCE VALIDATION OF THE BDA-SVM MODEL

To validate the performance of the proposed BDA-SVM model, this paper designed a series of comparative experiments to compare the diagnostic effectiveness of several traditional classification algorithms, including decision trees (DT), KNN, and the original SVM. The purpose of the experiment is to demonstrate the effectiveness of BDA-SVM in handling distribution inconsistency issues through model comparisons and to evaluate its diagnostic accuracy in actual fault classification tasks. The experimental results are shown in Fig. 6.

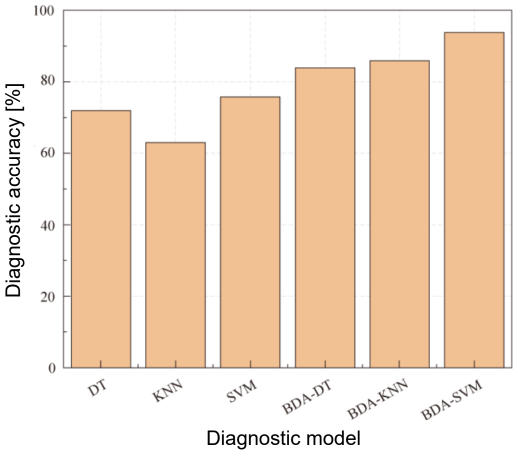

FIG. 6. Diagnostic results of different models.

As can be seen from the comparison results in Fig. 6, the traditional DT and KNN models perform the worst in cross-domain fault diagnosis tasks. Specifically, the diagnostic accuracy of KNN is only 63 %, while the accuracy of the DT model is slightly higher at 72 %. The SVM achieves the highest diagnostic accuracy, but it still only reaches 76 %. These traditional models cannot effectively adapt to the target-domain data without addressing data distribution differences, resulting in poor cross-domain diagnostic performance. These results indicate that relying solely on traditional machine learning classifiers is insufficient to address the distribution inconsistency issue in cross-domain fault diagnosis, resulting in limited classification performance. As shown in the figure, incorporating BDA into traditional models significantly improves diagnostic accuracy, fully demonstrating the feasibility of combining BDV with classical machine learning and further validating the conclusions drawn in the previous section.

In contrast, the proposed BDA-SVM model demonstrates outstanding advantages in cross-domain fault diagnosis tasks. By introducing the BDA algorithm before the SVM model to adaptively adjust the feature distributions of the source and target domains, the diagnostic accuracy of the BDA-SVM model is significantly improved, increasing from 76 % when using SVM alone to over 94 %. This improvement is attributed to the substantial reduction in distribution differences between the source and target domains after BDA processing, enabling the SVM to better adapt to the target-domain data. Compared with the other models, whether it is DT, KNN, or the original SVM, BDA-SVM performs better in cross-domain fault diagnosis. Not only is the accuracy greatly improved, but the distribution robustness is also inevitably enhanced. These results indicate that the BDA-SVM model has stronger comprehensive performance in practical applications.

It is important to note that the performance ranking between BDA combined with SVM and BDA combined with KNN in our experiments differs from that reported in earlier comparative studies on laboratory datasets. In those studies [7], BDA with KNN achieved the highest accuracy because the source and target data were collected entirely under controlled laboratory conditions. The transferred features formed compact and well-separated clusters, enabling KNN to fully leverage its neighborhood-based decision mechanism.

In our work, however, the target domain includes real industrial data characterized by stronger noise, more complex operating conditions, and less consistent local feature density after domain adaptation. Under such circumstances, KNN becomes more sensitive to irregular neighborhood structures and boundary noise, which reduces its classification stability. In contrast, SVM relies on margin maximization and is less affected by local density fluctuations, resulting in higher robustness and better performance, as shown in Fig. 6.

5. CONCLUSION

This paper addressed the distribution differences between the source and target domains in cross-domain fault diagnosis and proposed a rolling bearing fault diagnosis strategy based on BDA-SVM. The BDA algorithm effectively reduced the distribution differences between the source and target domains at the feature level, thereby enhancing the model's generalization capability in cross-domain applications. The experimental results show that, compared with traditional machine learning algorithms (such as DT, KNN, SVM, etc.) that do not introduce transfer learning, BDA-SVM has significant advantages in cross-domain fault diagnosis tasks, with a significantly improved diagnosis accuracy of over 94 %, and demonstrating strong robustness and generalization capabilities.

Future research can build upon the existing model to further explore how to enhance the effectiveness of the method and apply it to more industrial scenarios. Combining deep learning techniques [23] or other advanced transfer learning methods [24] can further improve the model's performance in more complex and diverse cross-domain fault diagnosis tasks. However, this study still has certain limitations. In particular, the method's performance under extreme distribution shifts requires further investigation. Future work will focus on combining BDA-SVM with deep feature extraction techniques and extending the approach to more complex industrial scenarios with multiple fault modes and severe data imbalance.

Fundings

This research did not receive any specific grant from funding agencies in the public, commercial, or not-for-profit sectors.

Conflict of interest

The authors declare that there are no known competing financial interests or personal relationships that could have influenced the work described in this paper.

Authors' contributions

Dong Chen conceptualized the study and wrote the original draft. Mingshan Zhang conducted experiments, performed the analysis and contributed to data interpretation. Yaguang Gao performed the analysis and wrote the original draft. All authors reviewed and approved the final manuscript.

References

1. Xu H., Zhao Z., Xiao X., Wang Z., Bearing fault diagnosis method based on multi-adversarial and balanced distribution adaptation [in Chinese], *Journal of Vibration and Shock*, **44**(05): 302–313, 2025.
2. Lu H., Zheng D., Liu Y., Chang B., Bearing fault diagnosis method based on multi-component sparse representation [in Chinese], *Journal of Harbin University of Commerce*

(Natural Science Edition), **41**(04): 442–449, 2025, https://doi.org/10.19492/j.cnki.1672-0946.2025.04.012.

3. Chen J., Tang Z., Zhou J., Rolling bearing fault diagnosis based on improved SDP and FasterNet-GCAM [in Chinese], *Modern Manufacturing Engineering*, (07): 129–138+41, 2025, https://doi.org/10.16731/j.cnki.1671-3133.2025.07.016.
4. Zhang Y., Research progress on rolling bearing fault diagnosis based on 2D data sets [in Chinese], *Mechanical Management and Development*, **40**(07): 114–117+320, 2025, https://doi.org/10.16525/j.cnki.cn14-1134/th.2025.07.042.
5. Chen R., Zhu J., Hu X., Wu H., Xu X., Han X., Fault diagnosis method of rolling bearing based on multiple classifier ensemble of the weighted and balanced distribution adaptation under limited sample imbalance, *ISA Transactions*, **114**: 434–443, 2021, https://doi.org/10.1016/j.isatra.2020.12.034.
6. Zhou Q., Ma W., Zhang Y., Guo J., A multi-source domain adaptation approach with learning domain-specific representations for bearing fault diagnosis under limited samples, *Applied Soft Computing Journal*, **184**(Part A): 113727, 2025, https://doi.org/10.1016/j.asoc.2025.113727.
7. Ma J., Li C., Zhang G., Rolling bearing fault diagnosis based on deep learning and autoencoder information fusion, *Symmetry*, **14**(1): 13, 2021, https://doi.org/10.3390/sym14010013.
8. Lei Y., Yang B., Jiang X., Jia F., Li N., Nandi A.K., Applications of machine learning to machine fault diagnosis: A review and roadmap, *Mechanical Systems and Signal Processing*, **138**: 106587, 2020, https://doi.org/10.1016/j.ymssp.2019.106587.
9. Chen R., Zhu Y., Hu X., Zhao S., Zhang X., Rolling bearing fault diagnosis under different working conditions based on adaptive regularized transfer learning [in Chinese], *Chinese Journal of Scientific Instrument*, **42**(08): 95–103, 2021, https://doi.org/10.19650/j.cnki.cjsi.J2107721.
10. Zhou H., Wang Z., Tao Q., Rolling bearing fault diagnosis based on joint structure-preserving transfer of multi-source domains [in Chinese], *Journal of Vibration and Shock*, **44**(14): 302–310, 2025.
11. Fu J., Zhang G., Zhang S., Bearing fault diagnosis of cross-working grinding mill based on transfer learning [in Chinese], *Journal of Fujian University of Technology*, **22**(04): 393–400, 2024.
12. Pan X., Ge K., Dong F., Intelligent fault diagnosis of hoist bearing based on feature transfer learning [in Chinese], *Industrial and Mine Automation*, **48**(09): 1–7+32, 2022, https://doi.org/10.13272/j.issn.1671-251x.17980.
13. Wan A., Yang J., Wang J., Chen T., Liao X., Huang J., Du X., Aero engine gear fault diagnosis based on deep learning vibration [in Chinese], *Test and Diagnosis*, **42**(06): 1062–1067+1239, 2022, https://doi.org/10.16450/j.cnki.issn.1004-6801.2022.06.002.
14. Hu W., Zhang Y., Centrifugal pump rolling bearing fault diagnosis based on VMD and random forest [in Chinese], *Mechanical and Electrical Engineering Technology*, **51**(03): 78–82, 2022.
15. Wang J., Zhou C., Zhang Z., Meng N., Du G., Jin X., Zhang C., A fault diagnosis method using decomposition denoising improved multiscale weighted permutation entropy and one-versus-one least squares twin SVM, *Measurement*, **255**: 118012, 2025, https://doi.org/10.1016/j.measurement.2025.118012.

16. Liu J., Maimaitireyim A., Xiang Z., Xie L., Fan bearing fault diagnosis based on improved grey wolf optimization algorithm and SVM, *Journal of Mechanical Transmission*, **47**(09): 160–169, 2023, https://doi.org/10.16578/j.issn.1004.2539.2023.09.022.

17. Bu C., Liu Y., Zhang W., Fault diagnosis model of shearer bearing based on PSO-SVM [in Chinese], *Industrial and Mine Automation*, **51**(S1): 44–46, 2025.

18. Guo Y., Liu Y., Zhang Z., Wang Y., Xue P., Du C., Li W., Research on fault detection and diagnosis of carbon dioxide heat pump systems in buildings based on transfer learning, *Journal of Building Engineering*, **85**: 108774, 2024, https://doi.org/10.1016/j.jobe.2024.108774.

19. Wang B., Liu Y., Liao Y., Sensitivity analysis of time-domain characteristic indicators of rolling bearing fault signals [in Chinese], *Bearing*, (10): 45–48, 2015, https://doi.org/10.19533/j.issn1000-3762.2015.10.014.

20. Tang J., Wang E., Zhu J., Tan W., Research on fault diagnosis of automotive water pump bearings based on frequency domain features and support vector machines [in Chinese], *Machine Tool and Hydraulic*, **46**(13): 163–167+155, 2018, https://doi.org/10.3969/j.issn.1001-3881.2018.13.040.

21. Li D., Feng J., Fault diagnosis of rolling bearings in medical devices based on vibration signal analysis [in Chinese], *Value Engineering*, **44**(24): 21–23, 2025, https://doi.org/10.3969/j.issn.1006-4311.2025.24.007.

22. Wang T., Liu T., Liu Y., Wang Z., Bearing fault transfer diagnosis with balanced distribution adaptation under variable working conditions [in Chinese], *Mechanical Science and Technology*, **42**(08): 1316–1323, 2023, https://doi.org/10.13433/j.cnki.1003-8728.20220058.

23. Lei Y., Yang B., Jiang X., Jia F., Li N., Nandi A.K., Applications of machine learning to machine fault diagnosis: A review and roadmap, *Mechanical Systems and Signal Processing*, **138**: 106587, 2020, https://doi.org/10.1016/j.ymssp.2019.106587.

24. Weiss K., Khoshgoftaar T.M., Wang D., A survey of transfer learning, *Journal of Big Data*, **3**(1): 1–40, 2016, https://doi.org/10.1186/s40537-016-0043-6.

25. Wang J., Chen Y., Hao S., Feng W., Shen Z., Balanced distribution adaptation for transfer learning, [in:] *2017 IEEE International Conference on Data Mining (ICDM)*, pp. 1129–1134, 2017, https://doi.org/10.1109/ICDM.2017.150.

26. Cortes C., Vapnik V., Support-vector networks, *Machine Learning*, **20**: 273–297, 1995, https://doi.org/10.1007/BF00994018.

27. Schölkopf B., Smola A.J., *Learning with Kernels: Support Vector Machines, Regularization, Optimization, and Beyond*, MIT Press, 2002, https://doi.org/10.7551/mitpress/4175.001.0001.

Received August 31, 2025; accepted December 2, 2025;
available online April 7, 2026; version of record June 9, 2026;
published issue June 24, 2026.

Engineering Transactions, **74**(2): 207–230, 2026, https://doi.org/10.24423/engtrans.2025.3607
Institute of Fundamental Technological Research Polish Academy of Sciences (IPPT PAN)
Université de Lorraine • Poznan University of Technology

Research Paper

Non-Linear Analysis of Wrinkling Phenomena in Sandwich Beams with a Soft Core

Paweł Jasion[1)], Iwona Wstawska[1)*], Kamil Kołodziński[2)]

[1)] *Faculty of Mechanical Engineering*
[2)] *Faculty of Civil and Transport Engineering*

Poznan University of Technology
Poznań, Poland

*Corresponding Author: iwona.wstawska@put.poznan.pl

This work is devoted to the local stability analysis of sandwich beams with a light core. A linear as well as a non-linear numerical analysis is carried out with the use of the finite element method (FEM). Both material and geometrical nonlinearities are taken into account. The goal of the investigation is to examine the influence of the material model on the post-buckling behaviour of a sandwich beam, especially on the formation and development of wrinkles on the compressed face. A pure bending condition is considered for a beam simply supported at both ends. The results for materials of theoretical properties are presented as well as for data from experiments on aluminium sandwich beams. From the results, it is seen that the linear analysis of the wrinkling phenomenon for non-linear materials gives overestimated results and does not predict correctly the buckling shape.

Keywords: wrinkling, sandwich beams, bending, buckling, equilibrium path, non-linear analysis.

1. INTRODUCTION

The success in the design of a structure partially depends on the correct prediction, analytical or numerical, of the behaviour of this structure. Such a prediction is especially difficult when local phenomena play a fundamental role and when material properties are not uniform or change during the loading process. This is the case when sandwich structures are analysed, in which at least two substantially different materials are connected together, and a local loss of stability may appear in the form of short wrinkles.

The simplest approach to the stability analysis of sandwich structures is the application of methods that describe the problem in a linear way and that allow determination of the buckling load value and buckling shape. The linear approach to wrinkling problems has been studied, e.g., by Douville and Le Grognec [26]. Various possible failure modes were presented, and the values of the critical load were obtained with the use of analytical solution and finite element method (FEM). The influence of geometry and material on the buckling behaviour of the beam was widely investigated. The wrinkling phenomenon, as a linear problem, has also been described analytically by Jasion and Magnucki [2, 5], where it was assumed that the buckling shape has the form of uniform waves distributed equally on the compressed face. A more realistic form consists of waves with maximum amplitude at the mid-length, which fade when moving towards the supports. An analytical approach to wrinkling of a compressed composite facing has been discussed by Birman and Bert [9], where the core was treated as an elastic foundation and various models of it were taken into the consideration. A novel analytical solution for buckling of sandwich panels/beams has been formulated by Cao and Niu [15]. The transverse shear deformation of the face sheet has also been considered. The face of the sandwich panel was modelled as a linearly elastic beam or plate. The authors stated that the faces should be considered as one beam made of many short ones, each having the length of one buckling wavelength, rather than a single slender beam.

Short wrinkles mentioned above may appear in sandwich structures with thin faces [1]. However, if the structure is rigid enough as a whole, global loss of stability may occur. Analytical investigation of both global and local behaviour of sandwich beams has been presented by Léotoing *et al.* [23]. The authors, based on analytical solution, provided design guidelines in the form of diagrams. Global buckling and wrinkling analyses of sandwich plates with anisotropic faces and an orthotropic core have been conducted by Vescovini *et al.* [13]. The critical loads as well as wrinkling modes were analysed for foam and honeycomb core materials subjected to uniaxial and multiaxial loads. A new model incorporating local instabilities and global buckling in sandwich structures has been proposed by Mhada and Bourihane [14]. The model was based on the technique of slowly varying Fourier coefficients. The main advantage of the presented model was obtaining results similar to those acquired with the use of other extended models, while decreasing computational time. The analysis of elastic buckling of isotropic, laminated composite and sandwich beams subjected to various loads and boundary conditions has been carried out by Karamanli and Aydogdu [16]. It was acknowledged that the type of applied load has a significant influence on the values of critical loads and mode shapes, which are also closely associated with boundary conditions. Global buckling was also considered by Jasion and Magnucki [3]. In the paper sandwich beams with aluminium facings and aluminium foam in the core were considered. Analytical solution of the stability problem was presented and compared with experimental data.

A linear analysis of a structure has some well-known disadvantages. One of them is the assumption of ideal geometrical deformation after buckling, which in the case of sandwich beams means regular waves on the upper face, a situation rarely possible due to different types of imperfections in actual structures. Another issue is that the materials used for the core are often some kind of foam and because of this they may behave in a non-linear way during deformation, which cannot be included in linear analysis. For this reason, non-linear analysis should be performed to analyse the behaviour of sandwich structures. A vast investigation of the behaviour of different materials used for cores has been considered by Lolive and Berthelot [11]. The comparison between the experiment and the numerical simulation for three-point bending was presented. The significance of experimental investigation in such problems was pointed out. The non-linear behaviour of a sandwich panel has been investigated by Frostig *et al.* [12]. The panel consisted of two faces, upper and lower, as well as a functionally graded core. The wrinkling and post-wrinkling response of the construction were taken into the consideration. The analysis confirmed that a functionally graded core can substantially improve the wrinkling stability of sandwich structures.

The complexity of the stability problem makes it necessary to use numerical methods, among which the most popular is FEM. Such an approach has been proposed by Sjölander *et al.* [7]. The authors analysed the case of forming composite laminates and showed that by changing the stacking sequence, wrinkles can be eliminated in certain locations. Moreover, special finite elements proper for modelling sandwich beams have been created and studied by Sudhakar *et al.* [8]. Furthermore, semi-analytical methods have been implemented by Liu *et al.* [17], who carried out a buckling analysis of functionally graded sandwich beams. The material properties of each layer were assumed to be graded along the thickness of the beams. The studies revealed that the boundary conditions have a meaningful influence on the buckling response of beams. In addition, the critical buckling loads increase with an increase in the constraints.

When local stability is analysed, geometrical imperfections of the face play a crucial role since they may initiate wrinkling or folding phenomena. The problem of imperfections in sandwich structures has been described by El-Sayed and Sridharan [10]. The wrinkling phenomenon in sandwich panels has been discussed by Fagerberg and Zenkert [25]. The importance of initial imperfections was pointed out, and the analytical model with such imperfections was provided. The comparison between analytical solution obtained from the model and the results of laboratory and numerical experiments showed the correctness of this approach.

The wrinkling phenomenon is still vividly examined and is not limited to classical sandwich structures. Stretching of soft shells with variable curvatures has been presented by Wang *et al.* [18]. Numerical analysis of the wrinkling behaviour of shell surfaces was performed, and phase diagrams defining stability boundaries were depicted. The analysis indicated that varying curvature suppress wrinkles and control the wrinkling and smoothing responses. Wrinkling analysis of circular membranes has been carried out by Huang *et al.* [22]. The instability mechanics of an annular membrane under in-plane stretching has also been investigated. Furthermore, the analysis of instability of a circular thin plate under in-plane compression was conducted. It was shown, in the case of an annular plate, that the value of Poisson's ratio and geometric dimensions have superior influence on wrinkling behaviour. In the case of a compressed plate, the wrinkling phenomenon is associated with boundary conditions.

A new method for predicting wrinkling stress in sandwich panels has been introduced and employed by Su and Liu [19]. The analysis showed that the values of wrinkling stress were highly dependent on the cell size of the foam core. Moreover, the values obtained with the use of this model were compared with those available in the literature. Good agreement was observed. An extensive study of critical and final wrinkling of thin-walled sheet/tube parts under various loading conditions has been carried out by Li *et al.* [20]. The authors revealed that wrinkling mostly occurs under a tension-compression stress state. The influence of material properties on wrinkling behaviour was not taken into the consideration because of variable loading conditions. The effect of wrinkles on the failure of flat laminates has been formulated by Hu *et al.* [21]. It was concluded that local stress concentrations around the wrinkles, as well as location of the wrinkles, play an important role in the failure mechanism of the examined laminates.

In actual structures, it is difficult to analyse the wrinkling problem since there may be some interaction between two or more materials, which may behave in a different way. When waves form on a beam, one or more materials may enter the plastic range and this may influence subsequent behaviour of the whole structure. In this work, the wrinkling phenomenon in sandwich beams is investigated numerically taking into account changes taking place in the material during deformation. The obtained results provide answers to questions that arise during the modelling of sandwich structures, while also helping to understand the wrinkling phenomenon and relating material properties to the buckling behaviour of the beam. First of all, it is shown how the elastic/plastic properties of the faces and core affect the post-buckling behaviour of a beam and influence the formation of wrinkles or dents. This knowledge can help in the design of sandwich structures with desired behaviour. Additionally, some knowledge concerning the buckling and limit loads for beams made of materials with different properties is provided. Finally, the comparison of finite element (FE) and experimental results confirms that a simplified 2D numerical model can accurately predict the behaviour of the actual structure. An exemplary paper devoted to similar problem has been presented by Stiftinger and Rammerstorfer [6], in which the influence of plastic properties of the core and the face on the post-buckling behaviour of sandwich beams under pure compression was presented. The post-buckling behaviour of sandwich beams has also been analysed by Léotoing *et al.* [24]. Here, the influence of the size of imperfection as well as core material properties on this behaviour was pointed out.

The content of the article is organised as follows. Section 2 presents details concerning the numerical modelling of the beam, including geometry and material. Section 3 contains the results of the analyses and begins with a brief description of the procedures used in the investigation. This is followed by four subsections in which first, the influence of mechanical properties of materials on the post-buckling behaviour of the beam is investigated, secondly, the behaviour of the upper face for different Young's moduli is described, thirdly, the influence of imperfection shape and magnitude on the post-buckling behaviour is analysed, and fourthly, the application of the proposed FE model to the analysis of an actual beam is presented. The last subsection also serves as a validation stage. Section 4 is the summary presenting the main conclusions.

2. Numerical model of the beam

2.1. Models of materials

The feature that distinguishes sandwich structures from other ones is that they combine two usually very different materials. The faces are made of tough solid material that carries most of the load, whereas the core is usually a very light filler in the form of a foam. The above fact suggests that special attention has to be paid when defining the model of material for numerical analysis. Moreover, the influence of this model on the behaviour of structure has to be carefully investigated.

Three different models of material are taken into account in this work. The first one is a linear elastic model shown in Fig. 1 with dashed lines. The simplicity

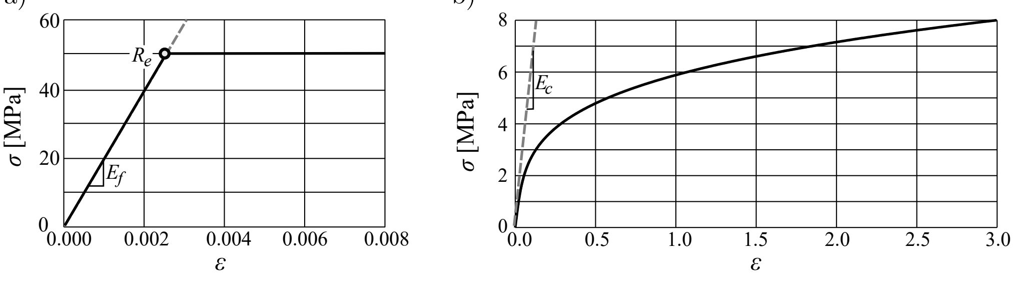

Fig. 1. Models of materials; linear elastic (dashed lines):
a) linear elastic-perfectly plastic, b) non-linear plastic.

of the model – the linear relationship between stress and strain – makes it very effective in numerical calculations. However, small strains assumed in this model are not applicable when the buckling phenomenon appears in a local range. Thus, when the mode of failure of the structure is to be analysed, a model that includes the plasticisation of material should be considered. The simplest approach is to choose an elastic-perfect plastic model. It assumes a linear stress-strain relationship up to the yield strength R_e and then the strains increase infinitely with a constant stress equal to R_e. Such a model is shown in Fig. 1a with a solid line.

The models described above are sufficient for materials such as steel or aluminium, which are often used as faces of sandwich structures. For manufacturing cores, lightweight materials such as foams made of plastic are used. Such materials may behave in a non-linear manner from the very beginning of loading process. Thus, in this case, a more proper model is a non-linear plastic one, shown in Fig. 1b with a solid line. Here, the stress-strain relationship is given by a series of points and described as

$$\varepsilon = \frac{\sigma}{E}\left[1 + c\left(\frac{\sigma}{E}\right)^{2m}\right], \tag{2.1}$$

where E is Young's modulus of the material at the beginning of the curve, and c and m are the constants determined based on experimental results. The shape of the curve is similar to that described by the classical formulae proposed by Ramberg and Osgood [27].

Since the goal of this work is to investigate the influence of material properties, or in other words, the material model, on the behaviour of a beam, the mechanical properties of selected materials have been chosen to allow for the observation of all desired phenomena. For the material of the faces there are the following properties: $E_f = 20 \times 10^3$ MPa, $\nu = 0.3$, $R_e = 50$ MPa. The model of the core was prepared based on Eq. (2.1) with the following parameters: $E = 50$ MPa, $\nu = 0.3$, $c = 3000$, $m = 1.4$.

2.2. Model of the beam

All numerical calculations were performed with the use of ANSYS software. The following dimensions of the model were assumed: total length of the beam $L = 400$ mm, thickness of the face $t_f = 0.3$ mm, thickness of the core $t_c = 20$ mm, and width of the beam $b = 100$ mm. The total beam thickness equals $t = 20.6$ mm. Since wrinkling of the upper face is a local phenomenon, a dense finite element mesh is required to represent short wrinkles that may appear under pure bending conditions. Thus, it was decided to use a 2D model of the beam, shown in Fig. 2, with the assumption of a plane state of stress.

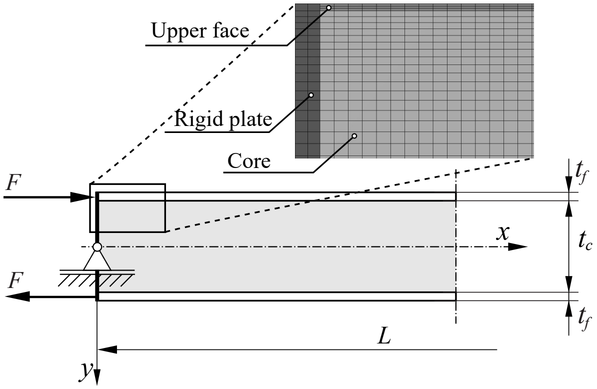

FIG. 2. FE model of the beam.

Moreover, symmetry conditions were used at the mid-length of the beam, and consequently only half of the beam was modelled having in mind that with this approach only symmetrical deformation is possible. The preliminary research shows that the effective approach to model pure bending conditions is to connect all three layers to a rigid plate. The plate has a thickness of 1 mm and Young's modulus 10^3 times greater than the face's modulus. The load in the form of moment is achieved by applying normal forces F to the faces through the rigid plate – compressing force to the upper face and tensile force to the lower one, as it can be seen in Fig. 2.

The model is supported at the mid-height of the rigid plate. At the point of support, vertical movement is removed, while axial displacements are allowed. Such conditions define a movable pin support allowing the rigid end of the beam to move horizontally and rotate about the point of support. The displacement of the entire model is prevented by symmetry conditions at the mid-length.

Higher-order elements PLANE183 have been chosen with eight nodes and three degrees of freedom per node. A non-uniform mesh through the thickness of the core was applied starting from the mid-height of the core. The mesh was densified with the scaling factor of 4, which means that the FE near the upper face is four times thinner than the one at the mid-height of the core. Since the loss of stability has the form of short wrinkles distributed along the length of the beam, the most crucial parameter of the mesh is the number of elements along the axis, which was set to 350. The conducted convergency study showed that both increasing and decreasing this number change the critical load value by only a fraction of a percent. Two other analysed parameters, that is, the normal stress in the face and the maximum deflection of the beam, remain practically unchanged.

A similar convergency study was performed for the number of elements through the thickness of the upper face to prevent excessive stiffening due to an insufficient number of elements. The obtained results revealed that, starting from only two elements through the thickness, the maximum deflection of the beam, maximum normal stress as well as the value of the critical moment are the same up to the fifth significant digit, regardless of the total number of elements. Bearing in mind that wrinkling is a local phenomenon, it was decided to use three elements rather than two through the thickness of the upper face in order to improve the representation of the actual beam behaviour in the model.

3. Results of studies

3.1. Procedures used in the analyses

Three types of analyses were conducted to investigate the behaviour of the beam during the whole loading process. First, a linear static analysis was performed to determine the stress distribution and to obtain input results for the next step, which was the linear buckling analysis. Here, the buckling loads, called critical moments, and the buckling shapes were determined. The first buckling mode served then as a geometry disturbance in the last, third type of analysis, namely the non-linear buckling one. This last step made it possible to include the non-linear behaviour of the material as well as geometrical imperfections into the model. As a result, equilibrium paths were derived, describing the post-buckling behaviour of the beam, including the limit load and the failure mode of the beam. The non-linear analyses were performed with the use of the arc-length method. The procedure available in the system makes it possible to follow the post-buckling behaviour of a structure, even in snap-through problems. The analysis was divided into 100 substeps, with 120 and 80 substeps as a possible maximum and minimum, respectively. The force convergence criterion was used to control the solution, which is a typical approach for the arc-length method. The available stabilisation option was turned off. A maximum displacement of the model, equal to 60 mm, was used as the criterion to stop the calculations.

3.2. Influence of mechanical properties of materials on the post-buckling behaviour of the beam

A typical buckling shape of a sandwich beam under pure bending has the form of short wrinkles in its upper part, as shown in Fig. 3a. Before wrinkles appear, the displacements are very small, and for many materials the process takes place in the elastic range. However, even for such small displacements, plastic strains may appear in a light core and this may influence the subsequent behaviour of the face. After buckling, plastic strains may appear also in stiff faces, since the deformation becomes much stronger. For these reasons, four different models of the beam with respect to materials will be considered.

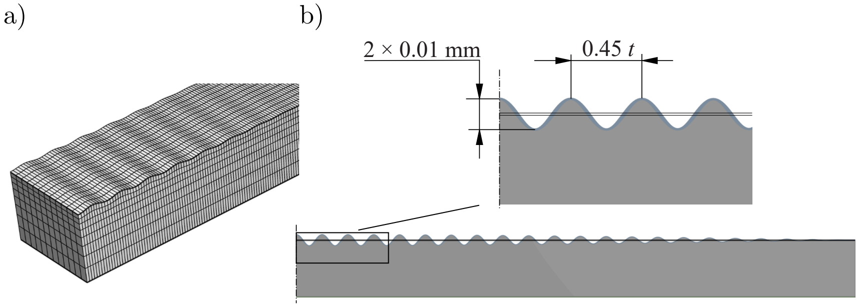

Fig. 3. Behaviour of the upper face of the bent beam: a) wrinkling phenomenon (exemplary FEM result), b) first eigenmode obtained from the linear buckling analysis, used as an imperfection pattern (increased scale).

All models are geometrically non-linear but differ in material formulation. The results of analyses are presented in the form of equilibrium paths; additionally, distributions of elastic or plastic strains, depending on material behaviour, are provided. The vertical axis of each path corresponds to the applied bending moment normalised by the critical moment; thus, a value equal to 1 corresponds to the buckling load, whereas the horizontal axis gives the value of displacement of the lower face measured at the mid-length of the beam. For the results presented in this subsection, geometrical imperfections in the form of the first eigenmode were used, which is a typical approach, at least at the initial stage of an investigation. According to Fig. 3b, these imperfections have the shape of a symmetrical fading sine wave with the maximum amplitude at the mid-length of the beam. Since the goal of the investigation is to analyse nearly perfect structures and to observe their response to different material properties, an amplitude of only 0.01 mm was used. The wavelength was approximately constant and equal to 0.45 of the total beam thickness. It should be noted that the number of waves results from the assumed mechanical properties of the materials and the geometry of the model.

In the first model, an elastic material model was ascribed to both the faces and the core. Two straight lines are visible on the equilibrium path (Fig. 4a). The first one, which is in the pre-buckling range, describes the linear behaviour of the structure. Here, the curvature of the beam increases, and the upper face remains plain with the exception of waves being the result of the initial geometrical imperfections. The second line describes the behaviour of the beam in the post-buckling range. The slope of this line, that is, the stiffness of the beam, is smaller due to the wrinkles on the upper face. The intersection of both lines, which can serve as an estimated buckling load, is about 3% lower than the linear buckling load corresponding to unity on the vertical axis. As it can be seen in Fig. 4b, in which elastic strains are shown, just after the moment of buckling wrinkles appear at the mid-part of the beam over $^2/_3$ of its length.

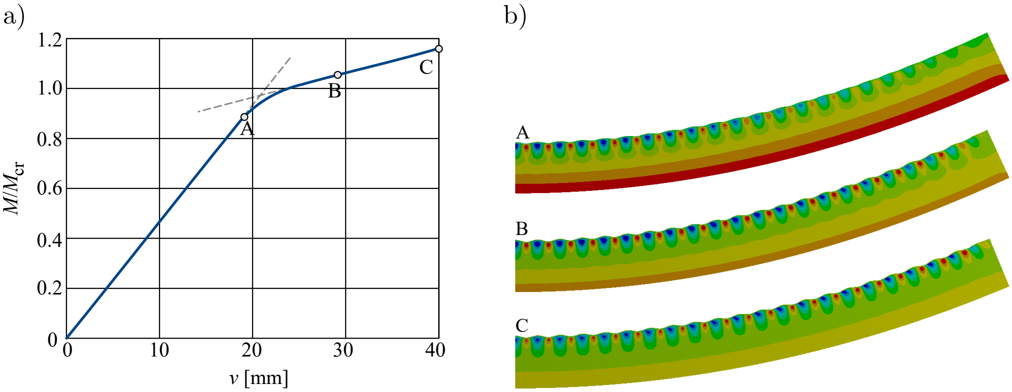

Fig. 4. Results of the post-buckling analysis of the beam with elastic faces and an elastic core: a) equilibrium path, b) distribution of elastic strain.

When the deflection increases, the wrinkles spread over the whole length of the structure. A further increase in deflection results in an increase in the amplitude of the wrinkles. It should be noted that the amplitude and the wavelength are the same along the entire beam.

In the second model of the beam, it is assumed that the core is made of a nonlinear material like the one described by the solid line in Fig. 1b. The material of the faces remains linear through the whole analysis. According to the equilibrium path shown in Fig. 5, initially, before point A, the wrinkles appear in the mid-part of the beam (image A in Fig. 5b). After that, the path bends sharply and then becomes almost horizontal, which indicates that the stiffness of the structure is very small. The reason is the formation of a single fold at the mid-length of the beam (image B in Fig. 5b). The amplitude of the other wrinkles diminishes. In the enlarged part of the plot, it is seen that, in the post-buckling

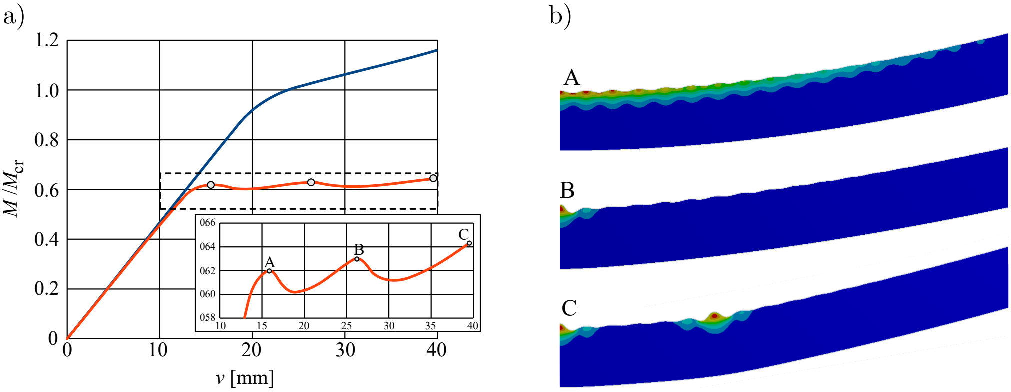

Fig. 5. Results of the post-buckling analysis of the beam with elastic faces and a plastic core: a) equilibrium path, b) distribution of plastic strain.

range, more peaks appear on the equilibrium path. The maximum of each corresponds to a change in the buckling mode, that is, to the start of formation of another single fold, as can be seen in image C in Fig. 5b. From the plot, it can be read that for this FE model, that is, with a plastic core, the buckling load is about 40 % smaller than that from the linear analysis. Since the plastic strains shown in Fig. 5b appear only in the core of the beam, the faces are not visible in the figure – they are transparent.

The third model consists of an elastic core and elastic-perfectly plastic faces. In this case, the buckling load drops considerably and constitutes only 22 % of the linear buckling load. As can be seen in Fig. 6a, after the loss of stability, the slope of the path sharply decreases and then remains approximately constant. The upper face deforms according to the imperfection shape. The size of wrinkles is very small, as can be seen in images A and B of Fig. 6b, even for large deflection of the beam. The distribution of elastic strains in the core at the final stage of the calculations is uniform.

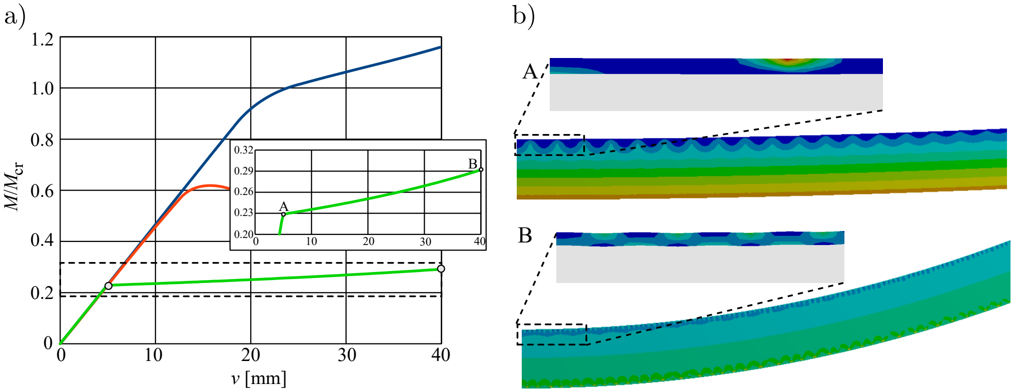

Fig. 6. Results of the post-buckling analysis of the beam with plastic faces and an elastic core: a) equilibrium path, b) distribution of elastic and plastic strain.

The fourth model analysed here is fully plastic. In this case, similarly to the previous case, the buckling load is only about 22 % of that obtained in the linear buckling analysis. The equilibrium path, shown in Fig. 7a, collapses sharply and then becomes horizontal. At the buckling load, a small plastic strain can be observed (Fig. 7b), with almost negligible wrinkles, and just after that point, one large fold directed inward forms near the mid-length of the beam. The enlarged part of the plots reveals that the formation of this fold is associated with a drop in the load up to some minimum, after which a small increase in the load is observed. In this model of the beam, both materials exhibit plastic behaviour, which can be observed in image B in Fig. 7b. Plastic strains are present in both the core and the faces.

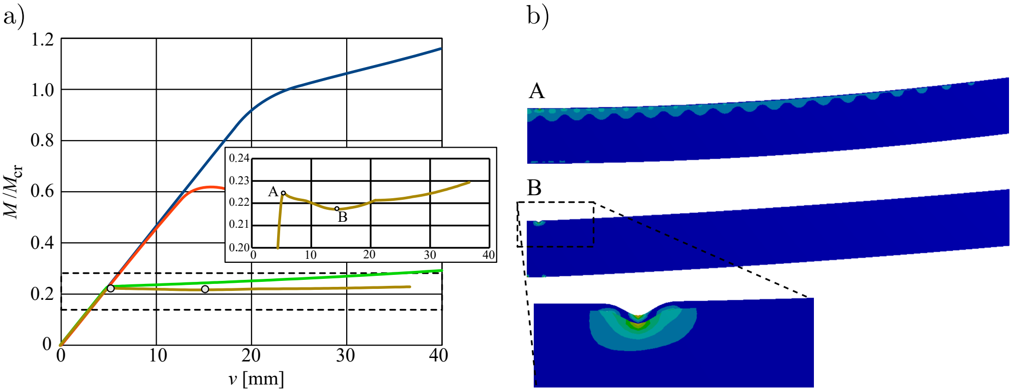

FIG. 7. Results of the post-buckling analysis of the beam with plastic faces and a plastic core: a) equilibrium path, b) distribution of plastic strain.

3.3. BEHAVIOUR OF THE UPPER FACE

Since the loss of stability of the sandwich beam depends on the behaviour of the upper face, it is reasonable to analyse the influence of the stiffness of this part as well as the foundation on which it rests, that is, the core, on the buckling behaviour of the whole structure. Since this study is focused on material properties, the stiffness will be modified by changing Young's modulus, while leaving the thickness of the face and the core unchanged. In the first group of models, the values of E_f will range from 1×10^3 MPa to 200×10^3 MPa, and E_c will remain unchanged and equal to 50 MPa. In the second group, the modulus of the face E_f equals 20×10^3 MPa and Young's modulus of the core E_c takes values equal to (10, 50, 100, 200, 300) MPa.

Let us start the considerations from the linear buckling analysis. As can be expected, the stiffness of the face influences the critical buckling load, which equals 20.3 Nm for $E_f = 1 \times 10^3$ MPa and 337.5 Nm for $E_f = 200 \times 10^3$ MPa. The mode of buckling is also different depending on Young's modulus. For lower values, a shorter wavelength is observed than for the highest analysed value, as can be seen in Fig. 8a. From the presented figures, it can be seen that the deformation of the core reaches much deeper when the stiffness of the face is higher.

When the stiffness of the core is considered to be variable, similar results are seen, that is, the higher Young's modulus, the higher the buckling load. In this case, the relationship is almost linear, as can be seen in Fig. 8b. The buckling shape is also influenced, but here the rise of stiffness increases the number of waves on the upper face.

More interesting information can be drawn when the same models of the beam are analysed with the use of a non-linear procedure. To observe the for-

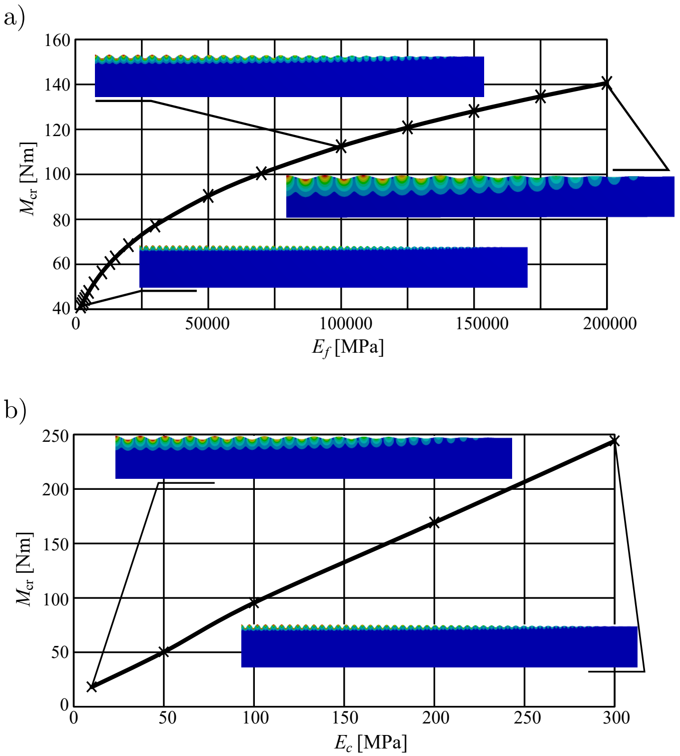

FIG. 8. Influence of Young's modulus of the face (a) and the core (b) on the critical load.

mation of wrinkles, the model of material of the faces is elastic, whereas the model for the core is a non-linear one and defined as in the previous analyses. The first thing that should be noted is the stiffness of the beam in the initial range of deformation, as indicated by the slope of the equilibrium paths shown in Fig. 9. When the absolute value of the load is taken into account, the stiffness of the beam, defined as the ratio of load to maximum deflection, increases from 0.2 for $E_f = 1 \times 10^3$ MPa to 30 for $E_f = 200 \times 10^3$ MPa, assuming that the stiffness of the core is the same for all models. Of course, the limit load also increases with the increase of E_f (see Fig. 9b). A different behaviour can be observed when Young's modulus of the core is variable. As can be seen in Fig. 9d, the stiffness of the beam is more or less constant and only the limit load increases with the increase of E_c.

Additional analysis of the obtained results is provided in Fig. 9a and Fig. 9c. In these plots, the vertical axis corresponds to the dimensionless load, that is, the applied moment divided by the critical moment being the results of the linear buckling analysis. Interestingly, the non-linear critical load for all models is similar and corresponds to about 62 % of the linear buckling load. In other words, regardless of the stiffness of the face, the critical load decreases by about 38 %.

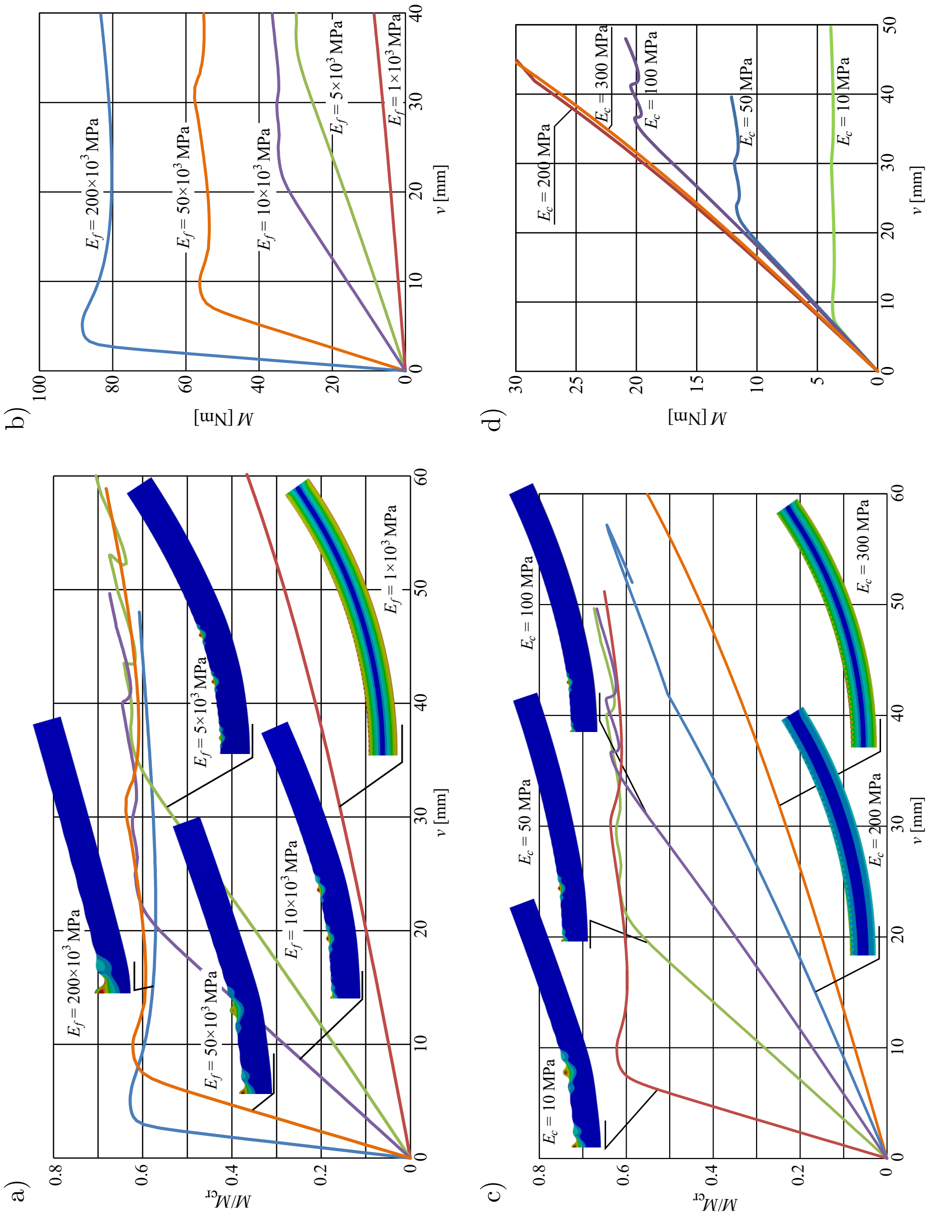

FIG. 9. Comparison of equilibrium paths and failure mode shapes for beams with different Young's moduli of the face (a), (b) and the core (c), (d).

This observation is valid for both series of models: the one in which the face varies and the one in which the core varies.

Aside from the buckling load, essential information is how the different models behave under the load and especially how the wrinkles form on the upper face. This is shown in the images added to the plots in Fig. 9a and Fig. 9c. In Fig. 9a, it is seen that for the face with the highest stiffness after the loss of stability, only one dimple forms and evolves with the increase of deflection. For lower values of Young's modulus, one dimple also appears, but with the increase of the deformation, additional dimples form, which is reflected in the path with additional peaks. In Fig. 9c, which corresponds to a fixed E_f and variable E_c, it is seen that the deformation has always the same form, two folds, the amplitude of which decreases with the increase of the core's stiffness. However, for $E_c = 200\,\mathrm{MPa}$ and higher, the deformation has the form of regular wrinkles that diminish near the support.

3.4. INVESTIGATION OF ALUMINIUM SANDWICH BEAMS

The presented results are based on an arbitrarily selected model of the beam as well as properties of the material. To verify how the proposed models work, an additional study is provided further. The data used are based on the results of an experimental investigation carried out as a part of scientific grant no. N N502 080738, selected findings of which were presented in a monograph by MAGNUCKI and SZYC [4]. The subject of the grant was aluminium sandwich beams with a metallic foam core, as shown in Fig. 10c. The beams consist of two solid pure aluminium faces and a core made of open-cell aluminium foam called Alporas®. All elements of the beam were glued together.

As an example, a beam with a width of 100 mm and a total thickness of 40 mm was chosen. The thickness of each face equals 1 mm. A four-point bending test was performed on the universal testing machine Zwick Z100, as shown in Fig. 10b to Fig. 10d. During the experimental test of the beam, the force was measured with a force transducer, and based on this value and the positions of the loading and support points, the bending moment was determined. The second measured value was the deflection at three points, recorded using inductive displacement transducers located in the central part of the beam, where pure bending conditions occurred. The displacement values at these three points were used as a guide to determine the curvature of the beam, assuming that cylindrical bending takes place. These two parameters, that is, the bending moment and curvature, were used to plot the results of experiments. The behaviour of the upper face of the beam was also monitored visually. However, the deformation had the character of small waves distributed randomly across the entire surface of the upper face. Therefore, it was not possible to determine

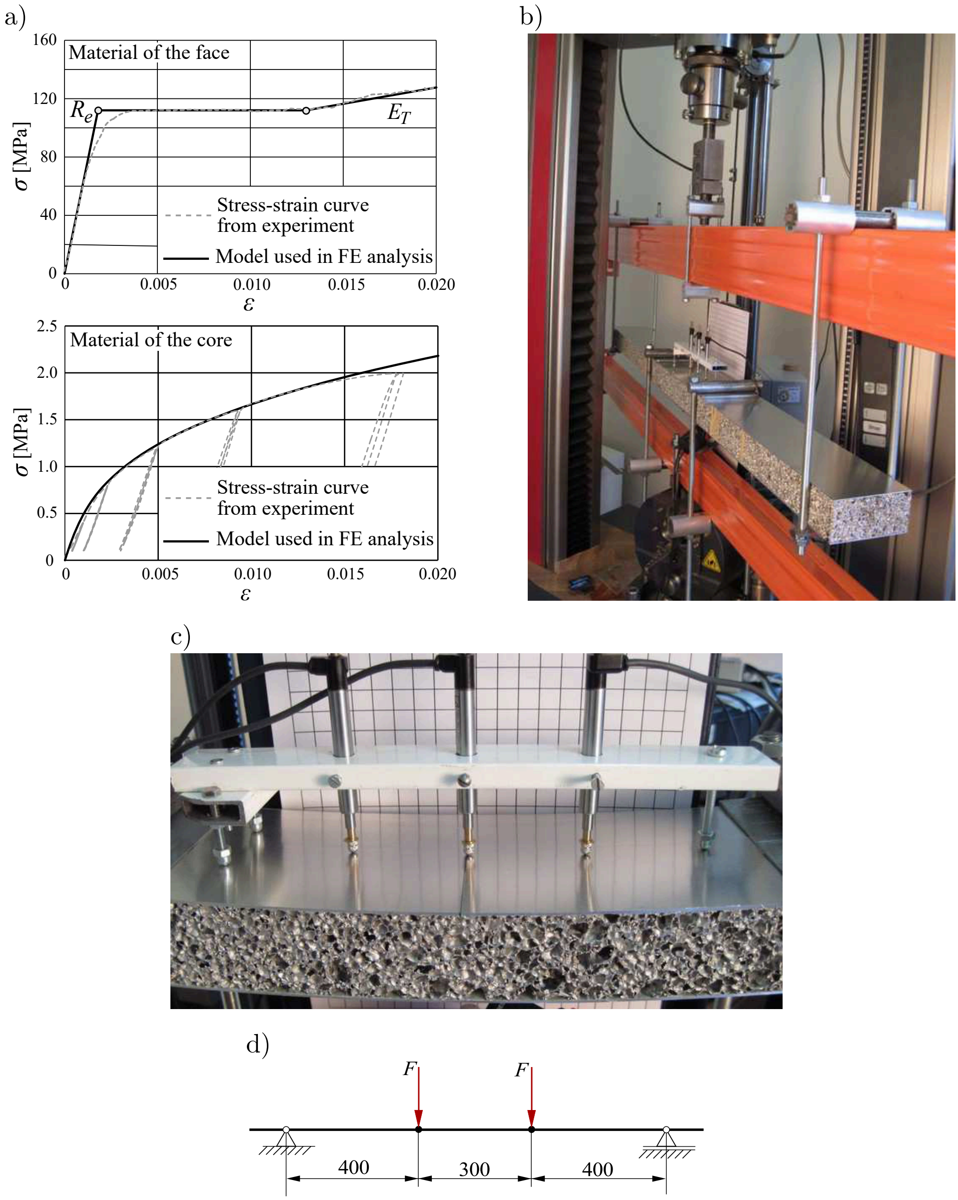

FIG. 10. Samples of structures used in experimental work: a) models of materials for FE analysis, b) and c) test stand, d) loading conditions.

critical changes in the global behaviour using this approach, unless there was a sudden decrease in stiffness, associated with local indentation resulting from delamination.

The material models of the faces and the core used to prepare the FE model are based on the results of static tests. In the case of solid aluminium used to make the faces, a static tensile test was performed. In turn, to determine the mechanical properties of the foam, more convenient approach is to perform a static compression test. This way, the problem of clamping the specimen in the machine's jaw is eliminated. Furthermore, since the foam exhibits non-linear behaviour from the very beginning of the test, unloading stages were included in the loading process to form hysteresis loops. Based on these loops, Young's modulus can be determined. The results of both tests are shown in Fig. 10a as stress-strain curves marked with dashed lines. In contrast, the models used in the FE analyses are marked with solid lines. It was assumed that both materials behave in the same way under tensile and compressive stresses. The mechanical properties of the faces material are as follows: Young's modulus $E_f = 65.6 \times 10^3\,\mathrm{MPa}$, Poisson's ratio $\nu = 0.3$, yield point $R_e = 112\,\mathrm{MPa}$, and tangent modulus in the hardening region $E_T = 2.235 \times 10^3\,\mathrm{MPa}$. The stress-strain relationship for the core is described by Eq. (2.1) using the following parameters: $c = 400\,000$, $m = 1.01$, $E_c = 609\,\mathrm{MPa}$.

The actual beams were tested until failure. For this reason, a fully-plastic FE model was used to compare the results of the experiment (blue line) with the behaviour of the beam model (red line) shown in Fig. 11.

It can be seen that the initial stiffness of the beam and the FE model are identical. What is more important, the loss of stability takes place at the same value of the load equal to about 460 Nm. The differences appear after this point. On the curve corresponding to the experiment, a plateau region is seen, after which the strain-hardening phenomenon can be distinguished. In the case of the FE simulation, after the loss of stability, two regions of strain hardening are visible. The final shape mode of failure is similar for both analyses and has the form of a single dent near the mid-length, and it corresponds to about the same curvature of the beam and the FE model. Because, in the FE model, neither the separation of the layers nor the material interruption were taken into account, the core follows the face deformation during the whole analysis. In the actual beam, the failure has the character of face separation. As can be seen from images A and B in Fig. 11, after the loss of stability, plastic deformations start to grow according to a pattern corresponding to the initial imperfections. The deformation of the upper face is very small. Finally, a local fold appears in the location where the plastic strains are the highest.

The results of additional analyses are presented below, in which different FE models were used to understand how the material formulation may influence the behaviour of the beam model. The equilibrium paths obtained from all models presented in the previous section are compared in Fig. 12. The curve obtained in the experiment is marked with a blue line. It can be seen that the crucial parameter is the plasticity of the face. For both models with a plastic face, the limit load has the same value as the one from the experiment. If the

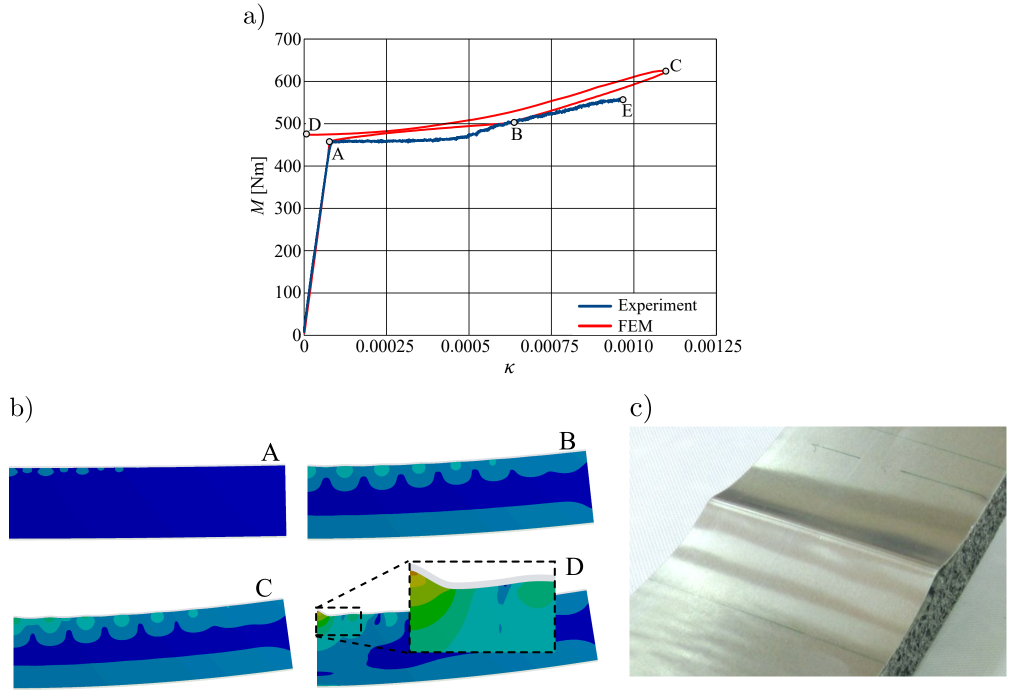

FIG. 11. Comparison of the results of the pure bending test: a) equilibrium paths, b) plastic strain in the FE model, c) failure of the tested beam.

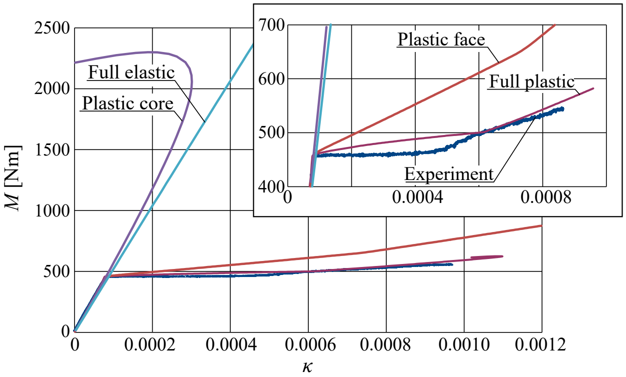

FIG. 12. Comparison of the behaviour of an actual beam and different FE models of the beam.

material of the face is an elastic one, the limit load increases up to 2.3 kNm for a plastic core. For the fully elastic model, the loss of stability is not observed. However, it should be noted that the value of the linear buckling load obtained in linear analysis equals about 7 kNm, which is 15 times higher than the value given by the plastic model and the experiment.

3.5. INFLUENCE OF IMPERFECTION SHAPE AND MAGNITUDE

One of the crucial parameter influencing the post-buckling behaviour of the structure is the shape and magnitude of initial geometrical imperfections. These parameters may change both the value of the critical load as well as the shape that the structure will take after the loss of stability. The research on this subject is performed on an aluminium beam of the same parameters as in the previous section, with the difference that the width of the beam equals 50 mm. Four different shapes of imperfections are examined corresponding to the 1st, 2nd, and 4th buckling modes, and the combination of these three. The third mode was omitted to avoid its interference with the first mode, since it may result in a large peak at the mid-span of the beam. The buckling modes are provided in Fig. 13a.

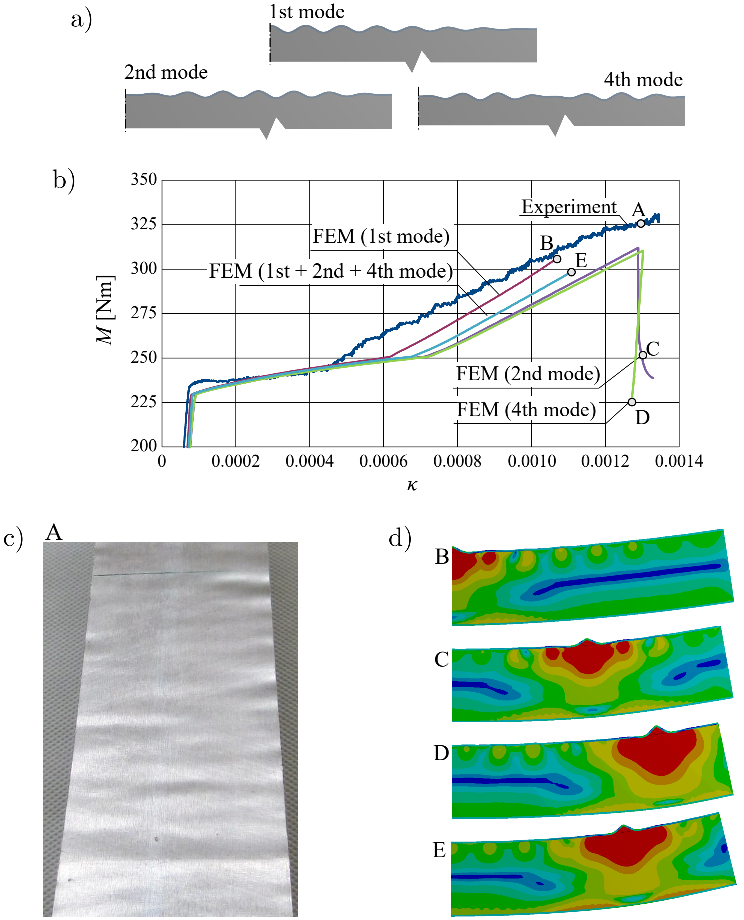

FIG. 13. Comparison of the results of the pure bending test: a) buckling modes, b) equilibrium paths, c) failure of the tested beam, d) elastic strain in the FE model.

They all have the shape of sine waves, which in the case of the 1st mode have a maximum at the mid-length and fade towards the support. In the case of the 2nd mode, the maximum is in the middle of the half-beam, fading towards the mid-length and the support. The last 4th mode is irregular. Since in this subsection the influence of the imperfection on the buckling behaviour is the main goal, a higher amplitude than before is assumed, that is, 0.1 mm. In the case of a combination of three different modes, each mode was introduced with a value equal to 0.0333 mm.

The results obtained from the FE analyses (fully plastic model) are presented in the form of equilibrium paths in Fig. 13b and compared with the plot obtained from the experiment. The comparison looks similar to that for the wider beam presented before. The initial stiffness of the FE model and the actual beam is the same. A small discrepancy, about 3 %, between the value of load at which the loss of stability takes place is visible. For the beam from experiment, the value is slightly higher, equal to 235 Nm, and after that point an almost flat region can be distinguished. For the FE model, a strain-hardening region can be seen. In general, the shape of the imperfection does not influence the post-buckling behaviour of the model. When the curves from Fig. 13b are compared, the difference appears only in the moment at which the local fold starts to form. The slope of the last part of all paths is comparable. The shape of the failure mode is also the same, with the difference that the location of the final single dent is determined by the initial imperfection. The failure of the actual beam is shown in Fig. 13c. Here, a number of plastic folds are spread on the whole upper face, without a single clearly visible dent.

An exemplary imperfection sensitivity analysis is performed for the second buckling mode. The magnitudes of imperfection are equal to (0.01, 0.05, 0.2, 0.5 and 1.0) mm. Also, in this analysis, the equilibrium paths are generated with the use of the FEM and are presented in Fig. 14. For small imperfections, the

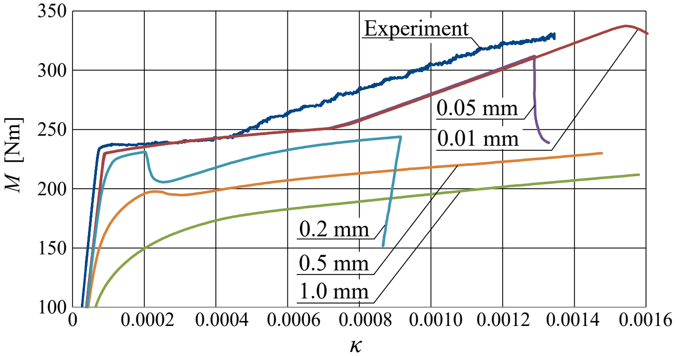

Fig. 14. Influence of the imperfection magnitude (2nd buckling mode) on the post-buckling behaviour of the model.

path looks the same, except for the point where it collapses. If the imperfection is higher, a sudden drop of the path can be observed, as in the case of the value equal to 0.2 mm. For the highest analysed imperfection, the path is smooth during the whole process of the beam deformation.

4. Conclusions

When analysing the results presented above, the first thing that comes to mind is that the phenomenon of local loss of stability of a sandwich beam is strongly influenced by the mechanical properties of the materials of the particular layers. By comparing the results of analyses for four different models of the beam, it can be seen that in the pre-buckling linear range there is no difference in the behaviour. Only elastic deformation appears, and the stiffness of all models is the same – the same slope of the initial part of the equilibrium paths (see Fig. 7a). This means that for deflection analysis in the small deformation range, any model should work correctly.

When it comes to the control of the buckling shape, it can be seen that a stiffer face leads to a small number of waves with large amplitude (Fig. 8a). On the contrary, by increasing the core stiffness, a large number of waves with small amplitude can be obtained (Fig. 8b). However, if the plastic behaviour of the material is taken into account, the deformation in the post-buckling range always takes the form of local folds, the number of which depends on the material and the magnitude of deformation.

An important information is that the stiffness of the beam can be barely increased by increasing Young's modulus of the core. From the example presented in Fig. 9d, it is seen that increasing the value from 10 to 200 MPa increases the stiffness of the model by about 22 %.

Since the present investigation was focused on the response of beams with different models of materials during loss of stability, only one type of initial geometrical imperfections was considered, namely that corresponding to the eigenmode obtained in the linear buckling analysis. However, further investigations are planned in which natural imperfections can be incorporated based on measurements of actual specimens. Also, other types of imperfections, such as delamination or voids, can be crucial, especially for new complex materials such as composites or foams.

It should be noted that the model presented in this paper is 2D. As a consequence, the wrinkles or folds that appear after the buckling are assumed to spread through the entire depth of the beam. As it was shown in Fig. 13c, in an actual beam, folds of various sizes spread across the entire upper face which, among others, can be the result of discontinuities of the foamed core. Such a simplified model may be a source of discrepancies between the results obtained with the two methods; however, when these results are compared, the values analysed in the investigation are similar and the discrepancies are acceptable.

Fundings

This work was developed based on the statutory activity of the Poznan University of Technology (grant of the Ministry of Science and Higher Education in Poland no. 0612/SBAD/3628).

Conflict of interest

The authors declare that there are no known competing financial interests or personal relationships that could have influenced the work described in this paper.

Authors' contributions

Paweł Jasion was responsible for the research concept and design, theory development, calculations and simulations, and preparation of the original draft. Iwona Wstawska was responsible for data collection and analysis, measurements and experiments, calculations and simulations, and manuscript review and editing. Kamil Kołodziński was responsible for formal analysis, interpretation of the results, and preparation of the conclusions. All authors reviewed and approved the final manuscript.

References

1. Hadi B.K., Wrinkling of sandwich column: Comparison between finite element analysis and analytical solutions, *Composite Structures*, **53**(4): 477–482, 2001, https://doi.org/10.1016/S0263-8223(01)00060-5.
2. Jasion P., Magnucki K., Buckling-wrinkling of a face of sandwich beam under pure bending [in Polish: Wyboczenie-zmarszczenie okładziny belki trójwarstwowej przy czystym zginaniu], *Modelowanie Inżynierskie*, **10**(41): 151–156, 2011.
3. Jasion P., Magnucki K., Global buckling of a sandwich column with metal foam core, *Journal of Sandwich Structures and Materials*, **15**(6): 718–732, 2013, https://doi.org/10.1177/1099636213499339.
4. Magnucki K., Szyc W., *Strength and Stability of Sandwich Beams and Plates with Aluminium Foam Core* [in Polish: *Wytrzymałość i Stateczność Belek i Płyt Trójwarstwowych z Rdzeniem z Pianki Aluminiowej*], Wydawnictwo Politechniki Poznańskiej, Poznań, 2012.
5. Jasion P., Magnucki K., Face wrinkling of sandwich beams under pure bending, *Journal of Theoretical and Applied Mechanics*, **50**(4): 933–941, 2012.

6. Stiftinger M.A., Rammerstorfer F.G., Face layer wrinkling in sandwich shells – Theoretical and experimental investigations, *Thin-Walled Structures*, **29**(1–4): 113–127, 1997, https://doi.org/10.1016/S0263-8231(97)00018-9.

7. Sjölander J., Hallander P., Åkermo M., Forming induced wrinkling of composite laminates: A numerical study on wrinkling mechanisms, *Composites Part A: Applied Science and Manufacturing*, **81**: 41–51, 2016, https://doi.org/10.1016/j.compositesa.2015.10.012.

8. Sudhakar V., Vijayaraju K., Gopalakrishnan S., Development of a new finite element for the analysis of sandwich beams with soft core, *Journal of Sandwich Structures and Materials*, **12**(6): 649–683, 2010, https://doi.org/10.1177/1099636210363340.

9. Birman V., Bert C.W., Wrinkling of composite-facing sandwich panels under biaxial loading, *Journal of Sandwich Structures and Materials*, **6**(3): 217–237, 2004, https://doi.org/10.1177/1099636204033643.

10. El-Sayed S., Sridharan S., Imperfection-sensitivity of integral and debonded sandwich beams under compression, *Journal of Sandwich Structures and Materials*, **4**(1): 49–69, 2002, https://doi.org/10.1177/1099636202004001223.

11. Lolive É., Berthelot J.-M., Non-linear behaviour of foam cores and sandwich materials, part 2: Indentation and three-point bending, *Journal of Sandwich Structures and Materials*, **4**(4): 297–352, 2002, https://doi.org/10.1106/109963602024046.

12. Frostig Y., Birman V., Kardomateas G.A., Non-linear wrinkling of a sandwich panel with functionally graded core – Extended high-order approach, *International Journal of Solids and Structures*, **148–149**: 122–139, 2018, https://doi.org/10.1016/j.ijsolstr.2018.02.023.

13. Vescovini R., D'Ottavio M., Dozio L., Polit O., Buckling and wrinkling of anisotropic sandwich plates, *International Journal of Engineering Science*, **130**: 136–156, 2018, https://doi.org/10.1016/j.ijengsci.2018.05.010.

14. Mhada K., Bourihane O., A multi-scale model for global buckling and local wrinkling interaction with application to sandwich beams, *Structures*, **32**: 1398–1407, 2021, https://doi.org/10.1016/j.istruc.2021.03.042.

15. Cao P., Niu K., New unified model of composite sandwich panels/beams buckling introducing interlayer shear effects, *Composite Structures*, **252**: 112722, 2020, https://doi.org/10.1016/j.compstruct.2020.112722.

16. Karamanli A., Aydogdu M., Buckling of laminated composite and sandwich beams due to axially varying in-plane loads, *Composite Structures*, **210**: 391–408, 2019, https://doi.org/10.1016/j.compstruct.2018.11.067.

17. Liu J., He B., Ye W., Yang F., High performance model for buckling of functionally graded sandwich beams using a new semi-analytical method, *Composite Structures*, **262**: 113614, 2021, https://doi.org/10.1016/j.compstruct.2021.113614.

18. Wang T., Liu F., Fu C., Zhang X., Wang K., Xu F., Curvature tunes wrinkling in shells, *International Journal of Engineering Science*, **164**: 103490, 2021, https://doi.org/10.1016/j.ijengsci.2021.103490.

19. Su W., Liu S., A couple-stress model to predict the wrinkling stress of sandwich panels with foam cores, *Composite Structures*, **268**: 113978, 2021, https://doi.org/10.1016/j.compstruct.2021.113978.

20. Li H., Sun H., Liu H., Liu N., Loading conditions constrained wrinkling behaviors of thin-walled sheet/tube parts during metal forming, *Journal of Materials Processing Technology*, **296**: 117199, 2021, https://doi.org/10.1016/j.jmatprotec.2021.117199.

21. Hu H., Cao D., Cao Z., Li S., Experimental and numerical investigations of wrinkle effect on failure behavior of curved composite laminates, *Composite Structures*, **261**: 113541, 2021, https://doi.org/10.1016/j.compstruct.2021.113541.

22. Huang W., Yan W., Xu R., Huang Q., Yang J., Trochu F., Hu H., Wrinkling analysis of circular membranes by a Fourier based reduced model, *Thin-Walled Structures*, **161**: 107512, 2021, https://doi.org/10.1016/j.tws.2021.107512.

23. Leotoing L., Drapier S., Vautrin A., Using new closed-form solutions to set up design rules and numerical investigations for global and local buckling of sandwich beams, *Journal of Sandwich Structures and Materials*, **6**(3): 263–289, 2004, https://doi.org/10.1177/1099636204034632.

24. Léotoing L., Drapier S., Vautrin A., Nonlinear interaction of geometrical and material properties in sandwich beam instabilities, *International Journal of Solids and Structures*, **39**(13–14): 3717–3739, 2002, https://doi.org/10.1016/S0020-7683(02)00181-6.

25. Fagerberg L., Zenkert D., Imperfection-induced wrinkling material failure in sandwich panels, *Journal of Sandwich Structures and Materials*, **7**(3): 195–219, 2005, https://doi.org/10.1177/1099636205048526.

26. Douville M.-A., Le Grognec P., Exact analytical solutions for the local and global buckling of sandwich beam-columns under various loadings, *International Journal of Solids and Structures*, **50**(16–17): 2597–2609, 2013, https://doi.org/10.1016/j.ijsolstr.2013.04.013.

27. Ramberg W., Osgood W.R., Description of stress-strain curves by three parameters, Technical Note no. 902, *NACA Technical Notes*, Washington, 1943.

Received July 10, 2025; revised November 20, 2025; accepted December 3, 2025;
available online December 11, 2025; version of record June 3, 2026;
published issue June 24, 2026.

Engineering Transactions, **74**(2): 231–247, 2026, https://doi.org/10.24423/engtrans.2025.3692
Institute of Fundamental Technological Research Polish Academy of Sciences (IPPT PAN)
Université de Lorraine • Poznan University of Technology

Research Paper

Collision Integral for Non-Equilibrium Distributions of 1D Bosons with Non-Linear Dispersions

Piotr CHUDZINSKI*, Wieslaw LARECKI

Institute of Fundamental Technological Research, Polish Academy of Sciences
Warsaw, Poland

*Corresponding Author: pchudzin@ippt.pan.pl

In order to understand transport phenomena in the quasi-classical regime, the Boltzmann transport equation (BTE) is one of the most frequently used tools. Therein, the key quantity is the collision integral – the quantity that encapsulates the properties of the medium under consideration. Usually the result of this integral is approximated by a single parameter, the relaxation time. However, this leaves one wondering if such a treatment is sufficient, for instance, if the dispersion of bosons is non-linear, what will be the influence of this non-linearity on the BTE. Here, we give a fully analytic solution of the collision integral for 1D bosonic gases with non-linear dispersion and far out of equilibrium. Our analytic result is given in terms of the Lerch transcendent function and it has been obtained for the case of two subsystems (one dragging the other), by taking a maximum-entropy displaced Bose–Einstein ansatz for their distributions. Currently, there are numerous experiments performed far from equilibrium, where distributions are massively shifted and our result may serve as a main building block for deriving distributions of bosons, and later linear and non-linear transport coefficients, in such regimes.

Keywords: Boltzmann transport equation, bosons with non-linear dispersions, non-equilibrium distributions.

1. INTRODUCTION

The Boltzmann transport equation (BTE) has been a foundation of quasi-classical transport theory for more than a century. In a general state, it reads:

$$\frac{\partial b}{\partial t} + \frac{p}{m} \cdot \nabla b + F \cdot \frac{\partial b}{\partial p} = \left(\frac{\partial b}{\partial t}\right)_{\text{coll}}. \tag{1.1}$$

In this differential equation we search for an unknown distribution of particles, e.g., bosons $b(k)$, where k is the boson wavevector, which can be associated with their momentum $p \equiv k$. On the left-hand side (LHS) of BTE, the first term is from an explicit dependence on time, the second term is the drift term, and the last one comes from an applied external forcing field $F(r)$. These terms depend on the specific setup where the force is applied. The right-hand side (RHS) of BTE is the collision term, which depends on the properties of the boson gas itself and is usually the hardest part to compute. Once the distribution $b(k)$ is known, one is able to evaluate all currents j, assuming quasi-classically that the current is carried by the particles, and thus obtain the relation between $j(F)$, the key quantity of interest from an experimental viewpoint. One usually assumes *a priori* a small distortion, called $g(k)$, from the equilibrium Bose–Einstein distribution to profit from the fact that there is no current in the equilibrium case; thus, current is entirely due to $g(k)$. Here, we will not resort to this assumption; instead, we shall take a non-perturbative, non-equilibrium distribution.

The aim of this work is to compute the collision term for the case of a non-equilibrium distribution of bosons. In short, we shall study the situation when one puts a strong current through one 1D subsystem and studies how another 1D subsystem is affected. Several research groups undertake intense efforts in this direction [1], there have also been remarkable theoretical achievements in this field [2–5]. It has turned out that the underlying dispersion relation of the bosons may play an important role. Here, we wish to study one specific question: how the fact that the bosons have a non-linear dispersion affects the resulting collision term?

We intend to study this problem in a strongly non-equilibrium setting. The presence of a current always puts the system away from an equilibrium and from experimental viewpoint one prefers strong current to arrive at a detection signal that is well above the noise level. From the theoretical point of view, studying system far-from-equilibrium is a challenge. However, over the last years significant progress have been made in this direction, and many solutions for systems far away from equilibrium have been derived [6]. This progress has been fueled mostly by research on cold-atom systems [7] and plasmon-polariton systems [8], i.e., bosonic systems that can be pushed much further away from equilibrium than any traditional solid-state material. We intend to build on these developments.

The outline of this work is as follows. In Sec. 2, we define the model under consideration. In Sec. 3, we outline previous theoretical work and provide an ansatz for the non-equilibrium distribution of bosons. In Sec. 4, we compute the collision integral in an analytical form and evaluate it by showing a few examples of the collision term. The paper concludes with a discussion in Sec. 5 and conclusions in Sec. 6.

2. Model

We study the problem of interacting bosons. We take 1D bosons since this simplifies the reasoning (although an isotropic higher-dimensional problem can also be tackled using spherical harmonics). The Hamiltonian of such a system generally reads:

$$H_0 = \sum_{ij} E_{ij} b_i^\dagger b_j + \sum_{ijkl} V_{ijkl} b_i^\dagger b_j b_k^\dagger b_l, \tag{2.1}$$

and the system is subjected to an external field F_{ij}:

$$H_F = \sum_{ij} F_{ij} b_i^\dagger b_j. \tag{2.2}$$

In the following, we shall assume that the system is translationally invariant; thus, the momentum is a good quantum number and diagonalizes the first term in H_0. The field F_{ij} is also defined in terms of spatial harmonics, so now $i, j \equiv k, k'$. Moreover, a part of interactions, that is, of a density-density type $\propto n_i n_l$ is assumed to be the strongest and it leads to a renormalization of the boson velocity, while keeping their dispersion linear, just as it happens in the Lieb–Liniger model [9] or in the random-phase approximation (RPA) treatment of acoustic phonons/plasmons [10]. For such a case, the quantum, $T = 0$, solution to the model given by Eq. (2.1) is known [11], and it has two phases: superfluid and insulator. However, it is also known that coupling to a strong multi-harmonic field $F(q_i)$, Eq. (2.2), leads to floating Aubry–André physics [12], and/or coupling to a dissipative environment leads to a metallic phase with a well-defined Drude peak [13, 14]. Then, using the BTE, Eq. (1.1) is justified. Our quantity of interest is then the average occupancy of bosonic modes $b(k) = \langle \widetilde{b}_k^\dagger \widetilde{b}_k \rangle$ in the high-temperature regime, when the low-energy physics may be integrated out and the eigenstates $\widetilde{b}_k$ of the interacting bosons, Eq. (2.1), emerge, see, e.g., Eq. (2.3). This implies that the effective susceptibility of the environment will contain some retardation effects, namely some non-trivial momentum dependence inherited from these averaged-out low-energy modes. In turn, this implies that the interactions $V(q)$ will have more complicated character and will not be entirely absorbed in a simple linear dispersion.

Furthermore, we assume that, upon interaction with the field F, the bosons can be divided into different ν-branches ($\equiv$ subsystems); for instance, phonons with different symmetries, such that their interaction with the external field $F(q)$ is different (e.g., due to dipole matrix selection rules). The simplest situation is that of two branches, although it can naturally be extended to more subsystems. The simplest system under consideration thus consists of two parts: 1) a 1D electron liquid (1D metal) that is subjected to a strong current (due to the applied force $F(q)$), and 2) a recipient 1D system that is subjected to the collisions with 1. Of the latter, we only need to assume that it can be described by a distribution that admits a local Taylor expansion. Thus, the locally induced voltage in the recipient system is linearly proportional to a distortion of local distribution of carriers, such that transverse transport coefficients (e.g., drag coefficients) can be potentially defined.

In a 1D system, in the presence of any density-density interaction V_0, the spectral weight is shifted from quasiparticles, to collective modes [15]. These collective modes are described by the following Hamiltonian:

$$H_{\text{mod}} = \sum_{\nu} u_{\nu}(q) q \widetilde{b}^{\dagger}_{\nu}(q) \widetilde{b}_{\nu}(q), \tag{2.3}$$

which we express here in terms of bosonic operators $\widetilde{b}^{\dagger}_{\nu}$ where the index ν spans over, e.g., charge and spin degrees of freedom to capture collective fluctuations in each of these sectors. This example defines separable ν-branches ($\equiv$ subsystems). Thanks, e.g., to spin-charge separation present in 1D, each of these modes can be indeed considered separately. In general, the velocities $v_{\nu}(q) \propto q^{\alpha_{\nu}-1}$ are determined by interactions, with the linear dispersion $\alpha_{\nu} = 1$ present for purely Hartree-type interactions. In many nanostructures, that are, e.g., deposited on the surface, the 1D charges can provide only partial screening. We then obtain some finite range, Coulomb-type interaction $\widetilde{V}_{\text{Coul}}(q)$, which affects these charged degrees of freedom. The velocity $v_{\rho}(q)$ is now determined by $\widetilde{V}_{\text{Coul}}(q)$, which in turn depends on the dielectric constant of the nanostructured environment within which the 1D system is embedded, namely: $\widetilde{V}_{\text{Coul}}(q) = V_{\text{Coul}}(q)/\epsilon(q)$. Here $V_{\text{Coul}}(q)$ is the bare Coulomb interaction (which can be assumed to be of the Hartree type), while $\epsilon(q)$ is the dielectric constant that has been evaluated analytically, for instance, in [16].

Our problem thus consist out of 1D charge-carrying bosons with a power-law dispersion:

$$\omega_{\rho}(q) = \widetilde{v}_{\rho} q^{\varsigma}, \tag{2.4}$$

which is equivalent to a velocity $v_{\rho}(q) \propto q^{\varsigma-1}$, where q is dimensionless and $\widetilde{v}_{\rho}$ is a proportionality constant that carries the dimension of energy.

In the following, we shall consider two copies of such 1D systems coupled through a momentum-carrying interaction:

$$H_{\text{tot}} = H^{(1)}_{\text{mod}} + H^{(2)}_{\text{mod}} + H^{(1-2)}_{d}, \tag{2.5}$$

where $H^{(1-2)}_{d}$ is the coupling term, which we assume to be weak enough to not destroy the modes' separation into the subsystems. Moreover, we assume that one of the modes is in a strongly non-equilibrium state, in the sense that a strong current flows through it.

The momentum relaxation term $H_d^{(1-2)}$ between the subsystems, with amplitude $\equiv \mathit{\Gamma}_0 = \text{constant}$, can potentially allow a transfer of part of the current to the other subsystem (in fact, $\mathit{\Gamma}_0$ has to have some ultra-violet (UV) cut-off, as in Yukawa potential). The remanent interaction induces the non-linearity of the spectrum (which can be interpreted as a self-energy effect), but it will also induce a vertex correction. From the Ward identity, we know that the self-energy $\Sigma(k \pm q)$ and the vertex correction $\mathit{\Gamma}(q)$ have to be related if a system is conserving. To be precise [17], in the low-energy limit $\mathit{\Gamma}(q) \propto \partial\Sigma(k)/\partial k|_{k=q}$. The non-linearity of the dispersion will thus induce anharmonic behavior of the bosons, i.e., boson-boson interactions. We then expect that in our particular case, when there is a deviation $\mathrm{Re}[\Sigma(k)] \approx \Delta\omega(k)$ from the linear dispersion, the vertex correction reads:

$$\mathit{\Gamma}(q) = (\partial_q \Delta\omega_\rho(q)/\partial q) = (\varsigma - 1)\widetilde{v}_\rho q^{\varsigma-1}, \tag{2.6}$$

and is therefore given by another power law. In deriving this we performed a Taylor expansion of $\omega(k \pm q)$ for a small values of exchanged momenta q and kept only the first term. This is justified by the fact that the postulated interactions $\widetilde{V}_{\mathrm{Coul}}(q)$ is of screened Coulomb type and thus favors small exchanged momentum processes. The most important implication of Eq. (2.6) is that, with such a generalized dispersion model, the vertex corrections are unavoidable. We emphasize that the formalism that we shall derive further can accommodate a vertex correction that is given by any power law. However, the specific form given by Eq. (2.6) is useful for demonstrating that such a correction will necessarily appear if one wants to keep a conserving approximation. Figure 1 presents a schematic illustration of our model. Two 1D subsystems are coupled by a momentum-dependent amplitude $\mathit{\Gamma}(k)$. There is a strong current j (yellow arrow) flowing through one of them. Each subsystem (mode) has a different distributions of bosons, shown (trimmed) on the top of each subsystem. We see different temperatures and a shift of the upper distribution due to the current flow. The ansatz for these distributions is given in Sec. 3.

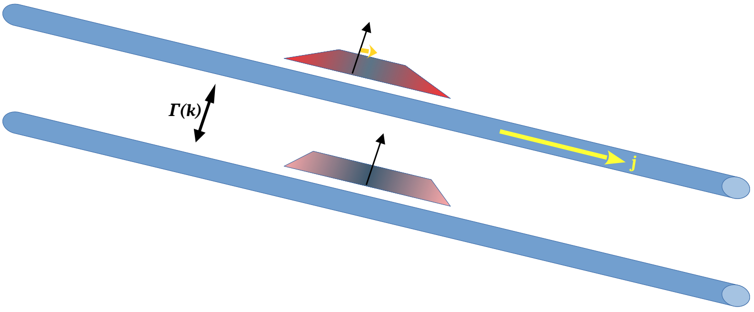

FIG. 1. Schematic illustration of our model.

3. Postulated non-equilibrium bosonic distributions

The non-equilibrium distribution of bosons is postulated in the form of a displaced Bose–Einstein distribution function (taking $k_B = 1$):

$$F_d = \frac{1}{2\pi}\left\{\exp[\omega(k)/T_e - kv_{\mathrm{drag}}/T_d]\right\}^{-1}, \tag{3.1}$$

the same as the one assumed for a strongly dragged (i.e., non-equilibrium) gas of bosons with an arbitrary dispersion relation $\omega(|k|)$. This form is known in the literature and has been used many times before, e.g., in [18–20]. Here, T_e is the temperature of a gas in equilibrium with the same energy density, and v_{drag} and T_d are the so-called drift velocity and drift temperature, respectively. For a bosonic gas represented by a distribution function $b[\chi(k);T]$ the energy density and momentum density read:

$$\epsilon := \frac{1}{\Omega_{\mathrm{BZ}}}\int\limits_{\mathrm{BZ}} \omega(|k|) b[\chi(k);T_{e,d}]\,\mathrm{d}k, \qquad p := \frac{1}{\Omega_{\mathrm{BZ}}}\int\limits_{\mathrm{BZ}} kb[\chi(k);T_{e,d}]\,\mathrm{d}k. \tag{3.2}$$

In [20, 21], the distribution of the form given by Eq. (3.1) was obtained from an optimization procedure of entropy written as a functional of the distribution $b(k)$:

$$s\,[b(k)] = \frac{1}{2\pi}\int \{(1+2\,\pi\, b(k))\ln(1+2\,\pi\, b(k)) - 2\,\pi\, b(k)\ln(2\,\pi\, b(k))\}\,\mathrm{d}k, \tag{3.3}$$

under a constrains corresponding to fixed values of the energy ϵ and momentum p, namely:

$$\delta\left(s(b(k)) + \alpha\left(\epsilon - \frac{1}{\Omega_{\mathrm{BZ}}}\int\limits_{\mathrm{BZ}} \omega(k)\, b(k)\,\mathrm{d}k\right) + a\left(p - \frac{1}{\Omega_{\mathrm{BZ}}}\int\limits_{\mathrm{BZ}} kb(k)\,\mathrm{d}k\right)\right) = 0, \tag{3.4}$$

where α and a are the Lagrange multipliers of this variational problem with constrains. Solving Eq. (3.4) for $b[\,]$ and comparing the result with Eq. (3.1) we find [20, 21] that the variational problem is indeed optimized by

$$b[\chi(k)] = F_d\,[\chi] = \frac{1}{2\pi\,\left(e^{\chi(k)}-1\right)}, \qquad \chi(k) = \alpha\,\omega(k) + ak, \tag{3.5}$$

where

$$\alpha = {T_e}^{-1}, \qquad a = -\frac{v_{\mathrm{drag}}}{T_d}. \tag{3.6}$$

Based on this result, in the following, to make correspondence with standard condensed-matter notation, we define for the i-th subsystem:

$$\alpha_i \equiv \beta_i = 1/T_i. \tag{3.7}$$

Moreover, we shall re-scale β_i with the 'bare' velocity $\widetilde{v}_{i\rho}$, that is, $\widetilde{v}_{i\rho}\beta_i \to \beta_i$ which is a shorthand dimensionless notation used in subsequent sections.

Naturally, the solution of the constrained variational problem reproduces the constrains, i.e., $\epsilon = \frac{1}{\Omega_{\mathrm{BZ}}} \int\limits_{\mathrm{BZ}} \omega(|k|) F_d[\chi(k)]\, \mathrm{d}k$ and $p = \frac{1}{\Omega_{\mathrm{BZ}}} \int\limits_{\mathrm{BZ}} k F_d[\chi(k)]\, \mathrm{d}k$. Moreover, when the gas of bosons tends to equilibrium, the constraint $p \to 0$ and consequently the corresponding Lagrange multiplier in the distribution $a \to 0$; thus, the distribution itself becomes the Bose–Einstein distribution. As shown explicitly in Subsec. 5.1, for the case of linear dispersion the quantities T_e, T_d, and v_{drag} can be expressed [21] as analytic functions of the given ϵ and p.

To close this subsection, we would like to emphasize that naturally the proposed ansatz for the distribution is obviously an approximation in which we assume that the emergent modes are weakly interacting. Such an assumption can be justified, for instance, when the interactions $V(q)$ are chosen such that the system is in the vicinity of Luther–Emery points. This issue is discussed further in Sec. 5.

4. COLLISION TERM AND RESULTING INTEGRAL

4.1. DERIVATION OF THE COLLISION INTEGRAL

We can substitute the postulated non-equilibrium distribution function F_d into the Boltzmann transport Eq. (1.1). Specifically, we are interested in evaluating the RHS of this equation, the collision integral, which depends on the inherent properties of the system, rather than on the specific form of the externally applied field. The collision integral that we want to evaluate reads:

$$\overline{\Gamma}_{\mathrm{coll}}(k) = \int\limits_0^{k_0} \mathrm{d}q \Gamma_0 \Gamma(q) b_{d1}(k+q) b_{d2}(k-q), \tag{4.1}$$

where k_0 is the upper cut-off momentum of the theory (e.g., the Brillouin zone boundary) and b_{di} is a short-hand notation displaced distribution, Eq. (3.5), in the i-th subsystem. This is a Bose–Einstein distribution with drag, a distribution parameterized by the pair (β_i, a_i). In order to make progress, we take a Taylor expansion of $\omega_\rho(k \pm q)$, which leads to a term $\beta((1+\varsigma)k^{\varsigma} \pm +\varsigma k^{\varsigma-1} q)$. The underlying assumption of a small q exchanges' dominance has already been discussed (Eq. (2.6)) and it clearly manifests in the last term of Eq. (22). Upon substituting it into the distributions, we find that:

$$b_{d1}(k+q)b_{d2}(k-q) = \exp\left\{-\frac{1}{2}(\beta_1+\beta_2)(1+\varsigma)k^{\varsigma}\right\} \tag{4.2}$$
$$\cdot\left(\exp\left\{\frac{1}{2}(\beta_1+\beta_2)(1+\varsigma)k^{\varsigma}\right\}\exp\left\{[(\beta_1+\beta_2)\varsigma k^{\varsigma-1}+(a_1+a_2)]q\right\}\right.$$
$$+\exp\left(\frac{1}{2}(\beta_1-\beta_2)(1+\varsigma)k^{\varsigma}\right)\exp\left\{[(\beta_1-\beta_2)\varsigma k^{\varsigma-1}+(a_1-a_2)]q\right\}$$
$$+\exp\left(\frac{1}{2}(-\beta_1+\beta_2)(1+\varsigma)k^{\varsigma}\right)\exp\left\{[(-\beta_1+\beta_2)\varsigma k^{\varsigma-1}+(-a_1+a_2)]q\right\}$$
$$\left.+\exp\left\{-\frac{1}{2}(\beta_1+\beta_2)(1+\varsigma)k^{\varsigma}\right\}\right)^{-1}.$$

Thus, the collision integral can now be cast in the following form:

$$\overline{\Gamma}_{\mathrm{coll}}(k) = \exp\left\{-\frac{1}{2}(\beta_1+\beta_2)(1+\varsigma)k^{\varsigma}\right\} \tag{4.3}$$
$$\int \mathrm{d}q \frac{(\varsigma-1)\Gamma_0 q^{\varsigma-1}\exp\left\{\frac{1}{2}[(\beta_1-\beta_2)\varsigma k^{\varsigma-1}+(a_1-a_2)]q\right\}\exp[-q/k_0]}{z(k)\exp\left\{[(\beta_1+\beta_2)\varsigma k^{\varsigma-1}+(a_1+a_2)]q\right\}-1},$$

where the numerator contains the inverse bosonic scattering amplitude $\Gamma(k)$ multiplied a Yukawa potential (which in the solid-state setting is equivalent to Thomas–Fermi screening), which we introduced both to accommodate the upper limit of the integral and to physically model the finite range of the interaction. In the denominator, there is a following function:

$$z(k) = \frac{\exp\left\{\frac{1}{2}(\beta_1+\beta_2)(1+\varsigma)k^{\varsigma}\right\}}{a^*}, \tag{4.4}$$

where

$$a^* = \exp\left(-\frac{1}{2}(\beta_1+\beta_2)(1+\varsigma)k^{\varsigma}\right)+\exp\left(\frac{1}{2}(\beta_1-\beta_2)(1+\varsigma)k^{\varsigma}\right)$$
$$+\exp\left(\frac{1}{2}(-\beta_1+\beta_2)(1+\varsigma)k^{\varsigma}\right).$$

It is well known that many integrals of canonical distribution functions can be given in terms of polylogarithms [22]. This is not sufficient to solve Eq. (4.3), we therefore shall move to a generalization of polylogarithm function, which is the Lerch transcendent function. Its integral form reads [23]:

$$\Phi(z,s,\overline{\overline{a}}) = \frac{1}{\Gamma(s)}\int_0^{\infty}\frac{x^{s-1}e^{-\overline{\overline{a}}x}}{1-ze^{-x}}\,\mathrm{d}x, \tag{4.5}$$

where the denominator has a form similar to a denominator of the canonical distribution and in the numerator there is a modified power law factor.

By comparing this with Eq. (4.3), we observe that after that substitution $x \to q$ our integral is indeed solvable through the Lerch transcendent function. The result of this integral reads:

$$\overline{\Gamma}_{\mathrm{coll}}(k) = \frac{\exp\left\{-\frac{1}{2}(\beta_1+\beta_2)(1+\varsigma)k^{\varsigma}\right\}}{[(\beta_1+\beta_2)\varsigma k^{\varsigma-1}+(a_1+a_2)]}\,\frac{(\varsigma-1)\Gamma_0}{\overline{\Gamma(\varsigma-1)}}\Phi\left(z(k),(\varsigma-1),-y(k)\right), \tag{4.6}$$

where

$$y(k) = \frac{\frac{1}{2}[(\beta_1-\beta_2)\varsigma k^{\varsigma-1}+(a_1-a_2)]-1/k_0}{[(\beta_1+\beta_2)\varsigma k^{\varsigma-1}+(a_1+a_2)]}, \tag{4.7}$$

and $\Phi(\,)$ is the Lerch transcendent function, and $\overline{\Gamma(\,)}$ is the gamma function. Actually, the Lerch transcendent special function, a generalization of polylogarithm functions (known to be integrals of quantum distributions), has already appeared in the literature as an integral of distributions with drag, see [24]. However, the full dependence on ς has not been explored. Equation (4.6), together with expressions for $z(k)$ (Eq. (4.4)) and $y(k)$ (Eq. (4.7)) provides a closed analytic form for the momentum-resolved collision integral. This is the central result of our work.

This result also allows the investigation of the energy-weighted and momentum-weighted integrals, which both must exist and be positive. This is because the Lagrange multipliers (as defined in Sec. 3) must be reproduced by these moments of the distribution. From properties of the Lerch function, we can now deduce that the positivity condition is equivalent to the positivity of distribution argument.

4.2. RESULTS

We shall now illustrate the results of Eq. (4.6). First, in Fig. 2, we plot the collision integral as a function of $a_1 \equiv v_{\mathrm{drag}}$. For simplicity, we take the case when one of the distributions is not shifted, i.e., $a_2 = 0$. We observe that the collision amplitude is strongest for the small electron momenta k. For larger value of ς (right panel), for small values of k, we see that the function is clearly non-monotonic: there exists an optimal value of the Lagrange multiplier a_1 for which the drag effect is strongest. Naturally, for the smallest values of a_1 the effect increases with the shift of the distribution. However, when the distribution is shifted too strongly, the carriers within the receiving subsystem cannot catch up with the rapid motion of non-equilibrium carriers. This is the reason why we call a_1 the drag velocity v_{drag}. For larger k, the effect monotonically increases with v_{drag}, although this tendency is much less pronounced. The same behavior

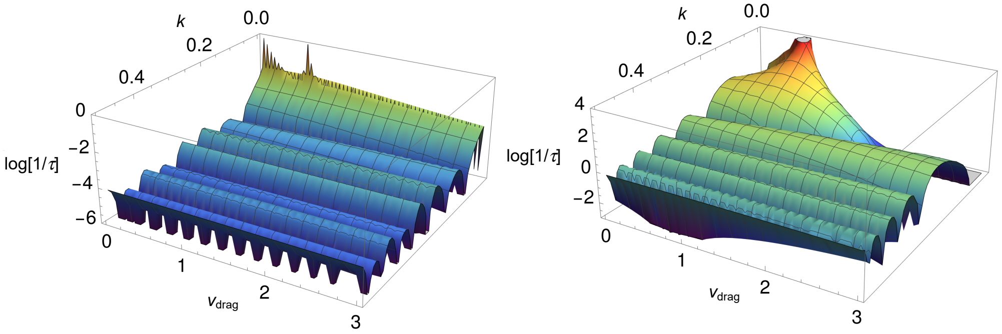

FIG. 2. Logarithm of the collision amplitude as a function of the electron momentum k and the drag velocity v_{drag} ($\equiv a_1$). On the left we show result for $\varsigma = 1.5$, on the right for $\varsigma = 2.5$. Both calculations were done for $\beta_1 = 30$, $\beta_2 = 20$, and $a_2 = 0$ (no initial shift of distribution). Other parameters: $\Gamma_0 = 2/3$, $q_0 = 3$. All the quantities are given in units of energy, where $\overline{v}_\rho = 1$, which is set by the characteristic kinetic energy of the system and in units of momentum set by the 1D density of particles n, just as in [9].

for large k is observed in the left panel (smaller ς). Interestingly, here for small k we cannot notice such a clear resonance: there is a noisy variation at small v_{drag} and then a collision amplitude monotonically decreases.

In Fig. 3, we plot the result of the collision amplitude as a function of temperature. We set the temperature of the recipient mode to $b_2 = 20$ and vary the temperature of the dragging subsystem. We observe that the largest effect, a strong maximum, exists when the temperature $b_1 = 20$, i.e., when $b_1 = b_2$. The effect indicates that the collision integral is strongest when the two distributions are most similar to each other.

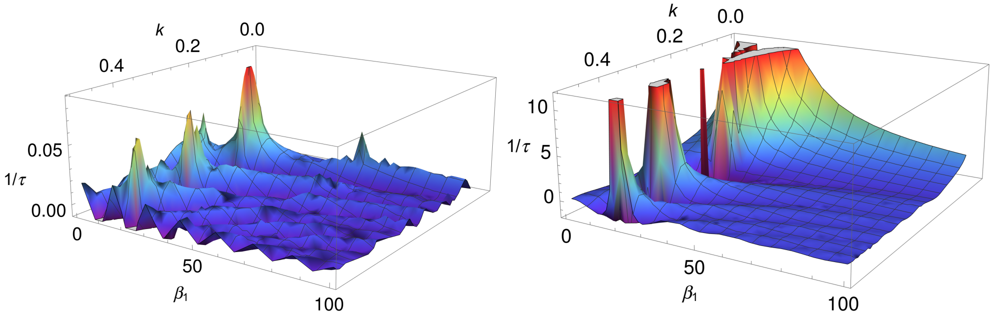

FIG. 3. Collision integral amplitude as a function of the electron momentum k and temperature $\beta_1 = T_{e1}^{-1}$. On the left we show result for $\varsigma = 1.5$, on the right for $\varsigma = 2.5$. Both calculations were done for $a_1 = 0.5$, $\beta_2 = 20$, and $a_2 = 0$ (no initial shift of the distribution). Other parameters: $\Gamma_0 = 2/3$, $q_0 = 3$.

However, the most important conclusions from all these calculations is the very strong dependence on ς: moving away from $\varsigma = 1$ can cause the result to grow by orders of magnitude. Thus, we see that the amplitude of the collision integral is a very susceptible measure of the non-linearity encoded in the value of ς.

5. DISCUSSION

5.1. CASE OF LINEAR DISPERSION

For the case of linear dispersion $\omega = c|k|$ we can derive analytic expressions for the Lagrange multipliers of the variable $\chi(k)$ [21], which now can be called the equilibrium temperature $T_e = \beta^{-1}$ and the drag temperature $T_d = a^{-1}\overline{v}_{\text{drag}}$, where we define the bare (normalized by T_d) drag velocity $\overline{v}_{\text{drag}}$:

$$T_d = \frac{T_e\,(1-u)}{\sqrt{1+u}}, \tag{5.1}$$

$$u = \frac{\epsilon - \sqrt{\epsilon^2 - c^2p^2}}{\epsilon + \sqrt{\epsilon^2 - c^2p^2}}, \tag{5.2}$$

where, as before in Sec. 3, the distribution $F_d[...]$ determines the average energy and momentum (normalized by the volume of the first Brillouin zone, Ω_{BZ}) that enter into the before mentioned formulas:

$$\epsilon = \frac{1}{\Omega_{\text{BZ}}} \int\limits_{\text{BZ}} c|k|\, F[\chi(k)); T_e]\, \mathrm{d}k, \tag{5.3}$$

$$p = \frac{1}{\Omega_{\text{BZ}}} \int\limits_{\text{BZ}} kF[\chi(k)); T_e]\, \mathrm{d}k, \tag{5.4}$$

where, because of the fixed relation Eq. (5.1), we can use only one temperature to parameterize the distribution. The latter quantity, the average momentum in a subsystem p, can be related to the bare drag velocity:

$$\overline{v}_{\text{drag}} = c\frac{cp}{\epsilon + \sqrt{\epsilon^2 - c^2p^2}}. \tag{5.5}$$

Thus, we see that for the linear distribution there is a unique solution to the shifted-density problem. Importantly, for the linear dispersion in 1D, the two integrals in Eq. (5.3) and Eq. (5.4) have the same form up to a unitary factor sign(k).

This observation can be generalized. It can be shown that in the case of linear dispersion, i.e., $\varsigma = 1$, the drag effect is expected to be zero, which is in agreement with our prediction. This is because the moment expansion $M_n = \int k^n F(\chi(k))\,\mathrm{d}k$ of a distribution forms a closed set, as we fixed the value of ϵ (total k) and p (difference between positive and negative k). As it was shown in [25], the drag is proportional to third cumulant, and from statistics we know that third cumulant is equal to the third moment (skewness). This general argument justifies our result. A similar conclusion, for more specific case of thermoelectric effect, was reached in [26], where it was traced back to the Mott relation for transport coefficients.

5.2. Limitations of our reasoning

There are two key limitations of our approach. The first one is that we have neglected the known quantum phases of the 1D boson model: superfluid and insulator. This may be justified in the regime of high temperature and in a dissipative environment, which is actually the same regime where the quasi-classical BTE approach itself is known to be applicable. Nevertheless, one has to keep in mind that our calculations are valid only in the quasi-classical regime and caution should be excercised when applying them to low-temperature systems subjected to highly coherent field $F(q)$.

Second, in Sec. 3, we adopted an ansatz for non-interacting bosonic distributions which is obviously an approximation when boson-boson interactions are present. Simply taking $V_{ijkl} = 0$ in Eq. (2.1) will not ameliorate the situation, as then we shall arrive at a bosonic liquid with a very high tendency toward Bose–Einstein condensation, a quantum phenomenon not accounted for in a simple BTE. There are two arguments that may justify our model. The first one is based on the existence of Luther–Emery points: for specific values of V_{ijkl}, the 1D system behaves as a system of an emergent non-interacting particles. This is why we emphasized that the modes on which the Hamiltonian in Eq. (2.3) is defined are emergent collective eigen modes. This is also the reason why, for these modes, both self-energies effects and vertex corrections may be substantial. The second argument is more pragmatic: the quantity on which we focus in this work is solely the collision integral. We limited ourselves and decided to not move toward full solution of the BTE. In this way, our result is more generic and can be applied to various configurations of the external $F(q)$. But, in this way, we also compute only a basic building block of a potentially more advanced approximation. One can consider including interaction corrections to the distribution $b(k)$ in a perturbative series (with all possible particle-hole cancellations) and then, at each term, the expressions provided by us here can be used. Nevertheless, we admit that future research, aiming at deriving the collision integral for fully interacting distributions of bosons, known as hypergeometric Beta functions [15], would be an exciting and important direction of research.

One posibble physical realization of the proposed model would be either a multi-wire or a multi-orbital 1D system. Here, it is pretty intuitive that the field F can interact strongly only with one selected orbital or – in the case of coaxial tubes (such multi-walled carbon nanotube (MWCNT)) or parallel wires – only to the outermost subsystem. Then, we naturally obtain subsystems with different distributions, and with different shifts. Moreover, since the subsystems are nearly orthogonal (in Hilbert space), tunneling requires reconstitution of the entire boson. This has been evidenced by experiments in [27]: the perpendicular transport measures the single-particle density of states. In such a specific case, it makes sense to use shifted Bose–Einstein distributions to compute collision integrals between these reconstituted particles.

5.3. Examples of experimental relevance

The connection between our postulated theoretical model and its real-life experimental realizations is a quite complicated but also fascinating problem. The two most promising platforms are nanostructured wires and cold atoms. In each of these systems, the ongoing research faces slightly different problems.

In cold atoms, where emergent bosons are created by trapping atoms in an optical lattice, the interactions can be relatively easily modified by changing the external magnetic field (in this way one tunes the scattering cross section through a Feshbach resonance). Moreover, one can add a fast, anti-adiabatic, fermionic component to a mixture of two bosons and vary their interaction through a Ruderman–Kittel–Kaqsuya–Yosida (RKKY) type mechanism. This has been experimentally employed in [28]. Therein, one finds that the characteristic kinetic energy can be of the order of 6.5 Hz while at the same time the interspecies scattering can be tuned to be as small as $\Gamma_0 \sim 0.5\,\mathrm{Hz}$. From the point of view of energy scales of these bosons, temperatures of the order of nK are indeed in the high-temperature regime that we discuss in our paper. The difficulty here lies in extracting the dispersion relation: the interaction is that of an extended Lieb–Liniger model, and from the Bethe-ansatz solution of the Lieb–Liniger model we know that there are higher-energy bosons with super-linear dispersion and low-energy bosons with sub-linear dispersions. A separate issue is how these dispersions will be modified by the optical trapping potential, see, e.g., [29], where the influence of a parabolic trap was analyzed. From the experimental viewpoint, the exponent ς can be extracted only indirectly from time-of-flight experiments, which are destructive for the trapped bosonic system itself.

In a system of nanowires, the plasmonic dispersion is governed by the geometry of the system. While in 3D plasmons have a constant frequency, in 2D their dispersion obeys $k^{1/2}$ whereas in 1D q^1 (this is all assuming a finite range interaction, the full Coulomb interaction would give a $\log(q)$ correction). These results are derived for simple geometry. For a corrugated surface, textbook result tells us that the interaction is, in general, given by a power law with a characteristic exponent dependent on a corrugation angle. However, in such a solid-state system, inter-boson interactions are much harder to control. One can modify the Thomas–Fermi screening length or submerge the system into a dielectric medium, thus modifying the interaction $\widetilde{V}(r)$, which implies also changing inter-boson interaction (scattering with finite momentum exchange). However, all these efforts are only indirect. An interesting situation, where inter-boson scattering indeed appear to play crucial role is reported in [30], where the plasmons' kinetic energy was reported as $1.2eV$ and the scattering amplitude was $\mathit{\Gamma}_0 \approx 0.2eV$. Other solid-state systems will have similar orders of magnitude and here we will need to take the operating temperature to be a room temperature or higher (as in the case of an aforementioned experiment) to remain in the high-temperature regime considered in this work.

6. Conclusions

In this paper, we have obtained a closed analytic formula for the collision integral between two 1D systems. This is a basic building block for obtaining solutions of the BTE, Eq. (1.1), and for determining transport coefficients in many experimentally/technologically motivated applications. The collision term in the BTE is the one that determines resistivity and the one that is notoriously the hardest to compute, especially in a non-linear non-equilibrium case. Our results enable researches to not only study the strength of the non-linearity ς in the charge sector, but also to directly access the non-equilibrium distributions through the Lagrange multipliers that are characterizing them. With this knowledge, researchers will be able to quantify the non-equilibrium state of the system for various experimental setups, as defined by the LHS of Eq. (1.1).

Upon completing this paper, we learned that experiments capable of probing this regime had indeed been performed very recently, see [31].

Fundings

Piotr Chudziński acknowledges financial support from Polish National Science Centre, grant no. 2021/43/B/ST8/03207.

Conflict of interest

The authors declare that there are no known competing financial interests or personal relationships that could have influenced the work described in this paper.

Authors' contributions

Both authors were involved in the conception of the paper. Wieslaw Larecki designed and drafted Sec. 3 and Subsec. 5.1. Piotr Chudziński designed and drafted all other sections including analysis and interpretation of the data in Sec. 4. All authors reviewed and approved the final manuscript.

References

1. Laroche D., Gervais G., Lilly M.P., Reno J.L., 1D-1D Coulomb drag signature of a Luttinger liquid, *Science*, **343**(6171): 631–634, 2014, https://doi.org/10.1126/science.1244152.
2. Aristov D.N., Luttinger liquids with curvature: Density correlations and coulomb drag effect, *Physical Review B*, **76**(8): 085327, 2007, https://doi.org/10.1103/PhysRevB.76.085327.
3. Kainaris N., Gornyi I.V., Levchenko A., Polyakov D.G., Coulomb drag between helical Luttinger liquids, *Physical Review B*, **95**(4): 045150, 2017, https://doi.org/10.1103/PhysRevB.95.045150.
4. Schlottmann P., Coulomb drag effect between Luttinger liquids, *Physical Review B*, **69**(3): 035110, 2004, https://doi.org/10.1103/PhysRevB.69.035110.
5. Flensberg F., Coulomb drag of Luttinger liquids and quantum hall edges, *Physical Review Letters*, **81**(1): 184–187, 1998, https://doi.org/10.1103/PhysRevLett.81.184.
6. Gasenzer T., Berges J., Schmidt M.H., Seco M., Ultracold atomic quantum gases far from equilibrium, *Nuclear Physics A*, **785**(1): 214–217, 2007, https://doi.org/10.1016/j.nuclphysa.2006.11.155.
7. Erne S., Bücker R., Gasenzer T., Berges J., Schmiedmayer J., Universal dynamics in an isolated one-dimensional Bose gas far from equilibrium, *Nature*, **563**(7730): 225–229, 2018, https://doi.org/10.1038/s41586-018-0667-0.
8. Comaron P. *et al.*, Coherence of a non-equilibrium polariton condensate across the interaction-mediated phase transition, *Communications Physics*, **8**(1): 94, 2025, https://doi.org/10.1038/s42005-025-01977-7.
9. Lieb E.H., Exact analysis of an interacting Bose gas. II. The excitation spectrum, *Physical Review*, **130**(4): 1616–1624, 1963, https://doi.org/10.1103/PhysRev.130.1616.
10. Chudzinski P., Giamarchi T., Collective excitations and low-temperature transport properties of bismuth, *Physical Review B*, **84**(12): 125105, 2011, https://doi.org/10.1103/PhysRevB.84.125105.
11. Cazalilla M.A., Citro R., Giamarchi T., Orignac E., Rigol M., One dimensional bosons: From condensed matter systems to ultracold gases, *Reviews of Modern Physics*, **83**(4): 1405–1466, 2011, https://doi.org/10.1103/RevModPhys.83.1405.
12. Aubry S., André G., Analyticity breaking and Anderson localization in incommensurate lattices, *Annals of the Israel Physical Society*, **3**(133): 18, 1980.
13. Lobos A.M., Giamarchi T., Dissipative phase fluctuations in superconducting wires capacitively coupled to diffusive metals, *Physical Review B*, **82**(10): 104517, 2010, https://doi.org/10.1103/PhysRevB.82.104517.
14. Devillard P., Josephson junction chains with long-range interactions: Phase slip proliferation versus Kosterlitz-Thouless transition, *Physical Review B*, **83**(9): 094509, 2011, https://doi.org/10.1103/PhysRevB.83.094509.

15. Giamarchi T., *Quantum Physics in One Dimension*, Oxford University Press, 2003.

16. Chudzinski P., Parameters of Tomonaga-Luttinger liquid in a quasi-one-dimensional material with coulomb interactions, *Physical Review B*, **103**(15): 155122, 2021, https://doi.org/10.1103/PhysRevB.103.155122.

17. Pandey S., Ward identity preserving approach for investigation of phonon spectrum with self-energy and vertex corrections, *Physical Review B*, **110**(6): 064321, 2024, https://doi.org/10.1103/PhysRevB.110.064321.

18. Dreyer W., Struchtrup H., Heat pulse experiments revisited, *Continuum Mechanics and Thermodynamics*, **5**(1): 3–50, 1993, https://doi.org/10.1007/BF01135371.

19. Dubroca B. Feugeas J., Theoretical and numerical study on a moment closure hierarchy for the radiative transfer equation [in French: Etude théorique et numérique d'une hiérarchie de modèles aux moments pour le transfert radiatif], *Comptes Rendus de l'Académie des Sciences – Series I – Mathematics*, **329**(10): 915–920, 1999, https://doi.org/10.1016/S0764-4442(00)87499-6.

20. Larecki W., Banach Z., Influence of nonlinearity of phonon dispersion relation on wave velocities in the four-moment maximum entropy phonon hydrodynamics, *Physica D: Nonlinear Phenomena*, **266**(1): 65–79, 2014, https://doi.org/10.1016/j.physd.2013.10.006.

21. Larecki W., Banach Z., Consistency of the phenomenological theories of wave-type heat transport with the hydrodynamics of a phonon gas, *Journal of Physics A: Mathematical and Theoretical*, **43**: 385501, 2010, https://doi.org/10.1088/1751-8113/43/38/385501.

22. Chudzinski P., Resonant plasmon-phonon coupling and its role in magneto-thermoelectricity in bismuth, *The European Physical Journal B*, **88**(12): 344, 2015, http://doi.org/10.1140/epjb/e2015-60674-3.

23. Erdélyi A. *et al.*, *Higher Transcendental Functions*, Vol. I., McGraw-Hill Book Company, New York-Toronto-London, 1953.

24. Aguado-Puente P., Chudzinski P., Thermal topological phase transition in SnTe from *ab initio* calculations, *Physical Review B*, **106**(8): L081103, 2022, https://doi.org/10.1103/PhysRevB.106.L081103.

25. Borin A., Safi I., Sukhorukov E., Coulomb drag effect induced by the third cumulant of current, *Physical Review B*, **99**(16): 165404, 2019, https://doi.org/10.1103/PhysRevB.99.165404.

26. Krive I.V., Romanovsky I.A., Bogachek E.N., Scherbakov A.G., Landman U., Thermoelectric effects in a Luttinger liquid, *Low Temperature Physics*, **27**(9): 821–830, 2001, https://doi.org/10.1063/1.1414571.

27. Moser J., Gabay M., Auban-Senzier P., Jérome D., Bechgaard K., Fabre J.M., Transverse transport in organic conductors: Possible evidence for a Luttinger liquid, *The European Physical Journal B – Condensed Matter and Complex Systems*, **1**(1): 39–46, 1998, https://doi.org/10.1007/s100510050150.

28. DeSalvo B.J., Patel P., Cai G., Chin C., Observation of fermion-mediated interactions between bosonic atoms, *Nature*, **568**(7750): 61–64, 2019, https://doi.org/10.1038/s41586-019-1055-0.

29. Garraway B.M., Minogin V.G., Theory of an optical dipole trap for cold atoms, *Physical Review A*, **62**(4): 043406, 2000, https://doi.org/10.1103/PhysRevA.62.043406.

30. Liu Y. *et al.*, Strong interaction between plasmon and topological surface state in $Bi_2Se_3/Cu_{2-x}S$ nanowires for solar-driven photothermal applications, *Science Advances*, **11**(11): eadt2884, 2025, https://doi.org/10.1126/sciadv.adt2884.

31. Zheng M., Makaju R., Gazizulin R., Levchenko A., Addamane S.J., Laroche D., Quasi-1D Coulomb drag in the nonlinear regime, *Physical Review Letters*, **134**(23): 236301, 2025, https://doi.org/10.1103/v3dn-bnrp.

Received November 13, 2025; revised December 2, 2025; accepted December 3, 2025; available online December 12, 2025; version of record June 16, 2026; published issue June 24, 2026.

Engineering Transactions, **74**(2): 249–266, 2026, https://doi.org/10.24423/engtrans.2025.3665
Institute of Fundamental Technological Research Polish Academy of Sciences (IPPT PAN)
Université de Lorraine • Poznan University of Technology

Research Paper

Sustainable Natural and Synthetic Fiber/Epoxy Composites: Mechanical Characterization and One-Way ANOVA Statistical Analysis

Sadashiva Kemparaju1)*, Bhanu Prathap Rangaswamy1),
Balaji Javaraiah1), Shwetha Mahadev2), Rathika Murugan1),
Tarakeshwar Jane1)

1) *Mechanical Engineering Department*
2) *Electronics and Communication Department*

Dr. Ambedkar Institute of Technology Bengaluru
Karnataka, India

*Corresponding Author: sadashiva41@gmail.com

It is now well recognized that the combination of natural and synthetic fibers in synergistic fiber-reinforced composite materials can greatly broaden their applications in engineering and technology. Natural fibers are gaining increasing attention because of their biodegradability, easy availability, durability, and resistance to corrosion, positioning them as eco-friendly substitutes for conventional materials. At the same time, fiber-reinforced composites are increasingly replacing metals in multiple sectors owing to their cost-effectiveness and energy efficiency. In this study, epoxy resin-based hybrid composites are prepared by incorporating glass, hemp and ramie fibers through the hand lay-up approach. The laminates are characterized for tensile, flexural, impact, and, hardness performance using ASTM standard methods. The greatest tensile strength, 73.10 MPa, is achieved in the glass/ramie fiber composite. The hybrid composites comprising glass, ramie, and hemp fibers exhibit enhanced flexural behavior of 18.22 MPa and impact resistance of 142.45 $\mathrm{kJ/m^2}$. Among the tested configurations, the glass/ramie fiber composite recorded the highest hardness value of 27.73 HV. Overall, the findings highlight that glass/ramie/hemp fiber-mixed epoxy composite materials can serve as prospective eco-friendly substitutes for conventional synthetic composites in non-structural applications, such as automotive interiors, by offering a balance of good mechanical performance and sustainability.

Keywords: hybrid composite, natural and synthetic fibers, mechanical properties, glass, ramie, hemp, hand lay-up method.

1. Introduction

Recent studies have highlighted the advanced mechanical performance of natural fiber-reinforced composite materials compared to their man-made counterparts. Owing to their inherent material characteristics, natural fibers have demonstrated enhanced behavior in key mechanical domains, including tensile strength, flexural performance, and impact resistance. Prior investigations have systematically evaluated these properties in polymer composites that incorporate both natural and synthetic reinforcements, considering variations in fiber type and content, as reported by Kemparaju *et al.* [1]. Sapuan *et al.* [2] reported notable improvements in mechanical performance through fiber hybridization, alongside reductions in environmental impact. Their study utilized banana fibers, an agricultural byproduct readily available in tropical regions such as South India and Malaysia, as reinforcement in epoxy-based composites. This approach not only leveraged the mechanical potential of natural fibers but also promoted sustainable material sourcing. In contrast to synthetic fibers, natural fibers present distinct advantages including commendable mechanical performance and superior environmental sustainability. Prior investigations have examined maximum stress responses in two principal orientations, together with the corresponding maximum deflection under varying loading conditions. These evaluations were conducted using three different specimen geometries, thereby facilitating a comparative analysis of mechanical behavior as influenced by variations in Young's modulus.

Recent investigation has increasingly emphasized the enhanced mechanical performance and eco-friendly characteristics of natural fiber-reinforced composites over their synthetic counterparts. Aravinth *et al.* [3] assessed the mechanical characteristics of epoxy composites developed with hybrid hemp/glass fiber reinforcement. The outcomes demonstrated that the hybrid laminates achieved notable enhancements in impact resistance and flexural behavior, surpassing the performance of composites relying solely on synthetic fibers. The addition of natural fibers not only improved energy absorption and toughness but also facilitated a more uniform stress distribution, thereby mitigating crack initiation and propagation under mechanical loading. Kandola *et al.* [4] emphasized the dual advantages of bio-based composites, showcasing both their mechanical viability and environmental sustainability. According to their findings, the integration of natural reinforcement such as flax, jute, and hemp into polymer composites led to a marked decrease in carbon emissions, without compromising the mechanical properties relative to traditional man-made fiber-based composite materials. Thapliyal *et al.* [5] found that incorporating natural fibers such as jute into glass fiber composites significantly enhanced tensile and impact strength. This improvement supports their suitability for superior structural applications. Mahakur *et al.* [6] highlighted that incorporating banana fibers into glass fiber composite materials promoted biodegradability while simultaneously providing comparable flexural strength and durability. Their results support the use of such composites in practical engineering applications. Islam *et al.* [7] revealed that combining sisal with carbon fibers produced composites with lower density and greater toughness, highlighting their potential for lightweight structural applications. By increasing impact resistance and energy-absorbing capacity, natural fibers demonstrate the viability of bio-based composites as sustainable replacements for synthetic materials. In [8], the flexural and tensile characteristics of hybrid composites were significantly improved through the incorporation of glass fibers into natural reinforcements such as jute or sisal. In [9], composites reinforced with banana and sisal fibers with epoxy were explored, and their water absorption, flexural behavior, tensile characteristics, and impact resistance were assessed. The findings presented in [9] highlighted the mechanical viability of natural fiber composite materials across multiple performance metrics. Hybridizing ramie and silk fibers in a 1:3 ratio for epoxy composites resulted in a significant reduction in water uptake and a marked enhancement in mechanical strength [10]. This displays the effectiveness of natural fiber combinations in improving composite performance. Due to their biocompatibility, fast-growing natural fibers are gaining attention for use in cost-effective, eco-friendly, and technically demanding applications. Additionally, treatment of these fibers with NaOH under saturated conditions was found to increase their mechanical properties without compromising structural performance [11]. YUANJIAN and ISAAC [12] conducted fatigue testing to evaluate the performance of hemp-based nonwoven composites fabricated with polyester bonding. BLEDZKI *et al.* [13] examined how water absorption correlates with toughness, flexural property, specific gravity, and compressive strength, in hemp fiber-reinforced composite (HFRC)-based materials. The investigation by KOBAYASHI *et al.* [14] established hemp fiber as a superior reinforcement material in textile composites, with its performance markedly improved through micro-braiding techniques. KABIR *et al.* [15] reported that surface functionalization and environmental exposure markedly affect the structural and physical properties of both synthetic and natural fibers. Their study also showed that adding paper layers to unidirectional flax/epoxy and hemp/epoxy composites significantly enhanced tensile strength compared to composites without paper reinforcement. ARISTRI *et al.* [16] identified the optimal plant fiber blend for jute-reinforced polymer composites intended for automotive applications, considering key factors such as weight, functional performance, and cost efficiency. TORRES *et al.* [17] proposed a hybrid composite consisting of ramie and hemp fibers with enhanced impact resistance, suitable for automotive components such as bumper beams. They also noted that optimizing structural parameters or material composition further improved impact performance.

This experimental investigation assesses the mechanical characteristics of epoxy-based materials reinforced with hemp, ramie and glass fibers. The specimens, produced through the hand lay-up approach, were subjected to mechanical testing to evaluate their tensile behavior, flexural performance, impact resistance and surface hardness. The results shows that the incorporation of hemp and ramie fibers significantly enhances the mechanical characteristics of glass fiber-reinforced composite materials.

2. Materials and methods

2.1. Materials

The composite laminates were fabricated using glass, hemp and ramie fibers as reinforcements within an epoxy resin matrix. Ramie and glass fibers were sourced from Vruksha Composites (Guntur, Andhra Pradesh, India), while hemp fibers, epoxy resin, and hardener HY951 were obtained from UltrananoTech Ltd. (Bengaluru, Karnataka, India). Figure 1 illustrates the raw fibers used, and Table 1 summarizes their key physical and mechanical properties.

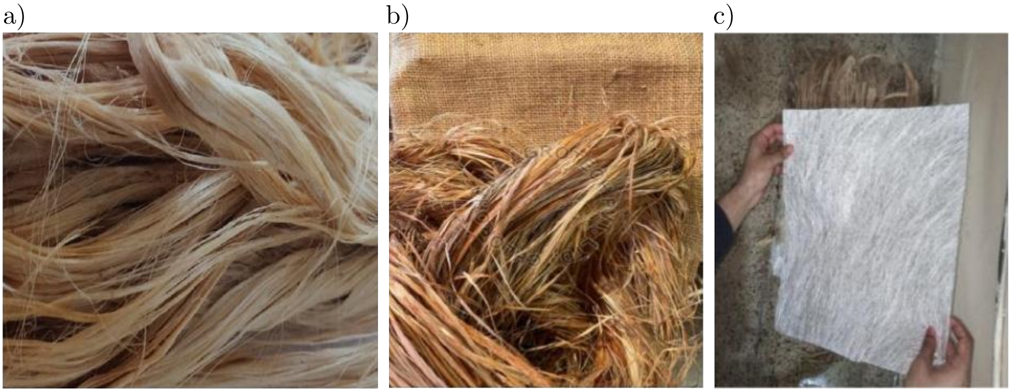

Fig. 1. Fibers used in the study: a) ramie fiber, b) hemp fiber, c) glass fiber.

Table 1. Mechanical characteristics of ramie and hemp fibers.

Properties	Ramie	Hemp
Density [g/cc]	1.52	1.4
Cellulose content [%]	52–57	48–52
Moisture content [%]	1.5–7.5	6-9
Young's modulus [GPa]	86	37

2.2. Fabrication technique

A conventional hand lay-up method was implemented for composite fabrication. To prevent adhesion to the mold surface, a teflon-coated sheet was placed at the base of the mold. The mold was first cleaned using abrasive paper to remove rust, followed by wiping with thinner and the application of teflon gel.

The reinforcement fibers were trimmed to the required dimensions and layered sequentially. Epoxy resin and hardener were mixed in a ratio of 10:1 to initiate curing and applied uniformly over each fiber layer using a roller to ensure proper wetting and adhesion. The hybrid laminates were constructed using three layers of glass fiber and two layers of natural fibers, arranged in an alternating sequence to ensure that glass fibers formed the outer layers. Three configurations were prepared: hemp/glass, ramie/glass, and hemp/ramie/glass composites. All laminates were cured under a constant load using a weighted press for 12 h to ensure uniform consolidation and optimal interfacial bonding.

3. Experimental framework

To design reliable composite structures, it is required to determine key mechanical characteristics such as stiffness and strength through targeted mechanical testing tailored to the specific material system. Adherence to ASTM standards ensures consistent evaluation procedures and facilitates accurate characterization of material behavior and performance.

3.1. Tensile behavior

Tensile samples were prepared in accordance with [22], the standard test method for evaluating the tensile behavior of composite laminates. For each laminate configuration, three samples were tested using a Universal Testing Machine (UTM), where tensile load was applied until fracture occurred. The procedure was repeated for all specimens and laminate configurations to determine the average tensile strength and corresponding stress values for comparative analysis.

3.2. Flexural behavior

Flexural test samples were prepared in accordance with [21], which outlines the standard procedure for analyzing the flexural characteristics of polymer composites. For each laminate type incorporating glass, hemp, and ramie fibers, three samples were tested using the UTM under a three-point bending configuration. During testing, both displacement and flexural strength were recorded to facilitate comparative analysis across the different composite systems. Figure 2 displays the prepared samples for mechanical testing, involving tensile, flexural, impact, and hardness evaluations.

3.3. Impact strength

To assess how the materials respond to sudden or dynamic loading, this study employs the impact behavior assessed using the Charpy V-notch test.

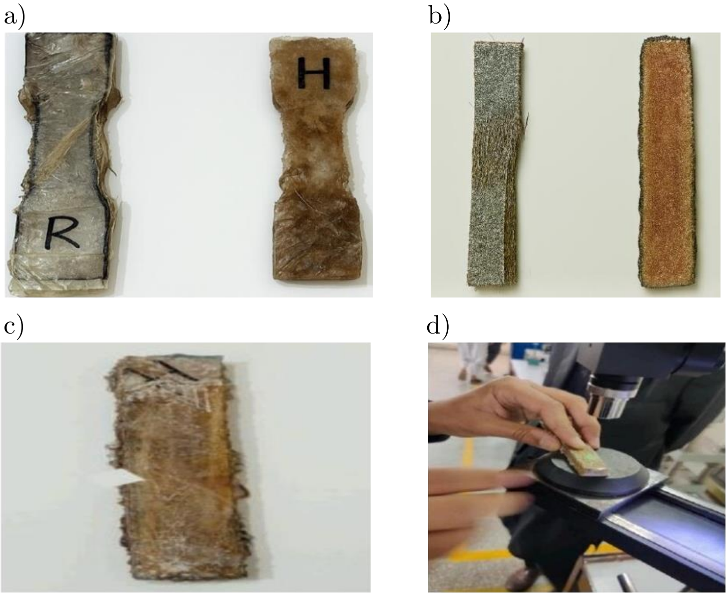

Fig. 2. Mechanical test specimens: a) tensile specimen, b) flexural specimen, c) impact specimen, d) hardness evaluation specimen.

This standardized procedure measures the energy absorbed by a specimen during fracture, thereby offering insight into its toughness under high strain-rate conditions. All specimens were prepared and tested in accordance with ASTM D6110 specifications.

3.4. Hardness test

Microhardness testing is commonly applied to materials such as metals, ceramics, and composites when conventional macro-scale hardness methods are unsuitable. This technique is particularly effective for examining hardness variations across a specimen cross-section, analyzing thin sheet-like materials, and evaluating localized microstructural features within a broader matrix. Typically, static loads of 1 kg or less are used to create small indentations, allowing precise measurement of surface hardness at the microscale.

4. Results and discussions

4.1. Tensile behavior study

The tensile behavior of the composite samples were tested using the UTM. During testing, the machine automatically generated a force-displacement curve, as illustrated in Fig. 3. The tensile behavior results of the different hybrid laminates are compared in Fig. 4. Among the tested samples, the ramie and glass

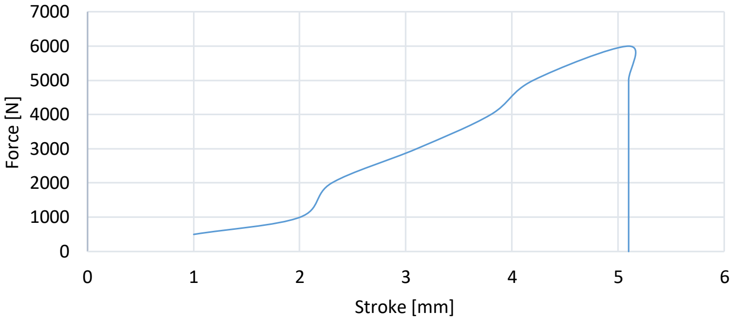

FIG. 3. Force-stroke curve obtained during tensile testing.

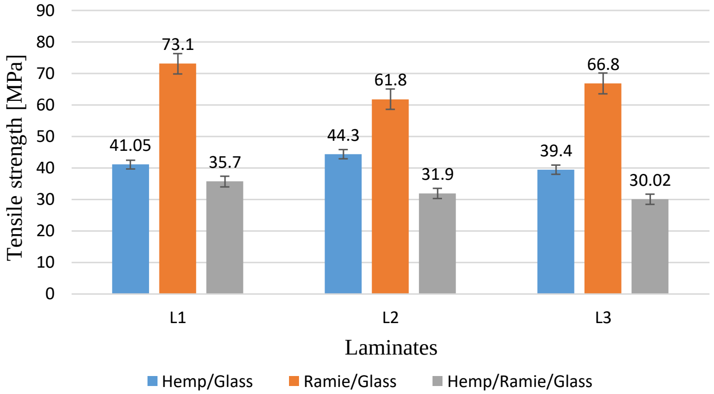

FIG. 4. Tensile strength performance of different hybrid fiber laminates.

fiber-reinforced composite showed an enhanced performance compared to the other laminate configurations. The tensile strength values of the three different laminate configurations: hemp/glass, ramie/glass, and hemp/ramie/glass were evaluated for three specimens (L1, L2, and L3). The results are summarized in the corresponding bar graph. The ramie/glass laminates consistently showed the highest tensile strength across all specimens, with 73.10 MPa for L1, 61.80 MPa for L2, and 66.80 MPa for L3. On average, this laminate achieved a tensile strength of 67.23 MPa, which is approximately 62 % higher than the average value of hemp/glass laminate (41.58 MPa) and more than double that of the hemp/ramie/glass laminate (32.54 MPa).

The hemp/glass laminates exhibited moderate tensile strength values ranging from 39.40 MPa to 44.30 MPa, with an average value of 41.58 MPa. This performance is about 27 % lower than that of ramie/glass laminate but 28 % higher than that of the hemp/ramie/glass laminate. The hemp/ramie/glass laminates recorded the lowest tensile strength, varying from 30.02 MPa to 35.70 MPa, with an average of 32.54 MPa. This indicates a reduction of nearly 52 % compared to the ramie/glass laminates. In terms of tensile performance, the ramie/glass composite demonstrates superior strength compared to the ramie/hemp/glass hybrid laminate. This enhancement is primarily attributed to the inherently more tensile capacity of glass fiber reinforcement relative to natural reinforcement including ramie and hemp. Since the tensile characteristics of a laminate is predominantly governed by the mechanical characteristics of its reinforcing constituents, a greater proportion of glass fibers contributes to improved load-bearing capability. Furthermore, the interfacial bonding between the matrix and the fibers plays a critical role in tensile behavior. Glass fibers exhibit stronger suitability with epoxy resins, facilitating more efficient stress transfer across the interface. In contrast, natural fibers such as hemp and ramie tend to have weaker adhesion with the matrix, making them more susceptible to fiber pull-out under tensile loading. This interfacial limitation reduces the overall tensile capacity of hybrid laminates consisting of both ramie and jute fibers, as reported by Yang *et al.* [18]. The adoption of hybrid laminate materials has experienced notable growth, driven by their environmentally sustainable characteristics, including recyclability, biodegradability, and reduced ecological impact [19].

Table 2. Tensile strength values of various composites.

Laminates	Hemp/glass [MPa]	Ramie/glass [MPa]	Hemp/ramie/glass [MPa]
L1	41.05	73.10	35.70
L2	44.30	61.80	31.90
L3	39.40	66.80	30.02
Average	41.58	67.23	32.54
Standard deviation	2.49	5.68	2.91

4.2. Flexural behavior study

The flexural performance of the hybrid composite specimens was systematically evaluated, as presented in Table 3. During mechanical testing, the force–stroke response was recorded in real time, with representative curves illustrated in Fig. 5. A comparative analysis of the flexural strength across the various hybrid configurations is illustrated in Fig. 6. The outcomes indicate that composites reinforced with a combination of ramie, hemp, and glass fibers exhibit enhanced flexural resistance compared to those reinforced solely with hemp/glass or ramie/glass fiber systems. The flexural strength results show that the hemp/ramie/glass laminate achieve the highest strength with an average of 17.79 MPa, which is considered 100 % performance. In comparison, the ramie/glass laminate recorded an average of 9.74 MPa, corresponding to about 54.7 % of the maximum strength, while the hemp/glass laminate had the lowest avarage value of 8.49 MPa, equivalent to 47.7 % of the maximum strength.

TABLE 3. Flexural strength values of various composites.

Laminates	Hemp/glass [MPa]	Ramie/glass [MPa]	Hemp/ramie/glass [MPa]
L1	8.52	10.25	18.22
L2	8.88	8.89	17.74
L3	8.06	10.07	17.42
Average	8.49	9.74	17.79
Standard deviation	0.42	0.74	0.41

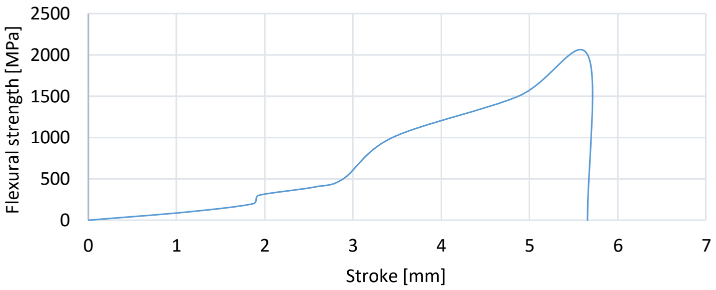

FIG. 5. Force-stroke curve obtained during flexural testing.

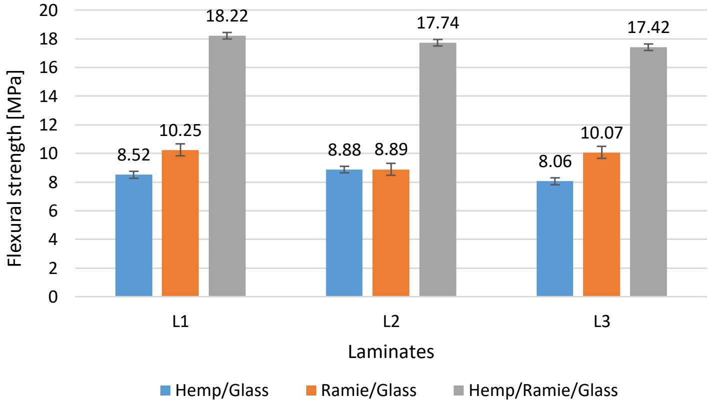

FIG. 6. Flexural strength performance of different hybrid fiber laminates.

The higher strength in the hemp/ramie/glass laminate is due to the synergistic effect of the three different fibers, where ramie adds stiffness, glass provides strength, and hemp improves flexibility, resulting in better stress distribution under bending loads. On the other hand, the hemp/glass laminate showed the lowest flexural strength because hemp fibers have relatively low stiffness, which limits their reinforcement capability. The ramie/glass laminate showed moderate strength, as ramie fibers have superior mechanical properties compared to hemp fibers; however, the absence of a third reinforcing fiber restricted its ability to distribute stress as effectively as the three-fiber hybrid laminate. The enhanced flexural and impact performance of the ramie/hemp/glass hybrid composites can further be attributed to the synergistic interaction among the constituent fibers. Each fiber type contributes distinct mechanical advantages: glass fibers impart high stiffness and impact resistance, while natural reinforcement such as hemp and ramie improve energy absorption and toughness.

These results exceed those reported by Sapuan *et al.* [2], where flexural strength values ranging from 0.3 kN/m^2 to 0.4 kN/m^2 were achieved in epoxy composites reinforced with woven banana fibers. The superior performance observed in the current study highlights the effectiveness of mixed-fiber configurations in enhancing flexural behavior. This multi-fiber architecture facilitates more uniform stress distribution under flexural and impact loading conditions. Additionally, the natural fibers play a critical role in bridging microcracks and inhibiting their propagation, thereby improving the composite's ability to resist deformation and absorb dynamic loads [20]. Moreover, the strategic layering of hemp, ramie, and glass fibers within the hybrid composite enhances load-transfer efficiency. This architecture proves especially advantageous under flexural stress, as the outer glass fiber layers deliver structural rigidity, while the inner natural fibers, namely ramie and hemp, offer improved toughness and ductility. The complementary roles of these fibers contribute to a more resilient and adaptable composite structure capable of withstanding bending forces with a reduced risk of failure.

4.3. Impact strength analysis of hybrid composites

This study incorporates impact testing using the Charpy technique to evaluate the load-bearing behavior and impact energy of several hybrid composite specimens. The absorbed energy was determined based on data recorded by the testing apparatus. Figure 7 illustrates the comparative impact strength across

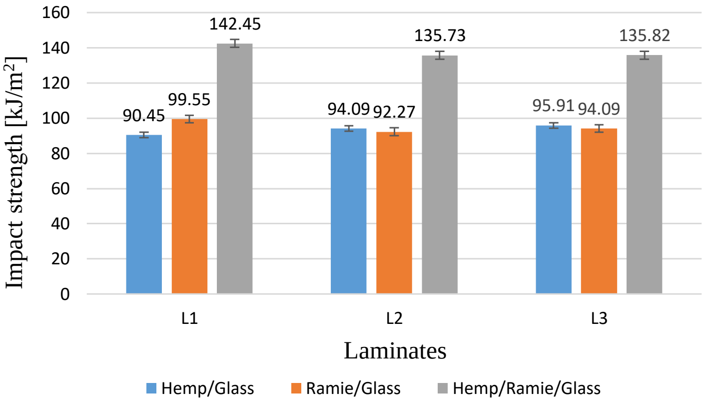

Fig. 7. Impact strength distribution among different hybrid laminate systems.

the different laminate configurations. Among them, the composite reinforced with hemp, ramie and glass fibers demonstrated superior impact resistance, reaching up to 142.45 kJ/m^2. Composites reinforced with glass and ramie fibers also showed comparable performance levels, as detailed in Table 4. Among the configurations, the hemp/ramie/glass composite demonstrated the highest impact resistance, with values ranging from 135.73 kJ/m^2 to 142.45 kJ/m^2, approximately 45 % to 50 % greater than the hemp/glass laminate and 40 % to 46 % higher than the ramie/hemp laminate. This enhanced performance is likely due to the combined effect of natural and synthetic fibers, which promotes better interfacial adhesion and improves the material's ability to absorb energy during sudden loading. Conversely, the hemp/glass laminate recorded the lowest impact strength, between 90.45 kJ/m^2 and 95.91 kJ/m^2, reflecting a reduction of about 36 % compared to the hemp/ramie/glass composite. This lower toughness may stem from the limited energy-dissipation capacity inherent to the dual-fiber system. The ramie/glass laminate exhibited intermediate values, ranging from 92.27 kJ/m^2 to 99.55 kJ/m^2, roughly 30 % to 33 % lower than those of the top-performing hybrid laminate. Its moderate behavior can be attributed to the predominance of natural fibers, which, although sustainable, offer lower resistance to crack propagation under impact loading. These findings underscore the effectiveness of integrating ramie fibers with hemp and glass fibers in enhancing the impact durability of epoxy-based hybrid laminates, making them promising candidates for implementations requiring high toughness and energy absorption. Natural fibers are increasingly being integrated into hybrid composite systems, offering a sustainable alternative to conventional materials. A growing body of research focuses on optimizing fiber hybridization to replace conventional metals and alloys in engineering advancements while maintaining structural integrity and cost efficiency. In the present study, composite laminates were fabricated by combining glass fibers with natural fibers such as ramie and hemp fibers. Test samples were subsequently prepared from these composites in accordance with ASTM standards to ensure consistency and reliability in mechanical evaluation. The hemp/ramie/glass fiber-reinforced composites developed in this study exhibited an impact strength of 142.45 kJ/m^2, closely aligning with the value

Table 4. Measured impact resistance across composite configurations.

Laminates	Hemp/glass [kJ/m^2]	Ramie/glass [kJ/m^2]	Hemp/ramie/glass [kJ/m^2]
L1	90.45	99.55	142.45
L2	94.09	92.27	135.73
L3	95.91	94.09	135.82
Average	93.48	95.30	138.00
Standard deviation	2.79	3.73	3.80

of 157.64 kJ/m^2 reported by BHOOPATHI *et al.* [23] and VENKATESHWARAN *et al.* [9] for banana-hemp-glass fiber laminates. This comparative performance underscores the mechanical robustness of the present hybrid configuration and reinforces its viability as a competitive alternative to previously investigated systems.

4.4. HARDNESS VALUE ANALYSIS

Figure 8 illustrates the Vickers hardness test results for composite specimens featuring various fiber combinations. Among the tested configurations, the ramie fiber-reinforced polymer composite exhibited the highest hardness value, reaching 27.73 HV. This performance notably surpasses that of the other laminates, as detailed in Table 5, thereby highlighting the effectiveness of ramie fibers in enhancing surface resistance. The hardness assessment revealed that the ramie/glass laminate exhibited the highest values, ranging from 26.12 HV to 27.73 HV, approximately 35 % to 40 % greater than that of the hemp/glass configuration and around 30 % higher than that the hemp/ramie/glass variant. This enhanced surface resistance is likely attributed to the robust interfacial bonding between ramie and glass fibers, which effectively limits localized defor-

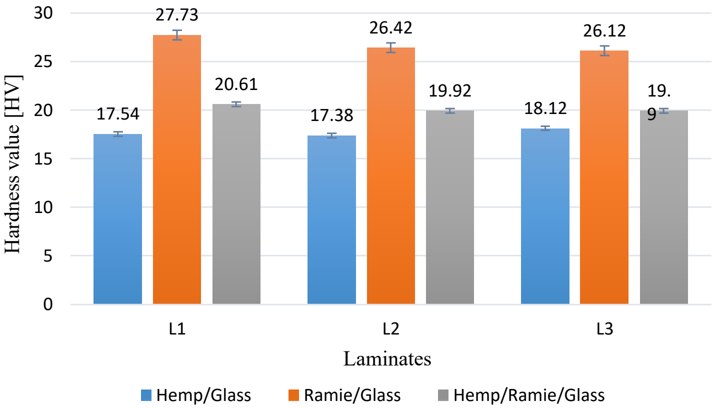

FIG. 8. Hardness performance of various hybrid composites.

TABLE 5. Hardness performance of hybrid composites.

Laminates	Hemp/glass [HV]	Ramie/glass [HV]	Hemp/ramie/glass [HV]
L1	17.54	27.73	20.61
L2	17.38	26.42	19.92
L3	18.12	26.12	19.90
Average	17.68	26.76	20.14
Standard deviation	0.39	0.83	0.40

mation under load. The hemp/ramie/glass laminate demonstrated intermediate hardness values, measured between 19.90 HV and 20.61 HV. While these values are 25 % to 28 % lower than those of the ramie/glass laminate, they remain 10 % to 15 % higher than those of the hemp/glass laminate. This moderate performance reflects the composite's balanced fiber architecture, where the reinforcing effect of ramie and glass fibers is partially offset by the relatively lower stiffness of hemp fibers. Among the tested laminates, the hemp/glass laminate recorded the lowest hardness, with values ranging from 17.38 HV to 18.12 HV approximately 36 % lower than those of the ramie/glass laminates and 10 % lower than the hybrid containing all three fibers. The reduced hardness is primarily due to the limited interfacial bonding and lower mechanical rigidity of hemp fibers, which restrict the material's resistance to indentation and surface wear. These findings suggest that the ramie/glass composites are particularly well suited for applications demanding high surface durability and resistance to concentrated mechanical stresses (see Table 6).

Table 6. Comparative values of tensile strength, flexural strength, impact resistance, and hardness for selected composites.

Composite type	Tensile behavior [MPa]	Flexural behavior [MPa]	Impact resistance [kJ/m^2]	Micro-hardness [HV]
Glass/ramie fiber-reinforced composite	73.10	10.25	99.55	27.73
Glass/hemp fiber-reinforced composite	44.30	8.88	95.91	18.12
Glass/hemp/ramie fiber-reinforced composite	35.70	18.22	142.45	20.61

4.5. Statistical analysis using one-way ANOVA

To evaluate whether the observed differences in tensile behavior, flexural behavior, impact resistance, and microhardness across the three composites are statistically significant one-way ANOVA was applied, and the corresponding F-statistics and p-values were computed to evaluate the significance of observed differences. A comprehensive overview of the statistical parameters is provided in Table 7.

4.5.1. Hypotheses

Null hypothesis (H_0): the mean values of mechanical properties such as tensile behavior, flexural behavior, impact resistance, and microhardness were found

Table 7. One-way ANOVA descriptive statistics for mechanical properties.

Property	Count	Mean value	Standard deviation (SD)	Minimum	25th percentile (Q1)	Median	75th percentile (Q3)	Maximum
Tensile behavior [MPa]	3	51.47	22.00	29.00	40.24	51.47	62.70	73.10
Flexural behavior [MPa]	3	12.15	6.00	6.00	9.08	12.15	15.22	18.22
Impact resistance [kJ/m^2]	3	95.30	47.15	47.15	71.23	95.30	119.37	142.45
Micro-hardness [HV]	3	18.61	9.12	9.12	13.86	18.61	23.47	27.73

to be similar across all composite types, indicating that the type of composite had no significant effect.

Alternative hypothesis (H_1): at least one composite type shows a statistically pronounced disparity in the mean values of the mechanical properties, suggesting that composite type influences the mechanical response.

4.6. MICROSTRUCTURE OF HYBRID FIBER-REINFORCED COMPOSITES

Hemp fibers are extracted from the matrix, leaving holes or cavities on the fracture surface, and glass fibers may remain partially bonded or protruding. The softer epoxy matrix surrounding hemp fibers cracks more easily, and gaps appear between fiber and matrix where debonding has occurred. The fracture is usually non-planar, hemp-rich regions show shear failure (diagonal cracking) while glass-rich regions show more brittle fracture with fiber breakage, as shown in Fig. 9a. Some ramie and glass fibers show clean breaks (transverse cracks), while others exhibit partial pull-out with attached matrix resin on the fiber surface, indicating strong fiber–matrix bonding. Fine cracks in the matrix radiate from broken fiber ends; voids or stress concentrations appear where fibers have debonded. Ramie/glass composites typically show flatter fracture surfaces than hemp/glass composites, with visible layering and fiber alignment dependent on the stacking sequence, as depicted in Fig. 9b. Figure 9c shows fiber pull-out, matrix crazing, rough texture, multiple microcracks radiating from hemp fiber breaks. A sharp, brittle transverse fracture is observed, with minimal pull-out, clean glass fiber ends, and little to no matrix deformation around glass fibers. Ramie and glass show good adhesion (resin attached to fiber), while hemp shows weaker adhesion [24, 25].

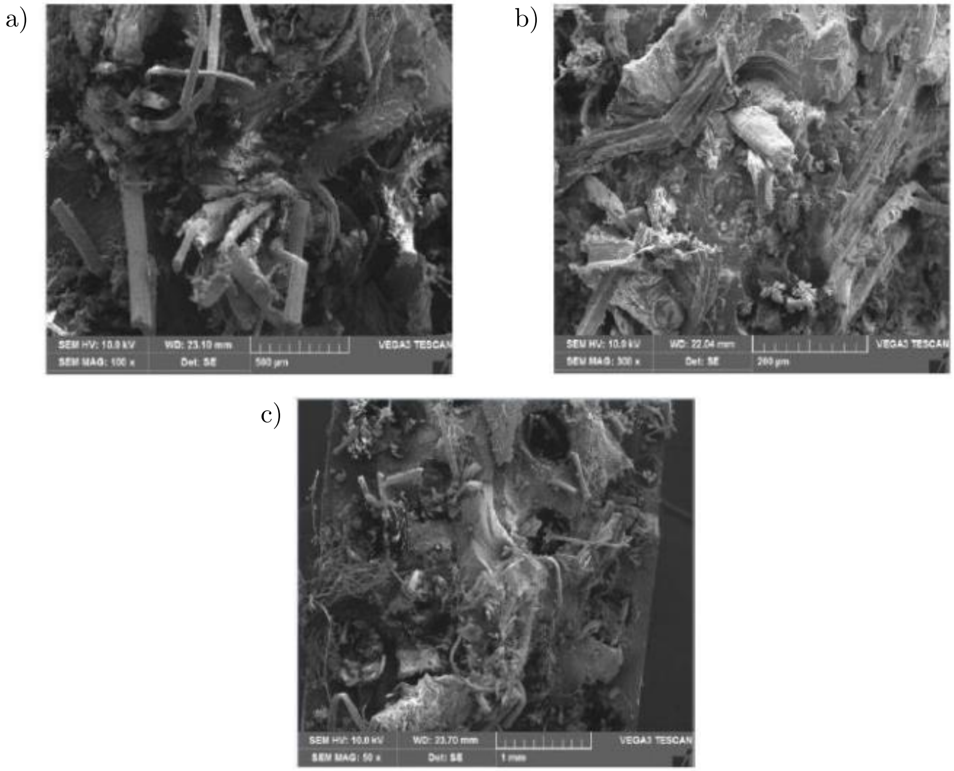

Fig. 9. SEM images of various hybrid composites:
a) hemp/glass, b) ramie/glass, c) hemp/ramie/glass.

5. RESULTS

The calculated p-value is 0.0025, which is less than the established level of significance (0.05); therefore, the findings reject null hypothesis. This means that differences observed in mechanical characteristics, such as tensile behavior, flexural behavior, impact resistance, and hardness, among the various composite types are statistically significant. This result gives confidence that these variations may be due to fiber types rather than random variation.

6. OVERALL SUMMARY AND INTERPRETATIONS

This study compared the mechanical characteristics: tensile behavior, flexural behavior, impact resistance, and microhardness of different hybrid composites made from glass/ramie, glass/hemp, and glass/hemp/ramie fibers. The tensile strength was highest in the glass/ramie composite (73.10 MPa), followed by glass/hemp (44.30 MPa), while the glass/hemp/ramie hybrid showed the lowest value (35.70 MPa). In contrast, flexural strength peaked in the glass/hemp/ramie hybrid (18.22 MPa), outperforming both glass/ramie and glass/hemp variants (10.25 MPa and 8.88 MPa, respectively). Impact strength exhibited a similar trend, with the glass/hemp/ramie composite achieving a significantly higher value (142.45 kJ/m^2) compared to glass/ramie composite (99.55 kJ/m^2) and glass/hemp composite (95.91 kJ/m^2). Hardness was greatest in the glass/ramie composite (27.73 HV), moderate in the hybrid (20.61 HV), and lowest in the glass/hemp configuration (18.12 HV). Statistical analysis using one-way ANOVA confirmed that the differences in flexural behavior, impact behavior, and microhardness across the composite types were statistically significant ($p < 0.05$), while variations in tensile strength were less pronounced. The outcomes emphasize the impact of fiber hybridization on mechanical performance and highlight the potential of multi-fiber composites for tailoring properties for specific engineering applications.

FUNDINGS

This research did not receive any specific grant from funding agencies in the public, commercial, or not-for-profit sectors.

CONFLICT OF INTEREST

The authors declare that there are no known competing financial interests or personal relationships that could have influenced the work described in this paper.

AUTHORS' CONTRIBUTIONS

Sadashiva Kemparaju: conceptualization, methodology, and writing – original draft preparation. Bhanu Prathap Rangaswamy: methodology and writing – review and editing. Balaji Javaraiah: validation, resources, and writing – review and editing. Shwetha Mahadev, Rathika Murugan, Tarakeshwar Jane: resources and literature survey. All authors reviewed and approved the final manuscript.

ACKNOWLEDGMENTS

The author gratefully acknowledges the Mechanical Engineering Department of Dr. Ambedkar Institute of Technology, Bengaluru, for offering the necessary research facilities and support that enabled the successful completion of this study.

References

1. Kemparaju S., Ganapathi S., Kemparaju R., Venkatrao S., Yagappa S., Experimental and validation of the mechanical characteristics of bio based hybrid composites, *Environmental Engineering & Management Journal*, **23**(1): 61–69, 2024, http://doi.org/10.30638/eemj.2024.006.

2. Sapuan S., Leenie A., Harimi M., Beng Y.K., Mechanical properties of woven banana fiber reinforced epoxy composites, *Materials & Design*, **27**(8): 689–693, 2006, https://doi.org/10.1016/j.matdes.2004.12.016.

3. Aravinth K., Sathish K., Ramakrishnan T., Balu Mahandiran S., Shiyam Sundhar S., Mechanical and thermal behavior of aligned coir fiber reinforced epoxy composites based on fiber orientation, fiber length, and fiber volume fraction, *Materials Today: Proceedings*, 2023, http://doi.org/10.1016/j.matpr.2023.05.436.

4. Kandola B.K., Pornwannachai W., Weclawski B., Ebdon J.R., Fully bio-based flax/furan versus carbon/glass epoxy composites: Scope and limitations in terms of fire, mechanical and thermal performances, *Polymer Composites*, **45**(12): 11004–11021, 2021, https://doi.org/10.1002/pc.28527.

5. Thapiyal D., Verma S., Sen P., Kumar R., Thakur A., Tiwari A.K., Singh D., Verros G.D., Kumar Arya R., Natural fibers composites: Origin, importance, consumption pattern, and challenges, *Journal of Composites Science*, **7**(12): 506, 2023, http://doi.org/10.3390/jcs7120506.

6. Mahakur V.K., Bhowmik S., Patowari P.K., Machining parametric study on the natural fiber reinforced composites: A review, *Proceedings of the Institution of Mechanical Engineers, Part C: Journal of Mechanical Engineering Science*, **236**(11): 6232–6249, 2021, https://doi.org/10.1177/09544062211063752.

7. Islam M.Z., Sabir E.C., Syduzzaman M., Experimental investigation of mechanical properties of jute/hemp fibers reinforced hybrid polyester composites, *SPE Polymers*, **5**(2): 192–205, 2023, https://doi.org/10.1002/pls2.10119.

8. Manjesh M., Palanikumar K., Reddy K.H., Comparative evaluation on properties of hybrid glass fiber-sisal/jute reinforced epoxy composites, *Procedia Engineering*, **51**: 745–750, 2023, https://doi.org/10.1016/j.proeng.2013.01.106.

9. Venkateshwaran N., ElayaPerumal A., Alavudeen A., Thiruchitrambalam M., Mechanical and thermal behavior evaluation of banana/sisal reinforced hybrid composites, *Materials & Design*, **32**(7): 4017–4021, 2011, http://doi.org/10.1016/j.matdes.2011.03.002.

10. Sadashiva K., Purushothama K.M., Physical and mechanical properties of bio based natural hybrid composites, *Journal of Materials and Environmental Science*, **14**(1): 131–140, 2023.

11. Ramesh M., Palanikumar K., Reddy K.H., Mechanical property evaluation of sisal–jute–glass fiber reinforced polyester composites, *Composites Part B: Engineering*, **48**: 1–9, 2012, https://doi.org/10.1016/j.compositesb.2012.12.004.

12. Yuanjian T., Isaac D., Impact and fatigue behaviour of hemp fibre composites, *Composites Science and Technology*, **67**(15–16): 3300–3307, 2007, http://doi.org/10.1016/j.compscitech.2007.03.039.

13. Bledzki A.K., Mamun A.A., Faruk O., Abaca fibre reinforced PP composites and comparison with jute and flax fibre PP composites, *Express Polymer Letters*, **1**(11): 755–762, 2007, http://doi.org/10.3144/expresspolymlett.2007.104.
14. Kobayashi S., Takada K., Nakamura R., Processing and characterization of hemp fiber textile composites with micro-braiding technique, *Composites Part A: Applied Science and Manufacturing*, **59**: 1–8, 2014, https://doi.org/10.1016/j.compositesa.2013.12.009.
15. Kabir M.M., Wang H., Lau K.T., Cardona F., Tensile properties of chemically treated hemp fibres as reinforcement for composites, *Composites Part B: Engineering*, **53**: 362–368, 2013, http://doi.org/10.1016/j.compositesb.2013.04.087.
16. Aristri M.A. *et al.*, Thermal and mechanical performance of ramie fibers modified with polyurethane resins derived from acacia mangium bark tannin, *Journal of Materials Research and Technology*, **18**: 2413–2427, 2022, https://doi.org/10.1016/j.jmrt.2022.03.131.
17. Torres-Arellano M., Renteria-Rodríguez V., Franco-Urquiza E., Mechanical properties of natural-fibre-reinforced bio-based epoxy resins manufactured by resin infusion process, *Polymers*, **12**(12): 2841, 2020, http://doi.org/10.3390/polym12122841.
18. Yang H. *et al.*, Load-bearing capacity and failure mechanism of integrated fluted-core composite sandwich cylinders, *Composites Science and Technology*, **221**: 109344, 2022, http://doi.org/10.1016/j.compscitech.2022.109344.
19. Sahari I., Sapuan S.M., Natural fibre reinforced biodegradable polymer composites, *Reviews on Advanced Materials Science*, **30**: 166–174, 2011.
20. Savastano J.Jr., Santos S.F., Radonjic M., Soboyejo W.O., Fracture and fatigue of natural fiber-reinforced cementitious composites, *Cement and Concrete Composites*, **31**(4): 232–243, 2009, http://doi.org/10.1016/j.cemconcomp.2009.02.006.
21. ASTM, *ASTM D790: Standard test methods for flexural properties of unreinforced and reinforced plastics and electrical insulating materials*, Annual Book of ASTM Standards, 1997.
22. ASTM, *ASTM D638-14: Standard test method for tensile properties of plastics*, ASTM International, 2014.
23. Bhoopathi R., Ramesh M., Deepa C., Fabrication and property evaluation of banana-hemp-glass fiber reinforced composites, *Procedia Engineering*, **97**: 2032–2041, 2014, https://doi.org/10.1016/j.proeng.2014.12.446.
24. Sadashiva K., Sarvamangala S.P., Shanshanka G., Tarakeshwar J., Pradeep Kumar P., Mechanical, tribological and morphological characteristics of glass and jute reinforced epoxy hybrid composite, *Journal of Materials and Environmental Science*, **15**(5): 700–711, 2024.
25. Prasad L., Kapri P., Patel R.V., Yadav A., Winczek J., Physical and mechanical behavior of ramie and glass fiber reinforced epoxy resin-based hybrid composites, *Journal of Natural Fibers*, **20**(2): 2234080, 2023, https://doi.org/10.1080/15440478.2023.2234080.

Received September 25, 2025; accepted December 15, 2025;
available online December 18, 2025; version of record June 8, 2026;
published issue June 24, 2026.

Engineering Transactions, **74**(2): 267–292, 2026, https://doi.org/10.24423/engtrans.2026.3641
Institute of Fundamental Technological Research Polish Academy of Sciences (IPPT PAN)
Université de Lorraine • Poznan University of Technology

Research Paper

Global Buckling of a Thin-Walled T-Frame with Consideration of the Shear Effect

Krzysztof MAGNUCKI[1], Paweł JASION[2]*

[1] *Łukasiewicz Research Network – Poznan Institute of Technology*
Poznań, Poland

[2] *Institute of Applied Mechanics, Poznan University of Technology*
Poznań, Poland

*Corresponding Author: pawel.jasion@put.poznan.pl

This work concerns a global elastic buckling problem of a thin-walled T-frame with consideration of the shear effect. A novel approach was used to account for this effect, namely, the non-linear shear deformation theory, which gives as a result the shear deformation function describing the behaviour of the beam cross section. This thin-walled T-frame consists of a horizontal beam and a vertical column made of the same standard H-beams. The shape of this standard H-beam and the dimensionless deformation function of the plane cross section, being the result of the shear effect, are analytically described. The buckling problem of the frame is analytically formulated and solved. The critical loads of exemplary beams are analytically determined. Moreover, a numerical model, based on the finite element method (FEM), of the frame is elaborated and the critical loads of exemplary frames are determined. Consequently, the research results obtained by both methods are compared, and the advantages of the proposed approach are discussed.

Keywords: elastic buckling, frame, H-beam, thin-walled beam, shear effect.

1. INTRODUCTION

Thin-walled beams used in the 20th century are still commonly used today, for example, in vehicles and steel building structures. They are parts of frames containing from several to several dozen beams. Particular beams may be subjected to different types of loading such as compression, torsion or bending; however usually a complex state of stress in each beam is present. For this reason, an effective tool is needed to analyse the state of stress in the beam, the phenomena occurring at the joints between beams as well as the influence of individual beams on each other. A detailed description of the strength and stability problems of thin-walled beams and selected structures is provided by Trahair *et al.* [1]. The authors described in detail problems related to tension and compression members, local buckling of thin-plate elements, bending and lateral buckling of beams, beam-columns, frames, joints, and torsion members.

The application of the generalised beam theory (GBT) to the analysis of thin-walled frames is presented by Basaglia *et al.* [2]. The buckling analysis of frames made of U- and I-sections is discussed, including problems related to joints. These considerations are continued in the paper by Basaglia *et al.* [3]. Here, local and distortional buckling are also studied. Exemplary calculations are made for L-shaped and portal frames made of open cross-section beams. The possibility of applying GBT-based finite element (FE) calculations to the analysis of frames made of thin-walled members of different cross sections is reported by Camotim *et al.* [4]. The analyses are extended to the non-linear range and the results are compared with those given by the commercial ANSYS code. Possible future developments of the proposed method are also discussed.

The behaviour of frames made of thin-walled members is influenced by the behaviour of their individual elements, i.e., a single beam. For this reason, an optimal shape of the cross section is sought that will provide the highest stiffness and resistance to buckling. Examples of atypical cross sections are presented by Magnucka-Blandzi and Magnucki [5]. Different types of channel beams are considered. An analytical formula for the critical stress is obtained followed by an optimisation process showing the relation between the geometrical dimensions of the cross section and the critical stress. For selected beams experimental results are shown.

Rectangular frames are parts of vehicle structures and thus subjected to combined loading, mainly bending and torsional moments. The analytical description of the global buckling of such frame made of thin-walled open cross sections is described by Magnucki and Milecki [6]. The critical values of the forces loading the frame in its plane are determined. The obtained results are compared with those from the finite element method (FEM). Stable and unstable regions of the structure are defined plots.

Large frames in the form of spatial structures are used in construction engineering, e.g., as supporting structures for warehouses. The behaviour of such large frames is analysed by Nagy *et al.* [7]. Three variants of the frame are modelled: a bare frame, a frame with a roof made of trapezoidal sheeting and a frame with a roof made of sandwich panels. Numerical analyses are performed and the differences in the behaviour of these three frames are discussed. The buckling length coefficient for frames was calculated by Krystosik [8] using three different approaches. The author concluded that the recommendations of the American and European codes, due to assumed simplifications, provide inaccurate results when compared with the FE approach. Thin-walled frames are also analysed by Zhang *et al.* [9]. A new approach is proposed in which the failure criteria is based on the sum of the structural exponential strain energy density. The buckling of frames and arches made of I cross sections is investigated by Liu *et al.* [10]. An analytical approach based on virtual work is applied to determine the critical loads for different geometries of structures. Different formulations of the joints between particular beams are considered. The effectiveness of the proposed solutions is proved by comparing the results with those obtained by the FEM.

One of the most popular shapes of the beam is the H-section, since it is the most effective one when bending load is considered. The H-section beam under unequal end bending moments is investigated by Giżejowski *et al.* [11]. The influence of the slenderness of the element and moment distribution on the critical state is analysed analytically. Two examples of frames made of H-section and circular section are considered loaded with a static and dynamic loading. The stability of columns and beams with H- and box-sections is analysed by Zhou *et al.* [12]. In the paper, the authors propose a beam-column element with a plastic hinge included making it possible to analyse global and local buckling. Only a single element is needed to predict the load-bearing capacity of columns and frames. Plane frames made of I-sections are investigated analytically by Wen *et al.* [13]. A new comprehensive approach based on the potential energy method is proposed. Different formulas are used to compare their effectiveness in determining the deformation of frames after the loss of stability. An numerical approach to the stability analysis of I-beam is presented by Yang *et al.* [14]. A 1D FE is proposed to solve local and global buckling problems.

Crucial importance for the load-carrying capacity of frames has the connection between particular beam-columns. Such a connection, in the form of K-shaped braced shear panel, is investigated in the paper by Xiang *et al.* [15]. The proposed new connection system is tested in laboratory under seismic load and its ability to dissipate energy is analysed. Experimental tests of frames are also described by Jůza *et al.* [16]. A number of tests are carried out for portal frames made of cold-rolled hollow sections. The influence of material nonlinearity on the deflection of frames is shown. The results are also compared with those from the FE analyses.

If a frame is composed of beams whose thickness is not small or beams that are short, shear stresses play a significant role. The analysis of these stresses is especially important when multilayered beams are considered. An example of research in this area is the work by Magnucki [17]. The author compares the classical zig-zag theory with a new proposal of nonlinear shear deformation theory. It is shown that the stress distribution differs significantly between models based on the two theories. The proposed approach refines the shear effect in multilayered beams. The same theory was applied to analyse the vibrations of wide-flange H-beam in [18]. The shear coefficient is derived analytically, which refines the formula for natural frequencies. It was shown that this coefficient should be taken into account for short beams, and its application reduces the value of the natural frequency.

In the present paper, the research on the application of the nonlinear shear deformation theory described by MAGNUCKI [17, 18] is continued. Here, the theory is applied to a thin-walled T-frame, shown in Fig. 1a, made of a horizontal H-beam of length L_1 and vertical H-beam-column of length L_2 rigidly connected together. The joint connecting the two beams of the T-frame is shown in Fig. 1b, where the dimensions of the H-section are presented that is the height of the web – h, and the width of the flange – b.

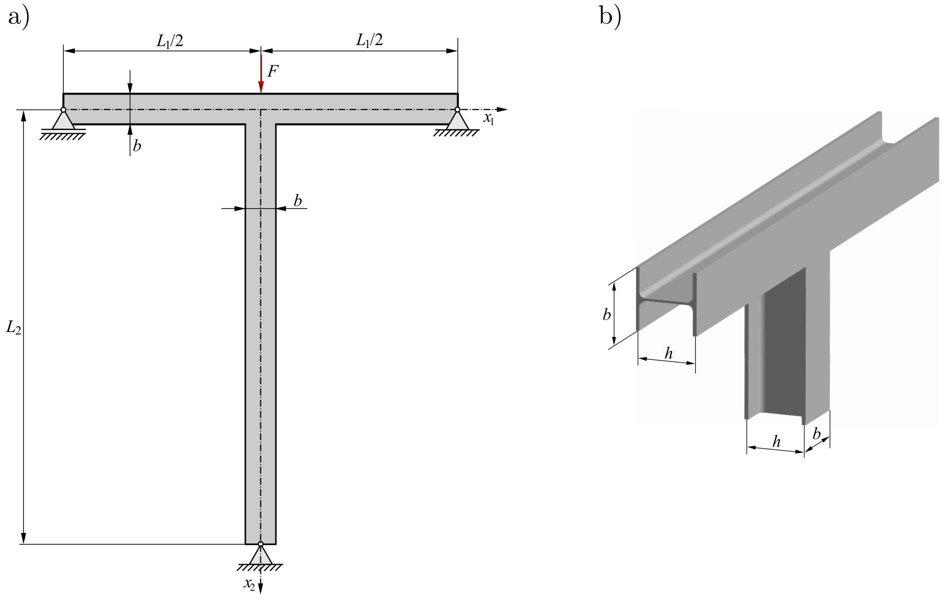

FIG. 1. Scheme of a thin-walled T-frame loaded with a force F.

The main goal of the paper is analytical and numerical FEM study of the elastic global buckling problem of the T-frame under the action of force F applied along the centroidal axis of the column.

2. ANALYTICAL MODEL OF THE H-BEAM

The detailed cross section of the H-beam is shown in Fig. 2. The thickness of the flange equals t_f and the thickness of the web is b_0. The radius between particular parts of the cross section is equal to r.

The analytical description of this cross section is formulated with consideration of the following dimensionless quantities: $\eta = y/b$ – coordinate, $\beta_0 = b_0/b$,

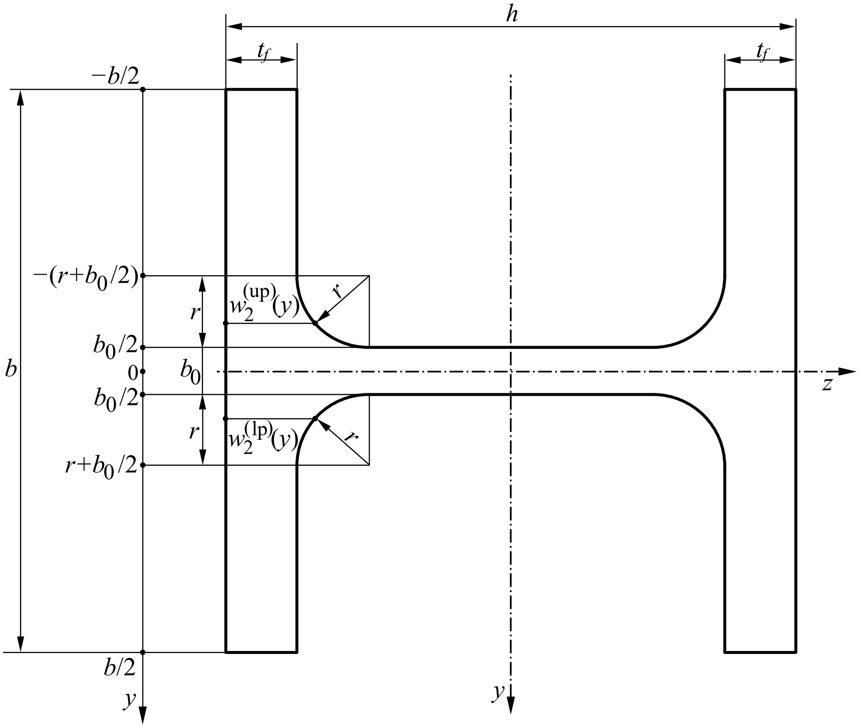

FIG. 2. Scheme of the H-beam cross section.

$\chi_f = t_f/b$, $\rho = r/b$ – dimensionless parameters. Thus, the dimensionless widths $\overline{w}$ of the successive parts:

– the first interval of the upper part $-1/2 \le \eta \le -(\rho + \beta_0/2)$:

$$\overline{w}_1^{(\mathrm{up})}(\eta) = \frac{w_1^{(\mathrm{up})}(\eta)}{b} = 2\chi_f, \tag{2.1}$$

– the second interval of the upper part $-(\rho + \beta_0/2) \le \eta \le -\beta_0/2$:

$$\overline{w}_2^{(\mathrm{up})}(\eta) = \frac{w_2^{(\mathrm{up})}(\eta)}{b} = 2\left\{\chi_f + \rho - \sqrt{-\left(\eta + \frac{1}{2}\beta_0\right)\left(\eta + 2\rho + \frac{1}{2}\beta_0\right)}\right\}, \tag{2.2}$$

– the middle part $-\beta_0/2 \le \eta \le \beta_0/2$:

$$\overline{w}^{(\mathrm{mp})}(\eta) = \frac{w^{(\mathrm{mp})}(\eta)}{b} = \frac{h}{b}, \tag{2.3}$$

– the second interval of the lower part $\beta_0/2 \le \eta \le \rho + \beta_0/2$:

$$\overline{w}_2^{(\mathrm{lp})}(\eta) = \frac{w_2^{(\mathrm{lp})}(\eta)}{b} = 2\left\{\chi_f + \rho - \sqrt{\left(\eta - \frac{1}{2}\beta_0\right)\left(-\eta + 2\rho + \frac{1}{2}\beta_0\right)}\right\}, \tag{2.4}$$

– the first interval of the lower part $\rho+\beta_0/2 \le \eta \le 1/2$:

$$\overline{w}_1^{(\mathrm{lp})}(\eta) = \frac{w_1^{(\mathrm{lp})}(\eta)}{b} = 2\chi_f. \tag{2.5}$$

The defined dimensionless widths allow the calculation of geometrical parameters of the cross section, that is, the first moment, necessary for calculated shears stress.

The scheme of the planar cross section deformation of this H-beam after bending-buckling is graphically presented in Fig. 3.

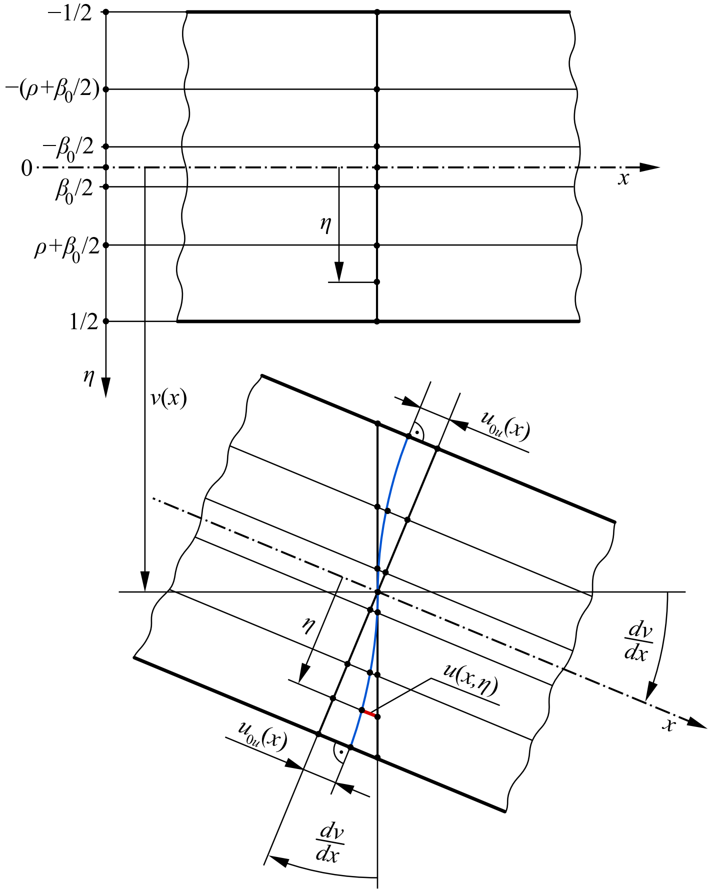

FIG. 3. Scheme of the planar cross section deformation of the H-beam.

The longitudinal displacements u, based on the scheme (Fig. 3), and consequently the normal ε_x and shear γ_{xy} strains, as well as normal σ_x and shear τ_{xy} stresses in the successive parts are as follows:

– the first interval of the upper part $-1/2 \leq \eta \leq -(\rho + \beta_0/2)$:

$$u_1^{(up)}(x,\eta) = -b\left[\eta\frac{dv}{dx} - f_{d1}^{(up)}(\eta)\psi(x)\right], \tag{2.6}$$

$$\varepsilon_{x1}^{(\mathrm{up})}(x,\eta) = -b\left[\eta\frac{d^2v}{dx^2} - f_{d1}^{(\mathrm{up})}(\eta)\frac{d\psi}{dx}\right], \tag{2.7}$$

$$\gamma_{xy1}^{(\mathrm{up})}(x,\eta) = \frac{df_{d1}^{(\mathrm{up})}}{d\eta}\psi(x), \tag{2.8}$$

$$\sigma_{x1}^{(\mathrm{up})}(x,\eta) = E\varepsilon_{x1}^{(\mathrm{up})}(x,\eta), \tag{2.9}$$

$$\tau_{xy1}^{(\mathrm{up})}(x,\eta) = \frac{E}{2(1+\nu)}\gamma_{xy1}^{(\mathrm{up})}(x,\eta), \tag{2.10}$$

– the second interval of the upper part $-(\rho + \beta_0/2) \leq \eta \leq -\beta_0/2$:

$$u_2^{(\mathrm{up})}(x,\eta) = -b\left[\eta\frac{dv}{dx} - f_{d2}^{(\mathrm{up})}(\eta)\psi(x)\right], \tag{2.11}$$

$$\varepsilon_{x2}^{(\mathrm{up})}(x,\eta) = -b\left[\eta\frac{d^2v}{dx^2} - f_{d2}^{(\mathrm{up})}(\eta)\frac{d\psi}{dx}\right], \tag{2.12}$$

$$\gamma_{xy2}^{(\mathrm{up})}(x,\eta) = \frac{df_{d2}^{(\mathrm{up})}}{d\eta}\psi(x), \tag{2.13}$$

$$\sigma_{x2}^{(\mathrm{up})}(x,\eta) = E\varepsilon_{x2}^{(\mathrm{up})}(x,\eta), \tag{2.14}$$

$$\tau_{xy2}^{(\mathrm{up})}(x,\eta) = \frac{E}{2(1+\nu)}\gamma_{xy2}^{(\mathrm{up})}(x,\eta), \tag{2.15}$$

– the middle part $-\beta_0/2 \leq \eta \leq \beta_0/2$:

$$u^{(\mathrm{mp})}(x,\eta) = -b\left[\eta\frac{dv}{dx} - f_d^{(\mathrm{mp})}(\eta)\psi(x)\right], \tag{2.16}$$

$$\varepsilon_x^{(\mathrm{mp})}(x,\eta) = -b\left[\eta\frac{d^2v}{dx^2} - f_d^{(\mathrm{mp})}(\eta)\frac{d\psi}{dx}\right], \tag{2.17}$$

$$\gamma_{xy}^{(\mathrm{mp})}(x,\eta) = \frac{df_d^{(\mathrm{mp})}}{d\eta}\psi(x), \tag{2.18}$$

$$\sigma_x^{(\mathrm{mp})}(x,\eta) = E\varepsilon_x^{(\mathrm{mp})}(x,\eta), \tag{2.19}$$

$$\tau_{xy}^{(\mathrm{mp})}(x,\eta) = \frac{E}{2(1+\nu)}\gamma_{xy}^{(\mathrm{mp})}(x,\eta), \tag{2.20}$$

– the second interval of the lower part $\beta_0/2 \le \eta \le \rho + \beta_0/2$:

$$u_2^{(\mathrm{lp})}(x,\eta) = -b\left[\eta\frac{dv}{dx} - f_{d2}^{(\mathrm{lp})}(\eta)\psi(x)\right], \tag{2.21}$$

$$\varepsilon_{x2}^{(\mathrm{lp})}(x,\eta) = -b\left[\eta\frac{d^2v}{dx^2} - f_{d2}^{(\mathrm{lp})}(\eta)\frac{d\psi}{dx}\right], \tag{2.22}$$

$$\gamma_{xy2}^{(\mathrm{lp})}(x,\eta) = \frac{df_{d2}^{(\mathrm{lp})}}{d\eta}\psi(x), \tag{2.23}$$

$$\sigma_{x2}^{(\mathrm{lp})}(x,\eta) = E\varepsilon_{x2}^{(\mathrm{lp})}(x,\eta), \tag{2.24}$$

$$\tau_{xy2}^{(\mathrm{lp})}(x,\eta) = \frac{E}{2(1+\nu)}\gamma_{xy2}^{(\mathrm{lp})}(x,\eta), \tag{2.25}$$

– the first interval of the lower part $\rho + \beta_0/2 \le \eta \le 1/2$:

$$u_1^{(\mathrm{lp})}(x,\eta) = -b\left[\eta\frac{dv}{dx} - f_{d1}^{(\mathrm{lp})}(\eta)\psi(x)\right], \tag{2.26}$$

$$\varepsilon_{x1}^{(\mathrm{lp})}(x,\eta) = -b\left[\eta\frac{d^2v}{dx^2} - f_{d1}^{(\mathrm{lp})}(\eta)\frac{d\psi}{dx}\right], \tag{2.27}$$

$$\gamma_{xy1}^{(\mathrm{lp})}(x,\eta) = \frac{df_{d1}^{(\mathrm{lp})}}{d\eta}\psi(x), \tag{2.28}$$

$$\sigma_{x1}^{(\mathrm{lp})}(x,\eta) = E\varepsilon_{x1}^{(\mathrm{lp})}(x,\eta), \tag{2.29}$$

$$\tau_{xy1}^{(\mathrm{lp})}(x,\eta) = \frac{E}{2(1+\nu)}\gamma_{xy1}^{(\mathrm{lp})}(x,\eta), \tag{2.30}$$

where $f_{d1}^{(\mathrm{up})}(\eta)$, $f_{d2}^{(\mathrm{up})}(\eta)$, $f_{d}^{(\mathrm{mp})}(\eta)$, $f_{d2}^{(\mathrm{lp})}(\eta)$, $f_{d1}^{(\mathrm{lp})}(\eta)$ are unknown dimensionless deformation functions, $v(x)$ is the deflection function, u_{0u} is the longitudinal displacement of the outside surfaces of the beam, $\psi(x) = u_{0u}/h$ is the dimensionless shear effect function, E is Young's modulus, and ν is Poisson's ratio.

The unknown dimensionless deformation functions are analytically derived in the successive parts and presented further. They are obtained by equating the shear stresses formulated above with Zhuravsky's classical shear stress formula and by taking into account the first moment of the cross section of the beam. Details of this procedure can be found in [17, 18]. Thus, for particular parts of the cross section there are:

– the first interval of the upper part $-1/2 \leq \eta \leq -(\rho + \beta_0/2)$:

$$f_{d1}^{(\mathrm{up})}(\eta) = -C_f + \frac{1}{8}\left(1 - \frac{4}{3}\eta^2\right)\eta, \tag{2.31}$$

– the second interval of the upper part $-(\rho + \beta_0/2) \leq \eta \leq -\beta_0/2$:

$$f_{d2}^{(\mathrm{up})}(\eta) = -C_{up} - C_{p2} + \int\limits_{-(\rho+\beta_0/2)}^{\eta} \frac{\overline{S}_{z2}^{(\mathrm{up})}(\eta)}{\overline{w}_2^{(\mathrm{up})}(\eta)} d\eta, \tag{2.32}$$

– the middle part $-\beta_0/2 \leq \eta \leq \beta_0/2$:

$$f_d^{(\mathrm{mp})}(\eta) = \frac{1}{24}\left(24\frac{b}{h}C_{sz2} + 3\beta_0^2 - 4\eta^2\right)\eta, \tag{2.33}$$

– the second interval of the lower part $\beta_0/2 \leq \eta \leq \rho + \beta_0/2$:

$$f_{d2}^{(\mathrm{lp})}(\eta) = C_{p2} + \int\limits_{\beta_0/2}^{\eta} \frac{\overline{S}_{z2}^{(lp)}(\eta)}{\overline{w}_2^{(\mathrm{lp})}(\eta)} d\eta, \tag{2.34}$$

– the first interval of the lower part $\rho + \beta_0/2 \leq \eta \leq 1/2$:

$$f_{d1}^{(\mathrm{lp})}(\eta) = C_f + \frac{1}{8}\left(1 - \frac{4}{3}\eta^2\right)\eta, \tag{2.35}$$

where the dimensionless coefficients are as follows:

$$C_{sz2} = \frac{1}{4}\left[1 - 4\left(\rho + \frac{1}{2}\beta_0^2\right)\right]\chi_f + \int\limits_{-(\rho+\beta_0/2)}^{-\beta_0/2} \overline{w}_2^{\mathrm{up}}(\eta)\eta d\eta,$$

$$C_{p2} = \frac{1}{24}\left(12\frac{b}{h}C_{sz2} + \beta_0^2\right)\beta_0, \qquad C_{p1} = C_{p2} + \int\limits_{\beta_0/2}^{\rho+\beta_0/2} \frac{\overline{S}_{z2}^{(\mathrm{lp})}(\eta)}{\overline{w}_2^{(\mathrm{lp})}(\eta)} d\eta,$$

$$C_{\mathrm{up}} = \int\limits_{-(\rho+\beta_0/2)}^{-\beta_0/2} \frac{\overline{S}_{z2}^{(\mathrm{up})}(\eta)}{\overline{w}_2^{(\mathrm{up})}(\eta)} d\eta, \qquad C_f = C_{p1} - \frac{1}{8}\left[1 - \frac{4}{3}\left(\rho + \frac{1}{2}\beta_0\right)^2\right]\left(\rho + \frac{1}{2}\beta_0\right),$$

and the dimensionless functions are given by

$$\overline{S}_{z2}^{(\mathrm{up})}(\eta) = \frac{1}{4}\left[1 - 4\left(\rho + \frac{1}{2}\beta_0\right)^2\right]\chi_f + \int\limits_{-(\rho+\beta_0/2)}^{\eta} \overline{w}_2^{(\mathrm{up})}(\eta)\eta d\eta,$$

$$\overline{S}_{z2}^{(\mathrm{lp})}(\eta) = C_{sz2} + \frac{1}{4}\left(\beta_0^2 - 4\eta^2\right)\left(\chi_f + \rho\right) + \int\limits_{-(\rho+\beta_0/2)}^{\eta} \overline{w}_2^{(\mathrm{up})}(\eta)\eta d\eta.$$

These dimensionless deformation functions satisfy the continuity conditions between the successive parts of the cross section.

To solve the stability problem, the principle of stationary total potential energy will be used in the form $\delta(U_{\varepsilon\gamma} - W) = 0$ (for details see [17]). The elastic strain energy $U_{\varepsilon\gamma}$ of the horizontal and vertical beam is defined as well as the work W of external load. After substituting them into the principle of stationary total potential energy and performing simple transformation, the system of two differential equations of equilibrium for this H-beam is obtained in the following form:

$$\overline{J}_z \frac{d^2 v}{dx^2} - C_{v\psi}\frac{d\psi}{dx} = -\frac{M_b(x)}{Eb^3 h}, \tag{2.36}$$

$$C_{v\psi}\frac{d^3 v}{dx^3} - C_{\psi\psi}\frac{d^2\psi}{dx^2} + C_{\psi}\frac{\psi(x)}{bh} = 0, \tag{2.37}$$

where the dimensionless coefficients are as follows:

$$\overline{J}_z = \frac{1}{12}\beta_0^3 + \frac{1}{6}\left[1 - 8\left(\rho + \frac{1}{2}\beta_0\right)^3\right]\frac{b}{h}\chi_f + 2\frac{b}{h}\int\limits_{\beta_0/2}^{\rho+\beta_0/2} \eta^2 \overline{w}_2^{(\mathrm{lp})}(\eta)d\eta,$$

$$C_{v\psi} = \int\limits_{-\beta_0/2}^{\beta_0/2} \eta f_d^{(\mathrm{mp})}(\eta)d\eta + 2\frac{b}{h}\left\{\int\limits_{\beta_0/2}^{\rho+\beta_0/2} \eta f_{d2}^{(\mathrm{lp})}(\eta)\overline{w}_2^{(\mathrm{lp})}(\eta)d\eta + 2\chi_f \int\limits_{\rho+\beta_0/2}^{1/2} \eta f_{d1}^{(\mathrm{lp})}(\eta)d\eta\right\},$$

$$\begin{aligned} C_{\psi\psi} = \int\limits_{-\beta_0/2}^{\beta_0/2} \left[f_d^{(\mathrm{mp})}(\eta)\right]^2 d\eta + 2\frac{b}{h}\Bigg\{&\int\limits_{\beta_0/2}^{\rho+\beta_0/2} \left[f_{d2}^{(\mathrm{lp})}(\eta)\right]^2 \overline{w}_2^{(\mathrm{lp})}(\eta)d\eta \\ &+ 2\chi_f \int\limits_{\rho+\beta_0/2}^{1/2} \left[f_{d1}^{(\mathrm{lp})}(\eta)\right]^2 d\eta\Bigg\}, \end{aligned}$$

$$C_\psi = \frac{1}{2(1+\nu)} \left\{ \int\limits_{-\beta_0/2}^{\beta_0/2} \left[\frac{b}{h} C_{sz2} + \frac{1}{8} \left(\beta_0^2 - 4\eta^2 \right) \right]^2 d\eta \right.$$
$$\left. + 2\frac{b}{h} \int\limits_{\beta_0/2}^{\rho+\beta_0/2} \frac{\left[\overline{S}_{z2}^{(\mathrm{lp})}(\eta) \right]^2}{\overline{w}_2^{(\mathrm{lp})}(\eta)} d\eta + \frac{\chi_f}{16} \frac{b}{h} \int\limits_{\rho+\beta_0/2}^{1/2} \left(1 - 4\eta^2 \right)^2 d\eta \right\}.$$

These two differential equations of equilibrium, (2.36) and (2.37), are fundamental in the analysis of the T-frame buckling problem.

3. ANALYTICAL MODEL OF THE THIN-WALLED T-FRAME TAKING INTO ACCOUNT THE SHEAR EFFECT

3.1. PRE-BUCKLING STATE

The T-frame is a statically indeterminate structure. The disconnected beams with the interaction force F_c are shown in Fig. 4. The detailed scheme of the

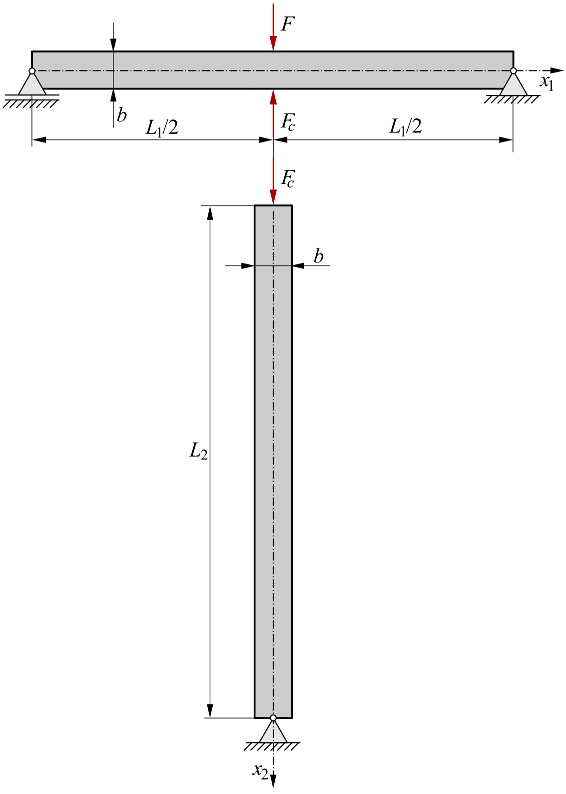

FIG. 4. Scheme of the interaction force F_c of two beams.

horizontal beam subjected to loading is shown in Fig. 5. The bending moment based on this scheme is as follows:

$$M_b(\xi_1) = \frac{1}{2}\xi_1\left(F - F_c\right)b\lambda_1, \tag{3.1}$$

where $\xi_1 = x_1/L_1$ is the dimensionless coordinate $(0 \leq \xi_1 \leq 1/2)$ and $\lambda_1 = L_1/b$ is the relative length of the horizontal beam.

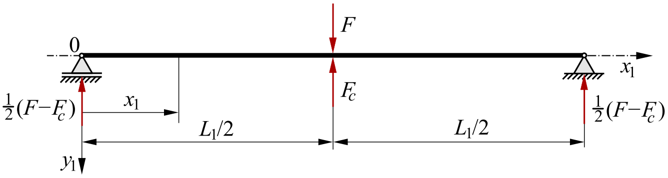

FIG. 5. Scheme of the horizontal beam with the load.

Thus, the equations of equilibrium, (2.36) and (2.37), expressed in terms of the dimensionless coordinate ξ_1, with consideration of Eq. (3.1), are in the following form:

$$\overline{J}_z\frac{d^2v}{d\xi_1^2} - C_{v\psi}L_1\frac{d\psi_{11}}{d\xi_1} = -\frac{1}{2}\xi_1\lambda_1^3\frac{F - F_c}{Eh}, \tag{3.2}$$

$$C_{v\psi}\frac{d^3v}{d\xi_1^3} - C_{\psi\psi}L_1\frac{d^2\psi_{11}}{d\xi_1^2} + C_\psi\lambda_1^2L_1\frac{b}{h}\psi_{11}(\xi_1) = 0. \tag{3.3}$$

Equation (3.2) and Eq. (3.3), after simple transformation, are reduced to a single equation in the form:

$$\frac{d^2\psi_{11}}{d\xi_1^2} - \alpha^2\lambda_1^2\frac{b}{h}\psi_{11}(\xi_1) = -\frac{1}{2}\lambda_1^2\frac{C_{v\psi}}{\overline{J}_zC_{\psi\psi} - C_{v\psi}^2}\frac{F - F_c}{Ebh}, \tag{3.4}$$

where $\alpha = \sqrt{\frac{\overline{J}_zC_\psi}{\overline{J}_zC_{\psi\psi} - C_{v\psi}^2}}$ is the dimensionless coefficient. The solution of Eq. (3.4) is given by the following function:

$$\psi_{11}(\xi_1) = \frac{1}{2}\left\{1 - \frac{\cosh\left(\alpha\lambda_1\sqrt{b/h}\,\xi_1\right)}{\cosh\left(0.5\alpha\lambda_1\sqrt{b/h}\right)}\right\}\frac{C_{v\psi}}{\overline{J}_zC_\psi}\frac{F - F_c}{Eb^2}. \tag{3.5}$$

This function satisfies the conditions: $d\psi_1/d\xi_1\big|_0 = 0$ and $\psi_1(1/2) = 0$. Substituting function (3.5) into Eq. (3.2), after integration and simple transformation, one obtains the beam deflection line:

$$v(\xi_1) = \left[\left(\xi_1 - \frac{4}{3}\xi_1^3\right)\frac{b}{h} + \frac{8}{\lambda_1^2}f_{v\psi}(\xi_1)\frac{C_{v\psi}^2}{\overline{J}_zC_\psi}\right]\frac{\lambda_1^3}{16\overline{J}_z}\frac{F - F_c}{Eb}, \tag{3.6}$$

where

$$f_{v\psi}(\xi_1) = \xi_1 - \frac{\sinh\left(\alpha\lambda_1\sqrt{b/h}\xi_1\right)}{\alpha\lambda_1\sqrt{b/h}\cosh\left(0.5\alpha\lambda_1\sqrt{b/h}\right)}.$$

Function (3.6) satisfies the conditions: $dv/d\xi_1\big|_{1/2} = 0$ and $v(0) = 0$. Thus, the maximum deflection of the horizontal beam is as follows:

$$v_1 = (1 + C_{se1})\frac{\lambda_1^3}{48\overline{J}_z}\frac{F - F_c}{Eh}, \tag{3.7}$$

where the dimensionless shear coefficient:

$$C_{se1} = \frac{12}{\lambda_1^2}\frac{h}{b}\left[1 - \frac{2}{\alpha\lambda_1}\sqrt{\frac{h}{b}}\tanh\left(\frac{1}{2}\alpha\lambda_1\sqrt{\frac{b}{h}}\right)\right]\frac{C_{v\psi}^2}{\overline{J}_z C_\psi}. \tag{3.8}$$

The shortening of the vertical H-beam-column under the action of force F_c (Fig. 4) is as follows:

$$\Delta L_2 = \frac{F_c\lambda_2}{E\overline{A}h}, \tag{3.9}$$

where

$$\overline{A} = \beta_0 + 2\left\{\left[1 - 2\left(\rho + \frac{1}{2}\beta_0\right)\right]\chi_f + \int_{\beta_0/2}^{\rho+\beta_0/2} \overline{w}_2^{(\mathrm{lp})}(\eta)d\eta\right\}\frac{b}{h}$$

is the dimensionless cross section area, and $\lambda_2 = L_2/b$ is the relative length of the beam-column.

Based on the condition $v_1 = \Delta L_2$, which states that the deflection of the horizontal beam is consistent with the shortening of the beam-column, one obtains the force:

$$F_c = \frac{(1 + C_{se1})\overline{A}\lambda_1^3}{48\overline{J}_z\lambda_2 + (1 + C_{se1})\overline{A}\lambda_1^3}F. \tag{3.10}$$

3.2. Buckling state

The form of the horizontal H-beam bending line of the T-frame after its buckling is shown in Fig. 6. The bending moment, based on this scheme, in the dimensionless coordinate $\xi_1 = x_1/L_1$ for the first interval ($0 \leq \xi_1 \leq 1/2$), is as follows:

$$M_b(\xi_1) = -\xi_1 M_0, \tag{3.11}$$

where M_0 is the moment at the joint connecting the two beams.

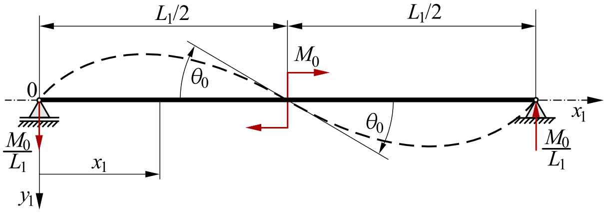

Fig. 6. Scheme of the deflection line of the horizontal H-beam.

Therefore, the equation of equilibrium (2.36) in the dimensionless coordinate ξ_1, with consideration of Eq. (3.11), is in the following form:

$$\overline{J}_z \frac{d^2 v}{d\xi_1^2} - C_{v\psi} L_1 \frac{d\psi_{12}}{d\xi_1} = \xi_1 \lambda_1^2 \frac{M_0}{Ebh}. \tag{3.12}$$

However, Eq. (2.37) is of the form of Eq. (3.3), with the dimensionless function $\psi_{12}(\xi_1)$. Solving Eq. (3.12) and Eq. (3.3), after simple transformation, one obtains the dimensionless function:

$$\psi_{12}(\xi_1) = -\left\{1 - \frac{\cosh\left(\alpha\lambda_1\sqrt{b/h}\,\xi_1\right)}{\cosh\left(0.5\alpha\lambda_1\sqrt{b/h}\right)}\right\} \frac{C_{v\psi}}{\overline{J}_z C_\psi} \frac{1}{\lambda_1} \frac{M_0}{Eb^3}, \tag{3.13}$$

and the rotation angle of the center of the deflection line:

$$\theta_0 = (1 + C_{se1}) \frac{\lambda_1}{12\overline{J}_z} \frac{b}{h} \frac{M_0}{Eb^3}, \tag{3.14}$$

where C_{se1} is the dimensionless shear coefficient consistent with Eq. (3.8).

The buckling line form of the vertical H-beam-column is shown in Fig. 7. The bending moment, based on this scheme, in the dimensionless coordinate, is as follows:

$$M_b(\xi_2) = -(1 - \xi_2)M_0 + F_c v(\xi_2), \tag{3.15}$$

where $\xi_2 = x_2/L_2$ is the dimensionless coordinate ($0 \le \xi_2 \le 1$), $\lambda_2 = L_2/b$ is the relative length of the vertical beam-column.

Consequently, the equilibrium Eq. (2.36) and Eq. (2.37), in the dimensionless coordinate ξ_2, with consideration of the bending moment (3.15), are in the following form:

$$\overline{J}_z \frac{d^2 v}{d\xi_2^2} - C_{v\psi} L_2 \frac{d\psi_2}{d\xi_2} = \left[(1 - \xi_2)M_0 - F_c v(\xi_2)\right] \lambda_2^2 \frac{1}{Ebh}, \tag{3.16}$$

$$C_{v\psi} \frac{d^3 v}{d\xi_2^3} - C_{\psi\psi} L_{12} \frac{d^2 \psi_2}{d\xi_2^2} + C_\psi \lambda_2^2 L_2 \frac{b}{h} \psi_2(\xi_2) = 0. \tag{3.17}$$

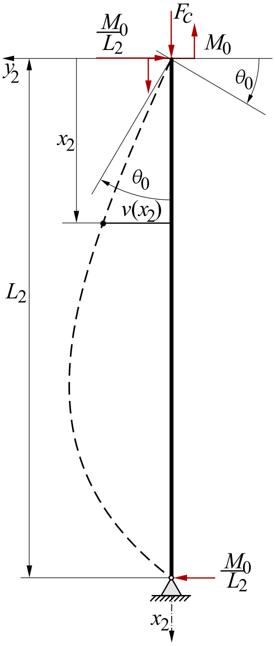

FIG. 7. Scheme buckling line form of the vertical H-beam-column.

These two differential equations, after simple transformations, are reduced to a fourth-order differential equation in the following form:

$$\frac{d^4v}{d\xi_2^4} - k_1\frac{d^2v}{d\xi_2^2} - k_2 v(\xi_2) = -(1-\xi_2)\alpha^2\frac{\lambda_2^4}{\overline{J}_z}\left(\frac{b}{h}\right)^2\frac{M_0}{Eb^2}, \tag{3.18}$$

where $k_1 = \alpha^2\lambda_2^2\frac{b}{h}\left(1 - \frac{C_{v\psi}}{\overline{J}_z C_\psi}\overline{F}_c\right)$ and $k_2 = \alpha^2\frac{\lambda_2^4}{\overline{J}_z}\left(\frac{b}{h}\right)^2\overline{F}_c$ are the dimensionless coefficients, and $\overline{F}_c = F_c/Eb^2$ is the dimensionless force.

Solving Eq. (3.18), taking into account the boundary conditions $v(0) = v(1) = 0$, one obtains the buckling line of the vertical beam-column in the form:

$$v(\xi_2) = \left\{1 - \xi_2 - \frac{\sin\left[(1-\xi_2)p\right]}{\sin(p)}\right\}\frac{1}{\overline{F}_c}\frac{M_0}{Eb^2}, \tag{3.19}$$

where $p = \frac{1}{\sqrt{2}}\sqrt{-k_1 + \sqrt{k_1^2 + 4k_2}}$ is the dimensionless coefficient. Consequently, the rotation angle at the beginning of this line ($\xi_2 = 0$) is as follows:

$$\theta_0 = \left.\frac{dv}{L_2 d\xi_2}\right|_0 = \left[\frac{p}{\tan(p)} - 1\right]\frac{1}{\overline{F}_c}\frac{1}{\lambda_2}\frac{M_0}{Eb^3}. \tag{3.20}$$

By equating the rotation angles (3.14) and (3.20), one obtains the algebraic equation:

$$(1 + C_{se1})\frac{\lambda_1}{12}\frac{\lambda_2}{\overline{J}_z}\frac{b}{h}\overline{F}_c + 1 - \frac{p}{\tan(p)} = 0. \tag{3.21}$$

Based on Eq. (3.21), the dimensionless critical force $\overline{F}_{c,\mathrm{CR}}$ for the vertical beam-column alone is determined, and consequently, taking into account Eq. (3.10), one obtains the dimensionless critical force for the whole frame:

$$\overline{F}_{\mathrm{CR}} = \left[1 + \frac{48\overline{J}_z\lambda_2}{(1 + C_{se1})\overline{A}\lambda_1^3}\right]\overline{F}_{c,\mathrm{CR}}. \tag{3.22}$$

4. ANALYTICAL MODEL OF THE THIN-WALLED T-FRAME NEGLECTING SHEAR EFFECT

This presented frame model is a simplification of the model presented in Sec. 3 and is developed on the basis of the Bernoulli–Euler beam theory.

4.1. PRE-BUCKLING STATE

Equation (3.2), describing the horizontal beam bending in the first interval $(0 \le \xi_1 \le 1/2)$ (Fig. 5), without the dimensionless shear effect function $\psi_{11}(\xi_1)$, is in the following form:

$$\overline{J}_z\frac{d^2v}{d\xi_1^2} = -\frac{1}{2}\xi_1\lambda_1^3\frac{F^{(o)} - F_c^{(o)}}{Eh}, \tag{4.1}$$

where the superscript (o) in the forces refers to the variant without the shear effect. After integrating this equation twice and taking into account the following conditions: $v(0) = 0$ and $dv/d\xi_1|_{1/2} = 0$, one obtains the deflection line in the form:

$$v(\xi_1) = \left(3 - 4\xi_1^2\right)\xi_1\frac{\lambda_1^3}{48\overline{J}_z}\frac{F^{(o)} - F_c^{(o)}}{Eh}. \tag{4.2}$$

Thus, the maximum deflection of this beam is as follows:

$$v_1 = v\left(\frac{1}{2}\right) = \frac{\lambda_1^3}{48\overline{J}_z}\frac{F^{(o)} - F_c^{(o)}}{Eh}. \tag{4.3}$$

It is easy to see that this expression is the same as Eq. (3.7) for $C_{se1} = 0$, when the shear effect is omitted.

The shortening of the vertical H-beam-column under the action of the force (Fig. 5) is in the form of Eq. (3.9). Based on the condition $v_1 = \Delta L_2$, one obtains the relationship between the forces $F_c^{(o)}$ and $F^{(o)}$ in the form:

$$F_c^{(o)} = \frac{\overline{A}\lambda_1^3}{48\overline{J}_z\lambda_2 + \overline{A}\lambda_1^3} F^{(o)}, \tag{4.4}$$

or

$$F^{(o)} = \left(1 + \frac{48\overline{J}_z\lambda_2}{\overline{A}\lambda_1^3}\right) F_c^{(o)}. \tag{4.5}$$

It is easy to see that Eq. (4.4) is the same as Eq. (3.10) for $C_{se1} = 0$, when the shear effect is omitted.

4.2. Buckling state

Taking into account Fig. 6, and Eq. (3.12), without the dimensionless shear effect function $\psi_{12}(\xi_1)$, the equilibrium equation is in the following form:

$$\overline{J}_z \frac{d^2 v}{d\xi_1^2} = \xi_1 \lambda_1^2 \frac{M_0^{(o)}}{Ebh}. \tag{4.6}$$

Integrating Eq. (4.6) twice and taking into account the conditions: $v(0) = 0$ and $v(1/2) = 0$, one obtains the horizontal beam deflection line in the form:

$$v(\xi_1) = -\left(1 - 4\xi_1^2\right)\xi_1 \frac{\lambda_1^2}{24\overline{J}_z} \frac{M_0^{(o)}}{Eb^2 h}, \tag{4.7}$$

and consequently, the slope of this beam deflection line is as follows:

$$\frac{dv}{L_1 d\xi_1} = \left(12\xi_1^2 - 1\right) \frac{\lambda_1}{24\overline{J}_z} \frac{M_0^{(o)}}{Eb^2 h}. \tag{4.8}$$

Thus, the rotation angle at the center of the deflection line is as follows:

$$\theta_0 = \left.\frac{dv}{L_1 d\xi_1}\right|_{1/2} = \frac{\lambda_1}{12\overline{J}_z} \frac{1}{h} \overline{M}_0^{(o)}, \tag{4.9}$$

where $\overline{M}_0^{(o)} = M_0^{(o)}/Eb^2$ is the dimensionless moment. It is easy to see that this expression is the same as Eq. (3.14) for $C_{se1} = 0$, when the shear effect is omitted.

Taking into account Fig. 7, and Eq. (3.16), without the dimensionless shear effect function $\psi_2(\xi_2)$, after simple transformation, the governing equation is in the following form:

$$\frac{d^2 v}{d\xi_2^2} + \frac{\lambda_2^2}{\overline{J}_z}\frac{b}{h}\overline{F}_c^{(o)} v(\xi_2) = (1-\xi_2)\frac{\lambda_2^2}{\overline{J}_z}\frac{b}{h}\overline{M}_0^{(o)}, \tag{4.10}$$

where $\overline{F}_c^{(o)} = F_c^{(o)}/Eb^2$ is the dimensionless force. Solving this second-order differential equation, taking into account two boundary conditions $v(0) = v(1) = 0$, after simple transformation, one obtains the buckling line of the vertical beam-column in the form:

$$v(\xi_2) = \left\{1 - \xi_2 - \frac{\sin\left[(1-\xi_2)\, p^{(o)}\right]}{\sin\left(p^{(o)}\right)}\right\} \frac{\overline{M}_0^{(o)}}{\overline{F}_c^{(o)}}, \tag{4.11}$$

where $p^{(o)} = \lambda_2 \sqrt{\frac{b}{h}\frac{\overline{F}_c^{(o)}}{\overline{J}_z}}$ is the dimensionless coefficient.

The slope of this buckling line is as follows:

$$\frac{dv}{L_2 d\xi_2} = \left\{-1 + f_{\text{CR}} \frac{\cos\left[(1-\xi_2)\, p^{(o)}\right]}{\sin\left(p^{(o)}\right)}\right\} \frac{\overline{M}_0^{(o)}}{L_2 \overline{F}_c^{(o)}}. \tag{4.12}$$

Thus, the rotation angle at the beginning of this buckling line is as follows:

$$\theta_0 = \left.\frac{dv}{L_2 d\xi_1}\right|_0 = \left[\frac{p^{(o)}}{\tan\left(p^{(o)}\right)} - 1\right] \frac{\overline{M}_0^{(o)}}{L_2 \overline{F}_c^{(o)}}. \tag{4.13}$$

By equating the rotations angles (4.9) and (4.13), one obtains the algebraic equation:

$$\frac{\lambda_1 \lambda_2}{12 \overline{J}_z}\frac{b}{h}\overline{F}_{c,\text{CR}}^{(o)} + 1 - \frac{p^{(o)}}{\tan\left(p^{(o)}\right)} = 0. \tag{4.14}$$

Based on Eq. (4.14), the dimensionless critical force $F_{c,\text{CR}}^{(o)}$ for the vertical beam-column is determined, and in accordance with Eq. (4.5), one obtains the dimensionless critical force for the T-frame without shear effect:

$$\overline{F}_{\text{CR}}^{(o)} = \left(1 + \frac{48 \overline{J}_z \lambda_2}{\overline{A} \lambda_1^3}\right) \overline{F}_{c,\text{CR}}^{(o)}. \tag{4.15}$$

It is easy to see that this expression is the same as Eq. (3.22) for $C_{se1} = 0$, when the shear effect is omitted.

5. ANALYTICAL STUDIES OF SELECTED T-FRAMES

Example analytical studies are carried out for a thin-walled T-frame made of a horizontal beam with relative lengths $\lambda_1 = 10, 15, 20, 30, 40$, and a vertical beam-column with relative length $\lambda_2 = 40$. Sizes of three standard H-beams are shown in Table 1.

TABLE 1. Dimensions of the three selected standard H-beams.

Sizes	h [mm]	b [mm]	b_0 [mm]	t_f [mm]	r [mm]
H-300	300	300	11.0	19.0	27.0
H-400	400	300	13.5	24.0	27.0
H-500	500	300	14.5	28.0	27.0

The values of the dimensionless critical forces calculated on the basis of Eq. (3.21) and Eq. (3.22) for the case of shear effect taken into account and Eq. (4.14) and Eq. (4.15), neglecting this effect are presented in Table 2, Table 3, and Table 4.

TABLE 2. Critical forces of T-frame made of standard H-300 beams.

λ_1	10	15	20	30	40
$10^4\overline{F}_{c,\mathrm{CR}}$	1.24240	1.22063	1.19980	1.16123	1.12664
$10^4\overline{F}^{(o)}_{c,\mathrm{CR}}$	1.28132	1.25771	1.23422	1.19230	1.15505
$10^4\overline{F}_{\mathrm{CR}}$	1.39063	1.26442	1.21805	1.16648	1.12880
$10^4\overline{F}^{(o)}_{\mathrm{CR}}$	1.43833	1.30273	1.25312	1.19771	1.15726

TABLE 3. Critical forces of T-frame made of standard H-400 beams.

λ_1	10	15	20	30	40
$10^4\overline{F}_{c,\mathrm{CR}}$	1.55404	1.52748	1.50195	1.45453	1.41189
$10^4\overline{F}^{(o)}_{c,\mathrm{CR}}$	1.61894	1.58832	1.55942	1.50646	1.45940
$10^4\overline{F}_{\mathrm{CR}}$	1.72912	1.57947	1.52337	1.46080	1.41446
$10^4\overline{F}^{(o)}_{\mathrm{CR}}$	1.80787	1.64324	1.58217	1.51297	1.46206

TABLE 4. Critical forces of T-frame made of standard H-500 beams.

λ_1	10	15	20	30	40
$10^4\overline{F}_{c,\mathrm{CR}}$	1.79638	1.76636	1.73741	1.68347	1.63484
$10^4\overline{F}^{(o)}_{c,\mathrm{CR}}$	1.88901	1.85329	1.81957	1.75777	1.70286
$10^4\overline{F}_{\mathrm{CR}}$	1.99066	1.82430	1.76165	1.69048	1.63777
$10^4\overline{F}^{(o)}_{\mathrm{CR}}$	2.10220	1.91526	1.84523	1.76512	1.70586

By comparing the values of critical forces determined analytically with and without taking into account the shear effect, it is easy to see that the shear effect reduces the values of the critical forces. Differences between these values of critical forces are specified in Table 5.

TABLE 5. Differences between the values of critical forces with and without the shear effect.

λ_1	10	15	20	30	40
$\Delta\overline{F}_{\mathrm{CR}}^{(\mathrm{H-300})}\%$	3.4	3.0	2.9	2.7	2.5
$\Delta\overline{F}_{\mathrm{CR}}^{(\mathrm{H-400})}\%$	4.6	4.0	3.9	3.6	3.4
$\Delta\overline{F}_{\mathrm{CR}}^{(\mathrm{H-500})}\%$	5.6	5.0	4.7	4.4	4.2

Moreover, these results of the exemplary calculations are graphically presented in the next section and compared with the results of FE analyses.

6. NUMERICAL (FEM) STUDIES OF SELECTED T-FRAMES

As a comparative study a FE analysis is performed. A 3D model of the whole frame is prepared. A linear buckling analysis is carried out using the Ansys[1)] software. The material model is assumed to be linear elastic with the following parameters: Young's modulus $E = 200\,000\,\mathrm{MPa}$ and Poisson's ratio $\nu = 0.3$. The boundary conditions applied to the model are shown in Fig. 8a. All three

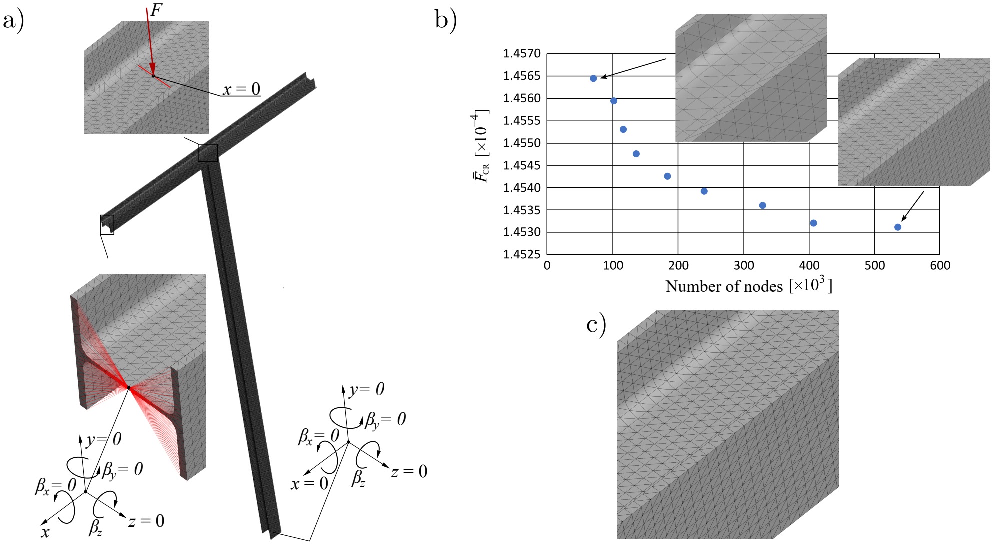

FIG. 8. FE model of the T-frame: a) boundary conditions, b) mesh convergence study, c) mesh pattern.

[1)] Ansys, Inc., Academic Research Mechanical Release 2023 R2.

ends of the frame are pin-supported. A remote displacement option was used to achieve this condition, which was applied to the whole cross section and realised at its centroid. At the bottom of the vertical part of the frame, displacements along three axes are blocked. Rotation about the z-axis is allowed. Both ends of the horizontal part can move horizontally and rotate about the z-axis. To avoid rigid-body motion, the horizontal displacement is taken away at one node at the mid-length of the horizontal beam. The force F is applied to the upper part of this beam, at the edge corresponding to the center line of the web of the vertical part of the frame (see Fig. 8a).

To discretise the model of the frame, solid elements are used marked as *SOLID186* which were tetrahedral, second-order FEs with 10 nodes and 3 degrees-of-freedom in each node – displacements in three directions. This choice provides the most effective model among those investigated, in which both tetrahedral and hexahedral elements were taken into account. The negative influence of using a single element over the thickness of the beam wall was also verified. The number of elements was established based on the mesh convergence analysis presented in Fig. 8b. It was decided to set the element size to 22, which gave about 400 000 nodes for the H-300 frame with the parameter $\lambda_1 = 10$. It should be noted that even for the two extreme cases considered, shown in Fig. 8b, the difference in value of the buckling load is only about 0.2 %. This comes from the fact that the buckling mode has a global character and the analysis is a linear one. The exemplary mesh used in all analyses is shown in Fig. 8c.

Typical buckling shapes corresponding to the H-300 frame are shown in Fig. 9 for selected lengths of the horizontal beam. The values of the buckling load for all considered frames are presented in Fig. 10, together with the results given by the analytical solution described in Sec. 5. They are given on the vertical axis whereas the horizontal axis corresponds to the length parameter λ_1 – the higher

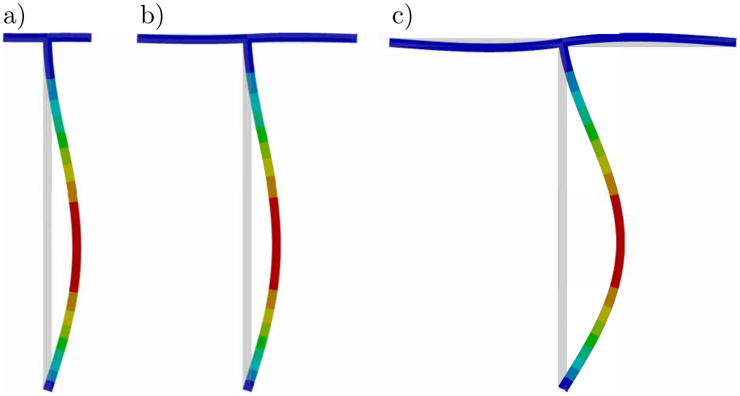

Fig. 9. First buckling mode of the H-300 T-frame for different λ_1:
a) $\lambda_1 = 10$, b) $\lambda_1 = 25$, c) $\lambda_1 = 40$ (scaled 10^3).

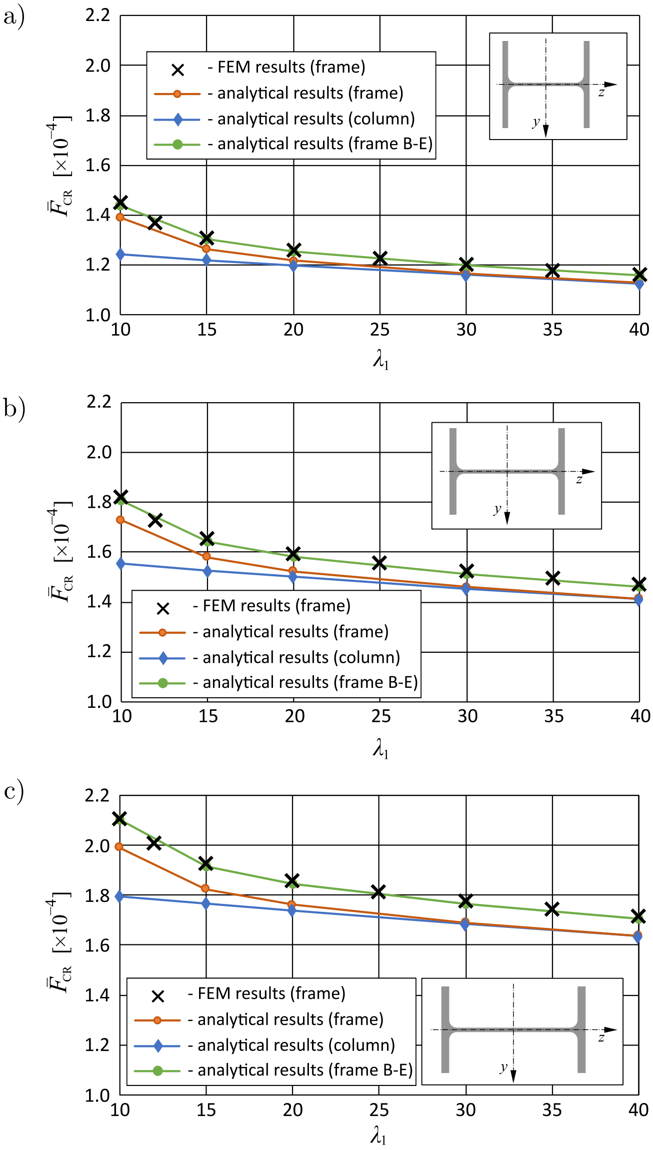

Fig. 10. Comparison of dimensionless buckling loads obtained with analytical and numerical approach: a) H-300, b) H-400, c) H-500.

its value, the longer the horizontal part of the frame. Regarding the analytical solution, two curves are shown. One of them corresponds to the buckling load for the whole frame – red line with circles, and the second one corresponds to the buckling of the vertical beam only – blue line with diamonds. In the FE analysis, only the whole frame was analysed and the results are marked with black crosses.

7. Discussion of the results

The presented results were obtained with the use of both the analytical model and numerical approach. In both cases linear behaviour of the material was assumed. In analytical model the shear stresses were taken into account.

For all considered examples, the shape of the frame after the loss of stability was the same and consistent with those shown in Fig. 9, in which the presented deformation is magnified 10^3 times for better visualisation. The vertical part buckles such as the column hinged supported at the bottom and either hinged or rigidly supported at the top. The latter depended on the length of the horizontal beam. If the beam is short it behaves similarly to the fixed support, and the rotation at this point is small. The longer the beam, the smaller its influence on the behaviour of the column, which will deform as hinged/supported column at both ends if the beam is long enough. This relationship is also visible in the values of the buckling loads obtained from the analytical solution. The longer the horizontal beam, the closer the value of the buckling load of the frame (red line in Fig. 10) is to the value corresponding to the case when only the column is considered (blue line). In the presented examples for $\lambda_1 = 40$, the buckling load for the frame is only 0.2 % higher than that of the column. This means that the influence of the horizontal beam on the stability of the whole structure is negligible.

The distribution of the results given by the FE analyses (black crosses in Fig. 10) is similar to those from the analytical solution. They are slightly above the red curve. The smallest difference was noted for the H-300 frame with $\lambda_1 = 40$ and was equal to 3 % and the biggest difference, 6 %, was observed for the H-500 frame with $\lambda_1 = 10$. However, the FE results are very close to the analytical solution in which shear effect is omitted (green line – B-E) – the discrepancy does not exceed 1 %. Since the influence of the FE type on the results was eliminated and a number of boundary conditions were verified, the agreement between the FE results and the B-E theory may be the result of the linear nature of the buckling analysis, which is not able to capture the shear effect phenomenon.

8. Conclusions

In the present work, the problem of stability of the T-frame was solved analytically and numerically. The novelty of the analytical approach proposed in the paper lies in the fact that the influence of shear stress on the deformation of the frame is taken into account in the model definition. This makes the analytical calculations more realistic, especially when short beams are considered, and at the same time makes the structure safer. The defined shear coefficient allows the contribution of shear stress to the critical load to be determined. The presented formulae give more conservative results even when compared with the numerical calculations since the inclusion of the shear effect reduces the stiffness of the structure and thus lowers the value of the buckling load. The obtained buckling loads are consistent for both approaches and the biggest difference between the analytical and numerical solution is equal to 6 %. Additional FE analyses have to be performed regarding the compatibility of both methods with emphasis on FE modelling details such as the type and number of elements or the method of applying the load and supports.

The presented approach has a general form and can be applied to different shapes of cross section. Further extensive investigation, including experimental tests, may validate its correctness and explain the influence of shear stress on the behaviour of engineering structures.

Fundings

The paper is developed based on the scientific activity of the Łukasiewicz Research Network – Poznan Institute of Technology and the statutory activity of the Poznan University of Technology (Grant of the Ministry of Science and Higher Education in Poland no. 0612/SBAD/3628).

Conflict of interest

The authors declare that there are no known competing financial interests or personal relationships that could have influenced the work described in this paper.

Authors' contributions

Krzysztof Magnucki: conceptualization, investigation, formal analysis, writing – original draft preparation, Paweł Jasion: investigation, methodology, visualization, writing – review and editing. All authors reviewed and approved the final manuscript.

References

1. Trahair N.S., Bradford M.A., Nethercot D.A., Gardner L., *The Behaviour and Design of Steel Structures to EC3*, 4 ed., Taylor & Francis, London, 2008.
2. Basaglia C., Camotim D., Silvestre N., Global buckling analysis of plane and space thin-walled frames in the context of GBT, *Thin-Walled Structures*, **46**(1): 79–101, 2008, https://doi.org/10.1016/j.tws.2007.07.007.

3. Basaglia C., Camotim D., Silvestre N., GBT-based local, distortional and global buckling analysis of thin-walled steel frames, *Thin-Walled Structures*, **47**(11): 1246–1264, 2009, https://doi.org/10.1016/j.tws.2009.04.003.

4. Camotim D., Basaglia C., Silvestre N., GBT buckling analysis of thin-walled steel frames: A state-of-the-art report, *Thin-Walled Structures*, **48**(10–11): 726–743, 2010, https://doi.org/10.1016/j.tws.2009.12.003.

5. Magnucka-Blandzi E., Magnucki K., Buckling and optimal design of cold-formed thin-walled beams: Review of selected problems, *Thin-Walled Structures*, **49**(5): 554–561, 2011, https://doi.org/10.1016/j.tws.2010.09.011.

6. Magnucki K., Milecki S., Elastic buckling of a thin-walled rectangular frame under in-plane compression, *Thin-Walled Structures*, **116**: 326–332, 2017, https://doi.org/10.1016/j.tws.2017.03.007.

7. Nagy Z., Kelemen A., Nedelcu M., The influence on portal frame buckling of different cladding systems – A comparative numerical study considering stressed skin effect, *Thin-Walled Structures*, **182**(Part B): 110310, 2023, https://doi.org/10.1016/j.tws.2022.110310.

8. Krystosik P., On the columns buckling length of unbraced steel frames with semi-rigid joints, *Archives of Civil Engineering*, **67**(1): 539–556, 2021, https://doi.org/10.24425/ace.2021.136488.

9. Zhang M., Xie X., Gao X., Pan Y., Parke G., Study on failure criterion of thin-walled steel frame structures based on the ESED parameter, *Thin-Walled Structures*, **161**: 107357, 2021, https://doi.org/10.1016/j.tws.2020.107357.

10. Liu Y.Z., Yang Y.B., C X.H., Guo D.Z., Lateral-distortional buckling of frames composed of non-aligned I-members by a simple distortional beam element considering angling effect, *Thin-Walled Structures*, **202**: 112146, 2024, https://doi.org/10.1016/j.tws.2024.112146.

11. Giżejowski M.A., Szczerba R.B., Stachura Z., Gajewski M.D., Buckling resistance of quasi-straight H-section beam-columns under unequal end moments, *Archives of Civil Engineering*, **67**(1): 323–349, 2021, https://doi.org/10.24425/ace.2021.136476.

12. Zhou Y., Ning S., Huang D., Li Y., Refined plastic hinge method for steel frames with local–global interactive buckling, *Thin-Walled Structures*, **181**: 110013, 2022, https://doi.org/10.1016/j.tws.2022.110013.

13. Wen Y., He W.J., Zhan W., Li B.H., Full beam formulation for the lateral torsional buckling analysis of elastic frames by considering the structural detail of beam-to-column joint, *Thin-Walled Structures*, **183**: 110414, 2023, https://doi.org/10.1016/j.tws.2022.110414.

14. Yang Y., Hui Y., Li P., Yang Y., Huang Q., Giunta G., Belouettar S., Hu H., Global/local buckling analysis of thin-walled I-section beams via hierarchical one-dimensional finite elements, *Engineering Structures*, **280**: 115705, 2023, https://doi.org/10.1016/j.engstruct.2023.115705.

15. Xiang Y., Zhou X., Shi Y., Zhou J., Ke K., Deng F., Study on the seismic performance of cold-formed thin-walled steel frame with K-shaped braced shear panel, *Thin-Walled Structures* **184**: 110449, 2023, https://doi.org/10.1016/j.tws.2022.110449.

16. Jůza J., Jandera M., Křemen T., Experimental investigation on the square and rectangular hollow section stainless steel portal frames, *Thin-Walled Structures*, **189**: 110897, 2023, https://doi.org/10.1016/j.tws.2023.110897.

17. Magnucki K., Bending of a five-layered composite beam with consideration of two analytical models, *Archive of Mechanical Engineering*, **71**(1): 27–46, 2024, https://doi.org/10.24425/ame.2024.149188.

18. Magnucki K., Free flexural vibrations of standard wide-flange H-beams with consideration of the shear effect, *Rail Vehicles/Pojazdy Szynowe*, (1–2): 46–50, 2024, https://doi.org/10.53502/RAIL-189244.

Received August 21, 2025; revised December 18, 2025; accepted December 22, 2025;
available online January 14, 2026; version of record June 8, 2026;
published issue June 24, 2026.

Engineering Transactions, **74**(2): 293–326, 2026, https://doi.org/10.24423/engtrans.2026.3505
Institute of Fundamental Technological Research Polish Academy of Sciences (IPPT PAN)
Université de Lorraine • Poznan University of Technology

Review Paper

Torsion of Functionally Graded Material Structures: An Overview

Mateusz Kumor[1)*], Artur Ganczarski[2)]

[1)] *Doctoral School*
[2)] *Chair of Applied Mechanics and Biomechanics*

Cracow University of Technology
Kraków, Poland

*Corresponding Author: mateusz.kumor@doktorant.pk.edu.pl

Examining torsion in functionally graded materials (FGMs) is crucial because their properties vary spatially. FGMs with continuously graded architectures provide a robust basis for investigating mechanical behavior. Current understanding of torsional response draws on analytical, numerical, and experimental approaches. This review synthesizes how material gradation influences stress distribution, stiffness, and failure modes, and compares advances in FGM torsion across diverse models and geometries. The theoretical background is framed by classical torsion theories, including the Saint-Venant theory, the Prandtl membrane analogy, and the Vlasov formulations. We further discuss modeling with isoparametric finite elements and summarize established homogenization schemes for FGMs. A tabulated overview of torsion-related results is also provided. The novelty of this review lies in its exclusive focus on torsion in FGMs, the systematic tabulation of prior contributions, and a coherent exposition of homogenization models and torsion theories tailored to FGM structures. To our knowledge, this is among the first reviews to focus specifically on torsion of FGM structures, distinguishing it from prior overviews that address torsion only briefly. Methodologically, we conduct a structured scoping review that screens peer-reviewed sources, classifies studies by geometry, torsion theory, homogenization scheme, and numerical strategy, and synthesizes observed trends. Finally, we present concise conclusions and future research directions. This review covers analytical, numerical, and experimental studies of torsion in FGMs, identified via a structured Google Scholar search and prioritized by citation impact and relevance.

Keywords: torsion, functionally graded materials, FGM structures, torsional stiffness.

1. INTRODUCTION

The concept of functionally graded materials (FGMs) was developed in Japan in the mid-1980s [1]. The established idea of materials providing a high through-thickness thermal barrier was crucial for space shuttle construction; Japanese engineers and scientists proposed functionally graded variations in thermal coefficients [2]. Since then, the FGM concept has advanced steadily. The literature on bending, tension, and compression is relatively extensive, whereas torsion remains comparatively underexplored. The spatial variation of graded structure in such materials underpins their usefulness in many automotive, aerospace, and biomedical applications. Figure 1 presents an example of property gradation in the x- and y-directions.

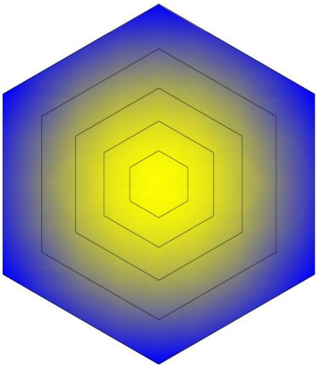

Fig. 1. Example of an FGM structure.

In the study of FGMs, one of the most important aspects is the behavior of such materials under torsional loads. A thorough exploration of the FGM torsion problem may yield substantial improvements and enable greater use of FGM layers in the design of parts that transmit significant twisting moments. These may include structural elements such as support beams with various cross-sectional areas, machine shafts, or even aircraft wings. Furthermore, the development of precise numerical torsion models could reduce design costs and time, thereby encouraging broader adoption of FGM structures in place of conventional materials. Therefore, a substantial task is to consider existing torsion theories and reflect on their potential improvements.

Valuable issues related to torsion in FGM structures have been presented in many articles. An analysis of the available literature shows that most torsion cases are approximated as linear elastic composites, often treated as isotropic models. Many of these works are based on anisotropic elasticity models developed by Lekhnitskii [3]. Horgan and Chan [4] investigated the influence of material inhomogeneity on the torsional behavior of linear elastic isotropic rods. They extended the work of Rooney *et al.* [5] and Lekhnitskii [3] by formulating the shear modulus as a function of the cross-sectional position. Batra [6] solved the torsion problem for an FGM cylinder in compressible and incompressible linear elastic materials with spatially varying moduli only in the axial direction. Arghavan and Hematiyan [7] formulated numerical models of FGM hollow tubes with arbitrary non-circular shapes. In another study, Horgan [8] extended the notation introduced by Chen and Wai [9], deriving unified formulas for the absence of warping effects in rods with elliptical cross sections. Barretta and Luciano [10] demonstrated a novel analogy between the Kirchhoff plate problem and the Saint-Venant torsion problem.

In recent years, numerous papers have examined the influence of torsion on FGM nanotubes and nanobars. Li and Hu [11] analyzed the behavior of 2D FGM microtubes under torsion using the modified couple-stress theory. Barretta *et al.* [12] investigated the torsion of FGM nanobeams based on the Eringen nonlocal elasticity theory. Moreover, many recent studies employ the Saint-Venant torsion theory, as evidenced by the work of Nikmehr and Lashkarbolok [13] and Darilmaz *et al.* [14]. The number of studies on beams with circular and square cross sections is substantial, whereas cases involving shafts with triangular, regular polygonal, and other non-circular cross sections are less frequent. The results of Akinlabi *et al.* [15] on torsion in triangular cross sections indicate clear room for expansion of this topic.

Furthermore, many investigations rely on finite element methods (FEM). Ganczarski *et al.* [16] offered a different perspective by solving torsion for Al-Ti FGM non-circular shafts using the finite difference method (FDM). Their work highlights significant potential for future research employing methods other than the FEM. In addition to aerospace and automotive applications, the torsion and shear-stress behavior of FGM structures is also relevant to the medical and energy sectors. Consequently, research in this area can support the design of innovative components across these industries.

Considering the current advances in the torsional behavior of functionally graded (FG) materials, we would like to highlight several of the most important findings from studies conducted in recent years. Hao *et al.* [99] analyzed bursting oscillations arising from bending–torsion coupling in cantilevered FGM conical sandwich panels driven by a static preload and slow in-plane harmonic forcing, and demonstrates with a nonautonomous, temperature-graded model that the onset is governed by symmetry-breaking pitchfork bifurcations. In turn, subsequent studies address the torsional behavior of nanotubes, nanorods, and microtubes. Using modified couple stress theory with radial, axial gradation, Aghazadeh *et al.* [100] derived, numerically solved, and validated torsion equations for bidirectional FG microtubes, quantifying how phase profile and geometry control twist and shear under distributed torque.

In turn, Civalek *et al.* [101] presented an exact nonlocal-elasticity solution for the torsional free vibration of restrained FGM nanotubes – modeling end restraints with torsional springs, deriving a characteristic matrix for natural frequencies, validating the results against prior studies, and quantifying the effects of the FG index and the length scale. Shakhlaviet *et al.* [102] studied von Kármán nonlinear torsional vibrations of FGM carbon nanotubes via nonlocal elasticity, deriving Hamiltonian equations, computing clamped–clamped free natural frequencies using the method of multiple scales, and quantifying the FG index, size, amplitude, and mode effects for design applications. Beni [103] examined the size-dependent, coupled electromechanical torsional behavior of porous, functionally graded flexoelectric microtubes and nanotubes. Barati and Norouzi [104] presented a nonlocal model for the static torsion of bidirectional FG microtubes under a longitudinal magnetic field – deriving the governing equation via the principle of minimum potential energy, validating the generalized differential quadrature method (GDQM) against a Galerkin solution, and showing that the torsional angle depends on the nonlocal parameter. Finally, Zarezadeh *et al.* [105] developed a nonlocal elasticity model for an FG nanorod on a torsional foundation under an axial magnetic field deriving the Navier equations and applying the Hamilton principle, solving them with GDQM, and showing that size effects, introduced through the nonlocal length scale, soften the response and reduce the natural frequencies.

Taking these considerations into account, issues related to the torsion problem, existing torsion theories, and torsion modeling methods are discussed and compared, together with a critical perspective on the topic.

2. FGM torsion problem

The torsional behavior of FGM structures is crucial for understanding their response and for designing proper and effective elements. The use of FGMs can provide improved performance and a more favorable stress gradient, which may result in better-designed components. The torsion of highly anisotropic or orthotropic materials differs markedly from that of isotropic structures. Nonhomogeneity, and thus variation of properties in all directions, makes the modeling process significantly more difficult. Another important problem is the definition of the graded composition. The most popular homogenization methods are based on linear approximations of the modulus of elasticity and the Poisson ratio. For the torsion of FGMs, it is possible to obtain the Kirchhoff modulus through homogenization, as shown by Reuss, Voigt, Hashin–Strikman, and Mori–Tanaka in their works. In contrast, isotropic torsion is much easier to analyze. The distribution of shear stresses is relatively straightforward for shafts with an isotropic and homogeneous microstructure. For a circular shaft, shear stresses are distributed linearly across the cross section and are an increasing function of the radius. This is not the case for twisting shafts with a graded structure, since differences in elastic moduli, and consequently various Kirchhoff modulus, lead to a significantly different distribution of shear stresses across the cross section (see Fig. 2).

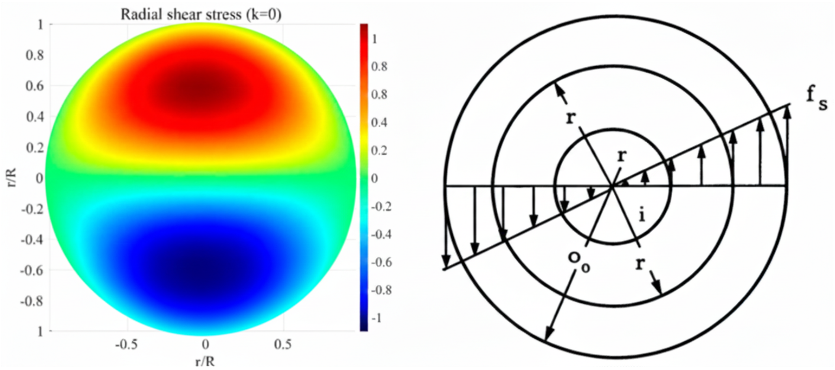

Fig. 2. Shear stress distribution in an isotropic round shaft and a FGM shaft with a metal core and ceramic inner surface, after [17].

The next issue of concern is the angle of twist. For an isotropic shaft with uniform torsional stiffness, the angle of twist is identical at every point on the surface of a circular bar. By contrast, for a functionally graded structure – even under linear homogenization – the torsional stiffness of each layer differs, which in turn affects the total angle of twist of a shaft subjected to a torque M (see Fig. 3).

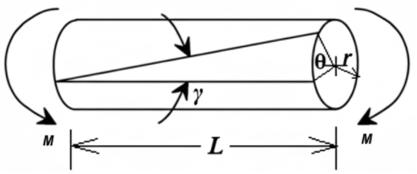

Fig. 3. Angle of twist in an isotropic shaft.

Therefore, when a round shaft is considered, the distribution of shear stresses and the angle of twist present a substantial challenge. An even greater problem arises for noncircular cross sections such as rectangular, elliptical, polygonal, or asymmetrical shapes, where, even for isotropic and homogeneous materials, obtaining accurate calculations and distributions of shear stresses and angles of twist requires multiple approximations and experimental methods. The first assumptions regarding torsion are based on the Prandtl membrane analogy. The membrane analogy is used to visualize the Prandtl stress function for any contour of a twisted shaft's cross section. The values of the Prandtl function at specific points within the cross section that follows a defined contour are related to the distance from this cross section to a membrane surface. This membrane is stretched across the cross-sectional contour and subjected to a uniform pressure acting perpendicular to the cross section. The Prandtl membrane analogy plays a significant role in describing the torsion of FGM structures.

The torsion equation is derived from the stress in a thin membrane subjected to the applied pressure p, which is always perpendicular to the membrane surface (see Fig. 4).

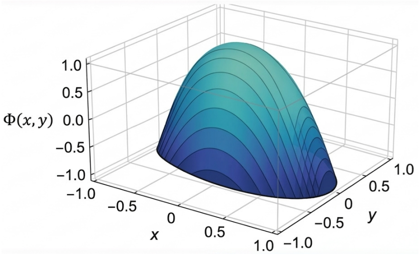

Fig. 4. Prandtl membrane analogy for anh elliptic isotropic cross section, visualization based on [18].

The analysis of an isotropic material is based on a Poisson-type partial differential equation that describes the torsional behavior of a shaft, thereby relating it to the membrane stress T. The following equation applies:

$$\nabla^2 \omega = -\frac{p}{T}, \tag{2.1}$$

where p is the distributed pressure across the membrane, analogous of torque, and T is the equivalent torsional stiffness.

In the case of FGMs, the mathematical formulation is more complicated, since the material properties, such as the Young modulus E, the Poisson ratio, and consequently the Kirchhoff modulus G must depend on the functions $p(y, z)$ and $T(y, z)$, which describe the change in material properties along the directions of gradation, according to the following equation:

$$\nabla^2 \omega = -\frac{p(y, z)}{T(y, z)}, \tag{2.2}$$

where $p(y, z)$ and $T(y, z)$ are functions describing the local material properties.

The application of Eq. (2.2) allows the changes in mechanical properties to vary in both the x- and y-directions. This approach is crucial for tailoring material behavior under mechanical stresses to specific directional requirements, thereby enhancing the design and functionality of advanced material systems such as FGMs, as shown in Fig. 5.

Numerous analogies for various FGMs can be found, among others, in the work of Barretta and Luciano [10], who established a new analogy between the orthotropic FGM Saint-Venant beam and the Kirchhoff plate. These studies demonstrated the aforementioned relationship and expanded upon earlier assumptions, see [19–27]. During the simulation of torsion processes in graded

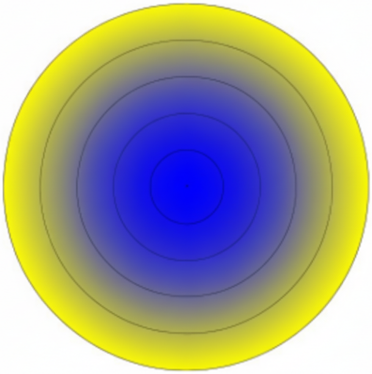

Fig. 5. Material gradation in a circular cross section.

materials, a number of approximation-related issues arise. To address these, numerous theories are employed, typically assuming material heterogeneity in one direction of the coordinate system. These approaches are discussed in the following sections.

3. Analytical torsion modeling methods

Modeling of FGMs primarily involves applying variable material properties along a single direction. To describe behavior under a twisting moment, existing torsion models are predominantly used with extensions that account for the property gradient in one direction and the dependence of changes in specific properties such as the Young modulus, Kirchhoff modulus, Poisson ratio, and density on variations along the chosen direction. The most widely used developments in torsion modeling include the classical Saint-Venant torsion model, the Prandtl membrane analogy, and the Vlasov model. These models are described further in the context of their application to FGMs.

3.1. Saint-Venant theorem

The beginnings of mathematical modeling of structures made from gradient materials can be traced back to issues raised by Saint-Venant. The Saint-Venant principle, although originally developed for homogeneous and isotropic materials, can also be applied to the analysis of FGMs. These materials are characterized by a gradual change in composition or structure, which leads to variations in their mechanical and thermal properties along a specified direction. The Saint-Venant formulation follows several assumptions. The shaft cross section rotates approximately as a rigid entity around a twist axis. This implies that during torsion the cross section retains its shape with minimal distortion, and every point on it moves in the circular trajectory around the twist axis.

The shaft features a prismatic cross section, meaning it is constant and uniform along its entire length. This uniformity simplifies the analysis since the same geometric and material properties apply to every cross section. Additionally, there is warping of the cross section that remains constant across all sections along the shaft length. Warping refers to the out-of-plane displacement of points in the cross section, accounting for the fact that in real materials the cross section is not perfectly rigid. These restrictions impose several limitations on the torsion model itself, especially when considering nonhomogeneous materials such as FGMs. Overcoming some of these limitations allows for a more comprehensive simulation of shaft torsion.

In FGMs, the Saint-Venant principle is particularly useful because it allows simplification of stress analysis in regions far from the point of load application. Despite the variable characteristics of the material, this principle assumes that local effects of loads, such as stress concentration or detailed stress distribution around the points of force application, diminish quickly as one moves away from the source of the load. Most examples are based on torsion analysis introduced by Saint-Venant. The characterization of torsional behavior is challenging for FGM structures. The original theory of torsion is based on isotropic shafts with a constant angle of twist. When it is applied to FGM structures, it is crucial to account properly for the spatial variation of material properties across the volume. FGMs are designed so that their mechanical, thermal, or electrical properties change gradually in response to specific application requirements. The Poisson-type equation is presented as follows [28, 29]:

$$\nabla^2\Phi + \left(\frac{\operatorname{grad} G}{G}\right)\cdot\nabla\Phi = -2G\theta. \tag{3.1}$$

The Poisson-type torsion equation is a partial differential equation in which, to describe changes in the Kirchhoff modulus G, the material properties must depend on variations in one direction. $\nabla^2\Phi$ denotes the Laplacian of the Prandtl function in the shaft cross section, $(\nabla G/G)\cdot\nabla\Phi$ represents the spatial variability of the Kirchhoff modulus G across the volume, and $-2G\theta$ captures the effect of the Kirchhoff modulus and the boundary-condition terms. The Saint-Venant torsion formulation relies on the dependence of the torsion function on material properties that vary in one or more directions. Because Saint-Venant theory is limited for FGM materials, it is necessary to improve and extend it to describe their torsional behavior more comprehensively and accurately. An important aspect is the proper treatment of material properties that vary with coordinate direction (usually a single direction), together with a fuller account of material inhomogeneity, which requires consideration of the equilibrium equations and boundary conditions. Another promising direction is the development of validation experiments to confirm and calibrate the theory.

3.2. PRANDTL MEMBRANE ANALOGY

The Prandtl torsion model addresses the torsion of prismatic shafts and primarily describes the distribution of shear stresses in prismatic shafts subjected to a twisting moment. Initially, the membrane analogy was applied only to isotropic and homogeneous materials, but over time it has been extended to nonhomogeneous materials such as FGMs. The Prandtl membrane analogy relates the torsion of a prismatic rod to a thin elastic membrane that is hypothetically stretched and conformed to the given cross section subjected to torsion. In the case of FGMs, applying this theory requires accounting for material dependence along the directions of gradation, x and y. For isotropic and homogeneous shafts, the Poisson-type equation is given by [30, 31]:

$$\nabla^2 \Phi = -2G\theta, \tag{3.2}$$

where Φ is the Prandtl function, G is the shear modulus (constant for homogeneous materials), and θ is the angle of twist per unit length.

In the case of FGM materials, to obtain the correct Prandtl function it is necessary to treat the Kirchhoff modulus as dependent on the spatially varying material properties, $G(x, y)$. This requires modifying the classical Prandtl equation by allowing G to depend on the x- and y-directions. After this modification, the Poisson-type equation for FGMs is as follows:

$$\nabla \cdot [G(x, y)\nabla \Phi] = -2G(x, y)\theta. \tag{3.3}$$

After modifying the differential equation and making it dependent on the derivatives of the material properties in the x- and y-directions, the equation is as follows [31]:

$$\frac{\partial}{\partial x}\left[G(x, y)\frac{\partial \Phi}{\partial x}\right] + \frac{\partial}{\partial y}\left[G(x, y)\frac{\partial \Phi}{\partial y}\right] = -2G(x, y)\theta. \tag{3.4}$$

The membrane analogy offers several advantages. It enables a relatively straightforward determination of shear stress distributions in cross sections of rods subjected to torsion and provides a clear visualization. It is applicable to various cross-sectional shapes, which makes it highly useful. For FGMs, however, applying the membrane analogy introduces computational complexity. The use of complex material models can make analytical solutions difficult to obtain and, in some cases, unattainable.

3.3. VLASOV TORSION MODEL

Another commonly used torsion model is the Vlasov torsion model. It extends the Saint-Venant model by incorporating the effects of warping restraint.

In this model, warping is not negligible, which introduces additional dependencies required to obtain accurate results. The theory is mainly applied to thin-walled beam elements, where the warping effect is particularly evident and significant.

The Vlasov torsion theory primarily accounts for warping effects in cross sections and for the interaction between cross-sectional torsion and bending deformation. Another key concept is the shear center, defined as the point where shear stresses do not induce additional torsional effects [32, 33]. The torsion equation for a thin-walled beam with cross-sectional warping, as presented by Vlasov, is given by [33–35]:

$$\frac{\partial}{\partial x}\left(G(x)J_t\frac{\partial\theta}{\partial x}\right)+E(x)I_w\frac{\partial^3\theta}{\partial x^3}=0, \tag{3.5}$$

where $G(x)$ is the shear modulus dependent on the direction of property changes, J_t is the polar moment of inertia of the cross section, $E(x)$ is the Young modulus dependent on the direction of material property changes, I_w is the warping constant (warping moment of inertia) for the characteristic cross section, and θ is the angle of twist of the given cross section. Many studies address the torsion problem for FG thin-walled beams. A few representative works are outlined further.

ADDESSI *et al.* [35] presented a comparison of the impact of warping effects on various thin-walled cross sections according to the Vlasov and Benscoter theories. They developed numerical models and compared the resulting predictions. Additional contributions include three works by MURÍN *et al.* [36–38], which present a series of extensions on the application of thin-walled theory to FGM beams, the role of warping during torsion, and the influence of graded property variation on the distribution of mode shapes, bimoment, and shear stresses in thin-walled beam cross sections.

4. MODELING METHODS

Due to the complexity of calculations and the sophisticated material models required to represent variable material properties, FGMs are of great interest in the contemporary scientific community. The potential for continuous improvements and the development of stiffer, stronger materials that can be applied across diverse industrial environments motivates researchers to conduct new experiments and studies on modeling the mechanics of various FGM structures.

The most commonly used methods for modeling structures with graded properties are the FEM and the FDM. With advanced numerical models, researchers can represent the behavior of FGM beams under loads, isolate the effects of cross-sectional warping, and analyze shear stress distributions during torsion, shear deformations, and mode shapes with reasonable accuracy. Every numerical model involves some degree of approximation and assumptions; therefore, it is never fully consistent with reality. FGMs, and the simulation of property variation in at least one direction, require homogenization and property approximation using established cross-sectional homogenization formulas. The accuracy of such models and simulations may be questioned because many publications do not include validation or calibration of the models. Further, issues related to these problems and the current state of knowledge in the scientific community are presented.

The internal structure of each FGM can be designed in different ways. Owing to variations in properties and their spatial distribution within a given structure, one can distinguish materials with different gradient architectures. Achieving a specific gradient profile depends on the manufacturing method used for the FGM. The following types of gradients are distinguished: (c), (f) – composition gradient; (d), (g) – orientation gradient; and (e), (h) – fraction gradient, as shown in Fig. 6.

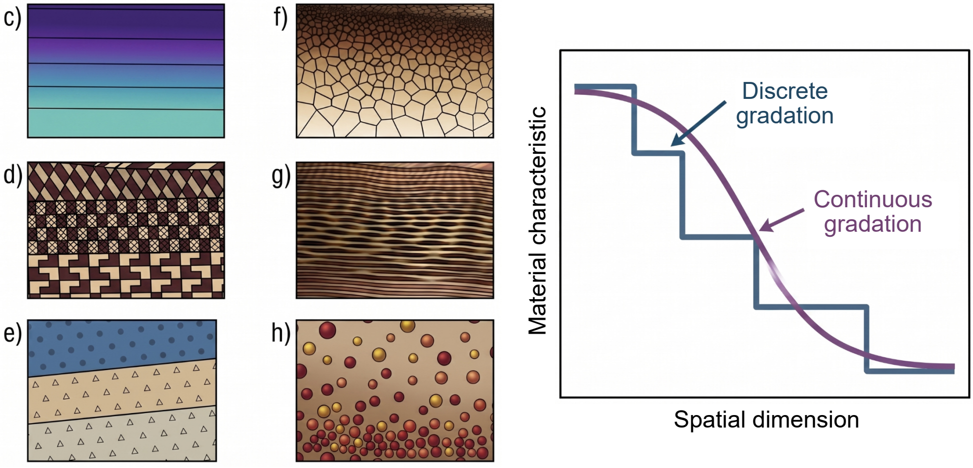

Fig. 6. FGM with various types of gradient, visualization based on [53, 54].

FGMs can be categorized into discontinuous and continuous types, as illustrated schematically in Fig. 6a and Fig. 6b. In discontinuous FGMs, the composition and microstructures change in a stepwise manner, typically across an interface. In continuous FGMs, the composition and microstructures vary gradually and continuously with position. Figure 6 schematically depicts various types of FGMs. Additionally, graded structures may occur throughout the entire material or within specific localized regions [54].

4.1. FEM modeling

Modeling of FGMs can be performed using two different approaches within the finite element formulation. The first is the classical method, which models finite elements that are homogeneous and isoparametric, following the principles used in commercial software such as Ansys. This approach is based on the formulation of isoparametric finite elements, which are defined by a prescribed shape functions and then used to approximate both the element geometry and the unknown field. In this method, the displacement vector and the coordinate vector are expressed as functions [39, 40, 42]:

$$\mathbf{u}_i^e = \sum_{i=1}^{n} \mathbf{N}_i \mathbf{u}^e, \qquad \mathbf{x} = \sum_{i=1}^{n} \mathbf{N}_i \mathbf{x}_i, \tag{4.1}$$

where $\mathbf{N}_i$ is the shape function, $\mathbf{u}_i$ is the nodal displacement, and n is the number of nodal points of the element. Here are examples of shape functions for a triangular element:

$$N_1 = 1 - \xi - \eta, \qquad N_2 = \xi, \qquad N_3 = \eta, \tag{4.2}$$

where ξ and η are the natural coordinates within the triangular element.

The constitutive relation between the stress tensor $\boldsymbol{\sigma}^{\mathrm{e}}$ and the strain is given by [40, 42]:

$$\boldsymbol{\sigma}^{\mathrm{e}} = \mathbf{D}^{\mathrm{e}} \boldsymbol{\epsilon}^{\mathrm{e}}, \tag{4.3}$$

where $\mathbf{D}^{\mathrm{e}}$ is the constitutive matrix and $\boldsymbol{\epsilon}^{\mathrm{e}}$ is the strain obtained from displacement. Thus, $\boldsymbol{\epsilon}^{\mathrm{e}}$ can be formulated as [40]:

$$\boldsymbol{\epsilon}^{\mathrm{e}} = \mathbf{B}^{\mathrm{e}} \mathbf{u}^{\mathrm{e}}, \tag{4.4}$$

where $\mathbf{B}^{\mathrm{e}}$ is the strain-displacement matrix of the shape function, and $\mathbf{u}^{\mathrm{e}}$ is the nodal displacement vector.

The main static equation based on the principle of virtual work is given by [40, 42]:

$$\mathbf{F}^{\mathrm{e}} = \mathbf{k}^{\mathrm{e}} \mathbf{u}^{\mathrm{e}}, \tag{4.5}$$

where $\mathbf{k}^{\mathrm{e}}$ is the force vector described with integration formula [40, 42]:

$$\mathbf{k}^{\mathrm{e}} = \int_{\Omega^{\mathrm{e}}} (\mathbf{B}^{\mathrm{e}})^{\mathrm{T}} \mathbf{D}^{\mathrm{e}} \mathbf{B}^{\mathrm{e}} \mathrm{d}\Omega^{\mathrm{e}}, \tag{4.6}$$

where the superscript $^{\mathrm{T}}$ describes the transpose and Ω^{e} is the domain of element (e). This type of classical formulation provides homogenous material properties, thus stiffness matrix remains constant. When the domain is discretized into finite elements, continuity between elements with different material properties is preserved, ensuring consistency of the properties at the Gauss integration points [39].

The next method of numerical representation is based on [41] and called isoparametric graded finite elements. This method involves interpolating material properties at each integration point from the material properties at each node using isoparametric shape functions, which have identical properties in the given coordinate system (x, y):

$$x = \sum_{i=1}^{n} N_i x_i, \qquad y = \sum_{i=1}^{n} N_i y_i, \tag{4.7}$$

and for the displacements:

$$u = \sum_{i=1}^{n} N_i u_i, \qquad v = \sum_{i=1}^{n} N_i v_i. \tag{4.8}$$

Using these properties, the Young modulus $E = E(x)$ and the Poisson ratio $\nu = \nu(x)$ functions can be interpolated using the isoparametric concept, as shown in Fig. 7:

$$E = \sum_{i=1}^{n} N_i E_i, \qquad \nu = \sum_{i=1}^{n} N_i \nu_i. \tag{4.9}$$

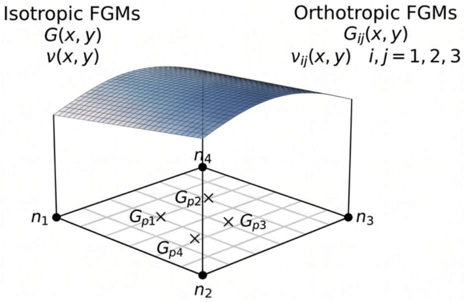

Fig. 7. Isoparametric formulation for isotropic and orthotropic FGMs, visualization based on [41].

This consideration presents the isoparametric formulation for an isotropic material. For an orthotropic material, it involves formulating four elastic parameters: the Young modulus $E_{11} = E_{11}(x)$, $E_{12} = E_{12}(x)$, the shear modulus

$G_{12} = G_{12}(x)$, and the Poisson ratio $\nu_{12} = \nu_{12}(x)$. The final formulation is given as [41, 43], as shown in Fig. 7:

$$\begin{aligned} E_{11} &= \sum_{i=1}^{n} N_i (E_{11})_i, \qquad & E_{22} &= \sum_{i=1}^{n} N_i (E_{22})_i, \\ G_{12} &= \sum_{i=1}^{n} N_i (G_{12})_i, \qquad & \nu_{12} &= \sum_{i=1}^{n} N_i (\nu_{12})_i. \end{aligned} \tag{4.10}$$

Another considered model is one that varies depending on the volume fraction V and the material phase p. For this type of model, the isoparametric formulation is carried out in the classical manner according to a given function with exponent V_i^p, where the values V^p correspond to the values at the nodal points [41, 43]:

$$V^p = \sum_{i=1}^{n} N_i V_i^p. \tag{4.11}$$

4.2. HOMOGENIZATION RULES

Due to the variable internal structure in terms of mechanical properties such as the Young modulus, the Poisson ratio, and the Kirchhoff modulus in torsion, each object must be approximated according to spatially varying properties. This is necessary to obtain accurate analyses and results. Material approximations or FGM models that represent property variation are described in various ways. To model material behavior under torsion correctly, it is essential to idealize mathematically the internal substructures of the materials and, consequently, the variation in volume fractions of its constituents within each unit length or volume of the FGM. The material model may be represented as a particulate model with defined mixing phases, or as a multilayer model in which each layer follows a graded approximation of properties. The first model presented is the Voigt material model [47], which describes changes in material properties in terms of changes in volume fraction. The expression for the Young modulus is given by the following equation [47]:

$$\overline{E}^{\mathrm{V}} = E_1 V_1 + E_2 V_2, \tag{4.12}$$

where V_1 and V_2 are the volume fractions of the two materials. Thus, the sum of the fractions must satisfy:

$$V_f = 1 - V_1. \tag{4.13}$$

According to Voigt, the fraction V_f can be written as

$$V_f = \left(0.5 + \frac{z}{h}\right)^k, \tag{4.14}$$

where k is the positive power-law exponent and z/h is the dimensionless coordinate ratio. The resulting relation for the Young modulus is

$$\overline{E}^{\mathrm{V}}(z) = E_2 + (E_1 - E_2)\left[1 - \left(0.5 + \frac{z}{h}\right)^k\right]. \tag{4.15}$$

Accordingly, the dependence of the Kirchhoff modulus on the phases is [47]:

$$\overline{G}^{\mathrm{V}}(V_f) = G_1 V_f + G_2(1 - V_f), \tag{4.16}$$

where G_1 and G_2 are the Kirchhoff moduli of the two constituent materials.

The next model is the Reuss model [44–46], which assumes a uniform stress distribution throughout the material. The Young modulus $E = E(V_f)$ is given by

$$\overline{E}^{\mathrm{R}}(V_f) = \frac{E_1 E_2}{E_1 V_f + E_2(1 - V_f)}, \tag{4.17}$$

where E_1 and E_2 are the Young moduli of the two materials and V_f is the same volume-fraction function as in the Voigt model. The corresponding Kirchhoff modulus is [46]:

$$\overline{G}^{\mathrm{R}}(V_f) = \frac{G_1 G_2}{G_1 V_f + G_2(1 - V_f)}. \tag{4.18}$$

The next model considered is the Mori–Tanaka material model. In this approach, the homogenized composite consists of two phases: inclusions that are uniformly distributed and assumed spherical, and a matrix that is randomly oriented. The influence of the Poisson ratio on the overall behavior is typically considered negligible and taken as constant. The Kirchhoff modulus according to the Mori–Tanaka scheme is [48, 49]:

$$\overline{G}^{\mathrm{MT}}(V_f) = G_1 + \frac{V_f(G_2 - G_1)G_1}{(1 - V_f)(G_2 - G_1)\beta_1 + G_1}, \tag{4.19}$$

where

$$\beta_1 = \frac{6(K_1 + 2G_1)}{5(3K_1 + 4G_1)}, \tag{4.20}$$

and K is the bulk modulus.

Hashin and Shtrikman [51] proposed narrower bounds using the principle of minimum potential energy and polarization concepts, thereby defining rigorous upper and lower bounds for homogenized properties. The upper bound of the Kirchhoff modulus is [50, 51]:

$$\overline{G}^{\mathrm{HS}+}(V_f) = G_2 + \frac{(G_1 - G_2)V_f}{1 + \zeta(1 - V_f)(G_1/G_2 - 1)}, \tag{4.21}$$

where

$$\zeta = \frac{1+\nu}{3(1-\nu)}. \tag{4.22}$$

The lower bound is [50, 51]:

$$\overline{G}^{\mathrm{HS}-}(V_f) = G_1 + \frac{(G_2 - G_1)(1 - V_f)}{1 + \zeta V_f(G_2/G_1 - 1)}. \tag{4.23}$$

Each of these theories specifies the Kirchhoff modulus as a function of the volume fraction. As shown in Fig. 8, the Voigt and Reuss models yield substantially wider bounds than the Hashin–Shtrikman bounds, which provide tighter constraints. These bounds depend solely on the volume fractions of the phases and are therefore scale-independent.

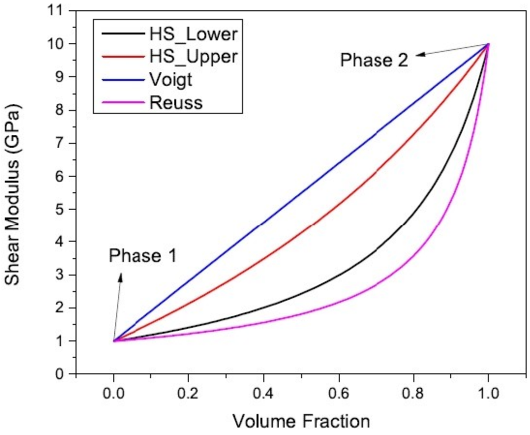

Fig. 8. Shear modulus between two phases as a function of volume fraction, after [52].

Another material model is the exponential material model (EMM). In this formulation, properties vary according to an exponential function, producing smooth transitions through the FGM thickness. This approximation can be applied to properties such as the Young modulus, the Kirchhoff modulus, or thermal conductivity. If the property variation through the thickness is exponential, the Kirchhoff modulus can be approximated as [53]:

$$\overline{G}^{\mathrm{EMM}}(z) = G_2 \exp(\beta z), \tag{4.24}$$

where $\beta = \frac{1}{h} \ln\left(\frac{G_1}{G_2}\right)$, and G_1 and G_2 are the Kirchhoff moduli of the two materials, h is the thickness, and z is the coordinate varying from 0 to h.

The power-law material model is also widely used for FGMs. The volume-fraction variation of an FGM layer can be represented as

$$V_f = f(z) = \left(\frac{z + h/2}{h}\right)^n, \tag{4.25}$$

where $f(z)$ denotes the volume fraction of one constituent; accordingly, the other constituent has fraction $1 - V_f$. Once the local volume fraction is known, pointwise properties follow from the rule of mixtures. In particular, the Kirchhoff modulus $G(z)$ within the layer is [53]:

$$\overline{G}^{\mathrm{PLMM}}(z) = G_1 V_f + G_2(1 - V_f), \tag{4.26}$$

where G_1 and G_2 are the Kirchhoff moduli of the two materials.

Another important model is the linear variation model. Here, the Poisson ratio $\nu(x)$ is taken as constant, while the Young modulus and the Kirchhoff modulus vary linearly with the gradation. The elastic modulus $E(x)$ and the Kirchhoff modulus $G(x)$ are expressed as [41]:

$$\overline{E}^{\mathrm{LVM}}(x) = E + \gamma x, \qquad \overline{G}^{\mathrm{LVM}}(x) = G + \gamma x, \tag{4.27}$$

where x is the graded coordinate, and γ is the parameter of nonhomogeneity defined by [41]:

$$\gamma = \frac{G(W) - G(0)}{W}, \qquad \gamma = \frac{E(W) - E(0)}{W}, \tag{4.28}$$

where W denotes the width of the graded region.

The final model is the sigmoid material model. It uses two functions to represent the change in properties with gradation, effectively partitioning the beam into two regions and describing the behavior in each. For one coordinate direction, changes are defined on the domains $-h/2$ to 0 and 0 to $h/2$, where h is the graded height. The expressions for the Young modulus are

$$\overline{E}^{\mathrm{SMM}}(z) = E_2 + (E_1 - E_2)\left[1 - \frac{1}{2}\left(\frac{z}{h} + \frac{1}{2}\right)^k\right] \tag{4.29}$$

for $-h/2 \leq z \leq 0$, and

$$\overline{E}^{\text{SMM}}(z) = E_1 + \frac{E_1 - E_2}{2}\left(\frac{z}{h} + \frac{1}{2}\right)^k \tag{4.30}$$

for $0 \leq z \leq h/2$.

4.3. ACCURACY OF RESULTS

Modeling FGM properties typically uses either homogeneous or heterogeneous finite elements. KIM and PAULINO [41] were the first to model FGMs using heterogeneous elements, moving beyond classical homogeneous elements for, which only midpoint responses match the FGM solution.

Partitioning the domain into equal segments and assigning homogeneous elements does not accurately represent heterogeneous behavior, as shown by HERNIK [39]. In contrast, using heterogeneous elements that account for spatial variation in the Young modulus and Kirchhoff modulus at each point along the graded layer leads to markedly improved simulation outcomes in FGM regions. Figure 9 and Fig. 10 show x-direction displacements and the differences between homogeneous and heterogeneous finite elements.

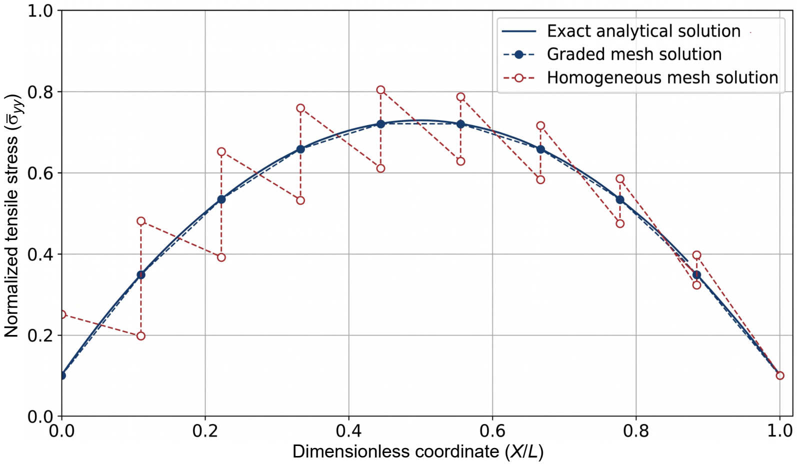

FIG. 9. Stress-distribution differences among exact, graded, and homogeneous elements, visualization based on [41].

According to KIM and PAULINO [41], employing heterogeneous elements yields more accurate stress and deformation predictions in tensile tests. Mesh refinement reduces discrepancies between homogeneous and heterogeneous formulations for all considered cases [41].

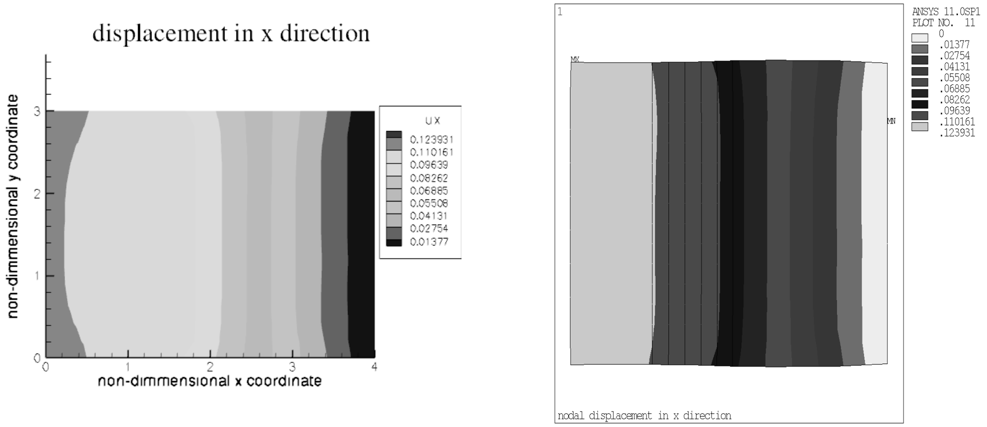

Fig. 10. Differences in x-direction displacement for homogeneous versus heterogeneous finite elements, after [39].

5. Comparison of achievements

5.1. Achievements

The torsional mechanics of structures made from FGMs presents a range of challenges across various formulations, including homogenization of the material model, mixing rules for individual graded phases, and approaches to homogenizing the gradation direction itself. Many studies model gradation along the longitudinal direction for beams or rods, while others focus on homogenization of the cross section. Over time, approaches to analyzing FGMs have evolved. Numerous limitations have been identified when using homogeneous elements in FEM, including inaccuracies in representing gradient variations. The comparison presented in Table 1 summarizes advances in the torsion of FGMs developed over the past several decades, with the aim of compiling these results in a concise form for comparison.

5.2. Comparison

The torsional response of structures and bars made from FGMs has been extensively studied, with the literature emphasizing their importance for understanding material behavior under complex loading conditions. Foundational work by Rooney and Ferrari [5] made a significant contribution through the analysis of FG shafts with rectangular cross sections. They examined the torsion and bending of bars with variable shear modulus, determined stiffness bounds, and presented solutions for specific cases such as laminates and cylindrical bars. The results were used to evaluate graded material properties.

Table 1. Comparison of key findings in torsion of FGMs over decades.

No.	Scientists	Landmark achievement
1	Rooney, Ferrari [55]	Investigation of the torsion of an FGM shaft with a rectangular cross section.
2	Rooney, Ferrari [56]	Analysis of torsional behavior in various classes of FG shafts.
3	Rooney, Ferrari [5]	Combination of torsion and flexure in inhomogeneous elements, exploring the relationship between material properties and structural response.
4	Horgan, Chan [4]	Analysis of isotropic, linearly elastic bars with a functional gradient, showing stress distribution across these bars.
5	Horgan, Chan [57]	Presentation of the stress response in rotating isotropic FGM disks, considering the effect of the gradient.
6	Ting *et al.* [58]	Demonstration that neutrality occurs when the geometric mean of the cylinder's shear moduli equals the shear modulus of the shaft, and out-lining criteria for preserving rigidity with embedded cylinders.
7	Singh *et al.* [59]	Analysis of torsional vibrations of graded cylinders, considering shear moduli and densities as functions of radius and axis.
8	Batra [6]	Examination of the torsion of cylindrical bars with material moduli varying along the axis.
9	Sofiyev, Schnack [60]	Study of the stability of FG cylindrical shells under dynamic torsional loading as a linear function of time.
10	Li *et al.* [61]	Examination of a cylindrical crack in a graded layer between coaxial cylinders subjected to dynamic torsional loading.
11	Hematiyan, Estakhrian [62]	Development of an approximate analytical method for analyzing the torsion of FG open-section members with uniform thickness.
12	Arghavan, Hematiyan [63]	Study of the torsion of hollow tubes with a functional gradient, identifying the impact of the gradient on stiffness and torsional resistance.
13	Gholami Bazehhour, Rezaeepazhand [64]	Analysis of the torsion of multilayered tubes with non-circular cross sections, focusing on the influence of material properties.

Table 1. [Cont.]

No.	Scientists	Landmark achievement
14	Vasiliev [65]	Analysis of the torsion of a circular punch on a half-space with a graded coating, reducing the problem to integral equations and deriving an ex-plicit solution.
15	Wang *et al.* [66]	Solution for torsional vibrations in FG finite hollow cylinders, focusing on the analysis of transient behavior and vibration characteristics.
16	Shen *et al.* [67]	Development of a size-dependent gradient shaft model to study the effects of microstructure and material scale on torsional wave propagation, free vibration, and static torsion, considering radial variation of material properties.
17	Bayat, Ekhteraei Toussi [68]	Study of the elasto-plastic torsion of FGM shafts with a ceramic-metal structure, where the plastic zone may develop on the surfaces or within the thickness of the shaft, depending on material inhomogeneity and thickness.
18	Huang *et al.* [69]	Analysis of the elasto-plastic buckling of cylindrical FGM shells under axial and torsional loads using the Tamura–Tomota–Ozawa (TTO) model and the Ritz method.
19	Tsiatas, Babouskos [70]	Presentation of a new solution to the elasto-plastic torsion problem of FGM bars using an iterative numerical method based on BEM and AEM.
20	Murín *et al.* [71]	Presentation of an elastostatic analysis of spatial beam structures made of FGMs, considering smoothly varying material properties along the longitudinal direction and symmetric variations in the transverse and lateral directions.
21	Barretta *et al.* [12]	Formulation of the elastostatic problem of FG circular nanobeams under torsion, incorporating nonlocal elastic behavior based on the Eringens theory.
22	Liaghat *et al.* [72]	Investigation of material tailoring in FG hollow rods with arbitrary cross sections under torsion.
23	Barretta *et al.* [73]	Analysis of the torsion of linearly elastic, isotropic beams with inhomogeneities in the cross section and along the beam axis.
24	Bayat *et al.* [74]	Presentation of torsion problem for hollow cylinders made of FGM, considering arbitrary variations of the Young modulus and the Poisson ratio in the radial direction.

Table 1. [Cont.]

No.	Scientists	Landmark achievement
25	Rizov [75]	Analysis of a cylindrical surface crack in circular shafts under torsional loading, considering nonlinear material behavior.
26	Rahaeifard [76]	Examination of the size-dependent behavior of FG microbars based on the modified couple stress theory, defining two length scale parameters to describe their mechanical properties.
27	Aminbaghai *et al.* [77]	Analysis of the impact of torsional warping and secondary deformations on the deformation and stress states in thin-walled FGM beams with longitudinally varying properties.
28	Murín *et al.* [78]	Analysis of warping torsion in FGM beams with spatially varying properties, analysis of torsional behavior.
29	Murín *et al.* [38]	Investigation of torsional warping eigenmodes in FGM beams with longitudinally varying properties, determining modal characteristics.
30	Guendouz *et al.* [79]	Torsional-bending in FGM beams using a 3D Saint-Venant refined beam theory.
31	Murín *et al.* [80]	Investigation of the effect of longitudinal variation in material properties on deformation and stresses in thin-walled FGM beams under non-uniform torsion.
32	Guendouz *et al.* [81]	Analysis of the static bending-torsion behavior of FG cantilever beams using an advanced 1D/3D beam theory.
33	Murín *et al.* [36]	Extension of the 3D FGM Timoshenko finite element to include the warping torsion effect for non-uniform torsion.
34	Barati *et al.* [82]	Solution for static torsion in a microtube composed of bidirectional FGMs (BDFGMs).
35	Naghibi *et al.* [83]	Determination of defects in hollow cylinders coated with FGMs under torsion, identifying their impact on stress results.
36	Singh *et al.* [84]	Analysis of shear stresses in FGM bars under pure torsional loading, considering different cross-sectional shapes (circular, square, triangular) and varying thicknesses.
37	Zhang *et al.* [85]	Study of the buckling of FGM cylindrical shells under torsional impact loading using the symplectic method, considering torsional stress waves.

Table 1. [Cont.]

No.	Scientists	Landmark achievement
38	Noroozi *et al.* [86]	Investigation of multiple cylindrical interface cracks between a homogeneous circular cylinder and its FGM coating under torsional impact loading.
39	Li, Hu [87]	Analysis of torsional statics of two-dimensionally FG microtubes, focusing on stress distribution and material properties.
40	Karaca, Alyavuz [88]	Examination of the torsional behavior of beams with one- and two-directional gradation under large displacements and angular deformations, considering power law and sinusoidal functions.
41	Barretta *et al.* [89]	Development of a nonlocal strain gradient theory of elasticity, combining the Eringen nonlocal integral convolution and the Lam strain gradient model through a variational approach.
42	Soltani, Asgarian [90]	Analysis of a lateral buckling of simply supported web- and/or flange-tapered I-beams made of axially FGMs under uniformly distributed loads.
43	Murín *et al.* [91]	Extension of previous research by investigating the effect of spatially varying material properties on torsional eigenvibrations of FGM beams.
44	Hajhashemkhani, Hematiyan [92]	Analysis of inflation, extension, and torsion in hyperelastic rods and tubes, focusing on rubber-like materials and soft biological tissues.
45	Nie *et al.* [93]	Presentation of analytical solutions for the torsion of bidirectional FG, linearly elastic truncated conical cylinders, considering six different functional forms of shear modulus variations in both radial and axial directions.
46	Baksa [94]	Study of analytical solution for Saint-Venant torsion of a circular bar with a slit extending radially from the boundary to the axis.
47	Rizov [95]	Analysis of cylindrical delamination in a multilayered FG circular shaft under torsional loading, based on the Ramberg–Osgood equation.

Their subsequent paper [56] focused on the torsion of bars with inhomogeneous shear modulus and arbitrary geometry, where the modulus varies across the cross section as a function of coordinates with the additional assumption of constancy at the boundary. Solutions were also presented for the torsion of a circular cylindrical bar with angular symmetry.

Further studies by Horgan and Chan [4] extended the analysis to isotropic, linearly elastic bars with functional gradients, providing deeper insight into stress and strain fields. Their additional works [8, 57] addressed rotating bodies and yielded exact solutions for a power-law variation of the Young modulus, showing that stress distributions differ from homogeneous cases and that maximum stresses are not always located at the center. Ting *et al.* [58] investigated the design of neutral cylinders under torsion, considering cylinders with multiple coatings or a graded shear modulus in the cross section. A multilayer cylinder with piecewise-varying shear modulus was generalized to a graded cylinder with continuous radial variation of the shear modulus. The warping field of the neutral graded cylinder is governed by a second-order differential equation, with solutions obtained using the Frobenius method. Singh *et al.* [59] studied torsional vibrations of FG finite cylinders and demonstrated resonance behavior influenced by material gradation, improving the understanding of vibrational responses in graded structures.

Batra [6] provided exact solutions for torsional behavior in FG cylinders, refining theoretical models, while Sofiyev and Schnack [60] examined the stability of FG cylindrical shells under dynamic torsional loads and highlighted the effects of transient stresses. Li *et al.* [61] analyzed a cylindrical crack in a FG interlayer between two coaxial elastic cylinders under torsional impact. The shear modulus and density of the FGM layer varied continuously. The problem was solved numerically, and the dynamic stress intensity factor was computed, showing that increasing the FGM gradient can significantly reduce this factor.

Continued contributions by Horgan [4, 8, 57] on anisotropic, linearly elastic bars with functional gradients, together with the study by Gholami Bazehhour and Rezaeepazhand [64] on multilayered tubes with non-circular cross sections, provided additional depth for complex geometries. Vasiliev [65] presented an analytical solution for the torsion of a circular punch on a transversely isotropic elastic half space with a FG coating. Wang *et al.* [66] provided exact solutions for transient torsional responses of a finitely long FG hollow cylinder under free–free, free–fixed, and fixed–fixed boundary conditions. Shen *et al.* [67] developed a size-dependent shaft model within the framework of nonlocal strain gradient theory, accounting for radial power-law variation in a two-constituent FGM and investigating small-scale effects on static and dynamic torsion, including material length scale and nonlocal parameters.

Huang *et al.* [69] proposed a method for elastoplastic buckling of cylindrical shells made of FGMs under axial and torsional loads, with properties varying according to a power law. The Ritz method and stress-state analysis were used to determine the critical condition and the location of the elastoplastic interface. Tsiatas and Babouskos [70] provided solutions for the elastic-plastic torsion problem of FG bars with arbitrary cross sections and property variation across the section, introducing a simplified nonlinear procedure using the BEM and the AEM. Elastostatic analyses by Murín *et al.* [71], as well as the study by Barretta *et al.* [73] on torsion in nonlocal viscoelastic nanobeams, highlighted novel modeling techniques for FGMs. Liaghat *et al.* [72] examined material tailoring for FG rods under torsion, and Barretta *et al.* [73] presented closed-form solutions for the torsion of linearly elastic isotropic beams with axial and cross-sectional inhomogeneities. New solutions were derived by analyzing axial distributions of longitudinal and shear moduli, and the effects of warping and shear modulus variation on the torsional behavior of elliptic and equilateral triangular beams were discussed.

Ongoing efforts by Bayat *et al.* [74] on generalized solutions for hollow cylinders, Rizov's [75] elastic-plastic fracture analysis, and Rahaeifard's [76] studies on size-dependent torsion illustrate substantial advances in predicting FGM behavior under diverse conditions. Aminbaghai [77] analyzed the influence of torsional warping on the elastostatic behavior of thin-walled twisted FGM beams with longitudinal material variation and secondary deformations due to the twist angle. Murín *et al.* [78] examined the effect of spatially varying properties on the warping torsion of I-section FGM beams using the reference beam method and the FGM-warping tension (WT) finite element. Extended stress equations accounting for secondary torsional moment and warping were applied, reinforcing the importance of torsional analysis for the development of these materials.

Future research directions include expanding understanding and application of FGMs under torsional loads. Promising areas are the development of multifunctional FGMs that combine torsional resistance with enhanced thermal or electrical performance, and the advancement of modeling techniques to capture interactions among torsion, bending, and axial loads in complex geometries. Experimental validation and improved materials characterization are essential for representing gradients accurately in practice. Experimental torsion testing of FGM shafts faces significant reliability challenges. Residual stresses arising from manufacturing (e.g., additive manufacturing (AM), sintering, deposition) and non-ideal material interfaces across graded transitions can distort the measured response. Maintaining perfect coaxiality and geometric tolerances is difficult, even small deviations introduce parasitic bending, compromising data quality. In thin-walled specimens, warping effects are pronounced and often amplified by gradation further obscuring a pure shear state. Finally, the absence of standardized torsion test protocols for FGMs hinders cross-laboratory validation and benchmarking. Investigation of fatigue and long-term durability under cyclic torsional loading is also important, with direct implications for aerospace, automotive, and civil engineering. While significant progress has been achieved, substantial opportunities remain to improve the design and application of FGMs across engineering disciplines.

6. Conclusion and future research

Torsion in FGMs can be described reliably within classical theories, provided they are generalized to account for the spatial variability of elastic parameters. It is essential to introduce $G(x,y)$, $E(x,y)$, and $\nu(x,y)$ explicitly into the torsion equations and to model gradation consistently. Here are the concise conclusions and brief research pointers:

- generalized classical theories in the context of torsion: Saint-Venant, Prandtl, and Vlasov formulations remain applicable when the spatial variability of G, E, and ν is explicitly incorporated and appropriate boundary conditions are enforced;
- gradation modeling: Voigt, Reuss, Hashin–Shtrikman, and Mori–Tanaka schemes as well as power law or exponential profiles are useful; in practice, the tighter Hashin–Shtrikman bounds and Mori–Tanaka estimates typically yield more stable predictions of torsional stiffness;
- numerical methods: isoparametric graded finite elements (per Kim–Paulino formulation) capture heterogeneity more faithfully than classical piecewise-homogeneous meshes and provide a robust basis for torsion analyses of FGMs;
- future research: a promising direction is to implement torsion modeling in commercial solvers such as Ansys, moving beyond the prevalent Ansys parametric design language (APDL)-based studies. Representing material gradation with isoparametric graded finite elements offers a more rigorous, scalable path for complex geometries. Further steps include coupling torsion models with additive manufacturing process simulations to quantify porosity and residual-stress effects, and expanding experimental validation, especially for FGM shafts and thin-walled members where warping complicates the realization of pure shear state. Future work should also assess fatigue and creep under torsion, develop multifunctional FGMs [96] that add thermal, damping, or conductive capabilities, and advance modeling [97, 98] that can capture coupled torsion–bending–axial behavior with explicit material, geometric nonlinearities and anisotropy.

FUNDINGS

This research did not receive any specific grant from funding agencies in the public, commercial, or not-for-profit sectors.

CONFLICT OF INTEREST

The authors declare that there are no known competing financial interests or personal relationships that could have influenced the work described in this paper.

AUTHORS' CONTRIBUTIONS

Mateusz Kumor performed the analysis and wrote the original draft. Artur Ganczarski performed the analysis and contributed to data interpretation. All authors reviewed and approved the final manuscript.

REFERENCES

1. Niino M., Hirai T., Watanabe R., Functionally gradient materials. In pursuit of super heat resisting materials for spacecraft, *Journal of the Japan Society for Composite Materials*, **13**(6): 257–264, 1987, https://doi.org/10.6089/jscm.13.257.
2. Pasha A., Rajaprakash B.M., Functionally graded materials (FGM) fabrication and its potential challenges & applications, *Materials Today: Proceedings*, **52**(3): 413–418, 2022, https://doi.org/10.1016/j.matpr.2021.09.077.
3. Lekhnitskii S.G., *Theory of Elasticity of an Anisotropic Body*, Mir Publishers, Moscow, 1981.
4. Horgan C.O., Chan A.M., Torsion of functionally graded isotropic linearly elastic bars, *Journal of Elasticity*, **52**: 181–199, 1998, https://doi.org/10.1023/A:1007544011803.
5. Rooney F.J., Ferrari M., Torsion and flexure of inhomogeneous elements, *Composites Engineering*, **5**(7): 901–911, 1995, https://doi.org/10.1016/0961-9526(95)00043-M.
6. Batra R.C., Torsion of a functionally graded cylinder, *AIAA Journal*, **44**(6): 1363–1365, 2006, https://doi.org/10.2514/1.19555.
7. Arghavan S., Hematiyan M.R., Torsion of functionally graded hollow tubes, *European Journal of Mechanics – A/Solids*, **28**(3): 551–559, 2009, https://doi.org/10.1016/j.euromechsol.2008.07.009.
8. Horgan C.O., On the torsion of functionally graded anisotropic linearly elastic bars, *IMA Journal of Applied Mathematics*, **72**(5): 556–562, 2007, https://doi.org/10.1093/imamat/hxm027.
9. Chen T., Wei C.-J., Saint-Venant torsion of anisotropic shafts: Theoretical frameworks, extremal bounds and affine transformations, *The Quarterly Journal of Mechanics and Applied Mathematics*, **58**(2): 269–287, 2005, https://doi.org/10.1093/qjmamj/hbi013.

10. Barretta R., Luciano L., Analogies between Kirchhoff plates and functionally graded Saint-Venant beams under torsion, *Continuum Mechanics and Thermodynamics*, **27**: 499–505, 2015, https://doi.org/10.1007/s00161-014-0385-2.

11. Li L., Hu Y., Torsional statics of two-dimensionally functionally graded microtubes, *Mechanics of Advanced Materials and Structures*, **26**(5): 430–442, 2019, https://doi.org/10.1080/15376494.2017.1400617.

12. Barretta R., Feo L., Luciano R., Torsion of functionally graded nonlocal viscoelastic circular nanobeams, *Composites Part B: Engineering*, **72**: 217–222, 2015, https://doi.org/10.1016/j.compositesb.2014.12.018.

13. Nikmehr N., Lashkarbolok M., A numerical investigation on the torsional rigidity of bars with functionally graded material (FGM) cross sections weakened by cracks, *Iranian Journal of Science and Technology, Transactions of Civil Engineering*, **43**: 117–123, 2019, https://doi.org/10.1007/s40996-018-0147-7.

14. Darilmaz K., Orakdöğen E., Girgin K., Saint-Venant torsion of arbitrarily shaped orthotropic composite or FGM sections by a hybrid finite element approach, *Acta Mechanica*, **229**: 1387–1398, 2018, https://doi.org/10.1007/s00707-017-2067-1.

15. Akinlabi E.T., Mikhin M.N., Murashkin E.V., Functionally graded prismatic triangular rod under torsion, *Journal of Physics: Conference Series*, **1474**(1): 012003, 2020, https://doi.org/10.1088/1742-6596/1474/1/012003.

16. Ganczarski A., Szubartowski D., Kumor M., Torsion of non-circular functionally graded material shafts, [in:] *State of the Art and Future Trends in Materials Modelling 2*, Altenbach H., Öchsner A. [Eds], Springer, pp. 115–131, 2024, https://doi.org/10.1007/978-3-031-72900-3_9.

17. Duan T.C., Li X.Y., Xiao Y., Zhang L., Chen C., Li Z.J., A modified lower-order theory for FG beam with circular cross-section, *Frontiers in Materials*, **9**: 1020820, 2022, https://doi.org/10.3389/fmats.2022.1020820.

18. Gil-Martín L.M., Palomares A., Hernández-Montes E., Approximate expression of the Prandtl membrane analogy in linear elastic pure torsion of open thin-walled cross sections and regular polygons, *International Journal of Solids and Structures*, **210–211**: 109–118, 2021, https://doi.org/10.1016/j.ijsolstr.2020.11.020.

19. Timoshenko S., A membrane analogy to flexure, *Proceedings of the London Mathematical Society*, **s2–20**(1): 398–407, 1922, https://doi.org/10.1112/plms/s2-20.1.398.

20. Irschik H., Analogies between bending of plates and torsion problem, *Journal of Engineering Mechanics*, **117**(11): 2503–2508, 1991, https://doi.org/10.1061/(ASCE)0733-9399(1991)117:11(2503).

21. Irschik H., Analogy between refined beam theories and the Bernoulli-Euler theory, *International Journal of Solids and Structures*, **28**(9): 1105–1112, 1991, https://doi.org/10.1016/0020-7683(91)90105-O.

22. Furukawa T., Irschik H., Body-force analogy for one-dimensional coupled dynamic problems of thermoelasticity, *Journal of Thermal Stresses*, **28**(4): 455–464, 2005, https://doi.org/10.1080/01495730590916713.

23. Irschik H., Gusenbauer M., Body force analogy for transient thermal stresses, *Journal of Thermal Stresses*, **30**(9–10): 965–975, 2007, https://doi.org/10.1080/01495730701499024.

24. Irschik H., Nader M., Actuator placement in static bending of smart beams utilizing Mohr's analogy, *Engineering Structures*, **31**(8): 1698–1706, 2009, https://doi.org/10.1016/j.engstruct.2009.02.026.

25. Irschik H., Krommer M., Zehetner C., A generalized body force analogy for the dynamic theory of thermoelasticity, *Journal of Thermal Stresses*, **35**(1–3): 235–247, 2012, https://doi.org/10.1080/01495739.2012.637826.

26. Romano G., Diaco M., Barretta R., Variational formulation of the first principle of continuum thermodynamics, *Continuum Mechanics and Thermodynamics*, **22**: 177–187, 2010, https://doi.org/10.1007/s00161-009-0119-z.

27. Barretta R., Marotti de Sciarra F., Analogies between nonlocal and local Bernoulli–Euler nanobeams, *Archive of Applied Mechanics*, **85**: 89–99, 2015, https://doi.org/10.1007/s00419-014-0901-7.

28. Ugural A.C., Fenster S.K., *Advanced Mechanics of Materials and Applied Elasticity*, Pearson Education, 2011.

29. Makai E., A proof of Saint-Venant's theorem on torsional rigidity, *Acta Mathematica Academiae Scientiarum Hungarica*, **17**: 419–422, 1966, https://doi.org/10.1007/BF01894885.

30. Nikmehr O., Lashkarbolok M., A numerical investigation on the torsional rigidity of bars with functionally graded material (FGM) cross sections weakened by cracks, *Iranian Journal of Science and Technology, Transactions of Civil Engineering*, **43**: 117–123, 2019, https://doi.org/10.1007/s40996-018-0147-7.

31. Prandtl L., Torsion of prismatic rods [in German: Zür torsion von prismatischen stäben], *Phys. Z*, **4**: 758–770, 1903.

32. Pegoraro F., Califano F., Manfredi C., Morrison P.J., Theory and applications of the Vlasov equation, *The European Physical Journal D*, **69**: 68, 2015, https://doi.org/10.1140/epjd/e2015-60082-y.

33. Vlasov V.Z., *Thin-Walled Elastic Beams*, Oldbourne Press, London, 1961.

34. Reddy J.N., *Mechanics of Laminated Composite Plates and Shells: Theory and Analysis*, 2nd ed., CRC Press, 2003.

35. Addessi D., Di Re P., Cimarello G., Enriched beam finite element models with torsion and shear warping for the analysis of thin-walled structures, *Thin-Walled Structures*, **159**: 107259, 2021, https://doi.org/10.1016/j.tws.2020.107259.

36. Murín J., Hrabovský J., Aminbaghai M., Kutiš V., Paulech J., Kugler S., Extension of the FGM beam finite element by warping torsion, *Strojnícky časopis – Journal of Mechanical Engineering*, **69**(2): 57–76, 2019, https://doi.org/10.2478/scjme-2019-0017.

37. Murin J., Aminbaghai M., Hrabovsky J., Balduzzi G., Dorn M., Mang H.A., Torsional warping eigenmodes of FGM beams with longitudinally varying material properties, *Engineering Structures*, **175**: 912–925, 2018, https://doi.org/10.1016/j.engstruct.2018.08.048.

38. Murin J., Kugler S., Habrovsky J., Kutis V., Paulech J., Aminbaghai M., Influence of spatially varying material properties on the bimoment normal and shear stresses by warping torsion of FGM beams, *Composite Structures*, **256**: 113043, 2021, https://doi.org/10.1016/j.compstruct.2020.113043.

39. Hernik S., New concept of finite element method for FGM materials, *Czasopismo Techniczne. Mechanika*, **107**(8): 99–106, 2010.

40. Ansys, *Theory reference, Ansys 2021 R2*, Ansys INC, 2021, https://www.scribd.com/document/665578059/Ansys-Mechanical-APDL-Theory-Reference.

41. Kim J.-H., Paulino G.H., Isoparametric graded finite elements for nonhomogeneous isotropic and orthotropic materials, *Journal of Applied Mechanics*, **69**(4): 502–514, 2002, https://doi.org/10.1115/1.1467094.

42. Hughes T.J.R., *The Finite Element Method: Linear Static and Dynamic Finite Element Analysis*, Dover Publication, 2012.

43. Jin Z.-H., Paulino G.H., Dodds Jr. R.H., Finite element investigation of quasi-static crack growth in functionally graded materials using a novel cohesive zone fracture model, *Journal of Applied Mechanics*, **69**(3): 370–379, 2002, https://doi.org/10.1115/1.1467092.

44. Năstăsescu V., Marzavan S., An overview of functionally graded material models, *Proceedings of the Romanian Academy, Series A: Mathematics, Physics, Technical Sciences, Information Science*, **23**(3): 259–267, 2022.

45. Mathew C., Oluomachi E., Mechanics and computational homogenization of effective material properties of functionally graded (composite) material plate FGM, *International Journal of Scientific and Research Publications*, **13**(9): 128–150, 2023, https://doi.org/10.29322/IJSRP.13.09.2023.p14120.

46. Reuss A., Calculation of the yield point of mixed crystals on the basis of the plasticity condition for single crystals [in German: Berechnung der fließgrenze von mischkristallen auf grund der plastizitätsbedingung für einkristalle], *ZAMM – Journal of Applied Mathematics and Mechanics / Zeitschrift für Angewandte Mathematik und Mechanik*, **9**(1): 49–58, 1929, https://doi.org/10.1002/zamm.19290090104.

47. Voigt W., On the relationship between the two elasticity constants of isotropic bodies [in German: Über die Beziehung zwischen den beiden Elasticitätsconstanten isotroper Körper], *Annalen der Physik*, **274**(12): 573–587, 1889, https://doi.org/10.1002/andp.18892741206.

48. Aboudi J., Arnold S.M., Bednarcyk B.A., *Micromechanics of Composite Materials: A Generalized Multiscale Analysis Approach*, Butterworth-Heinemann, 2013, https://doi.org/10.1016/C2011-0-05224-9.

49. Mori T., Tanaka K., Average stress in matrix and average elastic energy of materials with misfitting inclusions, *Acta Metallurgica*, **21**(5): 571–574, 1973, https://doi.org/10.1016/0001-6160(73)90064-3.

50. Pobedra B., *Mechanics of Composite Materials* [in Russian], Moscow University, Moscow, 1984.

51. Hashin Z., Shtrikman S., A variational approach to the theory of the elastic behaviour of multiphase materials, *Journal of the Mechanics and Physics of Solids*, **11**(2): 127–140, 1963, https://doi.org/10.1016/0022-5096(63)90060-7.

52. Saharan A., *Homogenization and elastic-plastic transitions in random and FGM microstructures*, Ph.D. Thesis, University of Illinois at Urbana-Champaign, 2015.

53. El-Galy I.M., Bassiouny I.S., Mahmoud H.A., Functionally graded materials classifications and development trends from industrial point of view, *SN Applied Sciences*, **1**: 1378, 2019, https://doi.org/10.1007/s42452-019-1413-4.

54. Zhang C. *et al.*, Additive manufacturing of functionally graded materials: A review, *Materials Science and Engineering: A*, **764**: 138209, 2019, https://doi.org/10.1016/j.msea.2019.138209.

55. Rooney F.J., Ferrari M., *Torsion of a Functionally Graded Shaft With Rectangular Cross Section*, American Society of Mechanical Engineers, New York, 1994, https://www.osti.gov/biblio/82883.

56. Rooney F.J., Ferrari M., Torsion of a class of functionally graded shafts, Conference paper, *American Society of Mechanical Engineers*, 1995, https://www.osti.gov/biblio/86253.

57. Horgan C.O., Chan A.M., The stress response of functionally graded isotropic linearly elastic rotating disks, *Journal of Elasticity*, **55**: 219–230, 1999, https://doi.org/10.1023/A:1007644331856.

58. Ting T.C.T., Chen T., Li K.S., Torsion of an isotropic shaft of arbitrary cross-section embedded with multicoated or graded circular cylinders of cylindrically orthotropic materials, *The Quarterly Journal of Mechanics and Applied Mathematics*, **57**(3): 347–362, 2004, https://doi.org/10.1093/qjmam/57.3.347.

59. Singh B.M., Rokne J., Dhaliwal R.S., Torsional vibrations of functionally graded finite cylinders, *Meccanica*, **41**: 459–470, 2006, https://doi.org/10.1007/s11012-006-0003-x.

60. Sofiyev A.H., Schnack E., The stability of functionally graded cylindrical shells under linearly increasing dynamic torsional loading, *Engineering Structures*, **26**(10): 1321–1331, 2004, https://doi.org/10.1016/j.engstruct.2004.03.016.

61. Li C., Weng G.J., Duan Z., Dynamic behavior of a cylindrical crack in a functionally graded interlayer under torsional loading, *International Journal of Solids and Structures*, **38**(42–43): 7473–7485, 2001, https://doi.org/10.1016/S0020-7683(01)00046-4.

62. Hematiyan M.R., Estakhrian E., Torsion of functionally graded open-section members, *International Journal of Applied Mechanics*, **4**(2): 1250020, 2012, https://doi.org/10.1142/S1758825112500202.

63. Arghavan S., Hematiyan M.R., Torsion of functionally graded hollow tubes, *European Journal of Mechanics – A/Solids*, **28**(3): 551–559, 2009, https://doi.org/10.1016/j.euromechsol.2008.07.009.

64. Gholami Bazehhour B., Rezaeepazhand J., Approximate torsional analysis of multilayered tubes with non-circular cross-sections, *Applied Composite Materials*, **18**: 485–497, 2011, https://doi.org/10.1007/s10443-011-9213-z.

65. Vasiliev A., Sevostianov I., Aizikovich S., Jeng Y.-R., Torsion of a punch attached to transversely-isotropic half-space with functionally graded coating, *International Journal of Engineering Science*, **61**: 24–35, 2012, https://doi.org/10.1016/j.ijengsci.2012.06.006.

66. Wang H.M., Liu C.B., Ding H.J., Exact solution and transient behavior for torsional vibration of functionally graded finite hollow cylinders, *Acta Mechanica Sinica*, **25**: 555–563, 2009, https://doi.org/10.1007/s10409-009-0251-9.

67. Shen Y., Chen Y., Li L., Torsion of a functionally graded material, *International Journal of Engineering Science*, **109**: 14–28, 2016, https://doi.org/10.1016/j.ijengsci.2016.09.003.

68. Bayat Y., Ekhteraei Toussi H., Elastoplastic torsion of hollow FGM circular shaft, *Journal of Computational & Applied Research in Mechanical Engineering (JCARME)*, **4**(2): 165–180, 2015, https://doi.org/10.22061/jcarme.2015.274.

69. Huang H., Zhang Y., Han Q., Inelastic buckling of FGM cylindrical shells subjected to combined axial and torsional loads, *International Journal of Structural Stability and Dynamics*, **17**(9): 1771010, 2017, https://doi.org/10.1142/S0219455417710109.

70. Tsiatas G.C., Babouskos N.G., Elastic-plastic analysis of functionally graded bars under torsional loading, *Composite Structures*, **176**: 254–267, 2017, https://doi.org/10.1016/j.compstruct.2017.05.044.

71. Murín J., Aminbaghai M., Hrabovský J., Elastostatic analysis of the spatial FGM structures, *Strojnícky časopis – Journal of Mechanical Engineering*, **65**(1): 27–56, 2015, https://doi.org/10.1515/scjme-2016-0003.

72. Liaghat F., Hematiyan M.R., Khosravifard A., Material tailoring in functionally graded rods under torsion, *Proceedings of the Institution of Mechanical Engineers, Part C: Journal of Mechanical Engineering Science*, **228**(18): 3283–3295, 2014, https://doi.org/10.1177/0954406214529557.

73. Barretta R., Feo L., Luciano R., Some closed-form solutions of functionally graded beams undergoing nonuniform torsion, *Composite Structures*, **123**: 132–136, 2015, https://doi.org/10.1016/j.compstruct.2014.12.027.

74. Bayat Y., Alizadeh M., Bayat A., Generalized solution of functionally graded hollow cylinder under torsional load, *Journal of Computational & Applied Research in Mechanical Engineering (JCARME)*, **2**(2): 23–32, 2013, https://doi.org/10.22061/jcarme.2013.50.

75. Rizov V.I., Elastic-plastic fracture of functionally graded circular shafts in torsion, *Advances in Materials Research*, **5**(4): 299–318, 2016, https://doi.org/10.12989/amr.2016.5.4.299.

76. Rahaeifard M., Size-dependent torsion of functionally graded bars, *Composites Part B: Engineering*, **82**: 205–211, 2015, https://doi.org/10.1016/j.compositesb.2015.08.011.

77. Aminbaghai M., Murin J., Kutiš V., Hrabovsky J., Kostolani M., Mang H.A., Torsional warping elastostatic analysis of FGM beams with longitudinally varying material properties, *Engineering Structures*, **200**: 109694, 2019, https://doi.org/10.1016/j.engstruct.2019.109694.

78. Murín J., Kugler S., Habrovsky J., Kutiš V., Paulech J., Aminbaghai M., Warping torsion of FGM beams with spatially varying material properties, *Composite Structures*, **291**: 115592, 2022, https://doi.org/10.1016/j.compstruct.2022.115592.

79. Guendouz I., Khebizi M., Guenfoud H., Guenfoud M., El Fatmi R., Analysis of torsional-bending FGM beam by 3D Saint-Venant refined beam theory, *Structural Engineering and Mechanics*, **84**(3): 423–435, 2022, https://doi.org/10.12989/.2022.84.3.423.

80. Murín J., Hrabovsky J., Kugler S., Kutiš V., Aminbaghai M., Effect of longitudinal variation of material properties in warping torsion of FGM beams, [in:] *Analysis of Shells, Plates, and Beams: A State of the Art Report*, Altenbach H., Chinchaladze N., Kienzler R., Müller W.H. [Eds], pp. 243–296, 2020, https://doi.org/10.1007/978-3-030-47491-1_14.

81. Guendouz I., Khebizi M., Guenfoud H., Guenfoud M., Analysis of FGM cantilever beams under bending-torsional behavior using a refined 1D beam theory, *Periodica Polytechnica Civil Engineering*, **66**(4): 1262–1277, 2022, https://doi.org/10.3311/PPci.20595.

82. Barati A., Adeli M.M., Hadi A., Static torsion of bi-directional functionally graded microtube based on the couple stress theory under magnetic field, *International Journal of Applied Mechanics*, **12**(2): 2050021, 2020, https://doi.org/10.1142/S1758825120500210.

83. Naghibi S.R., Wang W., Ghavi M.R., Gollou R.M., Several defects in a hollow cylinder coated by a functionally graded material (FGM) subjected to torsional loading, *Iranian Journal of Science and Technology, Transactions of Mechanical Engineering*, **47**: 109–131, 2023, https://doi.org/10.1007/s40997-022-00492-2.

84. Singh P.K., Kumar M., Mishra S., Finite element analysis of functionally graded bar under torsional load, *Materials Today: Proceedings*, **56**(5): 2960–2966, 2022, https://doi.org/10.1016/j.matpr.2021.11.012.

85. Zhang J., Chen S., Chen L., Dynamic buckling of FGM cylindrical shells under torsional impact loads, [in:] *New Trends in Nonlinear Dynamics: Proceedings of the First International Nonlinear Dynamics Conference (NODYCON 2019), Volume III*, Lacarbonara W., Balachandran B., Ma J., Machado J.T.A., Stepan G. [Eds], Springer, 2020, https://doi.org/10.1007/978-3-030-34724-6_12.

86. Noroozi M., Ghassemi A., Atrian A., Vahabi M., Multiple cylindrical interface cracks in FGM coated cylinders under torsional transient loading, *Theoretical and Applied Fracture Mechanics*, **97**: 258–264, 2018, https://doi.org/10.1016/j.tafmec.2018.08.015.

87. Li L., Hu Y., Torsional statics of two-dimensionally functionally graded microtubes, *Mechanics of Advanced Materials and Structures*, **26**(5): 430–442, 2019, https://doi.org/10.1080/15376494.2017.1400617.

88. Karaca M., Alyavuz B., Non-linear behavior of functionally graded elastoplastic beam under torsion, *Journal of Scientific Reports-A*, **57**: 27–50, 2023, https://doi.org/10.59313/jsr-a.1415211.

89. Barretta R., Ali Faghidian S., Marotti de Sciarra F., Penna R., Pinnola F.P., On torsion of nonlocal Lam strain gradient FG elastic beams, *Composite Structures*, **233**: 111550, 2020, https://doi.org/10.1016/j.compstruct.2019.111550.

90. Soltani M., Asgarian B., Lateral-torsional stability analysis of a simply supported axially functionally graded beam with a tapered I-section, *Mechanics of Composite Materials*, **56**: 39–54, 2020, https://doi.org/10.1007/s11029-020-09859-5.

91. Murín J., Aminbaghai M., Hrabovsky J., Kutis V., Kugler S., Paulech J., Non-uniform Torsional Eigenmodes of FGM Beams, [in:] *Proceedings of the 14th International Conference on Vibration Problems*, 2021, https://doi.org/10.1007/978-981-15-8049-9_17.

92. Hajhashemkhani M., Hematiyan M.R., Inflation, extension and torsion analysis of compressible functionally graded hyperelastic tubes, *Acta Mechanica*, **231**: 3947–3960, 2020, https://doi.org/10.1007/s00707-020-02742-3.

93. Nie G.J., Pydah A., Batra R.C., Torsion of bi-directional functionally graded truncated conical cylinders, *Composite Structures*, **210**: 831–839, 2019, https://doi.org/10.1016/j.compstruct.2018.11.081.

94. Baksa A., Saint-Venant torsion of a functionally graded circular bar with a radial slit, *Journal of Theoretical and Applied Mechanics*, **50**: 83–101, 2020, https://doi.org/10.7546/JTAM.50.20.01.08.

95. Rizov V.I., Nonlinear delamination analysis of multilayered functionally graded circular shafts in torsion, *Journal of Applied Mechanics and Technical Physics*, **59**: 1104–1110, 2018, https://doi.org/10.1134/S0021894418060160.

96. Chen D., Liu L., Chu L., Liu Q., Analytical solution of thermo–mechanical properties of functionally graded materials by asymptotic homogenization method, *Materials*, **15**(9): 3073, 2022, https://doi.org/10.3390/ma15093073.

97. Yadav S., Liu S., Kumar Singh R., Kumar Sharma A., Rawat P., A state-of-art review on functionally graded materials (FGMs) manufactured by 3D printing techniques: Advantages, existing challenges, and future scope, *Journal of Manufacturing Processes*, **131**: 2051–2072, 2024, https://doi.org/10.1016/j.jmapro.2024.10.026.

98. Alkunte S., Fidan I., Naikwadi V., Gudavasov S., Alshaikh Ali M., Mahmudov M., Hasanov S., Cheepu M., Advancements and challenges in additively manufactured functionally graded materials: A comprehensive review, *Journal of Manufacturing and Materials Processing*, **8**(1): 23, 2024, https://doi.org/10.3390/jmmp8010023.

99. Hao Y.X., Wang M.X., Zhang W., Yang S.W., Liu L.T., Qian Y.H., Bending-torsion coupling bursting oscillation of a sandwich conical panel under parametric excitation, *Journal of Sound and Vibration*, **495**: 115904, 2021, https://doi.org/10.1016/j.jsv.2020.115904.

100. Aghazadeh R., Rafighi M., Kumar R., Al Awadh M., Material gradation effects on twisting statics of bi-directional functionally graded micro-tubes, *AIP Advances*, **14**(2): 025228, 2024, https://doi.org/10.1063/5.0194270.

101. Civalek Ö., Uzun B., Yayli M.Ö., Torsional vibrations of functionally graded restrained nanotubes, *The European Physical Journal Plus*, **137**: 113, 2022, https://doi.org/10.1140/epjp/s13360-021-02309-8.

102. Shakhlavi S.J., Hosseini-Hashemi S., Nazemnezhad R., Torsional vibrations of functionally graded restrained nanotubes, *International Journal of Non-Linear Mechanics*, **124**: 103513, 2020, https://doi.org/10.1016/j.ijnonlinmec.2020.103513.

103. Beni Y.T., Size dependent coupled electromechanical torsional analysis of porous FG flexoelectric micro/nanotubes, *Mechanical Systems and Signal Processing*, **178**: 109281, 2022, https://doi.org/10.1016/j.ymssp.2022.109281.

104. Barati A., Norouzi S., Nonlocal elasticity theory for static torsion of the bi-directional functionally graded microtube under magnetic field, *Journal of Computational Applied Mechanics*, **51**(1): 30–36, 2020, https://doi.org/10.22059/jcamech.2019.294263.462.

105. Zarezadeh E., Hosseini V., Hadi A., Torsional vibration of functionally graded nanorod under magnetic field supported by a generalized torsional foundation based on nonlocal elasticity theory, *Mechanics Based Design of Structures and Machines*, **48**(4): 480–495, 2020, https://doi.org/10.1080/15397734.2019.1642766.

Received January 21, 2025; revised October 28, 2025; accepted November 27, 2025;
available online January 20, 2026; version of record June 3, 2026;
published issue June 24, 2026.

Engineering Transactions, **74**(2): 327–354, 2026, https://doi.org/10.24423/engtrans.2025.3681
Institute of Fundamental Technological Research Polish Academy of Sciences (IPPT PAN)
Université de Lorraine • Poznan University of Technology

Technical Note

Analytical Approach and Shooting Method for the Solution of a Nonlocal Eringen Elasticity Problem of Nanorods

Aleksandra MANECKA-PADAŻ[1)*], Ewa Eliza ROŻKO[1),2)],
Zdzisław NOWAK[1)], Piotr CHUDZIŃSKI[1)]

[1)] *Institute of Fundamental Technological Research, Polish Academy of Sciences*
Warsaw, Poland

[2)] *Institute of Outcomes Research, Maria Sklodowska-Curie Medical Academy*
Warsaw, Poland

*Corresponding Author: amanecka@ippt.pan.pl

The aim of this paper is to study the post-buckling behavior of nanorods, taking into account small scale effects. In this paper, the buckling of a nanorod column subjected to a tip load is investigated. The nanorod is on a clamped support at one end, while the other end is simply supported and subjected to axial compression. At this end, the nanorod is movable only in the horizontal direction. The governing differential equation describing the behavior of the nanorod is derived from the moment–curvature relationship, in analogy with the classical Euler–Bernoulli beam theory, together with the equilibrium equations, including the effects of nonlocal elasticity, as well as the corresponding boundary conditions. A numerical shooting method is derived and employed to solve the differential equations in this problem. The results, including nonlocal elasticity, reveal that nanorods have decreased structural stiffness and show a significant effect of geometrical parameters on the stability of buckled nanorods, emphasizing the importance of accounting for their interaction in the design of nanostructural systems.

Keywords: nonlocal elasticity theory, nanorods, small-scale effect, postbuckling behavior.

1. INTRODUCTION

For a slender elastic beam under axial compression, the classical Euler theory predicts a bifurcation of the straight configuration of the beam when the critical load is reached. The elastica problem was experimentally investigated by Pieter van Musschenbrock, see [1], and then mathematically studied by Bernoulli and Euler, see [2]. Finally, it was solved by Euler in 1744, who obtained nine classes of solutions of the elastic curve and named them elasticae, see [3]. Motivated by recent progress in experiments on nanorods, here we study how these elastica solutions change upon adding nonlocality to the model, described by a single nonlocal parameter μ.

Over the years, many researchers have been interested in the elastica problem, and there exist many studies focused on various aspects of this issue. KIRCHHOFF [4] found an analogy between the equations describing the equilibrium state of an elastic rod and those describing the dynamics of a simple swinging pendulum. BORN [5] studied the exact elastica curves in his Ph.D. thesis. NISHINARI [6] partially analyzed the nonlinear dynamics of elastic rods and applied the soliton approach to analyze the nonlinear deformation of real elastic rods, clarifying the physical meaning of the assumed velocities. CHUCHEEPSAKUL and MONPRAPUSSORN [7] studied a highly nonlinear problem of instability of a flexible elastic pipe transporting fluid. They based their analysis on the inextensible elastica theory of rods, and the solution was obtained by using elliptic integrals and the numerical shooting method. VASSILEV *et al.* [8] presented the fluid membrane equilibrium shape equation in the form of a generalization of Euler's elastica. KIBACH *et al.* [9] investigated the post-buckled free vibration problem of an elastica around one of its vibration modes. The main contribution of their work is the detection of nonlinear frequencies of the elastica, i.e., its different backbone curves, around one of its post-buckled configurations, without any assumptions on the order of magnitude of curvature, rotation, or response. The detected nonlinear frequency relationships provide tools for tuning parameters of the elastica in order to achieve specific types of behavior around one of its buckling and vibration modes.

In the paper by TALONI *et al.* [10], a general expression for the strain energy of a homogeneous, isotropic, plane extensible elastic body with an arbitrary undeformed configuration was derived. This expression appears to be suitable for one-dimensional models of polymers or vesicles, whose natural configuration is characterized by locally changing curvature. The authors discuss the relevance of their model for describing real biological non-homogeneous filaments. LEANZA *et al.* [11] determined the axial buckling behavior for an elastic beam or rod with uniform natural curvature. In the elastica problems, this significantly enriches the variety of buckling behaviors exhibited by rods or beams that are straightened by pure bending and clamped at their ends. While the classical elastica displays stable post-buckling behavior, the elastica with natural curvature exhibits a wide range of behaviors from stable to highly unstable. The stability of the interesting limiting case, in which the maximum uniform natural curvature is imposed on a rod or beam clamped at both ends, has also been determined via initial post-bifurcation analysis.

PHUNGPAINGAM and CHUCHEEPSAKUL [12] analyzed the behavior of a variable-arc-length elastica subjected to end loading with a rotational spring joint within the span length of the elastica. Lai *et al.* [13] investigated the buckling behavior of the compression of high-strength concrete-encased steel columns through experimental, numerical and analytical analyses. Wang *et al.* [14] studied the instability of an elastica under bilateral displacement control at a material point. Fraldi *et al.* [15] studied both compressive and tensile buckling in the case of human finger luxation, demonstrating that the phenomenon can be interpreted as an elastic bifurcation in a natural system. Hathaipichitchai *et al.* [16] investigated the post-buckling behavior of a variable-arc-length elastica pipe caused by internal fluid transport motion, including the effect of pressure variability. Curatolo *et al.* [17] employed a modified Euler elastica model for optimizing catapult mechanism conditions due to the catapult emerging in a soft rod. Wang and Qiu [18] proposed an extended elastica-plastica theory for Euler–Bernoulli beams. Matsutani [19] studied the mechanics of elastica as a model for the shapes of supercoiled DNA. The elastica problem has been intensively investigated over the years and has played a major role in the development of mathematics, including Jacobi elliptic functions and also numerical methods.

In recent decades, nanotechnology has been a main subject of interest for researchers from all over the world. Materials such as thin films, nanorods, and nanotubes may exhibit unusual properties not noticed at the macroscale [20]. Modeling and optimization of nanoscale devices require an extended characterization of material at such a small scale. The elastica issue at the nanoscale has also become of great interest over time. Wang and Feng [21] measured the mechanical properties of compressed nanowires based on the Euler buckling model. Moradi *et al.* [22] examined the mechanical behavior of polystyrene nanorods using the classical Euler–Bernoulli beam model.

Recently, further studies at the nanoscale have been undertaken, mainly based on Eringen's nonlocal elasticity theory. This theory assumes that the stress at a point is a function of the strains at adjacent points in the continuum [23]. This approach has become an efficient tool for the analysis of the influence of size effects in small-scale structures. Thongyothee and Chucheepsakul [24] investigated the stability of nanobeams, including small-scale effects and surface stress. Challamel *et al.* [25] studied the elastica problem using an equivalent nonlocal continuum approach and compared it with a discrete physical model. Lembo [26] researched post-buckling configurations of nanorods with various end conditions using Eringen's nonlocal theory. A comparison of results for nonlocal and classical rods showed a significant impact of the nonlocal parameter on the post-buckling behavior of rods.

Tang and Qing [27] numerically examined the effects of nonlocal parameters on static bending, elastic buckling, and free vibration of Timoshenko beams under different boundary and loading conditions. Their study showed that a consistent softening effect can be obtained. Hussain and Naeem [28] applied Eringen's theory to calculate the frequency of single-wall carbon nanotubes (SWCNT). The outcome revealed that increasing the nonlocal parameter results in significantly reducing the natural frequencies of the SWCNT. Berecki *et al.* [29] compared Eringen's two-phase local/nonlocal model with Eringen's differential model in order to perform bifurcation analysis of a nanotube through which a nanostring passes.

It is also worth mentioning that an interesting result was obtained using the integral (stress-driven) form of nonlocal elasticity theory. Darban *et al.* [30] investigated size-dependent buckling of cracked nanocantilevers, with results applicable to a wide range of mechanical nanosensors. In [31], Darban analyzed nonuniform beams with multiple sub-beams. The model was based on a stress-driven nonlocal theory, which can be applied to control the flexural response of a nanobeam. In [32], Darban's approach provides explicit solutions for displacements and deflections, showing how size effects alter beam stiffness and behavior relative to classical theory using a variational approach and a transfer matrix method.

Although Eringen's nonlocal theory provides valuable analytical frameworks, most practical problems – especially those involving complex boundary conditions or nonlinear constitutive terms – require robust numerical techniques for their solution. Several computational methods have therefore been developed and applied within the nonlocal elasticity framework. The finite difference method (FDM) and the finite element method (FEM) remain the most frequently used numerical tools for static and dynamic analyses of nonlocal beams and plates, as reported by Reddy *et al.* [33], Phadikar and Pradhan [34]. The differential quadrature method (DQM) has also been implemented successfully for solving higher-order nonlocal governing equations, providing excellent accuracy for small-scale effects [35].

In addition, variational and Galerkin formulations were proposed by Challamel and Wang [36] to handle mixed local–nonlocal boundary conditions and to study bifurcation phenomena. For nonlinear problems, especially in buckling and post-buckling regimes, the shooting method has proven to be a reliable approach, offering high numerical stability and physical interpretability [37, 38]. Recently, a stress-driven nonlocal theory based on the Bernoulli–Euler model was presented for size-dependent free vibrations of nanobeams with multiple edge cracks [39].

These numerical developments confirm that, while the classical analytical formulations of the nonlocal theory remain essential for model validation, the integration of advanced computational techniques is crucial for studying complex geometries, heterogeneity, and boundary interactions in nanostructures. The numerical solution of Eringen's nonlocal beam equation requires a robust and accurate method capable of handling nonlinear second-order boundary value problems (BVPs) with boundary conditions prescribed at opposite ends of the spatial domain. As demonstrated in several recent works (e.g., [40]), classical numerical approaches such as FDM or collocation schemes often fail when applied to highly nonlinear systems, especially those involving nonlocal constitutive terms. In the case of Eringen's beam, the governing equation contains nonlinear denominators of the form $(EI - \mu F \cos(\theta(s))) - 1(EI - \mu F \cos\theta(s)) - 1$, which can lead to local singularities and numerical instabilities when using grid-based methods.

As shown, there are plenty of works that focus on the elastica problem. Elastica theory plays an important role in the study of large displacements of slender rods. However, the majority of these studies are still limited to purely elastic material. In [41], the traditional elastica theory was extended to an elastica-plastica theory. However, buckling analysis remains not fully understood, especially at the nanoscale. This paper is, therefore, devoted to studying the influence of nonlocal theory on the post-buckling behavior of nanorods. The validity of the method proposed in this paper is confirmed through comparison with existing researches. The current results are expected to be useful for predicting nanorod strength and for the design of nanostructures and nanodevices related to nanorods.

The paper is divided into five sections. In Sec. 2, we formulate the elastica problem in the presence of nonlocal strain in the form of a second-order ordinary differential equation. We also discuss the value of the critical load causing the loss of structural stability. Section 3 presents our numerical solution using the built-in shooting method in *Wolfram Mathematica*, combining adaptive Runge–Kutta integration with iterative boundary-condition correction. In Sec. 4, we report the results and analyze the influence of the nonlocal parameter. Section 5 provides concluding remarks. In Appendix, an analytical solution for the local nonlinear elasticity theory is provided.

2. Elastica problem

First, in order to study scale effect in the elastica problem, Eringen's nonlocal theory is applied. Then, a numerical study of this problem is shown. Moreover, the critical load value calculations are demonstrated.

2.1. Nonlocal theory formulation

The nonlocal stress-gradient theory combines aspects of both nonlocal elasticity and stress-gradient theories, thereby considering both long-range interactions and higher-order stress gradients. Within this framework, the stress state at a point x is influenced by the strains at all other points in the body. In particular, the nonlocal stress-gradient theory can be reduced to both classical nonlocal elasticity theory and stress-gradient theory, hence offering a comprehensive method that encompasses both theoretical concepts. The nonlocal elasticity theory was initially formulated by ERINGEN [42] and ERINGEN and EDELEN [43] by means of an integral constitutive equation. Within the framework of continuum mechanics, the nonlocal elasticity theory proposed by Eringen has become a widely used approach for modeling structures at the nanoscale.

The only nonzero strain in the Euler–Bernoulli beam theory, accounting for the Kirchhoff assumption, is [24]:

$$\varepsilon_{xx} = \frac{\mathrm{d}u_1}{\mathrm{d}x} - y\frac{\mathrm{d}^2 u_2}{\mathrm{d}x^2} = \varepsilon_{xx0} + y\kappa, \tag{2.1a}$$

where $\varepsilon_{xx0} = \frac{\mathrm{d}u_1}{\mathrm{d}x}$ is the extensional strain and $y\kappa$ represents the bending strain.

Eringen's theory can be expressed either in an integral form, which explicitly accounts for long-range interactions, or in an equivalent differential form that is often more convenient for analytical and numerical treatment. In this paper, Eringen's differential form is examined, and the governing equations for the nonlocal model can be written as [44]:

$$\sigma_{xx} - \mu\frac{\mathrm{d}^2\sigma_{xx}}{\mathrm{d}x^2} = E\varepsilon_{xx}, \tag{2.1}$$

where σ_{xx}, ε_{xx}, E, and μ denote the normal stress, normal strain, Young's modulus, and the nonlocal parameter, respectively. The model of an elastic medium based on the equation of state (2.1), and its relationship with Eringen's nonlocal theory, was also analyzed by ROMANO and BARRETTA [45], and by other researchers, e.g., NOBILI and PRAMANIK [46]. BARRETTA *et al.* [47] identified a simple constitutive strategy for nanotechnological applications using an improved differential law with contributions from FERNÁNDEZ-SÁEZ *et al.* [48]. The newly developed method is consistent with the integral method [47]. The present work is motivated by the enhanced Eringen's differential model for all boundary conditions developed by BARRETTA *et al.* [47]. It has to be emphasized, however, that the connection between the differential and integral forms is still an open question. The equations are based on a specific assumption about the propagator (kernel) in the integral form. Several recent works have investigated various forms of propagators and the constitutive boundary conditions they imply, see, e.g., [49–58].

Both approaches – integral and differential – require the use of material and geometric parameters, and their clear interpretation is necessary for accurate analysis. The effect of nonlocality is incorporated into the constitutive differential Eq. (2.1) by the nonlocal parameter μ. The nonlocal parameter value

Table 1. Various ways to introduce the nonlocal parameter.

Parameter	Symbol	Magnitude	Researcher	Material
Internal characteristic length [nm]	a	0.142	Eringen [44]	Carbon nanostructures
Scale coefficient	e_0	0.39; 0.50; 0.70	Timesli [61]	Mathematical model
		0.288–0.5	Wang, Zhang [62]	Carbon nanostructures
		0–1	Reddy, Pang [63]	Carbon nanotubes
		0.288	Wang, Hu [64]	Carbon nanostructures
		0.39	Eringen [44]	Single-walled carbon nanotubes
Product of nonlocal parameter and internal characteristic length [nm]	e_0a	1	Akpinar *et al.* [65]	Carbon nanorods and nanotubes
		0; 2.0; 4.0	Natsuki *et al.* [66]	Single-walled carbon nanotubes
		1	Uzun *et al.* [67]	Porous functionally graded nanostructures
		0; 1.0; 1.5	Ebrahimi [68]	Single-walled carbon nanotubes
		0.5	Murmu [69]	Single-walled carbon nanotubes
		0–1	Wang *et al.* [70]	Single-walled carbon nanotubes
Nonlocal parameter squared	$\mu = (e_0a/l)^2$	0-1	Khaniki [71]	Carbon nanorod
		0.04	Thongyothee [72]	Mathematical model
Nonlocal parameter	e_0a/h_0	0–0.8	Karličić, Murmu [59]	Multi-walled carbon nanotubes
		0–0.6	Lu [73]	Multi-walled carbon nanotubes
Normalized nonlocal parameter	$\psi = e_0a/l$	0–0.20	De Rosa *et al.* [74]	Single-walled carbon nanotubes

depends on the material and the geometry of the element and it is largely determined experimentally; however, the exact value of the nonlocal parameter μ is still not known. Here, we take it as a free parameter in order to study its influence. Table 1 provides a literature overview of the main terms used for the nonlocal theory description; here, e_0 denotes a material constant, a is an internal characteristic length, which can represent a granular size or the distance between C-C bonds [59], and e_0 is a characteristic magnitude of the structure, for example, the nanotube diameter [60].

Table 1 summarizes different ways in which researchers have introduced the nonlocal parameter in Eringen's nonlocal elasticity theory, highlighting the lack of a single universal definition. The reported values vary depending on the adopted model, material characteristics, and the methodological choices. Importantly, research in this field is still very active, and new studies continue to refine the interpretation and application of the nonlocal parameter to improve predictive models for advanced nanomaterials. In this study, we aim to evaluate the nonlocal parameter value to contribute to the ongoing discussion, provide further insights into its proper application, and establish hypotheses for subsequent experimental validation.

The standard theory for describing the buckling phenomenon is the well-established Euler theory. This is the starting point of our calculations, and we present it in Appendix. In Euler's theory, we describe the deflection and change in the curvature of the compressed rod due to the applied force. Equation (A.7) and Eq. (A.8) can be used to plot elastics to calculate the deflection and displacement of the rod's end. In this work, we use Eringen's theory to describe the deflected shape of the nanorods, where the moment-curvature equation (Eq. (A.3)) is modified into [44]:

$$\frac{\mathrm{d}\theta(s)}{\mathrm{d}s} = -\frac{1}{EI}\left(M - \mu\frac{\mathrm{d}^2 M}{\mathrm{d}x^2}\right), \tag{2.2}$$

where M is the bending moment at any point along the rod axis, and the nonlocal part is expressed by the second derivative of the moment.

The study introduces a differential version of Eringen's nonlocal beam theory for elastic materials, constructed separately from the original integral framework. Our aim now is to solve Eq. (2.2) and obtain a solution that can estimate the influence of the nonlocal parameter μ on the elastica shape.

The small segment shown in Fig. 1 is consistent with the calculations presented further and is provided for discussion. In this work, we adopt a reference frame that is more suitable for our purposes; however, we wish to emphasize that it is the reverse of the one used in [24], due to adaptation to the coordinate system applied here.

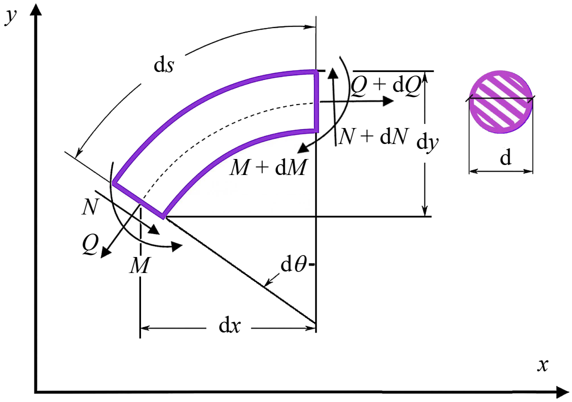

FIG. 1. Small segment of the compressed nanorod shown in the present reference frame (based on [24]).

The equilibrium equations relating the gradients of the normal force N, shear force Q, and bending moment M along the arc-length s to the curvature κ are as follows:

$$\frac{\mathrm{d}N}{\mathrm{d}s} = \kappa Q, \tag{2.3}$$

$$\frac{\mathrm{d}Q}{\mathrm{d}s} = -\kappa N, \tag{2.4}$$

$$\frac{\mathrm{d}M}{\mathrm{d}s} = Q. \tag{2.5}$$

Then, in Eringen's notation:

$$\frac{\mathrm{d}M}{\mathrm{d}x} = \frac{\mathrm{d}M}{\mathrm{d}s} \cdot \frac{\mathrm{d}s}{\mathrm{d}x} = \eta Q. \tag{2.6}$$

The factor $\frac{\mathrm{d}s}{\mathrm{d}x}$ is not defined; however, it is established that strain may be expressed in this form, namely:

$$\sigma_{(\mathrm{d}s)} = E\varepsilon_{(\mathrm{d}s)}, \tag{2.7}$$

where E, $\sigma_{(\mathrm{d}s)}$, and $\varepsilon_{(\mathrm{d}s)}$ denote Young's modulus, normal stress, and strain, respectively.

The normal strain can be measured as the difference between the current and reference configurations along the axis, and the unknown factor $\frac{\mathrm{d}s}{\mathrm{d}x}$ can be denoted as η:

$$\varepsilon_{(\mathrm{d}s)} = \frac{\mathrm{d}s}{\mathrm{d}x} - \frac{\mathrm{d}x}{\mathrm{d}x} = \eta - 1. \tag{2.8}$$

As is well known, the stress $\sigma_{(ds)}$ can be expressed in terms of the axial normal force N and the cross-sectional area A as:

$$\sigma_{(\mathrm{d}s)} = \frac{N}{A}. \tag{2.9}$$

We can now express Eq. (2.7) as follows:

$$\frac{N}{A} = E\,(\eta - 1)\,, \tag{2.10}$$

$$\eta = \frac{N}{EA} + 1. \tag{2.11}$$

The bending behavior is described by the bending moment M. As it is presented in Fig. 2 for the loading considered, this moment is caused by the axial force F acting at the deflection $u_2(s)$:

$$M = Fu_2(s). \tag{2.12}$$

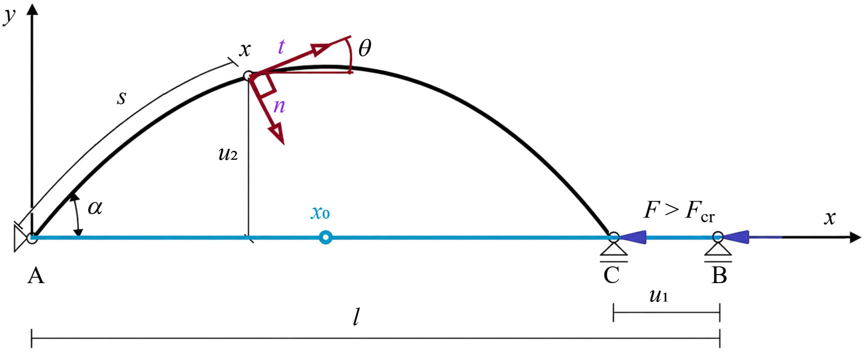

FIG. 2. Compression of the rod due to the applied force F.

The corresponding shear force Q is obtained as the derivative of the bending moment with respect to the arc-length coordinate s. Making use of the kinematic relation between deflection and rotation angle of the cross-section $\theta(s)$ leads to:

$$Q = \frac{\mathrm{d}M}{\mathrm{d}s} = \mathrm{d}\frac{Fu_2(s)}{\mathrm{d}s} = F\sin\theta(s). \tag{2.13}$$

We can now express Eq. (2.3) as follows:

$$\begin{aligned} N &= \frac{-1}{\frac{\mathrm{d}\theta(s)}{\mathrm{d}s}} \cdot \frac{\mathrm{d}Q}{\mathrm{d}s} = \frac{-1}{\frac{\mathrm{d}\theta(s)}{\mathrm{d}s}} \cdot \frac{\mathrm{d}}{\mathrm{d}s}\left(F\sin\theta(s)\right) \\ &= \frac{-1}{\frac{\mathrm{d}\theta(s)}{\mathrm{d}s}} \cdot F\cos\theta(s)\frac{\mathrm{d}\theta(s)}{\mathrm{d}s} = -F\cos\theta(s). \end{aligned} \tag{2.14}$$

We can express η as

$$\eta = \frac{N}{EA} + 1 = -\frac{F\cos\theta(s)}{EA} + 1. \tag{2.15}$$

Then:

$$\frac{\mathrm{d}M}{\mathrm{d}x} = \frac{\mathrm{d}M}{\mathrm{d}s} \cdot \frac{\mathrm{d}s}{\mathrm{d}x} = \eta Q = \left(\frac{N}{EA} + 1\right) \cdot Q. \tag{2.16}$$

Then, we can obtain:

$$\begin{aligned} \frac{\mathrm{d}^2M}{\mathrm{d}x^2} = \frac{\mathrm{d}}{\mathrm{d}x}\left(\frac{QN}{EA} + Q\right) &= \frac{1}{EA}\frac{\mathrm{d}}{\mathrm{d}x}(QN) + \frac{\mathrm{d}Q}{\mathrm{d}x} \\ &= \frac{1}{EA}\left(\frac{\mathrm{d}Q}{\mathrm{d}x} \cdot N + \frac{\mathrm{d}N}{\mathrm{d}x} \cdot Q\right) + \frac{\mathrm{d}Q}{\mathrm{d}x}. \end{aligned} \tag{2.17}$$

Subsequently, the derivatives are determined:

$$\frac{\mathrm{d}Q}{\mathrm{d}x} = \frac{\mathrm{d}Q}{\mathrm{d}s} \cdot \eta = -\kappa\eta N, \tag{2.18}$$

$$\frac{\mathrm{d}N}{\mathrm{d}x} = \frac{\mathrm{d}N}{\mathrm{d}x} \cdot \eta = \kappa\eta Q. \tag{2.19}$$

Then, using Eq. (2.18) and Eq. (2.19), we obtain:

$$\frac{\mathrm{d}^2M}{\mathrm{d}x^2} = \frac{1}{EA}\left(-\kappa\eta N^2 + \kappa\eta Q^2\right) - \kappa\eta N = \frac{1}{EA}\left(\kappa\eta\left(Q^2 - N^2\right)\right) - \kappa\eta N. \tag{2.20}$$

Then, using Eq. (2.2), we obtain:

$$\frac{\mathrm{d}\theta(s)}{\mathrm{d}s} = -\frac{1}{EI}\left(M - \mu\left(\frac{1}{EA}\left(\frac{\mathrm{d}\theta(s)}{\mathrm{d}s}\eta\left(Q^2 - N^2\right)\right) - \frac{\mathrm{d}\theta(s)}{\mathrm{d}s}\eta N\right)\right), \tag{2.21}$$

$$\frac{\mathrm{d}\theta(s)}{\mathrm{d}s}\left(1 - \frac{\mu}{EIEA}\eta\left(Q^2 - N^2\right) + \frac{\eta\mu N}{EI}\right) = -\frac{M}{EI}, \tag{2.22}$$

$$\frac{\mathrm{d}\theta(s)}{\mathrm{d}s} = -\frac{M}{EI} \cdot \left(\frac{1}{1 - \frac{\mu\eta}{EIEA}\left(Q^2 - N^2\right) + \frac{\eta\mu N}{EI}}\right). \tag{2.23}$$

This expression is identical to that given in [24].

Now, we seek the second derivative of θ with respect to s:

$$\frac{\mathrm{d}^2\theta}{\mathrm{d}s^2} = -\frac{1}{EI}\frac{\mathrm{d}}{\mathrm{d}s}\left(\frac{M}{1 - \frac{\mu\eta}{EIEA}\left(Q^2 - N^2\right) + \frac{\eta\mu N}{EI}}\right). \tag{2.24}$$

Expanded versions of Eq. (2.24) after substituting the physical quantities are as follows:

$$\frac{\mathrm{d}^2\theta}{\mathrm{d}s^2} = -\frac{1}{EI}\frac{\mathrm{d}}{\mathrm{d}s}\left(\frac{Fu_2(s)}{a^*}\right), \tag{2.25}$$

$$\frac{\mathrm{d}^2\theta}{\mathrm{d}s^2} = -\frac{1}{EI}\frac{\mathrm{d}}{\mathrm{d}s}\left(\frac{Fu_2(s)}{b^*}\right), \tag{2.26}$$

where

$$a^* = 1 - \frac{\mu}{EIEA}\left(F^2 - \frac{F^3\cos\theta(s)}{EA} + \frac{2F^3\cos^3\theta(s)}{EA} - 2F^2\cos^2\theta(s)\right) + \left(\frac{\mu F^2\cos^2\theta(s)}{EIEA} - \frac{\mu F\cos\theta(s)}{EI}\right),$$

$$b^* = 1 - \frac{\mu F^2}{EIEA} + \frac{\mu F^3\cos\theta(s)}{EIEAEA} - \frac{2\mu F^3\cos^3\theta(s)}{EIEAEA} + \frac{3\mu F^2\cos^2\theta(s)}{EIEA} - \frac{\mu F\cos\theta(s)}{EI}.$$

To the best of our knowledge, Eq. (2.26) with the second derivative has not been presented in the literature. It is worth mentioning that for $\mu = 0$, Eringen's theory reduces to the classical Euler's theory (see Eq. (A.2)).

2.2. CRITICAL LOAD VALUE

According to Euler's theory, we can calculate the critical load causing the loss of the stability of the structure using the following formula [75]:

$$P_{crE} = EI\left(\frac{\pi n}{l}\right)^2, \tag{2.27}$$

where $n = 0, 1, 3...$

From the engineering point of view, it is very useful to apply this formula to obtain a discrete set of values of the load for a particular material to prevent buckling phenomena. However, in nonlinear elasticity theory, the critical load value is not a constant and depends on the elliptic integral of the first kind $K(k)$, related to the initial angle $\alpha = \theta(0)$. We can calculate it using Bigoni's formula [76]:

$$P_{cr} = EI\left(\frac{m}{l}\right)^2\left[2K\left(\sin\frac{\alpha}{2}\right)\right]^2. \tag{2.28}$$

Equation (2.28) is used in Sec. 3 in order to estimate the reference axial force value.

3. NUMERICAL SOLUTION OF THE ELASTICA PROBLEM

3.1. METHOD

In this section, we adopt the shooting method, as implemented in *Wolfram Mathematica*, to obtain the solution of the second-order nonlinear differential equation governing the nonlocal Eringen's beam (Eq. (2.26)). This approach converts a boundary value problem (BVP) into an equivalent initial value problem (IVP), which is iteratively solved until the boundary conditions at both ends of the beam are satisfied.

The shooting method was chosen because of its numerical stability and robustness when dealing with nonlinear differential equations containing trigonometric terms and variable coefficients in the denominator, such as in Eringen's model. Alternative approaches, such as finite difference or collocation methods, often lead to convergence issues near points where the denominator in Eq. (2.26) becomes small. In contrast, the shooting method allows direct control over the boundary conditions and provides stable convergence even for strongly nonlinear systems.

In the numerical implementation, the built-in solver *NDSolve* was used with the option: Method → 'Shooting'. This solver internally applies an adaptive Runge–Kutta algorithm of variable order (Dormand–Prince/Fehlberg type). The algorithm automatically adjusts both the integration step and the order according to the local truncation error, ensuring high accuracy while maintaining computational efficiency.

3.2. IMPLEMENTATION DETAILS

The final algorithm was implemented as a BVP, solved by the built-in shooting method in *Wolfram Mathematica*. The governing system consisted of three first-order differential equations:

$$\theta'(s) = \kappa(s), \tag{3.1}$$

$$\kappa'(s) = -\frac{F}{EI - \mu F \cos\theta(s)} \sin\theta(s), \tag{3.2}$$

$$u_2'(s) = \sin\theta(s), \tag{3.3}$$

with mixed Dirichlet–von Neumann (clamped–pinned) boundary conditions:

$$\theta(s = 0) = \alpha, \tag{3.4}$$

$$\theta'(s = l) = 0, \tag{3.5}$$

$$u_2'(s = l) = 0. \tag{3.6}$$

These boundary conditions are motivated by recent experiment on nanorods reported by MANECKA-PADAŻ *et al.* [77]. The algorithm treats the initial curvature $\kappa(0)$ as a shooting parameter. For an assumed value of $\kappa(0)$, the system is integrated from $s = 0$ to $s = l$ using an adaptive Runge–Kutta scheme (Dormand–Prince type [78, 79]). After each integration, two residuals are evaluated:

$$R_1 = \theta' \left(l; \kappa(0)\right), \tag{3.7}$$

$$R_2 = u_2' \left(l; \kappa(0)\right). \tag{3.8}$$

The initial slope $\kappa(0)$ is then iteratively corrected using a secant or Newton-type update until both residuals satisfy the prescribed tolerance ($|R_1|, |R_2| < 10^{-6}$).

This procedure ensures that the end of the beam satisfies both mechanical and geometric constraints simultaneously. The adaptive step-size control built into the solver prevents numerical instabilities near regions where $EI - \mu F \cos\theta(s)$ approaches zero, ensuring smooth convergence even for relatively large values of the nonlocal parameter μ. The critical value μ_{cr} decreases with increasing value of initial angle $\alpha = \theta(0)$. This hybrid approach combines the accuracy of adaptive integration with the flexibility of iterative boundary correction, offering excellent numerical stability and control of the solution error. Moreover, the adaptive step-size control allows the solver to handle regions with steep curvature gradients or strong geometric nonlinearity without loss of accuracy.

The choice of the shooting method is also justified from a physical standpoint. Unlike mesh-based numerical techniques, which require additional artificial constraints, the shooting method directly mirrors the physical process of 'matching' the beam shape to the boundary conditions. This makes it particularly suitable for bifurcation-type problems and for analyzing stability modes of nanobeams.

3.3. MODEL PARAMETERS AND REFERENCE FORCE

In the numerical simulations, the material and geometric parameters were chosen to represent a slender nanobeam of length $l = 1000\,\mathrm{nm}$. The selected values correspond to realistic mechanical properties of nanostructures such as silicon nanobridges or carbon nanotubes and are consistent with earlier studies based on the Euler–Bernoulli beam model.

Numerical simulations were performed for a normalized beam model with the parameters $l = 1000\,\mathrm{nm}$ and $EI = EA = 1$, $m = 1$, and $\mu \in \{0; 0.01; 0.02, 0.03; 0.04; 0.05\}$. The parameters EI and EA were selected to ensure compatibility with the local Euler–Bernoulli model in the limit $\mu \to 0$, allowing direct comparison between classical and nonlocal solutions. To provide a consistent basis for comparison between local and nonlocal models, the reference axial force F was defined according to Eq. (2.28) mentioned in Subsec. 2.2. Employing Euler's critical force as the reference value ensures both physical and numerical consistency between the local and nonlocal formulations. This choice allows a direct evaluation of how the nonlocal parameter μ modifies the effective stiffness and the beam curvature distribution. As μ increases, the computed results reveal a clear structural softening effect: the deformation becomes more developed and the effective rigidity $EI_{\text{eff}} = EI - \mu F \cos\theta(s)$ decreases, confirming the expected nonlocal influence predicted by Eringen's theory.

The values of EI and EA for a circular cross-section (as in Fig. 1) can be calculated as

$$EI = \frac{E\pi\,\mathrm{d}^4}{64}, \tag{3.9}$$

$$EA = \frac{E\pi\,\mathrm{d}^2}{4}. \tag{3.10}$$

4. RESULTS

The numerical results obtained with this method showed good agreement with the classical Euler–Bernoulli solutions for $\mu = 0$. For increasing values of the nonlocal parameter μ, a clear structural softening effect was observed. This effect manifests as a reduction in the effective stiffness and a smoother distribution of curvature along the beam length, confirming the expected influence of nonlocality within Eringen's framework. The resulting solutions $\theta(s)$ and $u_2'(s)$ were subsequently used to reconstruct the beam profile $y(x)$.

In Fig. 3, we see that as the nonlocal parameter μ increases, the angle θ increases along the curvilinear coordinate s. For equal increments in μ, this change becomes more pronounced at higher values – there is a smaller difference in θ between $\mu = 0.01$ and $\mu = 0.03$ than between $\mu = 0.03$ and $\mu = 0.05$. With increasing initial angle $\alpha = \theta(0)$, this effect becomes less evident, and the θ-profile becomes more slender. For larger α (i.e., $\alpha = 95^\circ$ and 118°), the trend reverses: a critical point appears (the larger the α, the earlier it occurs), beyond which θ falls below the prediction of the local theory as s varies. In the θ' plot, the influence of μ on the rod curvature is substantial and it intensifies with increasing initial angle α. Further quantitative analysis of the results shown in Fig. 3 is presented in Table 2. To satisfy the boundary conditions, it was necessary to assume an extension of the nanorod, denoted as δl. For each μ, the necessary change in beam length δl is reported. We see that δl increases with μ and is largest for the smallest initial angles α.

As it is presented in Fig. 4, the shape of the elastica $y(x)$ also changes noticeably under the nonlocal theory. A softening of the compressed rod is evident – the larger the nonlocal parameter μ, the more compliant the rod becomes to shape change. The curves obtained under the nonlocal theory resemble those

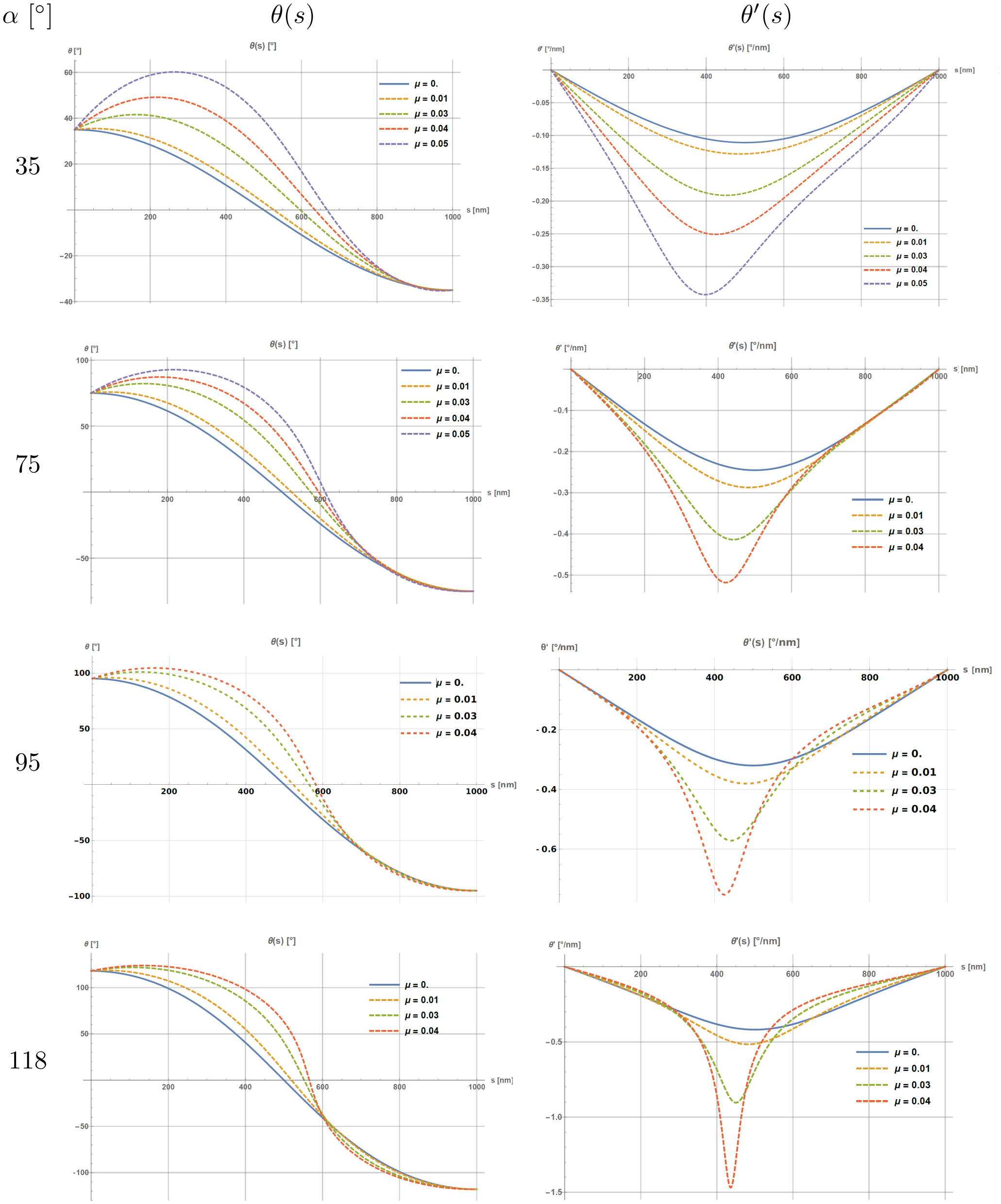

FIG. 3. Set of bending angles θ and their derivatives as functions of the curvilinear coordinate s. We present four pairs of plots for four different initial angles $\alpha = \theta(0)$. In each panel, results for different values of nonlocal parameters μ are shown.

corresponding to higher angles in the local theory (e.g., for $\alpha = 95°$, disregarding the boundary condition, the deformation pattern is similar to that of the local theory for 120°).

TABLE 2. Quantitative analysis of the results shown in Fig. 3.

μ	$\alpha = 35°$		$\alpha = 75°$		$\alpha = 95°$		$\alpha = 118°$	
	Δl [nm]	$\Delta l/l$ [%]	Δl [nm]	$\Delta l/l$ [%]	Δl [nm]	$\Delta l/l$ [%]	Δl [nm]	$\Delta l/l$ [%]
0.01	49.71	4.97	46.80	4.68	43.85	4.39	37.87	3.79
0.03	144.64	14.46	128.81	12.88	118.45	11.85	101.40	10.14
0.04	183.35	18.34	163.45	16.35	150.79	15.08	129.75	12.98

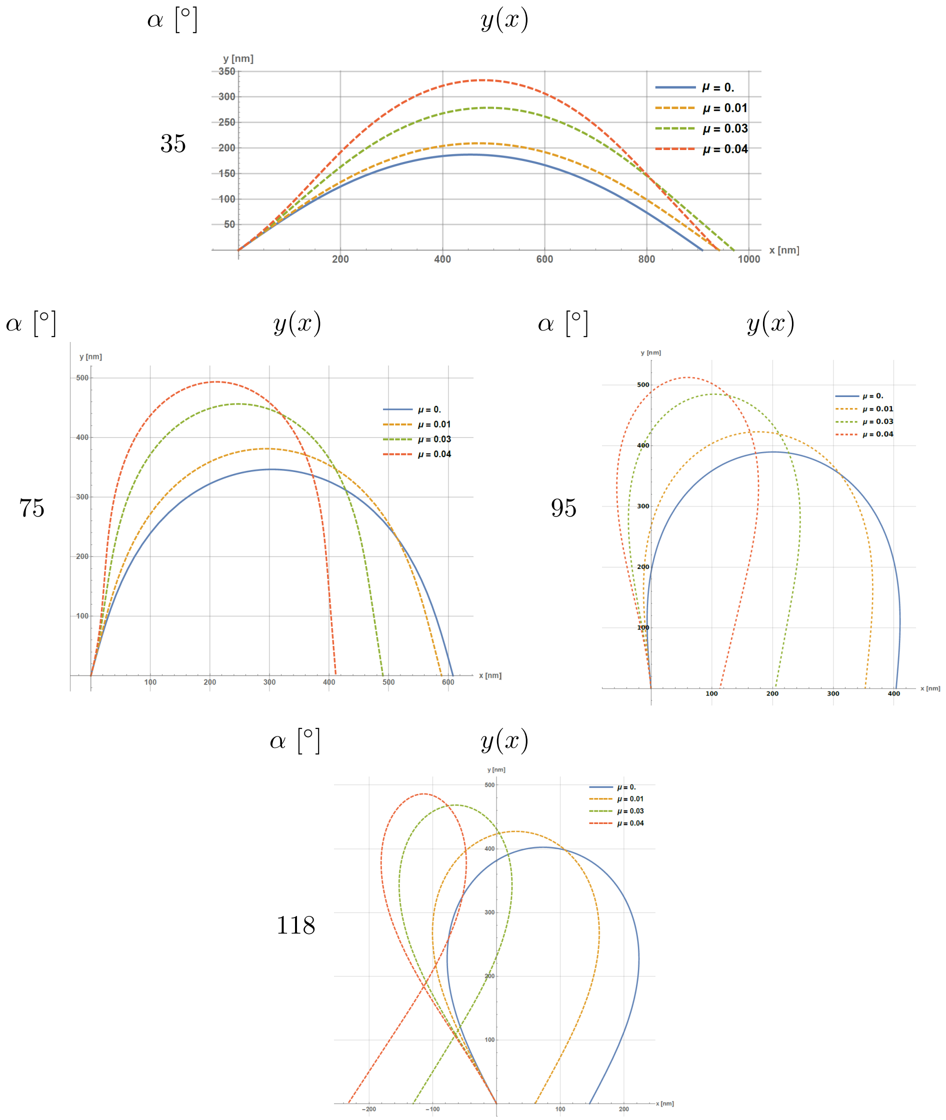

FIG. 4. Influence of the nonlocal theory on the shape of the elastica for given values of the initial angle α.

Further quantitative analysis of the maxima's position is presented in Table 3. It can be observed that the nonlocal theory implies an earlier onset of deformation, with a broadly similar overall form (though not identical, as evidenced by the left-side inflection of the rod). The maximum deflection does not occur at midspan (the problem becomes asymmetric, in contrast to the local formulation), and this tendency is most prominent for small initial angles. This is analyzed in detail in Table 3, where it can be seen that maximum is shifted from the midspan ($s = 500\,\text{nm}$) to higher values of s. Moreover, we observe a small left-hand-side inflection, which is more pronounced for smaller values of the initial angle and for larger values of μ. For each initial angle, we extract also a critical value of the nonlocal parameter μ_{cr} (last row in Table 3), where the theory on our level of approximation breaks down. This is because the dominator in Eq. (2.26) approaches zero. The values of μ_{cr} decrease with increasing initial angle α.

Table 3. Quantitative analysis of the maxima position and the critical value of the nonlocal parameter μ_{cr}.

μ	$\alpha = 35°$			$\alpha = 75°$			$\alpha = 95°$			$\alpha = 118°$		
	$x_{\max}$	$y_{\max}$	$s_{\max}$	$x_{\max}$	$y_{\max}$	$s_{\max}$	$x_{\max}$	$y_{\max}$	$s_{\max}$	$x_{\max}$	$y_{\max}$	$s_{\max}$
0.00	454.3	186.9	500.0	304.0	346.3	500.0	201.8	389.503	500.0	73.04	402.4	500.0
0.01	471.0	209.1	525.0	294.6	381.1	523.5	176.5	422.697	522.0	30.3	427.3	518.8
0.03	488.9	278.7	575.3	247.6	456.3	564.8	104.3	484.667	559.0	−64.1	468.5	550.2
0.04	478.6	332.6	598.3	210.5	493.4	582.3	60.3	512.3	574.57	−114.2	486.1	563.7
μ_{cr}	0.0967			0.0809			0.06978			0.0551		

5. Conclusions

There are two main results that we obtained in this work. Firstly, we derived the nonlocal constitutive laws within Eringen's theory. These are equations for the derivative of the beam curvature, and their form is very similar to that of the classical Euler's elastica. This allows for a direct comparison of the two theories. One observes that the nonlocality appears in the denominator, which, in principle, may lead to instability. The second main result is that we have solved these equations numerically using the shooting method. The development and application of a novel numerical approach are a valuable outcome in themselves, as demonstrated by the widely cited work of Civalek *et al.* [80].

The computed results reveal a clear structural softening effect – the deformation becomes smoother, and the effective rigidity $EI_{\text{eff}} = EI - \mu F \cos\theta(s)$ decreases, confirming the expected nonlocal influence predicted by Eringen's theory. We applied mixed boundary conditions at both ends, corresponding to physical situations encountered in experiments for nanorods. Interestingly, while classical Euler's elastica shows symmetric bending, within the Eringen's theory there is clear asymmetry: the maximum curvature is shifted toward the left side of the beam. This effect can be considered a hallmark of the presence of nonlocal elasticity when the beams are measured experimentally.

Increasing the nonlocal parameter μ and the initial angle α brings the system closer to instability, which manifest as singular behavior in the curvature derivative. Further extension of the theory is required to mitigate this effect. If one considers that elastica theory is an effective continuum description that emerges upon averaging microscopic degrees of freedom, then one may suspect that including anharmonicity of the underlying lattice could prevent the occurrence of excessively large local curvature.

Eringen's theory remains a subject of ongoing debate, particularly with respect to its differential formulation. The specific values of the nonlocal parameter μ, which directly accounts for nonlocality in a given structure, are not yet well established. Since the problem has not been fully explored, a promising direction for the authors' future work is the implementation of constitutive boundary conditions, especially in studies that incorporate experimental data for specific materials. As described in Subsec. 2.1, constitutive boundary conditions are mathematically derived for a given propagator, and they allow to build a connection between differential and integral formulations of the theory. It is not clear what is their relationship to physically observed boundary conditions. In the future, one could add constitutive BCs into the shooting optimization procedure and/or investigate which propagators are imposed by a given physical setting. We believe these directions are fascinating future avenues for further research on nonlocality in nanostructures.

Appendix

Euler's formula

We consider a simply supported, elastic, inextensible circular rod of length l, subjected to a compressive load F applied at point B, as shown in Fig. 2. During compression, the rod changes its curvature and we can denote α as the initial angle at point A, u_1 is the displacement of the end of the rod at the right support from point B to C, and u_2 is the deflection at point X. The vectors $\mathbf{t}$ and $\mathbf{n}$ are the tangent and normal directions at point X, respectively.

The governing differential equation for the elastica can be expressed as [44]:

$$\theta(s)'' + \lambda^2 \sin\theta(s) = 0, \tag{A.1}$$

where θ is the angle of inclination of the tangent $\mathbf{t}$ to the elastica at point X, $\lambda^2 = \frac{F}{EI}$, F is the axially applied load, E is Young's modulus, I is the moment of inertia, and $s \in [0, l]$ is the nondimensional arc-length parameter defined by its centerline.

From basic geometric considerations relating to the displacement vector (from point X_0 to X), we obtain the standard relation between curvature and the rotation angle of the tangent:

$$\varkappa = \frac{\mathrm{d}\theta}{\mathrm{d}s}. \tag{A.2}$$

The moment-curvature relationship can be expressed as [66]:

$$\varkappa = \frac{\mathrm{d}\theta}{\mathrm{d}s} = \frac{M}{EI}. \tag{A.3}$$

The boundary conditions for a simply supported beam are:

$$u_1(0) = 0, \tag{A.4}$$

$$u_2(0) = u_2(l) = 0, \tag{A.5}$$

$$\theta'(0) = \theta'(l) = 0. \tag{A.6}$$

These boundary conditions describe the theoretical framework of the classical Euler's buckling case, in which a slender elastic rod is subjected to axial compression between two hinged supports. In this formulation, the supports prevent transverse displacements while permitting free rotation, thereby providing a coherent mathematical representation of the problem. In our approach, we aim to obtain the elastica shape for a given initial angle and bifurcation mode m. In this case, the system of equations describing the elastica determines the corresponding coordinates x and y for each chosen point X along the rod axis.

Taking into account the boundary conditions (Eq. (A.4), Eq. (A.5), and Eq. (A.6)) and using elliptic integrals, we can solve the governing Eq. (2.1), obtaining the solution presented in [76]:

$$x = -s + \frac{2}{\lambda}\big\{E\left[am\left(s\lambda + K(k), k\right), k\right] - E\left[am\left(K(k), k\right), k\right]\big\}, \tag{A.7}$$

$$y = -\frac{2k}{\lambda} cn\left(s\lambda + K(k), k\right), \tag{A.8}$$

where $x, y \in \langle 0, l\rangle$ are the coordinates along the rod axes, $E(k)$ is the incomplete elliptic integral of the second kind with $E(x,k) = \int\limits_0^x \sqrt{1 - k\sin^2 t\,\mathrm{d}t}$, $k = \sin\frac{\alpha}{2}$, α is the initial angle with $\alpha = \theta(0)$ and $0 \leq \alpha \leq \pi$, and $K(k)$ is the complete elliptic integral of the first kind, defined as $K(k) = \int\limits_0^{\pi/2} \frac{\mathrm{d}\phi}{\sqrt{1-k^2\sin^2\phi}}$.

Using Eq. (A.7) and Eq. (A.8), the solution for a given initial angle α and mode m can be plotted. In Fig. A1, the elastica curves are shown for various values of the initial angles ($\alpha = 30°$, $60°$, $90°$, $120°$, $170°$, and $179°$) and for bifurcation modes $m = 1, 2, 3$, and 4. These results illustrate the post-critical behavior of the compressed rod. Figure A1 visualizes how the nonlinear post-buckling shapes evolve with different bifurcation modes m. Higher values of m lead to more complex deflection patterns and richer branches of solutions. The first mode ($m = 1$) is the most critical case, because it occurs at the lowest load and produces the largest midspan deflection. In the second mode ($m = 2$), the rod bends into two half-waves with a node at the midpoint. The midspan deflection is approximately half that of the first mode ($m = 1$) and occurs symmetrically upward and downward along the axis. It needs four times the critical load value of the first mode. In the third mode ($m = 3$), the rod exhibits three half-waves with two interior nodes. The midspan deflection is around three times smaller than that in the first mode $m = 1$, requiring nine times the critical load value. In the fourth mode ($m = 4$), the rod deforms into four half-waves with

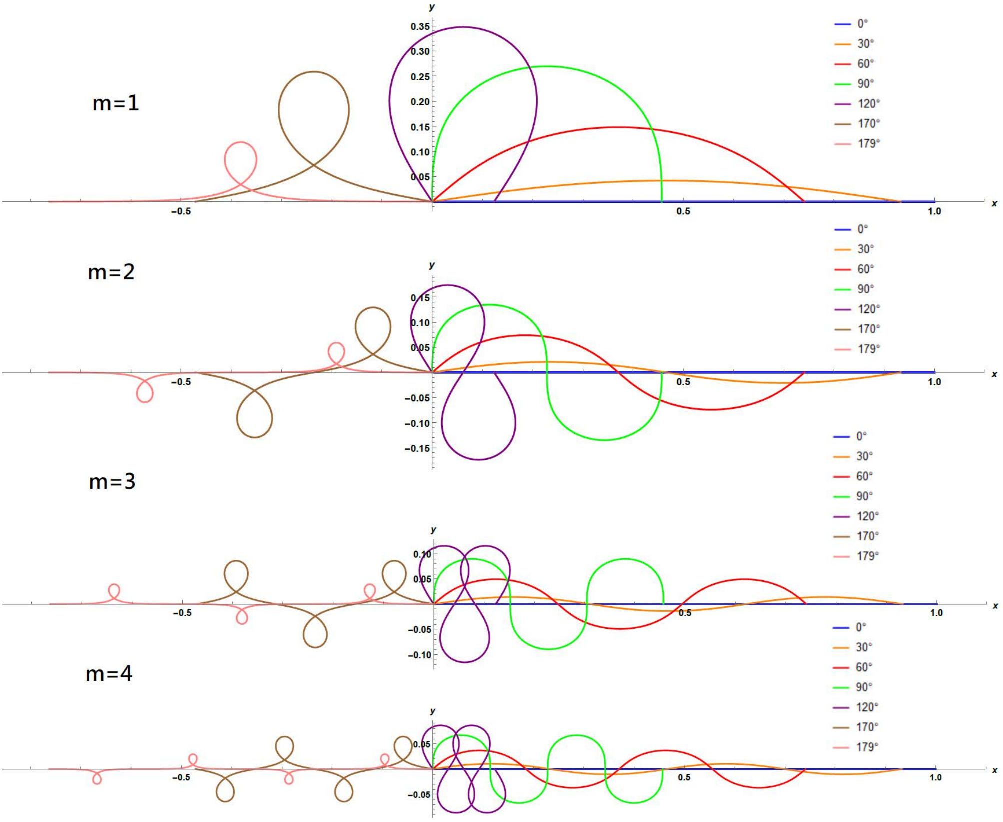

FIG. A1. Various shapes of elastica for given initial angles α and m-th modes of bifurcation.

three internal nodes. The maximum deflection is about one-quarter of that in the first mode ($m = 1$), while requiring a sixteen-fold increase in the critical load. The inherent symmetry of the problem is clearly reflected in these deformation patterns.

These particular initial angles (0°, 30°, 60°, 90°, 120°, 170°, 179°) were selected to illustrate the full spectrum of elastica behavior. For small angles (0° to 30°), the rod shows relatively gentle deflections with smooth, gradually increasing curvature. Medium angles (60° to 120°) highlight the stronger nonlinear character of the elastica, with curves bending more significantly and beginning to form loops, particularly in higher buckling cases. Very large angles (170° to 179°) correspond to extreme cases, where the rod shape approaches self-intersecting loops and folding. Because of its expected relevance for future experimental validation, the analysis concentrates mainly on the first buckling mode.

Fundings

This research did not receive any specific grant from funding agencies in the public, commercial, or not-for-profit sectors.

Conflict of interests

The authors declare that there are no known competing financial interests or personal relationships that could have influenced the work described in this paper.

Authors' contribution

Aleksandra Manecka-Padaż: supervision, conceptualization, methodology, validation, formal analysis, investigation, writing original draft. Ewa Eliza Rożko: methodology, data curation, validation, formal analysis, investigation, review and editing. Zdzisław Nowak: methodology, validation, formal analysis, investigation, review. Piotr Chudziński: methodology, validation, formal analysis, investigation, review. All authors reviewed and approved the final manuscript.

References

1. Zaccaria D., Bigoni D., Noselli G., Misseroni D., Structures buckling under tensile dead load, *Proceedings of the Royal Society A: Mathematical, Physical and Engineering Sciences*, **467**(2130): 1686–1700, 2011, https://doi.org/10.1098/rspa.2010.0505.
2. Bistafa S.R., Euler's variational approach to the elastica, *Euleriana*, **3**(2): 156–175, 2023, https://doi.org/10.56031/2693-9908.1055.

3. Matsutani S., Euler's elastica and beyond, *Journal of Geometry and Symmetry in Physics*, **17**: 45–86, 2010, https://projecteuclid.org/journalArticle/Download?urlId=10.7546%2Fjgsp-17-2010-45-86.

4. Kirchhoff G., On the equilibrium and motion of an elastic disc [in German: Über das Gleichgewicht und die Bewegung einer elastischen Scheibe], *Journal für die reine und angewandte Mathematik*, **40**: 5–88, 1850, http://eudml.org/doc/147439.

5. Born M., *Studies on the stability of the elastic line in the plane and in space under different limiting conditions* [in German: *Untersuchungen über die stabilität der elastischen Linie in Ebene und Raum: Unter verschiedenen Grenzbedingungen*], Vandenhoeck & Ruprecht, 1906.

6. Nishinari K., Nonlinear dynamics of solitary waves in an extensible rod, *Proceedings of the Royal Society A: Mathematical, Physical and Engineering Sciences*, **453**(1959): 817–833, 1997, https://doi.org/10.1098/rspa.1997.0045.

7. Chucheepsakul S., Monprapussorn T., Divergence instability of variable-arc-length elastica pipes transporting fluid, *Journal of Fluids and Structures*, **14**(6): 895–916, 2000, https://doi.org/10.1006/jfls.2000.0301.

8. Vassilev V.M., Djondjorov P.A., Mladenov I.M., Cylindrical equilibrium shapes of fluid membranes, *Journal of Physics A: Mathematical and Theoretical*, **41**: 435201, 2008, https://doi.org/10.1088/1751-8113/41/43/435201.

9. Kibach H., Ture Savadkoohi A., Lamarque C.-H., Free vibrations of an elastica around its post-buckled configurations, *International Journal of Non-Linear Mechanics*, **179**: 105250, 2025, https://doi.org/10.1016/j.ijnonlinmec.2025.105250.

10. Taloni A., Vilone D., Ruta G., General theory for plane extensible elastica with arbitrary undeformed shape, *International Journal of Engineering Science*, **193**: 103941, 2023, https://doi.org/10.1016/j.ijengsci.2023.103941.

11. Leanza S., Zhao R.R., Hutchinson J.W., The elastica with pre-stress due to natural curvature, *Journal of the Mechanics and Physics of Solids*, **190**: 105690, 2024, https://doi.org/10.1016/j.jmps.2024.105690.

12. Phungpaingam B., Chucheepsakul S., Postbuckling behavior of variable-arc-length elastica connected with a rotational spring joint including the effect of configurational force, *Meccanica*, **53**(10): 2619–2636, 2018, https://doi.org/10.1007/s11012-018-0847-x.

13. Lai B., Liew J.Y.R., Wang T., Buckling behaviour of high strength concrete encased steel composite columns, *Journal of Constructional Steel Research*, **154**: 27–42, 2019, https://doi.org/10.1016/j.jcsr.2018.11.023.

14. Wang Q., Zou H.L., Deng Z.C., Snap-through of an elastica under bilateral displacement control at a material point, *Acta Mechanica Sinica*, **36**(3): 727–734, 2020, https://doi.org/10.1007/s10409-020-00937-4.

15. Fraldi M., Palumbo S., Cutolo A., Carotenuto A.R., Bigoni D., Bimodal buckling governs human fingers' luxation, *Proceedings of the National Academy of Sciences of the United States of America*, **120**(44): e2311637120, 2023, https://doi.org/10.1073/pnas.2311637120.

16. Hathaipichitchai P., Klaycham K., Jiammeepreecha W., Athisakul C., Chucheepsakul S., Postbuckling behavior of variable-arc-length elastica pipe conveying fluid including effects of self-weight and pressure variation, *International Journal of Non-Linear Mechanics*, **164**: 104760, 2024, https://doi.org/10.1016/j.ijnonlinmec.2024.104760.

17. Curatolo M., Napoli G., Nardinocchi P., Turzi S., Swelling-driven soft elastic catapults, *International Journal of Non-Linear Mechanics,* **162**: 104727, 2024, https://doi.org/10.1016/j.ijnonlinmec.2024.104727.

18. Wang X., Qiu X., Elastica-plastica theory of Euler-Bernoulli beams subjected to concentrated loads, *Applied Mathematical Modelling*, **136**: 115623, 2024, https://doi.org/10.1016/j.apm.2024.07.030.

19. Matsutani S., Statistical mechanics of elastica for the shape of supercoiled DNA: Hyperelliptic elastica of genus three, *Physica A: Statistical Mechanics and its Applications*, **643**: 129799, 2024, https://doi.org/10.1016/j.physa.2024.129799.

20. Duan H.L., Wang J., Karihaloo B.L., Theory of elasticity at the nanoscale, [in:] *Advances in Applied Mechanics*, **42**: 1–68, 2009, https://doi.org/10.1016/S0065-2156(08)00001-X.

21. Wang G.-F., Feng X.-Q., Surface effects on buckling of nanowires under uniaxial compression, *Applied Physics Letters*, **94**(14): 141913, 2009, https://doi.org/10.1063/1.3117505.

22. Moradi M., Fereidon A.H., Sadeghzadeh S., Dynamic modeling for nanomanipulation of polystyrene nanorod by atomic force microscope, *Scientia Iranica*, **18**(3): 808–815, 2011, https://doi.org/10.1016/j.scient.2011.06.003.

23. Liu J.L., Mei Y., Xia R., Zhu W.L., Large displacement of a static bending nanowire with surface effects, *Physica E: Low-Dimensional Systems and Nanostructures*, **44**(10): 2050–2055, 2012, https://doi.org/10.1016/j.physe.2012.06.009.

24. Thongyothee C., Chucheepsakul S., Postbuckling of unknown-length nanobeam considering the effects of nonlocal elasticity and surface stress, *International Journal of Applied Mechanics*, **7**(3): 1550042, 2015, https://doi.org/10.1142/S1758825115500428.

25. Challamel N., Kocsis A., Wang C.M., Discrete and nonlocal elastica, *International Journal of Non-Linear Mechanics*, **77**: 128–140, 2015, https://doi.org/10.1016/j.ijnonlinmec.2015.06.012.

26. Lembo M., Exact solutions for postbuckling deformations of nanorods, *Acta Mechanica*, **228**(6): 2283–2298, 2017, https://doi.org/10.1007/s00707-017-1834-3.

27. Tang Y., Qing H., Bending, buckling and free vibration of Timoshenko beam-based plane frame via FEM with nonlocal integral model, *Journal of Mechanics of Materials and Structures*, **18**(3): 355–374, 2023, https://doi.org/10.2140/jomms.2023.18.355.

28. Hussain M., Naeem M.N., Vibration characteristics of single-walled carbon nanotubes based on nonlocal elasticity theory using wave propagation approach (WPA) including chirality, [in:] *Perspective of Carbon Nanotubes*, El-Din Saleh H., El-Sheikh S.M.M. [Eds], 2019, https://doi.org/10.5772/intechopen.85948.

29. Berecki D., Glavardanov V.B., Grahovac N.M., Zigic M.M., Bifurcation analysis of a nanotube through which passes a nanostring, *Acta Mechanica*, **235**: 6867–6888, 2024, https://doi.org/10.1007/s00707-024-04076-w.

30. Darban H., Fabbrocino F., Feo L., Luciano R., Size-dependent buckling analysis of nanobeams resting on two-parameter elastic foundation through stress-driven nonlocal elasticity model, *Mechanics of Advanced Materials and Structures*, **28**(23): 2408–2416, 2021, https://doi.org/10.1080/15376494.2020.1739357.

31. Darban H., Luciano R., Darban R., Buckling of cracked micro- and nanocantilevers, *Acta Mechanica*, **234**(2): 693–704, 2023, https://doi.org/10.1007/s00707-022-03417-x.

32. Darban H., Elastostatics of nonuniform miniaturized beams: Explicit solutions through a nonlocal transfer matrix formulation, *International Journal of Engineering Science*, **198**: 104054, 2024, https://doi.org/10.1016/j.ijengsci.2024.104054.

33. Reddy J.N., Nonlocal theories for bending, buckling and vibration of beams, *International Journal of Engineering Science*, **45**(2–8): 288–307, 2007, https://doi.org/10.1016/j.ijengsci.2007.04.004.

34. Phadikar J.K., Pradhan S.C., Variational formulation and finite element analysis for nonlocal elastic nanobeams and nanoplate, *Computational Materials Science*, **49**(3): 492–499, 2010, https://doi.org/10.1016/j.commatsci.2010.05.040.

35. Aydogdu M., A general nonlocal beam theory: Its application to nanobeam bending, buckling and vibration, *Physica E: Low-dimensional Systems and Nanostructures*, **41**(9): 1651–1655, 2009, https://doi.org/10.1016/j.physe.2009.05.014.

36. Challamel N., Wang C.M., Elisahakoff I., Discrete systems behave as nonlocal structural elements: Bending, buckling and vibration analysis, *European Journal of Mechanics – A/Solids*, **44**: 125–135, 2014, https://doi.org/10.1016/j.euromechsol.2013.10.007.

37. Shaat M., Abdelkefi A., New insights on the applicability of Eringen's nonlocal theory, *International Journal of Mechanical Sciences*, **121**: 67–75, 2017, https://doi.org/10.1016/j.ijmecsci.2016.12.013.

38. Surmont F., Coache D., Geometrically exact static 3D Cosserat rods problem solved using a shooting method, *International Journal of Non-Linear Mechanics*, **119**: 103330, 2020, https://doi.org/10.1016/j.ijnonlinmec.2019.103330.

39. Darban H., Luciano R., Basista M., Free transverse vibrations of nanobeams with multiple cracks, *International Journal of Engineering Science*, **177**: 103703, 2022, https://doi.org/10.1016/j.ijengsci.2022.103703.

40. Singh J., Shooting method for solving two-point boundary value problems in ODEs numerically, [in:] *Artificial Intelligence Technology in Healthcare*, CRC Press, 2024, https://doi.org/10.1201/9781003377818-7.

41. Zorić A., Trajković-Milenković M., Zlatkov D., Vacev T., Semi-analytical solution for elastoplastic deflection of non-prismatic cantilever beams with circular cross-section, *Applied Sciences*, **12**(11): 5439, 2022, https://doi.org/10.3390/app12115439.

42. Eringen A.C., Linear theory of nonlocal elasticity and dispersion of plane waves, *International Journal of Engineering Science*, **10**(5): 425–435, 1972, https://doi.org/10.1016/0020-7225(72)90050-X.

43. Eringen A.C., Edelen D.G.B., On nonlocal elasticity, *International Journal of Engineering Science*, **10**(3): 233–248, 1972, https://doi.org/10.1016/0020-7225(72)90039-0.

44. Eringen A.C., On differential equations of nonlocal elasticity and solutions of screw dislocation and surface waves, *Journal of Applied Physics*, **54**(9): 4703–4710, 1983, https://doi.org/10.1063/1.332803.

45. Romano G., Barretta R., Nonlocal elasticity in nanobeams: The stress-driven integral model, *International Journal of Engineering Science*, **115**: 14–27, 2017, https://doi.org/10.1016/j.ijengsci.2017.03.002.

46. Nobili A., Pramanik D., A well-posed theory of linear nonlocal elasticity, *International Journal of Engineering Science*, **215**: 104314, 2025, https://doi.org/10.1016/j.ijengsci.2025.104314.

47. Barretta R., Feo L., Luciano R., Marotti de Sciarra F., Application of an enhanced version of the Eringen differential model to nanotechnology, *Composites Part B: Engineering*, **96**: 274–280, 2016, https://doi.org/10.1016/j.compositesb.2016.04.023.

48. Fernández-Sáez J., Zaera R., Loya J.A., Reddy J.N., Bending of Euler–Bernoulli beams using Eringen's integral formulation: A paradox resolved, *International Journal of Engineering Science*, **99**: 107–116, 2016, https://doi.org/10.1016/j.ijengsci.2015.10.013.

49. Ceballes S., Larkin K., Rojas E., Ghaffari S.S., Abdelkefi A., Nonlocal elasticity and boundary condition paradoxes: A review, *Journal of Nanoparticle Research*, **23**: 66, 2021, https://doi.org/10.1007/s11051-020-05107-y.

50. Kaplunov J., Prikazchikov D.A., Prikazchikova L., On integral and differential formulations in nonlocal elasticity, *European Journal of Mechanics – A/Solids*, **100**: 104497, 2023, https://doi.org/10.1016/j.euromechsol.2021.104497.

51. Pham C.V., Vu T.N.A., On the well-posedness of Eringen's non-local elasticity for harmonic plane wave problems, *Proceedings of the Royal Society A: Mathematical, Physical and Engineering Sciences*, **480**(2293): 20230814, 2024, https://doi.org/10.1098/rspa.2023.0814.

52. Barretta R., Luciano R., Marotti de Sciarra F.M., Vaccaro M.S., Modelling issues and advances in nonlocal beams mechanics, *International Journal of Engineering Science*, **198**: 104042, https://doi.org/10.1016/j.ijengsci.2024.104042.

53. Song Z.W., Lai S.K., Lim C.W., Li C., Theoretical examination for the consistency of Eringen's nonlocal theories in nanomaterial modeling, *International Journal of Applied Mechanics*, **17**(06): 2550044, 2025, https://doi.org/10.1142/S1758825125500449.

54. Pramanik D., Nobili A., A well-posed non-local theory in 1D linear elastodynamics, *International Journal of Solids and Structures*, **320**: 113511, 2025, https://doi.org/10.1016/j.ijsolstr.2025.113511.

55. Pisano A.A., Fuschi P., Polizzotto C., Euler–Bernoulli elastic beam models of Eringen's differential nonlocal type revisited within a C^0 – Continuous displacement framework, *Meccanica*, **56**: 2323–2337, 2021, https://doi.org/10.1007/s11012-021-01361-z.

56. Song Z.W., Lai S.K., Lim C.W., A new insight into the paradoxical integral and differential constitutive relations of Eringen nonlocal theory, *Journal of Engineering Mechanics*, **151**(2): 04024112, 2025, https://doi.org/10.1061/JENMDT.EMENG-8021.

57. Song Z.W., Lai S.K., Lim C.W., On the truth of integral and differential constitutive forms in strain-driven nonlocal theories with bi-Helmholtz kernels for nanobeam analysis, *Thin-Walled Structures*, **214**: 113338, 2025, https://doi.org/10.1016/j.tws.2025.113338.

58. Song Z.W., Lai S.K., Lim C.W., On the nature of constitutive boundary and interface conditions in stress-driven nonlocal integral model for nanobeams, *Applied Mathematical Modelling*, **144**: 115949, 2025, https://doi.org/10.1016/j.apm.2025.115949.

59. Karličić D., Murmu T., Adhikari S., McCarthy M., *Nonlocal Structural Mechanics*, John Wiley & Sons, 2016, https://doi.org/10.1002/9781118572030.

60. Lu P., Lee H.P., Lu C., Zhang P.Q., Dynamic properties of flexural beams using a nonlocal elasticity model, *Journal of Applied Physics*, **99**(7): 073510, 2006, https://doi.org/10.1063/1.2189213.

61. Timesli A., An efficient approach for prediction of the nonlocal critical buckling load of double-walled carbon nanotubes using the nonlocal Donnell shell theory, *SN Applied Sciences*, **2**: 407, 2020, https://doi.org/10.1007/s42452-020-2182-9.

62. Wang C.M., Zhang Y.Y., Ramesh S.S., Kitipornchai S., Buckling analysis of micro- and nano-rods/tubes based on nonlocal Timoshenko beam theory, *Journal of Applied Physics*, **39**(17): 3904–3909, 2006, https://doi.org/10.1088/0022-3727/39/17/029.

63. Reddy J.N., Pang S.D., Nonlocal continuum theories of beams for the analysis of carbon nanotubes, *Journal of Applied Physics*, **103**(2): 023511, 2008, https://doi.org/10.1063/1.2833431.

64. Wang L., Hu H., Flexural wave propagation in single-walled carbon nanotubes, *Physical Review B – Condensed Matter and Materials Physics*, **71**(19): 195412, 2005, https://doi.org/10.1103/PhysRevB.71.195412.

65. Akpinar M., Uzun B., Yayli M.Ö., Dynamic response of axially loaded carbon nanotubes considering armchair, chiral, and zigzag configurations, *Mechanics Based Design of Structures and Machines*, **54**(1): 2553325, 2025, https://doi.org/10.1080/15397734.2025.2553325.

66. Natsuki J., Lei X.-W., Wu S., Natsuki T., Modeling and vibration analysis of carbon nanotubes as nanomechanical resonators for force sensing, *Micromachines*, **15**(9): 1134, 2024, https://doi.org/10.3390/mi15091134.

67. Uzun B., Yayli M.Ö., Civalek Ö., Elastic medium and torsional spring effects on the nonlocal dynamic of functionally graded porous nanotubes, *Archive of Applied Mechanics*, **94**: 1291–1311, 2024, https://doi.org/10.1007/s00419-024-02576-8.

68. Ebrahimi R., Chaotic vibrations of carbon nanotubes subjected to a traversing force considering nonlocal elasticity theory, *Proceedings of the Institution of Mechanical Engineers, Part N: Journal of Nanomaterials, Nanoengineering and Nanosystems*, **236**(1–2): 31–40, 2022, https://doi.org/10.1177/23977914211063309.

69. Murmu T., Pradhan S.C., Small-scale effect on the vibration of nonuniform nanocantilever based on nonlocal elasticity theory, *Physica E: Low-dimensional Systems and Nanostructures*, **41**: 1451–1456, 2009, https://doi.org/10.1016/j.physe.2009.04.015.

70. Wang C.M., Zhang Z., Challamel N., Duan W.H., Calibration of Eringen's small length scale coefficient for initially stressed vibrating nonlocal Euler beams based on microstructured beam model, *Journal of Physics D: Applied Physics*, **46**(34): 345501, 2013, https://doi.org/10.1088/0022-3727/46/34/345501.

71. Khaniki H.B., Hosseini-Hashemi S., Buckling analysis of tapered nanobeams using nonlocal strain gradient theory and a generalized differential quadrature method, *Materials Research Express*, **4**(6): 065003, 2017, https://doi.org/10.1088/2053-1591/aa7111.

72. Thongyothee Ch., Chucheepsakul S., Postbuckling behaviors of nanorods including the effects of nonlocal elasticity theory and surface stress, *Journal of Applied Physics*, **114**(24): 243507, 2013, https://doi.org/10.1063/1.4829896.

73. Lu P., Lee H.P., Lu C., Zhang P.Q., Dynamic properties of flexural beams using a nonlocal elasticity model, *Journal of Applied Physics*, **99**(7): 073510, 2017, https://doi.org/10.1063/1.2189213.

74. De Rosa M.A., Lippiello M., Babilio E., Ceraldi C., Nonlocal vibration analysis of a nonuniform carbon nanotube with elastic constraints and an attached mass, *Materials*, **14**(13): 3445, 2021, https://doi.org/10.3390/ma14133445.

75. Euler L., On stability of column [in Latin: De motu columnarum erectarum], [in:] *Novi Commentarii academiae scientiarum Petropolitanae*, **10**: 99–140, 1757 (published 1759).

76. Bigoni D., *Nonlinear Solid Mechanics: Bifurcation Theory and Material Instability*, Cambridge University Press, 2012.

77. Manecka-Padaż A., Jenczyk P., Pęcherski R.B., Nykiel A., Experimental investigation of Euler's elastica: In-situ SEM nanowire post-buckling, *Bulletin of the Polish Academy of Sciences, Technical Sciences*, **70**(6): e143648, 2022, https://doi.org/10.24425/bpasts.2022.143648.

78. Dormand J.R., Prince P.J., A family of embedded Runge-Kutta formulae, *Journal of Computational and Applied Mathematics*, **6**(1): 19–26, 1980, https://doi.org/10.1016/0771-050X(80)90013-3.

79. Calvo M., Montijano J.I., Randez L., A fifth-order interpolant for the Dormand and Prince Runge-Kutta method, *Journal of Computational and Applied Mathematics*, **29**(1): 91–100, 1990, https://doi.org/10.1016/0377-0427(90)90198-9.

80. Civalek Ö., Demir Ç., Bending analysis of microtubules using nonlocal Euler–Bernoulli beam theory, *Applied Mathematical Modelling*, **35**(5): 2053–2067, 2011, https://doi.org/10.1016/j.apm.2010.11.004.

Received October 31, 2025; revised December 1, 2025; accepted December 6, 2025;
available online December 12, 2025; version of record May 15, 2026;
published issue June 24, 2026.

Contents

Research Papers

Review Paper

Technical Note